CHARACTERIZATION OF A HIGH-DENSITY, LARGE-AREA VHF PLASMA SOURCE

THÈSE N^{O} 3495 (2006)

PRÉSENTÉE LE 21 AVRIL 2006
À LA FACULTÉ SCIENCES DE BASE
CRPP
SECTION DE PHYSIQUE

ÉCOLE POLYTECHNIQUE FÉDÉRALE DE LAUSANNE

POUR L'OBTENTION DU GRADE DE DOCTEUR ÈS SCIENCES

PAR

Hannes SCHMIDT

physicien diplômé EPF
de nationalité autrichienne

acceptée sur proposition du jury:

Prof. R. Schaller, président du jury
Dr Ch. Hollenstein, directeur de thèse
Prof. P. Rudolf von Rohr, rapporteur
Dr J. Schmitt, rapporteur
Prof. J. Winter, rapporteur

ÉCOLE POLYTECHNIQUE
FÉDÉRALE DE LAUSANNE
Lausanne, EPFL
2006

Abstract

Feasibility Study of Shaped Electrode

The objective of this project was a feasibility study of a novel, large-area plasma reactor for thin film production, based on a shaped electrode technique ("lens") to compensate the standing wave non-uniformity.

Cylindrical Test Reactor

In the first phase a cylindrical reactor was designed and constructed to show the "proof of principle" of a novel electrode design. The cylindrical geometry of the reactor was chosen in order to allow easier comparison with theory and simulations already performed by the CRPP. The reactor parameters were $100[\mathrm{cm}]$ electrode diameter at an excitation frequency of $67.8[\mathrm{MHz}]$. First it was shown that uniform electric fields can be obtained (a necessary condition for plasma homogeneity) and subsequently it was demonstrated that the special electrode design can compensate the standing wave effect at VHF.

Rectangular Industrial Reactor

The "proof of principle" for the cylindrical shaped electrode paved the way for the rectangular-shaped electrode. A process compatible in-situ optical uniformity measurement system enabled the measurement of the standing wave effect at typical industrial frequencies ($13.56[\mathrm{MHz}]$, $27.12[\mathrm{MHz}]$, $40.68[\mathrm{MHz}]$, $67.8[\mathrm{MHz}]$, $100.0[\mathrm{MHz}]$) in an industrial rectangular, parallel plate electrode reactor design. Operating at $100.0[\mathrm{MHz}]$ required the construction of a triple stub tuner, which is a interesting way of impedance matching at VHF for PECVD. In spite of parasitic edge plasma, the measurements carried out with the rectangular shaped electrode corroborated the conclusions of the cylindrical test reactor experiments.

Keywords: PECVD, Large-area Reactor, Capacitive Discharges, RF Discharges, VHF Plasma, Standing Wave, Shaped Electrode, Uniformity Improvement, Impedance Matching, Triple Stub Tuner.

Version abrégée

Électrode incurvée

Le but de ce projet était de faire une étude de faisabilité d'un nouveau réacteur plasma de grande surface pour la production de couches minces. Ce réacteur a été conçu avec une électrode incurvée de manière à compenser la non-uniformité du plasma provoquée par une onde stationnaire présente lors de l'utilisation de fréquences d'excitation élevées.

Réacteur cylindrique

La première phase consistait à tester le principe de cette nouvelle conception d'électrode en réalisant un réacteur cylindrique. Cette géométrie de réacteur a été choisie afin de faciliter la comparaison avec la théorie ainsi qu'avec les simulations déjà effectuées par le CRPP. Ce réacteur de $100[\mathrm{cm}]$ de diamètre a été conçu pour une fréquence d'excitation de $67.8[\mathrm{MHz}]$. Il a été montré qu'un champ électrique uniforme pouvait être produit (condition nécessaire à l'homogénéité du plasma) et en conséquence, il a été montré que cette nouvelle conception d'électrode pouvait compenser l'effet de l'onde stationnaire à très hautes fréquences (VHF) d'excitation.

Réacteur rectangulaire industriel

Le test effectué sur un réacteur cylindrique n'a été qu'une étape avant l'implémentation de cette technologie dans un réacteur ayant des électrodes rectangulaires. Un diagnostic in situ de l'uniformité optique du plasma a permis de mesurer l'effet de l'onde stationnaire lors de l'utilisation de fréquences d'excitation typiques ($13.56[\mathrm{MHz}]$, $27.12[\mathrm{MHz}]$, $40.68[\mathrm{MHz}]$, $67.8[\mathrm{MHz}]$, $100.0[\mathrm{MHz}]$) dans un réacteur rectangulaire industriel avec des électrodes planes. L'utilisation d'une fréquence d'excitation de $100.0[\mathrm{MHz}]$ a nécessité la construction d'un adaptateur d'impédance avec trois bras de réactance (“triple stub tuner”), qui est une première pour l'accord d'impédance à très haute fréquence pour des réacteurs PECVD. Malgré des plasmas parasites dans les bords du réacteur, les mesures effectuées avec une géométrie rectangulaire ont confirmé les découvertes mises à jour dans le réacteur cylindrique.

Mots-clés: PECVD, Réacteur de grande surface, Décharges capacitives, Décharges radio-fréquences (RF), Plasma à très haute fréquence (VHF), Onde stationnaire, Électrode incurvée, Amélioration de l'uniformité, Accord d'impédance, Triple Stub Tuner.

Contents

Chapter Synopsis

Part I: Introduction

Chapter 1: Introduction

1.1 Prologue

Substrate sizes

In 1992, the state-of-the-art fabrication machines for manufacturing liquid crystal displays (LCD) were able to handle $350[\mathrm{mm}] \times 450[\mathrm{mm}]$ substrates, which corresponds to two $10.4[\mathrm{inch}]$ laptop computer screens. Nowadays, in 2005, state-of-the-art facilities operate with $1900[\mathrm{mm}] \times 2200[\mathrm{mm}]$ substrates, which yield up to six $46[\mathrm{inch}]$ flat panel television (TV) screens per substrate. The substrate's diagonal has leapt from about $0.6[\mathrm{m}]$ at the outset to almost $3[\mathrm{m}]$ today, a factor of five. As for the substrate's area, it was enlarged from $0.16[\mathrm{m}^2]$ to $4.2[\mathrm{m}^2]$, thus the surface has grown twenty-six-fold.[1]

Gain in productivity imperative

The manufacturers of thin-film transistor (TFT) based flat panel displays and photovoltaic solar cells based on amorphous hydrogenated silicon (a-Si:H) thin films are constantly forced to raise their productivity from generation to generation of fabrication facilities, in plain terms they have to produce more in less time and to lower their production cost per unit area in order to remain competitive in their respective markets. Two general approaches are viable for the manufacturing process in order to improve the productivity:

1. Produce more in one batch: Increasing the lot size per batch for a large-area thin-film facility means enlarging the substrate size ("upscaling"). By the economy of scale the production becomes more cost-effective for small-sized products.
2. Produce one batch faster: Reducing the turnaround time for one batch means higher deposition or etching rate of thin films while keeping the same substrate size ("higher throughput").

Engineering solutions

Other engineering solutions to increase the overall throughput of a production line like parallel handling of several substrates ("parallelization"),[122] special architectures as clustering or stacked reactor or sophisticated mechanisms to speed up loading and unloading contribute as well, but do not touch the core of the thin-film production process and are thus deliberately left out of consideration here.

Technology enabler

Apart from the need of constantly lowering production costs, there was also always the very promising possibility to enable new consumer products by new manufacturing techniques. The economical production of new consumer products becomes feasible only with improvements and progress in production processes. New consumer products mean new markets and hold out the prospects of economic growth. In the last decade it was above all the flat panel display (FPD) market for computers which demanded larger volumes and monitor sizes. Currently, the high demand for flat TV screens can be determined as one of the key factors fuelling the rapid development of very large areas production techniques. Future applications are likely to be highly efficient photovoltaic solar cells and TFTs for FPDs built on organic light emitting diodes (OLED).

Industrial requirements

Various plasma-based techniques exist for forming thin films for FPDs or photovoltaic solar cells. A very common method is the plasma enhanced chemical vapour deposition (PECVD). PECVD relying on capacitively coupled plasmas (CCP) is the oldest technique and still widely used. Other techniques based on inductively coupled plasmas (ICP), microwave discharges etc. have been investigated and even showed thin films of superior quality. Physical vapour deposition (PVD) is suitable only for certain thin film types such as transparent conductors or metallization layers, but cannot replace CCPs for a-Si. Buyers of large-area equipment are requesting fabrication facilities of utmost reliability, short down-time and long mean-time between failures. At the same time, manufacturing constraints must be met and yield maintained or even improved from generation to generation. Only CCPs have so far been able to meet the industry's long-term requirements and to offer the possibility of easy upscaling.

1.2 The Uniformity Issue in Large Area Reactors

Large-area uniformity

One of the most important criteria for large-area thin-film fabrication facilities is their ability to comply with uniformity specifications. Buyers of fabrication equipment typically demand a guaranteed uniformity between 5% and 10% across the whole substrate area, except for a small border margin. This poses great challenges to the equipment manufacturer in terms of construction and process engineering, especially when the substrate size is upscaled.

Process parameters

There is a wide range of parameters which influences the uniformity and the properties of the thin film. There are parameters related to the hardware of the reactor, others are process parameters which can be easily changed from process to process without altering the mechanical setup of the reactor. Table 1-1 gives a brief outline of typical parameters which can influence a process and affect its reproducibility in a capacitively coupled plasma reactor. It is clear that with each additional parameter we add more complexity to the system under observation.

Table 1-1: Typical parameters for process engineering on CCP systems.

Hardware Parameters	Process Parameters
1. Interelectrode distance	1. Pressure
2. Electrode geometry (e.g. cylindrical, rectangular)[68]	2. Power
3. Electrode shape (e.g. flat, lens, ladder, double comb)	3. Gas composition
4. Electrode symmetry[73]	4. Frequency
5. Electrode surface materials & surface state (e.g. enhances or curbs secondary electron emission)[42][75][82]	5. Temperature
6. Location and number of RF feeding points[4][5][32][50][66][19]	6. Gasflow

1.2.1 What is Uniformity?

In the final application we want to have a uniform coating, either by deposition or by etching. This means for the underlying process a uniform plasma. A uniform plasma for thin film processing implies according to Schmitt[53] spatially uniform

1. plasma density and temperature (or distribution function),
2. RF electrode voltage,
3. sheath voltage (i.e. uniform ion impact energy)

and other process parameters such as gas composition, pressure and substrate temperature. Basically "uniform process" means that all plasma parameters are also uniform.

1.2.2 Very large-area Reactors

Upscaling problems

According to CHOI et al.[120] in the past, the basic principle behind the scale-up of PECVD processes was to maintain the intensive deposition parameters (such as reactor pressure, electrode spacing, RF excitation frequency and substrate temperature) constant, while proportionately increasing the extensive deposition parameters (such as process gas flow rates and RF power to the plasma). Intensive parameters are independent of scale whereas extensive parameters are proportional to scale, in our case the substrate area.[1] For instance, as aforementioned, the total injected power was increased 26 × during upscaling in order to maintain by way of calculation the power density per area. However, due to ever-increasing substrate sizes, which now have well exceeded $1[\mathrm{m}^2]$, most PECVD processes do not properly scale up by adjustment of extensive deposition parameters alone, for various reasons[38] such as standing wave effect and arcing phenomena. Furthermore, with respect to the extensive deposition parameters, fundamental problems arise in the uniformity of film thickness and other film properties across the substrate surface as a consequence of non-uniform RF power density within the reactor.

Electromagnetic effect

As shown in Fig. 1-1, increasing the substrate size in a RF driven CCP reactor brings about electromagnetic propagation effects. As we increase the reactor diagonal we decrease the ratio of the vacuum wavelength to the typical reactor dimension. The so-called standing wave effect will strongly contribute to a voltage non-uniformity across the substrate and becomes an appreciable perturbation in deposition[1] unless the frequency is reduced in inverse proportion to the size.

PECVD reactors are not the only technique to suffer from large-area problems. The ICP technique is difficult to scale and needs either a large distance to the substrate, or a special transmission grid otherwise an acceptable uniformity can only be achieved at very low pressures. PVD machines at very large area can show a deficit of the anode view in their centre (“anode hole”), which causes a drastic drop in the deposition rate.[119] Engineering solutions such as moving or rotating substrates[121] are not always possible due to size limitations or are not applicable due to inherent strong particle contamination generated by substrate movement and friction between mechanical parts during the process.[61]

Without technical innovation in terms of electromagnetic non-uniformity reduction no headway is possible in the field of large-area capacitively coupled RF plasmas used for thin film production.

1.3 How to achieve High Throughput?

High-density plasmas

High density plasmas are required for a high dissociation rate, which in turn enables a high deposition rate or etch rate. At low pressure such plasma can be obtained in the well-known inductively coupled plasma (ICP) source often driven by at an excitation frequency of $13.56[\mathrm{MHz}]$. But also microwave discharges working at an excitation frequency of $2.45[\mathrm{GHz}]$ are well suited as high density plasma sources. The typical electron densities achieved by these techniques can be as high as 10^{12} electrons per $[\mathrm{cm}^3]$ which is about two orders of magnitude higher than the densities reached in conventional capacitively-coupled RF plasma reactors driven at $13.56[\mathrm{MHz}]$. But changing to a different plasma source technology would mean foregoing the accepted advantages like reliability issues of CCPs.

---

[1] The terms *intensive* and *extensive* are used as defined in http://en.wikipedia.org/wiki/Intensive_and_extensive_properties

VHF CCP plasmas

There is an alternative way to achieve high density plasmas which consists of using very high excitation frequencies (VHF $20 - 150$ [MHz]) while keeping the design similar to parallel plate reactor design. It is clearly shown in the literature that the sheath voltage decreases rapidly with increasing excitation frequency.[11] This gives the possibility to couple much higher RF power into the plasma while keeping a moderate sheath voltage thus preventing the thin film from damage and electronic defects.[123][54][55][60] Electron densities higher than $10^{11}[\mathrm{cm}^{-3}]$ have already been obtained in Ar plasmas at higher gas pressures ($1[\mathrm{Torr}]$). However little is known about plasma operation at low gas pressures as typically applied in dry etch applications. In addition it has to be mentioned that the physics of the so-called VHF plasmas (about or higher than $100[\mathrm{MHz}]$) is not very well elucidated. Main motivation for VHF plasma is due to the higher deposition rate which is possible through a higher dissociation rate.[12] The trend to higher RF frequencies is also motivated by larger power in for less sheath bias, less ion bombardment, better film quality and reduced dust build up.[18][52]

Non-uniformity at VHF

But the debit-side of the VHF CCP plasma is that we reduce the ratio of the vacuum wavelength to the reactor diagonal and we run into the same difficulty as with very large area CCP reactors, namely the standing wave effect.

1.4 Conclusion

Compensation of Standing Wave Effect

Both approaches, "upscaling" and "higher throughput" by a high density plasma, have in common for a RF capacitively coupled PECVD production system that the ratio of RF wavelength to the typical system length decreases, then the typical dimensions of the reactor become non-negligible compared to the VHF wavelength and standing-wave non-uniformity problems arise as shown in Fig. 1-1. This effect is of electromagnetic origin and thus it is expected to be the most important contribution to non-uniformity at higher frequencies and in large-area reactors over a wide range of process parameters. SCHMITT pointed out that headway can only be expected in the field of capacitively coupled PECVD if the problem of the stand-

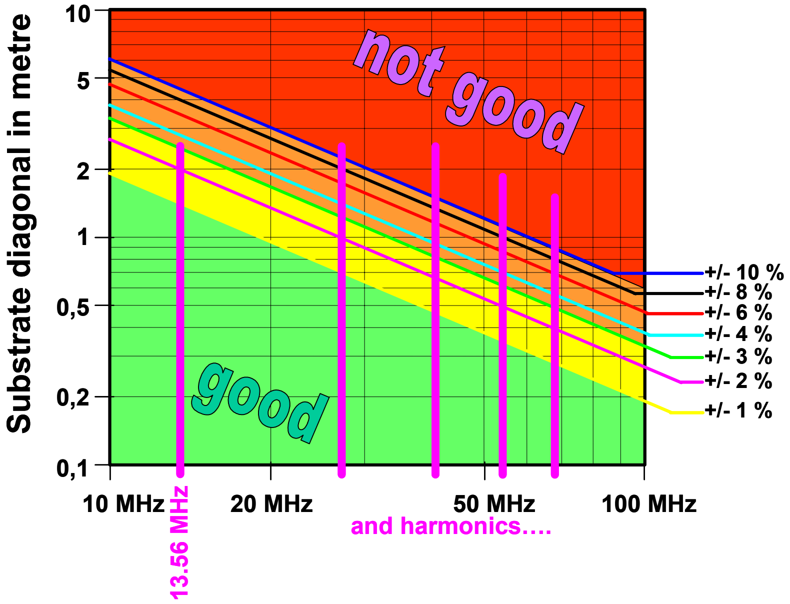

Fig. 1-1: Non-uniformity of RF power in the vacuum case due to the standing wave in a round capacitor. The abscissa gives the RF excitation frequency in [MHz], the ordinate the substrate diagonal in [m] and the percentages indicate the non-uniformity caused by standing wave. Reproduced from [53].

ing-wave-caused worsening of the uniformity is solved.[52] The removal of this source of inhomogeneity promises to be an important technological innovation in the field of application. Thus a thorough scientific investigation of the proposed method of SCHMITT[49] to reduce the non-uniformity is justified.

1.5 Solution and Proof of Principle

Starting point of thesis

In advance of this thesis, numerical studies by the CRPP and UNAXIS were performed to assess the feasibility of a special electrode which could eliminate the detrimental effect of standing wave on the uniformity as addressed above. It has been shown theoretically by SANSONNENS et al.[8] that in vacuum with a convenient shaping of the RF electrode, uniform RF voltages can be achieved, a necessary condition for uniform deposition or etching. The main aim of the present thesis is to experimentally verify these theories and simulations in the presence of plasma and to finish at the end of the thesis with a new high density plasma source suitable for deposition. The thesis started with the experimental work on the first of two reactors (see below) and its approach can be broken down into three basic steps of uniformity studies as outlined in Table 1-2. First the reference case at the low reference RF frequency $13.56[\mathrm{MHz}]$ is considered and it is verified that the uniformity is good. Then by increasing the excitation frequency the existence, significance and the extent of the standing wave effect is established. Finally it is to be shown, that the proposed shaped electrode can remove the non-uniformity. The dependence of dissociation rate at different frequencies was already established prior to this work by different authors in small-sized reactors (cf. 1.3 and cf. Chapter 2), where no uniformity limitation due to the standing wave occurs.

Table 1-2: Road map for proof of principle

Frequency	**Configuration**	**Uniformity**	**Dissociation Rate** $<n_e \cdot T_e>$
Reference ($13.56[\mathrm{MHz}]$)	Parallel Plate	Good	Low
VHF ($67.8[\mathrm{MHz}]$)	Parallel Plate	Bad	High
VHF ($67.8[\mathrm{MHz}]$)	Shaped Electrode	Good	High

Cylindrical reactor

The development of the new very high frequency plasma source for plasma enhanced chemical vapour deposition (PECVD) is made in two steps. In a first phase a cylindrical plasma reactor was designed and constructed at the CRPP. It allows an easy comparison with the theory and simulations already done beforehand. The reactor is used to show the “proof of principle” of the novel electrode design. The reactor parameters are RF electrodes with a diameter of $100[\mathrm{cm}]$ and relatively moderate RF power ($\leq 1[\mathrm{kW}]$) at an excitation frequency of $67.8[\mathrm{MHz}]$. In this first attempt only the noble gas Ar and H_2 are used. The reactor itself does not contain any sophisticated reactor features such as a showerhead and is not heated. The reactor is used to demonstrate that, with shaped electrodes, uniform electric fields can be obtained at very high excitation frequencies, a necessary condition for homogeneous etching and deposition.

Rectangular reactor

The second stage of the development of the new high density industrial plasma reactor is the design and construction, in collaboration with UNAXIS, of a rectangular plasma reactor including additional operational components such as showerhead, differential pumping system, substrate loading etc. The CRPP version of the reactor is not used for processing and similar to the cylindrical reactor, only Ar and H_2 are used. The parameters of the industrial reactor are a deposition area of about $1[\mathrm{m}^2]$ and an excitation frequency of $67.8[\mathrm{MHz}]$ including the novel electrode. The modification of the reactor is followed by an intensive testing of the plasma reactor for different non-reactive plasma processes for the flat and the shaped electrode. For this case the plasma and electric field uniformity are investigated.

Diagnostic by-products

The testing and process development on the new reactors requires the use of various plasmas diagnostics. During the reactor design, specific plasma diagnostic methods such as for the crucial measurement of the plasma uniformity were included. Optical methods using a fibre optic array and electrostatic surface probes were used in the cylindrical and rectangular plasma reactor to determine the uniformity of the plasma.

1.6 Industrial Collaboration

This thesis was supported by the *Commission Technique et Innovation (CTI)*, project no. 5602.1. In the scope of this project, the CRPP collaborated with UNAXIS BALZERS AG.

Part II: Theory

Chapter 2: RF Plasmas

2.1 Introduction

Macroscopic charge neutrality

Plasmas are ionized gases, which consist of positive (and sometimes negative) ions, electrons, as well as of neutral species in the ground and excited states. The ionization degree can vary from 100% (fully ionized gases) to very low values (e.g. $10^{-4} - 10^{-6}$; partially ionized gases). Ions are normally positively charged, except for plasmas containing gases with large electron affinities such as O_2 or halogen gases. For simplicity, we assume that the ions are singly and positively charged. The densities of the positive ions n_{i1}, n_{i2}, n_{i3},... and the electron density n_e should satisfy for the whole plasma (except the sheaths) the relation

$$n_e = n_{i1} + n_{i2} + n_{i3} + \ldots = n , \qquad \text{(Eq. 2-1)}$$

for macroscopic electrical charge neutrality, where n is called the plasma density. Much of the visible matter in the universe is in the plasma state, because stars, as well as all visible interstellar matter, are in the plasma state. Besides the astroplasmas, which are omnipresent in the universe, we can also distinguish two main groups of laboratory plasmas, i.e. the high-temperature or fusion plasmas, and the so-called low-temperature plasmas.[7] The latter group of plasmas is the subject of this thesis.

Non-thermal equilibrium and low-temperature plasma

In general, a subdivision can be made between plasmas which are in thermal equilibrium and those which are not in thermal equilibrium. Thermal equilibrium implies that the temperature of all species (electrons, ions, neutral species) is the same. High temperatures of the ion and neutral species are required to form these equilibrium plasmas ($4000[K]$ to $20\,000[K]$). On the other hand, non-thermal equilibrium plasma means that the temperatures of the different plasma species are not the same; in particular, that the electrons are characterized by a higher temperature than the heavy particles (ions, atoms, molecules). The heavy particle temperature is low, often not much higher than room temperature, but the electrons are at much higher temperatures, because they are light and easily accelerated by applied electromagnetic fields. The high electron temperature gives rise to inelastic electron collisions, which, on the one hand, sustain the plasma (e.g. electron impact ionization) and on the other hand, result in a 'chemically-rich' environment. Therefore it is customary for low temperature plasmas to be characterized by their electron energy T_e and their electron density n_e.

Ionization, breakdown and steady state

The most widely used method of generating and sustaining a low-temperature plasma for technological and technical application is by applying an electric field to a neutral gas. Any volume of a neutral gas always contains a few electrons and ions that are formed, for example, as the result of the interaction of cosmic rays or natural radioactive radiation with the gas. These free charge carriers are accelerated by the electric field and couple their energy via collisions to other particles. New charged particles may be created when these charge carriers collide with atoms and molecules in the gas or with the surfaces of the electrodes. This leads to an avalanche of charged particles that is eventually balanced by charge carrier losses via diffusion to the walls and recombination, etc. so that a steady-state plasma develops.

RF plasma

Electrical discharges are classified as DC discharges or AC discharges on the basis of the temporal behaviour of the sustaining electric field. The spatial and temporal characteristics of a plasma depend to a large degree on the particular application for which the plasma will be used. One of the most widely used configurations is the radio-frequency (RF) discharge between two plane electrodes as explained in the next section.

2.2 Capacitively Coupled RF Plasma

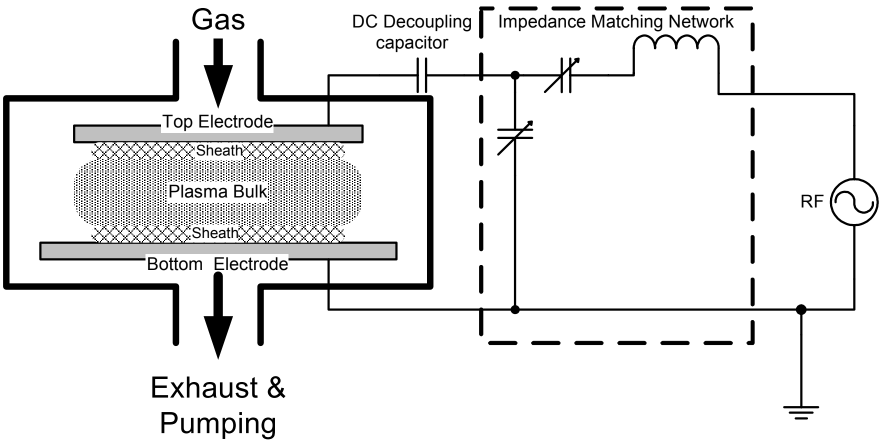

Fig. 2-1: Schematic of a simplified capacitively coupled discharge with plane parallel electrodes. The RF power is transmitted to the electrodes by an impedance matching network (here shown by an L-type). The decoupling capacitor is used for preventing DC current circulation irrespective of the type of matching.

Working principle

The radio-frequency (RF) glow discharge is ignited between two plane electrodes. In this configuration, the power is capacitively coupled to the plasma across the sheaths and the power supply interacts with the plasma almost exclusively by displacement currents. The advantage is that we can use the plasma even with electrodes covered by an insulating material. An impedance matching network is normally inserted between the RF power source and the plasma chamber to adjust the impedance of the load to the nominal $50[\Omega]$ line impedance of the RF source. An impedance matching network is necessary for maximum power transfer to the load and minimum reflected RF power (cf. Chapter 5). A DC blocking capacitor is needed to prevent DC current circulation. Gas pressures are typically in the range of 10 to $2000[\mathrm{mTorr}]$. Typical driving voltages are in the range of 100 to $1000[\mathrm{V}]$.

RF driving frequency

The frequency range is from a few $[\mathrm{kHz}]$ to $200[\mathrm{MHz}]$. In practice, many RF glow discharges processes operate at $13.56[\mathrm{MHz}]$ and its harmonics, because this base frequency is allotted by international communications authorities at which energy can be radiated without interfering with communications. $13.56[\mathrm{MHz}]$ is now a standard frequency for which commercial generators and matching boxes are easily available. Industry is more and more interested by higher process frequencies like $27.12[\mathrm{MHz}]$, $40.68[\mathrm{MHz}]$, $54.24[\mathrm{MHz}]$, $67.8[\mathrm{MHz}]$ (2nd, 3rd, 4th and 5th harmonics of $13.56[\mathrm{MHz}]$). The main interest for these higher frequencies stems from the fact that the films at these frequencies grow faster and are of higher quality (See 2.3).

Plasma sheath

The instantaneous electric field applied between the two electrodes is generally not equally distributed between both electrodes, but drops almost completely in the first millimetres in front of the electrodes. This region adjacent to the electrode, which is hence characterized by a strong electric field, is called the sheath. It is due to the much higher mobilities of the electrons: The net effect of this is an electric field that traps the electrons inside the plasma bulk while positive ions are accelerated through the sheath to bombard the surface. Near to the walls, the electron concentration rapidly decreases to zero leading to the formation of this thin positively charged layer. The mean electric potential is positive in the plasma centre and sharply decreases near both walls. [48]

Ion Energy

Ions are mainly produced by electron-impact ionization at the sheath edge of the glow discharge and are accelerated towards the electrodes. The energy gain of the ions depends mainly on the voltage drop across the sheaths (see also 2.3)

Equivalent circuit diagram and plasma impedance

The term 'capacitively coupled' refers to the way of coupling the input power into the discharge, i.e. by means of two electrodes and their sheaths forming a kind of capacitor. Fig. 2-2 shows the equivalent circuit of a glow discharge. The sheaths can be represented by a parallel combination of a rectifier, which indicates the asymmetrical characteristic for negative electron current and positive ion current, a capacitor, owing to the space charge in the sheaths[40], and a resistor to allow for the energy loss of the ions in the sheath. We see that the capacitance of the plasma originates from the sheath zones, whereas the plasma bulk is predominantly resistive. The impedances of the plasma bulk and sheaths vary with the frequency used and the discharge conditions (type of gas, pressure, RF power).

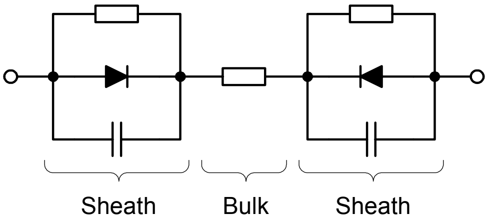

Fig. 2-2: Equivalent circuit of a RF discharge after [24].

Plasma frequencies

At the typical RF frequencies f_{RF} the electrons and ions have a totally different behaviour, which can be explained by their different masses which cause different mobilities in the electric field. The characteristic frequency of electrons or ions, or the so-called electron or ion plasma frequency, is given by

$$\omega_{p_{e,i}} = \sqrt{\frac{n_{e,i} \cdot e^2}{m_{e,i} \cdot \varepsilon_0}} \qquad \text{(Eq. 2-2)}$$

where $n_{e,i}$ is the electronic or ionic density, e the elementary charge unit, $m_{e,i}$ the mass of the respective particle and ε_0 the dielectric constant of free space. When the electron density varies from 10^{10} to $10^{13}[\mathrm{cm}^{-3}]$, the electronic plasma frequency ω_{pe} ranges from 9×10^8 to $3 \times 10^{10}[\mathrm{Hz}]$, which is much higher than the typical RF excitation frequency of $13.56[\mathrm{MHz}]$. Thus the light electrons can follow the instantaneous electric fields produced by the applied RF voltage. For typical RF frequencies it follows that the ionic plasma frequency $\omega_{pi} \ll \omega = 2\pi f_{RF}$, therefore the heavy ions can follow only the time averaged spatial field variations.

2.3 Frequency Effect of RF Plasmas at HF and VHF

The RF operating frequency affects the composition, densities and potentials of the plasma and therefore has a strong influence on the properties of the deposited film.[40]

Frequency effect in deposition

Curtins et. al.[123][54][77] first investigated systematically the influence of the plasma frequency f_{RF} in the range between 13.56 and 150[MHz] on the deposition rate $DR(f_{RF})$ and film properties of amorphous hydrogenated silicon. He observed a strong increase in DR between 25 and 60[MHz] (cf. Fig. 2-3-[A]) with its maximum at ≈70[MHz]; Above 80[MHz] the deposition rate falls off again which might be due to matching efficiency problems and reduced power dissipation in the plasma. Only minor changes occur in the defect density, optical bandgap and electrical conductivity over this frequency range, but surprisingly impurities seem to be less incorporated and less internal stress was present in 70[MHz] grown films. The strong dependence of $DR(f_{RF})$ on the frequency is attributed to a change of the electron energy distribution function (EEDF). At VHF the population of high-energy electron is suggested to increase in the tail of the EEDF, resulting in a higher ionisation efficiency, a larger total electron density, more efficient dissociation and thus a greater deposition rate $DR(f_{RF})$. Howling[12] and Sansonnens[59] confirm the findings up to a frequency of 70[MHz], also Heintze et al.[55] investigated the frequency range up to 250[MHz] confirming the trend of increasing deposition rate with excitation frequency.

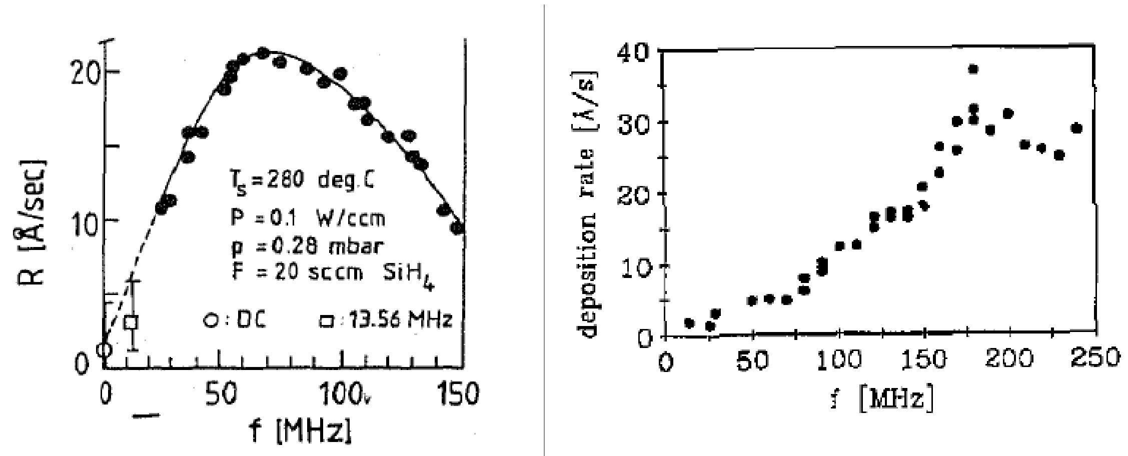

[B]

[A]

Fig. 2-3: [A] Deposition rate r as obtained by Curtins[54] in the frequency range 27.1 – 150[MHz]. The dashed line is an extrapolation to 13.56[MHz] and DC. The maximum attained DR at 70[MHz] is 5 – 8 times larger than at the standard frequency 13.56[MHz].
[B] Deposition rate as obtained by Heintze et al.[55].

Ion energy at VHF

Schwarzenbach et. al.[11] ascertained by experiments and particle-in-cell simulation, that with a rising RF excitation frequency the ion bombardment energy is decreasing at constant power (cf. Fig. 2-4). At VHF it asymptotically approaches the sheath floating potential. This frequency effect has far-reaching advantages for deposition in comparison to HF frequencies around 13.56[MHz]. With it goes thinner capacitive sheaths[76][80], a reduction of the sheath impedance and a reduced sheath voltage. Moderate ion bombardment is necessary for the surface species reactivity, but high ion energy can damage the film during plasma deposition at high power and low frequencies

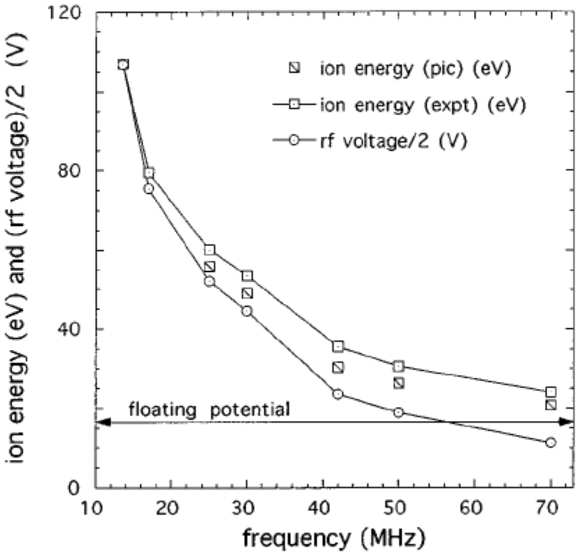

Fig. 2-4: Frequency scaling of the RF voltage and maximum ion energy (by experiment and simulation) for a constant RF plasma power of 3[W]. Reproduced from [11].

VHF advantages

Lower ion energies permit to inject more RF power. More available RF power allows to increase the dissociation rate. More available radicals in case of SiH_4 process gas means potentially higher deposition rate for a-Si and/or µc-Si. Generally, VHF plasmas bring higher deposition rates and better film quality.

Electron Density

Generally, for constant power the plasma density increases as the excitation frequency is increased. The electron dissociation rate at VHF may be due to a change in the electron distribution function. The exact correlation between plasma density and excitation frequency is however still subject of theoretical investigations.

2.4 Summary RF Plasmas

VHF advantages

The operation of RF plasmas in the VHF band ($30[\mathrm{MHz}]$ to $300[\mathrm{MHz}]$) offers some advantages compared to the HF range ($3[\mathrm{MHz}]$ to $30[\mathrm{MHz}]$): VHF plasmas are reported to show a reduced sheath voltage and thus a reduced ion bombardment energy. Because more energy can be coupled into the plasma bulk, higher dissociation rates and hence higher deposition rates can be achieved. VHF can improve the film quality. Fig. 2-5 summarizes the change of the RF power dissipation under an increase of the excitation frequency.

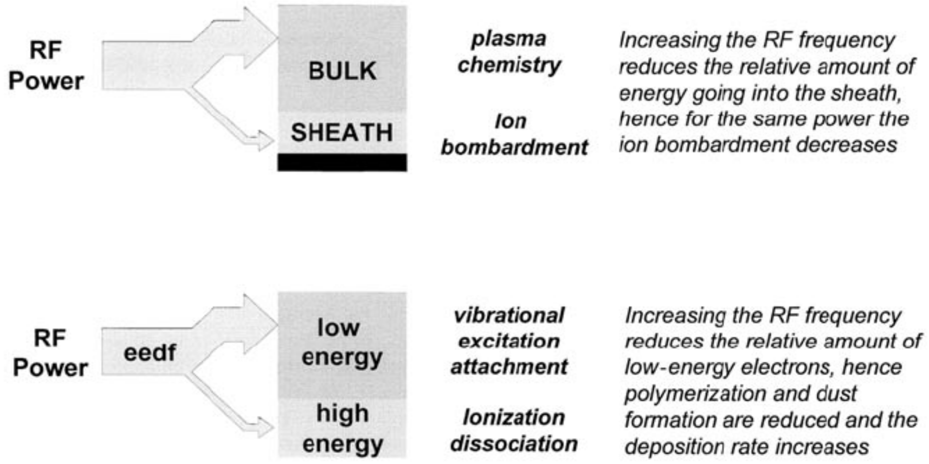

Fig. 2-5: Schematic diagram illustrating the energy trade-off of the RF power dissipation in a parallel-plate capacitively-coupled discharge. Reproduced from [61]

Chapter 3: Non-Uniformity in Large-Area RF Plasma Reactors and its Correction

3.1 Introduction

When studying the problem of homogeneity of a RF glow discharge in a large-area reactor, one finds that three important effects contribute to the plasma non-uniformity. These are:

I. the *Standing Wave Effect* (See 3.2),
II. the *Telegraph Effect* (See 3.5),
III. as well as *Fringing Fields* or evanescent edge modes.

Wavelength vs. Reactor dimension

To obtain a uniform plasma, the standing wave effect must be corrected if

$$L/\lambda_0 \geq 1/10 \qquad \text{(Eq. 3-1)}$$

holds, where λ_0 denotes the vacuum wavelength of the RF excitation used and L is the typical dimension of the reactor or the substrate (cf. Fig. 1-1). The non-uniformity is made worse either by enlarging a reactor, in which case L is increased, or by augmenting the RF excitation frequency, which reduces λ_0. In this thesis it is the frequency which is varied. The so-called telegraph effect is caused by the area asymmetry of the electrodes whereas edge effects are related to the issue on how to terminate the plasma properly.

Shaped electrode

This work reports principally on the demonstration that a shaped electrode can remove the first main source of non-uniformity, the standing wave effect. It will be shown that the shaped lens concept is viable for a wide range of plasma process conditions.

Spurious effects

Apart from the three effects mentioned above, other spurious effects may be important. This may be partly related to the poor quality of the used VHF equipment at high RF power, as for instance non-sinusoidal signals, frequency instabilities and extreme power fluctuations under mismatch conditions which may cause the ignition of parasitic discharges.

3.2 Standing Wave Effect (SWE) and Correction

SWE in 3D

In this section we shall look at two different geometries of planar capacitively coupled RF plasmas and how the standing wave effect (SWE) can be corrected in their particular configuration. First we will study the case of the *cylindrical* parallel plate vacuum capacitor (See 3.2.1). It is the only case which can be solved *analytically*. After this preparation the *rectangular* reactor geometry (See 3.2.2) is examined, which necessitates a *numerical* approach. The section closes with the expected limits of the SWE correction technique put forward for the 3D geometries. Both reactors are 3D objects, but for the mathematical treatment the cylindrical case can be reduced to a 2D (r,z) geometry whereas the rectangular is reduced to a 2D (x,y) geometry by an approximation over the z-axis.

Standing wave

Before we discuss any correction mechanism, it is necessary to define the SWE. Let's assume a forward $A_+(x,t)$ and a backward travelling wave $A_-(x,t)$ of the same frequency and magnitude. They can be written as:

$$A_+(x,t) = A \cdot e^{j(\omega t - kx)} \qquad A_-(x,t) = A \cdot e^{j(\omega t + kx)} \qquad \text{(Eq. 3-2)}$$

Their superposition $A(x,t) = A_+(x,t) + A_-(x,t)$ yields:

$$A(x,t) = A \cdot e^{j\omega t}\left[e^{-jkx} + e^{jkx}\right] = A \cdot e^{j\omega t} \cdot 2 \cdot \cos(kx) \qquad \text{(Eq. 3-3)}$$

As Eq. 3-3 is not of the form $f(\omega \cdot t \pm k \cdot x)$, it is not a travelling wave but a pure oscillation at a fixed location. It is called a *standing wave*.[1]

3.2.1 SWE in Cylindrical Geometry

Procedure

In this section first the MAXWELL equations for the cylindrical geometry are shown (3.2.1.1), then the BESSEL $J_0(r)$ function for the radial dependence of the vertical electrical field E_z in vacuum is introduced (3.2.1.2). In 3.2.1.3 we consider the effect of plasma and how the wavenumber is altered in its presence (3.2.1.4). In 3.2.1.5 the solution for the shape of the electrode is presented, which *uniformizes* the vertical electrical field E_z in vacuum across the diameter.

Reactor setup

We study a cylindrical parallel plate reactor as depicted in Fig. 3-1(a). The system is axisymmetric with respect to the z-axis. The plasma electrode gap d remains small compared to the reactor radius. The RF feeding point is in the centre and on the top of the RF electrode. The objective in 3.2.1.5 will be to find the electrode shape as depicted in Fig. 3-1(b) which suppresses the standing wave non-uniformity.

---

[1] *[13]*, p. 254

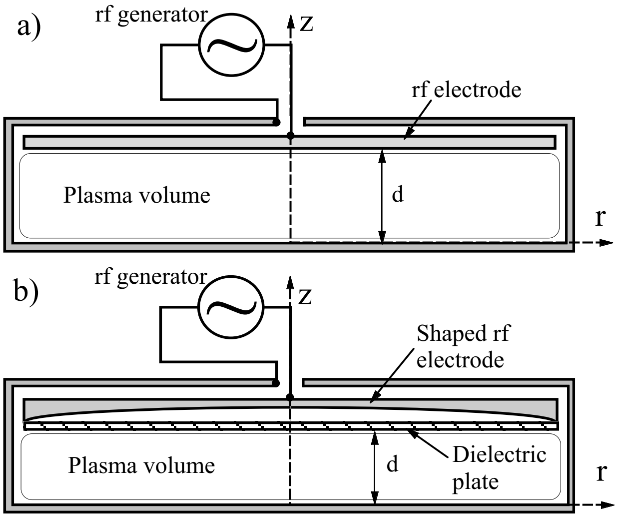

Fig. 3-1: (a) Cylindrical RF parallel plate plasma reactor, (b) plasma reactor with shaped RF electrode and dielectric sheet proposed for uniform plasma generation at high frequency (Diagrams are not to scale).

3.2.1.1 MAXWELL Equations

In cylindrical geometry, the magnetic field is purely azimuthal (B_ϕ) and the electrical field has only vertical (E_z) and radial (E_r) components.

$$\vec{B} = \begin{pmatrix} 0 \\ B_\phi \\ 0 \end{pmatrix} \qquad \vec{E} = \begin{pmatrix} E_r \\ 0 \\ E_z \end{pmatrix} \tag{Eq. 3-4}$$

In vacuum, and for sinusoidal excitation at an angular frequency ω, all fields have a time dependence $e^{j\omega t}$ and MAXWELL's equations reduce to

$$\frac{\partial B_\phi}{\partial z} = -j\omega\varepsilon_0\mu_0 E_r \tag{Eq. 3-5}$$

$$\frac{1}{r}\frac{\partial}{\partial r}(rB_\phi) = j\omega\varepsilon_0\mu_0 E_z \tag{Eq. 3-6}$$

$$\frac{\partial E_r}{\partial z} - \frac{\partial E_z}{\partial r} = -j\omega B_\phi \tag{Eq. 3-7}$$

where ε_0 and μ_0 are respectively the permittivity and permeability of free space.

3.2.1.2 Cylindrical Parallel Plate Vacuum Capacitor at VHF

Substitution of Eq. 3-5 and Eq. 3-6 in Eq. 3-7 gives the following wave equation for the azimuthal magnetic field:

$$\frac{1}{r}\frac{\partial}{\partial r}\left(r\frac{\partial B_\phi}{\partial r}\right) - \frac{B_\phi}{r^2} + \frac{\partial^2 B_\phi}{\partial z^2} + k_0^2 B_\phi = 0 \tag{Eq. 3-8}$$

This is the only equation that we need to solve for a cylindrical reactor and which completely defines the electromagnetic solution for the parallel plate case. The radial part gives a BESSEL equation of first order. In addition we need to stipulate the boundary condition Eq. 3-9 for metallic surfaces.

$$\vec{E} \times \vec{n} = 0 \tag{Eq. 3-9}$$

For the parallel plate case we can solve the wave equation of E_z

$$\nabla^2 E_z + k_0{}^2 E_z = 0 \tag{Eq. 3-10}$$

for the cylindrical coordinate system, whose radial part give a BESSEL equation of zeroth order:

$$\frac{1}{r}\frac{\partial}{\partial r}\left(r\frac{\partial E_z}{\partial r}\right)+\frac{\partial^2 E_z}{\partial z^2}+k_0^2 E_z = 0 \tag{Eq. 3-11}$$

Eq. 3-10 is only valid for the parallel plate case. For the general case it is necessary to solve the wave for E_z and E_r and to couple both components with the divergence constraint $\nabla \bullet \vec{E} = 0$. This means that if we are not in a parallel plate system, it is better to solve for the magnetic field.

BESSEL $J_0(\cdot)$

The solution of Eq. 3-11 for the cylindrical parallel plate reactor gives the well-known zero order BESSEL function of the first kind, $J_0(\cdot)$, for the vertical electrical field intensity

$$E_z(r) = E_0 \cdot J_0(k_0 \cdot r) \tag{Eq. 3-12}$$

$J_0(\cdot)$ and $\cos(\cdot)$

(where $k_0 = \omega / c$ and c is the vacuum light speed and E_0 is the vertical electrical field on axis), which has a maximum at $r = 0$ and a first zero at $r = 2.405 / k_0$. FEYNMAN[1] notes that the BESSEL-function $J_0(\cdot)$ is the cylindrical equivalent to the $\cos(\cdot)$ function of the straight line, which shows the analogy to the standing wave in one dimension. Fig. 3-2 plots the BESSEL function for five typical RF excitation frequencies in a $1[\mathrm{m}]$ diameter reactor. $J_0(\cdot)$ is very non-uniform across the diameter at the higher frequencies. We see, that in vacuum $J_0(k_0 \cdot r)$ does not have its first zero within the reactor boundary for the chosen frequencies and reactor dimension.

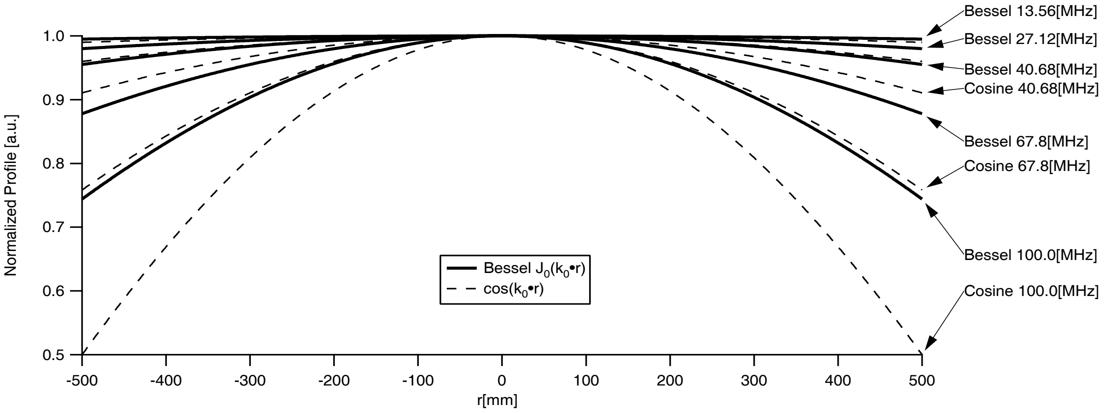

Fig. 3-2: BESSEL function profiles (solid lines) are given for a $1[\mathrm{m}]$ diameter reactor at several typical RF frequencies. For comparison the shape of the cosine function (dashed lines) at the same frequencies is also shown.

3.2.1.3 Implications of Plasma

Plasma as dielectric

The effect of the plasma requires that its relative permittivity ε_{pl} be introduced into the calculation for the volume occupied by the plasma. ε_{pl} is given by Eq. 3-13,

$$\varepsilon_{pl} = 1-\frac{\omega_{pe}^2}{\omega(\omega - j\nu_m)} = 1-\frac{\omega_{pe}^2}{\omega^2+\nu_m^2}-\frac{j\omega_{pe}^2\nu_m}{\omega^3+\omega\nu_m^2} \tag{Eq. 3-13}$$

where the electron plasma frequency ω_{pe} is given by

$$\omega_{pe} = \sqrt{n_e e^2/\varepsilon_0 m_e}, \tag{Eq. 3-14}$$

---

[1] [110], page 23-6

n_e is the electron density, e the elementary charge, m_e the mass of the free electron and ν_m the electron-neutral collision frequency. The presence of the plasma has two important consequences:

(i) Absorption due to the plasma resistance (energy coupled to the plasma) implies a damping of the travelling waves propagating in the electrode gap which modifies the standing wave profile.

(ii) When the plasma conductivity is very large (high density, low pressure plasma), the RF skin depth which is usually larger than the plasma thickness can become of the same order or smaller. In that case, the electromagnetic model departs strongly from the present vacuum model, and becomes closer to a model where the electromagnetic waves propagate in both sheath gaps.

Both aspects of the problem cannot be treated via the simple vacuum model described earlier; a more detailed calculation including edge effects would be required.[72]

3.2.1.4 Effective Dielectric Constant for the Parallel Plate Plasma Sheath System

The plasma in the cylindrical axisymmetric parallel-plate reactor is generated by the RF excitation propagating inwards from the circumference.[38][8] Since the spacing between the plates is much smaller than a half-wavelength, the frequencies used here are far below the cutoff of the first TM mode, and in vacuum, the excitation is a pure transverse electromagnetic (TEM) mode with an azimuthal magnetic field and a vertical electric field. In presence of plasma, the magnetic field remains purely azimuthal, but due to the inhomogeneous dielectric, a radial electric field arises and the vacuum TEM mode is transformed into a quasi-TEM mode.[106] The distribution of the vertical electric field in this case is nearly the same as for electrostatic fields (quasistatic approximation) and the effective relative permittivity is given by[8][1] Eq. 3-15,

$$\varepsilon_{eff} = \left[\frac{1}{d_{gap}}\int_0^{d_{gap}} \frac{dz}{\varepsilon(z)}\right]^{-1} \qquad \text{(Eq. 3-15)}$$

where d_{gap} is the electrode gap distance and $\varepsilon(z)$ the z-dependent relative permittivity. For a simple model consisting of a series combination of a uniform plasma slab $[\varepsilon(z) = \varepsilon_{pl}]$ and vacuum sheaths $[\varepsilon(z) = 1]$, widths d_{pl} and d_{sh}, respectively, (so that $d_{gap} = d_{pl} + 2\cdot d_{sh}$), the effective relative permittivity is given by Eq. 3-16.

$$\varepsilon_{eff} = \frac{d_{gap}\cdot\varepsilon_{pl}}{2d_{sh}\cdot\varepsilon_{pl} + d_{pl}} \qquad \text{(Eq. 3-16)}$$

For plasma conditions where the magnitude of the plasma relative permittivity ε_{pl} (given by Eq. 3-13) is much larger than 1, the effective relative permittivity can be approximated by Eq. 3-17.

$$\varepsilon_{eff} \approx \frac{d_{gap}}{2d_{sh}} \qquad \text{(Eq. 3-17)}$$

This simply means that the effective capacitance of the electrode gap, $C_{eff} = \varepsilon_0 \cdot \varepsilon_{eff} / d_{gap}$, is approximately equal to the series capacitance of the two sheaths, $\varepsilon_0 / 2d_{sh}$, because the plasma impedance is negligible in comparison. This approximation is good for the pressures investigated in this work provided that the electron density is above $2 \times 10^9[\mathrm{cm}^{-3}]$. The measured ion flux on axis was in the range $0.06 - 0.34[\mathrm{mA}\cdot\mathrm{cm}^{-2}]$ corresponding to electron densities from about $2.8 \times 10^9[\mathrm{cm}^{-3}]$ to $1.6 \times 10^{10}[\mathrm{cm}^{-3}]$ which is sufficient for validity of the approximation in Eq. 3-17 but not so high as to cause possible inductive skin effects.[38][17]

"Worsening Factor"

For a wave in a plasma, the wavenumber k_0 is changed to

$$k_{eff} = k_0 \cdot \Re(\sqrt{\varepsilon_{eff}}) \qquad \text{(Eq. 3-18)}$$

where k_{eff} is the increased wavenumber of the wave propagating in the dielectric (with complex relative permittivity ε_{eff}) formed by the plasma-sheath combination. Eq. 3-12 becomes:

$$E_z(r) = E_0 \cdot J_0(k_{eff} \cdot r) = E_0 \cdot J_0\left[k_0 \cdot r \cdot \Re(\sqrt{\varepsilon_{eff}})\right] \qquad \text{(Eq. 3-19)}$$

$\Re(\sqrt{\varepsilon_{eff}})$ is called the "wavelength reduction factor". The factor $\Re(\varepsilon_{eff})$ can be considered as a sort of uniformity "worsening factor" as introduced by SCHMITT et al.[1] which makes the uniformity of the electric field (and plasma) worse than for the vacuum case.

Sheath width

For the $30[\mathrm{mm}]$ electrode gap used in the experiments of Chapter 6, the range of wavelength reduction factor deduced from the measurements in section 6.5.1, namely $2 < \Re(\sqrt{\varepsilon_{eff}}) \approx \sqrt{d_{gap}/2d_{sh}} < 3.5$, corresponds to physically reasonable sheath widths of $3.75[\mathrm{mm}] > d_{sh} > 1.2[\mathrm{mm}]$. This expression is the same as the approximation for the standing wave wavelength correction factor in [38].

3.2.1.5 GAUSSIAN Lens Concept

Special solution

In this section we now try to find a solution that suppresses this radial non-uniformity due to the standing wave in the reactor and creates a *constant* vertical electrical field $E_z(r) = \mathrm{const.}$ We derive a special solution for the electromagnetic field in vacuum with appropriate properties. Then we calculate the shape of the electrode that complies with this special solution. By substituting the "Ansatz" for the special solution[8]

$$B_\phi = j \cdot \frac{E_0 k_0}{2c} \cdot f(z) r \qquad \text{(Eq. 3-20)}$$

into Eq. 3-8, we obtain the following equation for $f(z)$:

$$\frac{\partial^2}{\partial z^2} f(z) + k_0^2 \cdot f(z) = 0 \qquad \text{(Eq. 3-21)}$$

The boundary condition corresponding to a flat metallic electrode at $z = 0$ is $E_r(z = 0) = 0$. From Eq. 3-5 it follows that $f'(z = 0)$. With this boundary condition, the solution of Eq. 3-21 is simply $f(z) = \cos(k_0 \cdot z)$. Magnetic and electric fields are thus given by:

$$B_\phi(r, z) = j \cdot \frac{E_0 k_0}{2c} \cdot r \cdot \cos(k_0 z) \qquad \text{(Eq. 3-22)}$$

$$E_r(r, z) = \frac{E_0 k_0}{2} \cdot r \cdot \sin(k_0 z) \qquad \text{(Eq. 3-23)}$$

$$E_z(r, z) = E_0 \cdot \cos(k_0 z) \qquad \text{(Eq. 3-24)}$$

Capacitive and inductive coupling

This solution of MAXWELL's equations is interesting for the application to RF capacitively coupled reactors because the vertical electric field E_z is *independent* of r. The radial component of the electric field E_r is proportional to r. The radially uniform vertical electric field E_z will be responsible for the capacitive coupling of the electrical power to the plasma and the radial electric field E_r is responsible for inductive coupling. As long as the electrode gap remains small compared to the vacuum wavelength ($k_0 \cdot z \ll 1$), we have $E_z \rightarrow E_0$ and $E_r \rightarrow 0$, i.e. E_r remains small compared to E_z, and the non-uniform inductive coupling remains negligible compared to the uniform capacitive coupling of the electrical power.

GAUSSIAN shape

We are looking now for an electrode shape that will create such an electromagnetic field ($E_z \approx \mathrm{const}, E_r \approx 0$). A conducting electrode should be such that its surface is always perpendicular to the electric field (cf. Eq. 3-9). The surface of the electrode will therefore be defined by the solution of equation Eq. 3-25:

$$\frac{dr}{dz} = -\frac{E_z}{E_r} = -\frac{2}{rk_0}\cot(k_0 z) \qquad \text{(Eq. 3-25)}$$

Separation of the variables

$$-\frac{k_0}{2} \cdot r \cdot dr = \cot(k_0 \cdot z) \cdot dz \qquad \text{(Eq. 3-26)}$$

and using the primary function identities[1]

$$\begin{gathered} -\frac{k_0}{2} \cdot \int r dr = -\frac{k_0}{4} \cdot r^2 + C \\ \int \cot(k_0 \cdot z) dz = \frac{1}{k_0} \cdot \ln|\sin(k_0 \cdot z)| + C' \end{gathered} \qquad \text{(Eq. 3-27)}$$

yields the solution of Eq. 3-25

$$\sin(k_0 z) = a \cdot \exp\left(-\frac{k_0^2 r^2}{4}\right) \qquad \text{(Eq. 3-28)}$$

where a is an integration constant. For $k_0 \cdot z \ll 1$, Eq. 3-28 can be approximated by

$$z = a_0 \exp\left(-\frac{k_0^2 r^2}{4}\right) \qquad \text{(Eq. 3-29)}$$

which is a GAUSSIAN shape. a_0 corresponds to the electrode gap on the axis. This solution of the shape creates a uniform vertical electric field E_z.

Dielectric lens

To be uniform, not only a constant vertical electric field E_z, but also a constant geometrical thickness is required. Fig. 3-1(b) shows how this can be realized by a thin dielectric layer. Behind this layer we have the varying gap, the lens. No plasma should ignite in the lens concavity, as this would short-circuit the lens and destroy the lens function. The lens concavity may be filled with a dielectric to prevent this. For simplicity in the sections above we described only a vacuum lens, but it can be extended to a "dielectric lens". In this case, the wave vector k_0 in Eq. 3-28 is changed to the wave vector $k_1 = \sqrt{\varepsilon_r} \cdot k_0$, where ε_r is the relative permittivity of the material (cf. 3.3.1) and the design frequency is reduced by a factor $\sqrt{\varepsilon_r}$.

This is a vacuum solution only. CHABERT et al. confirmed that the lens is valid also in presence of the plasma.[36]

---

[1] [109], p. 1030

3.2.2 SWE in Rectangular Geometry

3.2.2.1 From Round to Rectangular

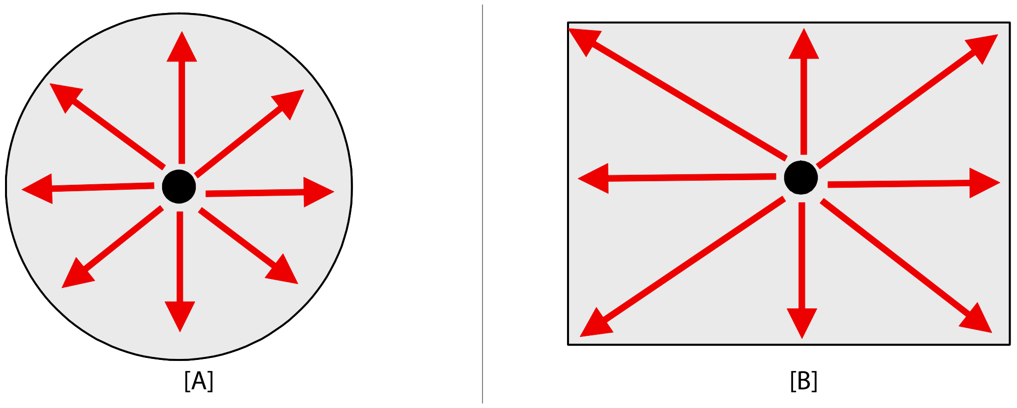

Fig. 3-3: Propagation of an RF wave on a round [A] and rectangular plate [B] from a single centred RF feeding point.

Cylindrical reactor

An important characteristic of the cylindrical reactor is that it has a uniform boundary condition at the edge due to the cylindrical symmetry as the travelling RF wave passes the same distance for all directions to reach the perimeter of the circular plate (Fig. 3-3-[A]). An analytical solution was possible to find the shaped electrode for this case.

GAUSSIAN lens for rectangular geometry?

The main question is now if a shape can be obtained for a rectangular electrode as depicted in Fig. 3-3-[B]. Before going into details we can already see that the distance for an RF wave to travel from the centred RF connection to the midpoint of a lateral edge and diagonally to a corner are different. Thus the boundary condition at the perimeter of rectangular plate is not intrinsically uniform, in contrast to Fig. 3-3-[A]. Thus we must expect that the GAUSSIAN shape may not be a solution to suppress the standing wave effect in rectangular geometry.[68]

Rectangular approach

In this section, we describe a two-dimensional quasiplanar circuit model in order to calculate the electrode shape that can suppress the standing wave non-uniformity in rectangular geometry.[10] The numerical calculations necessary to find the actual shape used in Chapter 7 are explained in part 3.3.2.

3.2.2.2 Derivation of the Quasiplanar Circuit Model from MAXWELL's Equations

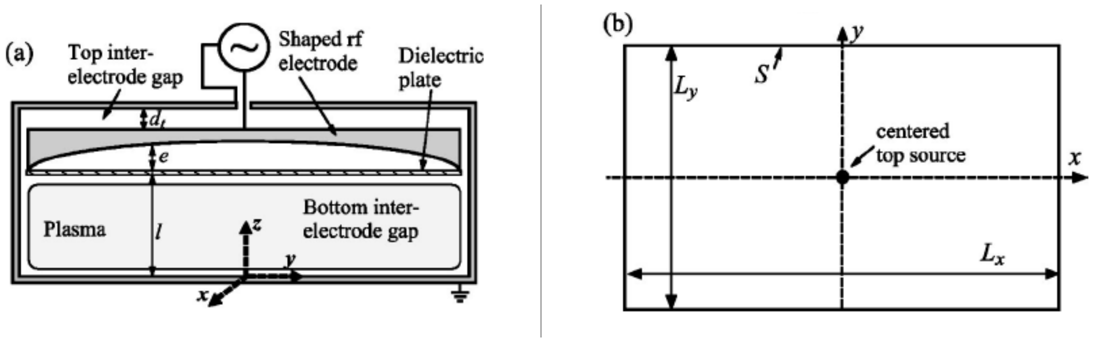

Fig. 3-4: (a) Schematic front view (not to scale) of a large area rectangular capacitively coupled RF plasma reactor with a shaped RF electrode and a single top centred RF connection and (b) equivalent two-dimensional domain for the top and bottom inter-electrode voltage calculation using the quasiplanar circuit model. Reproduced from [10].

We consider the case where the bottom electrode is flat and the second top electrode may be shaped (See Fig. 3-4). The CARTESIAN coordinate system is chosen such that the x, y plane is parallel to the flat electrode and z is the vertical axis directed from the bottom electrode towards the top electrode. The inter-electrode gap d is defined as the vertical distance between these two electrodes, and is therefore a function of the position (x, y) on the flat electrode. In this section, we neglect the details of electromagnetic fields at the edge of the electrodes and consider only the surface wave propagating in the central part of the reactor which is responsible for the standing wave effect. Perturbations due to the reactor edge design may be described in terms of evanescent modes[38] and telegraph effects (See 3.5).

In capacitively coupled RF plasma reactors, since d is small compared to the vacuum wavelength λ_0, the electromagnetic wave propagating between the two metallic electrodes is a purely transverse electromagnetic (TEM) mode for vacuum and becomes a quasi-TEM mode in the presence of a plasma. For these modes, the electric field is essentially vertical, but a small transverse component exists due to the curvature of the shaped electrode and due to the presence of a plasma.[38] However, for plasma conditions such that the electromagnetic skin depth in the plasma remains large enough such that skin effects remain negligible[38] and for small electrode curvature (quasiplanar electrode), this transverse component remains negligible compared to the vertical component of the electric field E_z. From these two conditions, we can also deduce that the magnetic field has only a transverse component $\vec{H}_t$, and that its intensity is constant along the vertical direction. Therefore MAXWELL's equations reduce to

$$\nabla_t \times \vec{H}_t = (j\omega\varepsilon_0\varepsilon_r E_z + J_z)\hat{z} \qquad \text{(Eq. 3-30)}$$

$$\nabla_t E_z = -j\omega\mu_0 \hat{z} \times \vec{H}_t \qquad \text{(Eq. 3-31)}$$

where

$$\nabla_t = \left(\frac{\partial}{\partial x}\right)\hat{x} + \left(\frac{\partial}{\partial y}\right)\hat{y} \qquad \text{(Eq. 3-32)}$$

is the two-dimensional transverse nabla operator, ε_r is the relative permittivity of the medium filling the inter-electrode space, and J_z is the current source. A time dependence $e^{j\omega t}$, where ω is the excitation angular frequency, has been used.

By integrating Eq. 3-30 and Eq. 3-31 along z from 0 to d and by substituting the definition of the inter-electrode voltage

$$V = \int_0^{\mathrm{d}} -E_z dz \qquad \text{(Eq. 3-33)}$$

and of the surface current at the top electrode

$$\vec{J}_s = \vec{n} \times \vec{H}_t \cong -\hat{z} \times \vec{H}_t \qquad \text{(Eq. 3-34)}$$

where $\vec{n}$ is the unit normal vector to the electrode surface directed outwards from the electrode volume, we obtain

$$\nabla_t \bullet \vec{J}_s = -\frac{j\omega\varepsilon_0}{\int_0^{\mathrm{d}}\left(\frac{1}{\varepsilon}\right)dz} + J_z = -YV + J_z \qquad \text{(Eq. 3-35)}$$

$$\nabla_t V = -j\omega\mu_0 d \cdot \vec{J}_s = -Z \cdot \vec{J}_s \qquad \text{(Eq. 3-36)}$$

These two equations are the quasiplanar circuit approximation of MAXWELL's equations for a quasi-TEM wave propagating between two metallic electrodes. Equation Eq. 3-35 is the surface current continuity equation and

$$Y = \frac{j\omega\varepsilon_0}{\int_0^{\mathrm{d}}\left(\frac{1}{\varepsilon}\right)dz} \qquad \text{(Eq. 3-37)}$$

represents the parallel admittance per unit area of the medium filling the inter-electrode gap. Equation Eq. 3-36 gives the lateral variation of the inter-electrode voltage due to the surface current flowing in the electrodes and

$$Z = j\omega\mu_0 d \tag{Eq. 3-38}$$

represents the series impedance per unit area of the electrodes due to the self-inductance associated with the electrode gap; it is independent of the plasma provided that the electromagnetic skin depth is large compared to the plasma thickness.

3.2.2.3 Description of the Quasiplanar Circuit Model

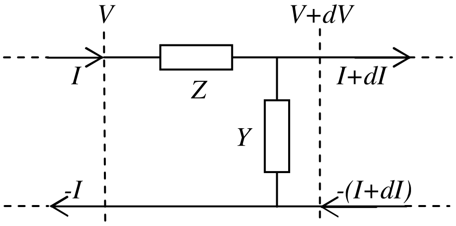

Fig. 3-5: Infinitesimal section of a two-dimensional transmission line with distributed sheet impedance per unit area $Z\,[\Omega\cdot m^{-2}]$, and distributed admittance per unit area $Y\,[\Omega^{-1}\cdot m^{-2}]$.

It was shown above that MAXWELL's equations for the propagation of the electromagnetic quasi-transverse electromagnetic (TEM) wave between two quasiplanar metallic electrodes can be reduced to Eq. 3-35 and Eq. 3-36. These two equations are two dimensional in the lateral x, y plane, z being the vertical inter-electrode direction. The value of Z is given by Eq. 3-38. We recall that it is independent of the presence of the plasma as long as the electromagnetic skin depth remains large compared to the plasma thickness. The value Y is defined by Eq. 3-37. For vacuum, we obtain

$$Y = \frac{j\varepsilon_0\omega}{d} \tag{Eq. 3-39}$$

and for the inter-electrode gap filled with a plasma of thickness l and a dielectric of thickness e such that $l + e = d$ (cf. Fig. 3-4), we obtain:

$$Y = \frac{j\varepsilon_0\omega}{\int_0^d \frac{1}{\varepsilon_p}dz + \frac{e}{\varepsilon_l}} = \left(\frac{1}{Y_p} + \frac{1}{Y_l}\right)^{-1} \tag{Eq. 3-40}$$

where ε_p is the relative permittivity of the plasma and ε_l is the relative permittivity of the dielectric. The total parallel admittance Y is therefore the series combination of the plasma admittance Y_p and of the dielectric admittance Y_l.

Combining Eq. 3-35 and Eq. 3-36, we obtain the second-order two-dimensional differential equation:

$$\nabla_t^2 V - \frac{\nabla_t Z}{Z} \cdot \nabla_t V - YZV = -ZJ_z. \tag{Eq. 3-41}$$

This equation represents the voltage wave equation for a two-dimensional quasiplanar circuit. It is a two-dimensional generalization of the voltage wave equation used in [36] for the one-dimensional quasiplanar transmission line case. Eq. 3-41 is also a generalization of the two-dimensional HELMHOLTZ equation used in [4], as it permits us to take into account the presence of the plasma and a possible small variation of the inter-electrode gap.

3.2.2.4 Application of the Quasiplanar Circuit Model

Fig. 3-4(a) shows a schematic front view of a large area rectangular capacitively coupled RF plasma reactor with a shaped RF electrode and a single top centred RF connection, and Fig. 3-4(b) shows the equivalent two-dimensional geometry used for the voltage calculation using the quasiplanar circuit model. In such reactors, the electromagnetic power flux propagates in the top inter-electrode gap from the RF connection towards the edge of the RF electrode and is then transmitted to the plasma area (bottom inter-electrode gap). Therefore, the electromagnetic solution for the plasma volume and the top inter-electrode gap are coupled together by the continuity at the electrode periphery. In Fig. 3-4 we have considered the case of a single RF connection, however, in large area rectangular reactors, the RF power may be distributed in more than one point. In that case, the model developed here remains valid as the source term J_z in Eq. 3-41 may be distributed over the different RF connection areas.[10]

In the two-dimensional quasiplanar circuit model used here, the three-dimensional electromagnetic fields have been integrated vertically across the inter-electrode gap, and the obtained voltage wave equation is solved on the corresponding two-dimensional geometry (shown in Fig. 3-4(b)) where the domain boundary S corresponds to the periphery of the RF electrode. Therefore, Eq. 3-41 has to be solved once for the inter-electrode voltage along the top vacuum gap V_t and once for the inter-electrode voltage along the bottom or plasma gap V_b, the two solutions being coupled together by the voltage and surface current continuity conditions along the electrode periphery S:[10]

$$V_b = V_t \tag{Eq. 3-42}$$

and

$$\frac{1}{Z_b}\frac{\partial V_b}{\partial \vec{\boldsymbol{n}}} = -\frac{1}{Z_t}\frac{\partial V_t}{\partial \vec{\boldsymbol{n}}} \tag{Eq. 3-43}$$

where $\vec{\boldsymbol{n}}$ is the normal outward unit vector to the periphery S.

Due to the quasiplanar circuit approximation used, the model presented here is only valid for the study and the suppression of the standing wave electromagnetic non-uniformity. Other electromagnetic effects related to the reactor wall geometry such as the evanescent modes described in [38] or the telegraph effect described later (See 3.5) are not described by this model. However, for large area reactors and high frequencies, both effects remain limited to the edge area of the reactors, while the standing wave non-uniformity is the dominant effect in the central area of the reactors.

Similarly to [37] for one-dimensional linear reactors, the model presented here could therefore be coupled to a local particle and energy balance model in order to study standing waves in a conventional parallel plate rectangular reactor. In that case the plasma and sheath admittance Y_p becomes a non-uniform function of the local voltage across the plasma V_p. However, as the aim of this section is to determine the electrode shape which can suppress the standing wave non-uniformity and give a uniform V_p, we will assume that the plasma and sheath admittance remain uniform over the whole electrode area. Similarly to [36] for the one-dimensional linear or cylindrical geometry, we first try to find an electrode shape that can generate an electromagnetic solution such that the voltage across the plasma V_p is constant for a laterally uniform plasma (constant value of Y_p). Using the current continuity across the parallel admittance, we obtain

$$V = \left(1 + \frac{Y_p}{Y_l}\right) \cdot V_p \tag{Eq. 3-44}$$

Validity of vacuum approximation for the plasma case

From this relation, we deduce that for a constant value of $Y_p \cdot V_p$, $\nabla_t^2 V$ and $\nabla_t V$ are proportional to $Y_p \cdot V_p$. We also note that $Y \cdot Z \cdot V = Z \cdot Y_p \cdot V_p$. Therefore, as all terms of Eq. 3-41 for the plasma area are proportional to $Y_p \cdot V_p$, Eq. 3-41 and the deduced electrode shape will be independent of the presence of the plasma. As a particular case, we can replace the plasma admittance by the vacuum admittance. This means that the electrode shape can be calculated for vacuum and will then remain valid in the presence of the plasma.

It should be noted that the fact that Eq. 3-41 is independent of the presence of the plasma is not a general property of Eq. 3-41, and is only valid for the electrode shape such that $Y_p \cdot V_p$ is constant. For any other shape, the dependence on the plasma will remain. As a particular case, we should note that for parallel plate electrodes, the presence of the plasma introduces a wavelength reduction, or worsening factor, compared with the vacuum voltage solution.[1][38]

Plasma perturbation

The presence of the plasma causes a perturbation of the current and the voltage continuity at the electrode periphery. In cylindrical geometry, this perturbation remains uniform along the periphery and has no consequences on the calculated voltage, i.e. the shape calculated in vacuum remains valid (cf. 6.4 and Fig. 6-1-[B]). In rectangular geometry, this perturbation causes a redistribution of the surface current and introduces a voltage perturbation. As a consequence the shape calculated for vacuum is not valid in presence of a plasma (cf. 7.3 and Fig. 7-3-[B]).[97]

3.2.2.5 Calculation of the Vacuum Lens

As shown above, the electrode shape that suppresses the standing wave can be calculated for vacuum.[10] For simplicity, we perform here the calculation for a vacuum dielectric lens ($\varepsilon_l = 1$). For a typical capacitively coupled reactor, we can suppose that all the RF connections are located on the top face of the RF electrode and that only the bottom face is shaped (we only need to suppress the standing wave for the plasma area). The equations to solve are therefore:[10]

$$\nabla_t^2 V_t(x, y) + k_0^2 V_t(x, y) = f(x, y) \qquad \text{(Eq. 3-45)}$$

$$\nabla_t^2 V_b(x, y) - \frac{\nabla_t d(x, y)}{d(x, y)} \cdot \nabla_t V_b(x, y) + k_0^2 V = 0 \qquad \text{(Eq. 3-46)}$$

where $k_0 = \omega / c$, and $f(x, y)$ is the source term corresponding to the RF connections, which is non-zero only over the small connection areas. These two equations are supplemented by the boundary condition $V_t = V_b$ (cf. Eq. 3-42) and

$$\frac{1}{d_t} \cdot \frac{\partial V_t}{\partial \vec{n}} = -\frac{1}{d} \cdot \frac{\partial V_b}{\partial \vec{n}} \qquad \text{(Eq. 3-47)}$$

on the electrode periphery, where d_t is the constant top inter-electrode gap (cf. Fig. 3-4). For the vacuum case, the condition that the voltage across the plasma gap l is constant is equivalent to the condition that the total voltage divided by the total electrode gap is constant. This means that the shape of the electrode that suppresses the standing wave can be obtained by imposing the constraint

$$\frac{d(x, y)}{d(x_0, y_0)} = \frac{V_b(x, y)}{V_b(x_0, y_0)} \qquad \text{(Eq. 3-48)}$$

where $d(x_0, y_0)$ and $V(x_0, y_0)$ correspond, respectively, to the desired inter-electrode distance and calculated voltage at the position (x_0, y_0). In [10], Eq. 3-45 and Eq. 3-46 have been solved numerically with the finite elements method using the commercial partial differential equation solver FlexPDE™ as outlined in section 3.3.2. The constraint Eq. 3-48 has been imposed by using an iterative procedure: Starting with the voltage solution for a flat electrode, the electrode shape $d(x, y)$ for the current iteration is calculated using the voltage $V_b(x, y)$ of the preceding iteration. This procedure is stopped when the non-uniformity of $V_b(x, y) / d(x, y)$ is considered sufficiently small over the whole electrode area (typically less than 0.01%).

3.2.3 Other Perturbations to the Shaped Electrode Technique

In this section we attempt to determine the plasma conditions for which the vacuum shape solution remains valid. To simplify the analysis, we refer to the cylindrical GAUSSIAN shaped electrode only.

3.2.3.1 Conducting substrates

If a metallic plate is on top of the curved side of the lens then the lens is entirely screened and the reactor is effectively a parallel plate reactor. However the effect of the dielectric substrate with a thin conducting layer is uncertain. If the conducting layer is a good conductor, then this layer will act as a flat conducting electrode and screen the electromagnetic effect of the shaped electrode beneath. If the conducting layer is a poor conductor (e.g. for a-Si:H), the properties of the shaped electrode should remain largely unaffected. For the transparent conducting oxide (TCO) used in photovoltaic applications (resistivity $\rho = 5 \times 10^{-4}[\Omega\cdot\mathrm{cm}]$ and thickness $d = 1[\mu\mathrm{m}]$), the estimated skin depth at $100[\mathrm{MHz}]$ is $d = 113[\mu\mathrm{m}]$ which is much larger than the conducting layer thickness d. Therefore, at first sight, the screening due to this conducting layer should be negligible. Experiments carried out by SANSONNENS et al.[97] however show that a thin conducting layer is sufficient to screen the electrode shape effect even when the electromagnetic skin depth is much larger than the conducting layer thickness. These experiments therefore demonstrate that the screening by the thin conducting layer cannot be explained simply in terms of the classical electromagnetic skin depth, but that a more detailed electromagnetic model taking into account the specific geometry of these experiments should be done to understand this screening effect.

3.2.3.2 Parasitic discharges in lens concavity

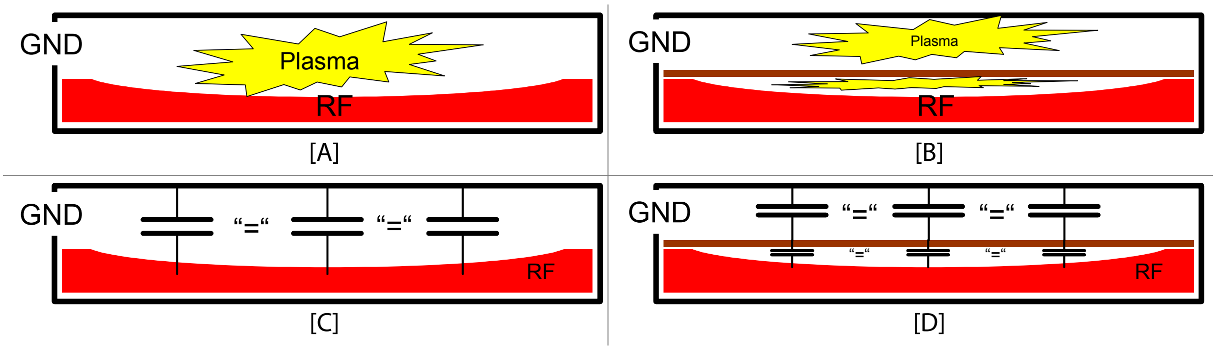

Fig. 3-6: Two possible configurations for plasma in the lens concavity: [A] shows the case where there is no separating thin dielectric and [B] the case as proposed in Fig. 3-1 with a thin dielectric sheet. [C] shows the simplified equivalent circuit model for [A], and [D] for [B]."GND" denotes the grounded housing of the reactor, and "RF" the driven shaped RF electrode.

A dielectric plate is necessary to guarantee the capacitive voltage division. If the plasma fills all the gap as shown in Fig. 3-6-[A], then the sheaths give approximately a uniform gap capacitance and the lens effect is absent. If a plasma is to ignite in the lens concavity as shown in Fig. 3-6-[B], then the capacitive voltage division is made impossible. This can be understood by the fact that the voltage fall across a RF plasma is mainly caused by the capacitance of the sheaths. If now there are only the sheaths and no variable gap any more, then the total capacitance depends only on the sheaths and no correction of the vertical electrical field takes place. The plasma literally short-circuits the lens. The consequence is a "quasi"-standing wave effect and case [B] gives almost the same situation as case [A]. This effect is documented by measurements in Chapter 6 and Chapter 7.

3.3 Design of the Shaped Electrodes used for Experiments

3.3.1 Cylindrical Geometry

Here we illustrate the calculation of the cylindrical shaped electrode as used for the experiments in Chapter 6. The reactor has an inter-electrode gap of $d_{gap} = 30[\mathrm{mm}]$ and a diameter of $1[\mathrm{m}]$. The vacuum design frequency was chosen to be $f_0 = 100[\mathrm{MHz}]$. From Eq. 3-29 it follows for the constant factor of the argument of the exponential function by using $k_0 = \omega / c$, $\omega = 2\pi f_0$ and c is the speed of light in vacuum:

$$-\frac{k_0^2}{4} = -\frac{1}{4}\left(\frac{\omega}{c}\right)^2 = -\frac{\pi^2 \cdot f_0^2}{c^2} = -1.098\times10^{-6}\left[\mathrm{mm}^{-2}\right] \qquad \text{(Eq. 3-49)}$$

Integration constant a_0

The lens is defined to end at a radius $r_{border} = 490[\mathrm{mm}]$, where it smoothly goes over to a $10[\mathrm{mm}]$ wide, flat border. To calculate the integration constant a_0 of Eq. 3-29, it is necessary to equate $z(r_{border}) = d_{gap}$. Then by evaluating the GAUSSIAN function for $r = r_{border}$ as shown in Eq. 3-50 we can find a_0:

$$a_0 = d_{gap} \cdot \exp\left(\frac{\pi^2 \cdot f_0^2}{c^2} \times r_{border}{}^2\right) = 39.050[\mathrm{mm}] \qquad \text{(Eq. 3-50)}$$

a_0 specifies the maximum gap at the centre of the lens. To obtain the lens depth, we need to subtract the inter-electrode gap d_{gap} from the gap distance $z(r)$ of Eq. 3-29. In our case it means that for the chosen inter-electrode gap and vacuum design frequency, the lens has in its centre a maximum depth of $a_0 - d_{gap} = 9.050[\mathrm{mm}]$. The final equation of the curvature is given in Eq. 3-51. This is the curvature which has to be fabricated by lathe-tooling a circular metal support. Fig. 3-7 sketches the profile of the resultant electrode.

$$\begin{aligned} \text{For } r = 0 \rightarrow 490[\mathrm{mm}]:\ z[\mathrm{mm}] &= 39.050 \times \exp(-1.098\times10^{-6} \cdot r^2) - 30 \\ \text{For } r = 490 \rightarrow 500[\mathrm{mm}]:\ z[\mathrm{mm}] &= 0 \end{aligned} \qquad \text{(Eq. 3-51)}$$

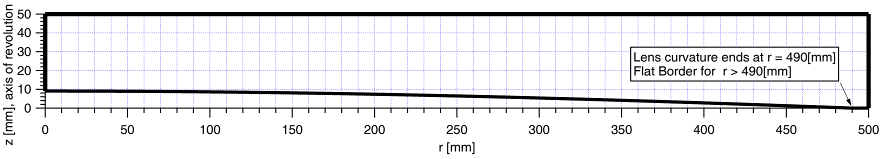

Fig. 3-7: Profile of a GAUSSIAN lens as described by Eq. 3-51. The supporting metal plate has a thickness of $50[\mathrm{mm}]$. The z-axis denotes the depth of the lens.

Dielectric lens

The calculations given above are the solution of the vacuum lens at $100[\mathrm{MHz}]$ design frequency. A dielectric convex "lens" can be used to fill the lens concavity to prevent any possible ignition of a parasitic plasma there. We keep the shape constant and replace the wave number in Eq. 3-29 by $k_1 = \sqrt{\varepsilon_r} \cdot k_0$, then the new design frequency f_1 is reduced by a factor $\sqrt{\varepsilon_r}$:

$$f_1 = f_0 / \sqrt{\varepsilon_r} \qquad \text{(Eq. 3-52)}$$

The dielectric used in this work was polytetrafluoroethylene (PTFE) (relative dielectric constant $\varepsilon_r = 2.1$) and so the modified design frequency of the lens filled with PTFE was $f_1 = 100[\mathrm{MHz}] / \sqrt{2.1} = 69.0[\mathrm{MHz}]$.

Scaling laws

We conclude this section with some remarks on scaling laws for the maximum lens depth with respect to the four system parameters design frequency f, inter-electrode gap d_{gap}, relative dielectric constant ε_r of the lens filling and electrode radius R. The maximum lens depth is important when designing a system. From Eq. 3-29 it follows directly for the gap

$$d_{gap} = a_0 \cdot \exp\left(-\frac{\pi^2 f^2 \varepsilon_r R^2}{c_0^2}\right) \qquad \text{(Eq. 3-53)}$$

and the lens depth accordingly

$$\text{lens depth} = a_0 - d_{gap} = d_{gap}\left[\exp\left(\frac{\pi^2 f^2 \varepsilon_r R^2}{c_0^2}\right) - 1\right]. \qquad \text{(Eq. 3-54)}$$

For a RF excitation wavelength (in the dielectric) which is much larger than the electrode radius, i.e. for

$$\lambda = \frac{c_0}{\sqrt{\varepsilon_r} \cdot f} \gg R \qquad \text{(Eq. 3-55)}$$

the argument of the exponential function in Eq. 3-54 is small and can be expanded as a first approximation to:

$$\text{lens depth} \approx d_{gap} \cdot \left[\frac{\pi^2 f^2 \varepsilon_r R^2}{c_0^2}\right] \qquad \text{(Eq. 3-56)}$$

For all else separately constant, the following approximate scaling laws hold:

$$\begin{cases} \text{lens depth} \propto f^2 \\ \text{lens depth} \propto \varepsilon_r \\ \text{lens depth} \propto d_{gap} \\ \text{lens depth} \propto R^2 \end{cases} \qquad \text{(Eq. 3-57)}$$

If we are to increase the RF excitation frequency f, for which we want to have uniform vertical electrical field, then the lens must be deeper. The approximate scaling law for the new maximum lens depth is shown in the first line of Eq. 3-57. Raising the relative dielectric constant ε_r, while keeping unchanged everything else, requires a deeper lens as well (second line of Eq. 3-57). The scaling law is linear in its first order approximation. A higher dielectric constant might be necessary if PTFE is to be replaced by a more plasma resilient material like alumina (Al_2O_3, $\varepsilon_r = 8.8$). Lowering the inter-electrode gap d_{gap} implies a less curved lens according to the third line of Eq. 3-57. The scaling law is a simple linear correlation between the maximum depth and d_{gap}. Finally the lens depth scales approximately with the square of the radius (last line of Eq. 3-57).

Lens invariant

For a constant depth, the following condition is a lens invariant according to the first order approximation Eq. 3-56:

$$d_{gap} \cdot f^2 \cdot \varepsilon_r \cdot R^2 = const \qquad \text{(Eq. 3-58)}$$

For a given reactor, i.e. where d_{gap} and R^2 are fixed Eq. 3-54 is simplified to:

$$f^2 \cdot \varepsilon_r = const \quad \text{(exact)} \qquad \text{(Eq. 3-59)}$$

In particular it follows for the frequency and the relative dielectric constant of the filling in the lens concavity

$$f \propto \frac{1}{\sqrt{\varepsilon_r}} \qquad \text{(Eq. 3-60)}$$

which is a confirmation of Eq. 3-52.

3.3.2 Rectangular Geometry

As already shown above (cf. 3.2.2) two coupled HELMHOLTZ equations, one for the top and one for the bottom of the RF electrode have to be solved,[69][72]

$$\nabla\bullet\left(\frac{\nabla V_i(\vec{x})}{a_i(\vec{x})}\right)+k^2\cdot\frac{V_i(\vec{x})}{a_i(\vec{x})} = 0,\ \text{for}\ i = t, b \qquad \text{(Eq. 3-61)}$$

where $i = t$ (top gap) and $i = b$ (bottom gap). The boundary conditions are on the one hand the *continuity of the voltage*

$$V_t(\vec{\boldsymbol{x}}_{\boldsymbol{b}}) = V_b(\vec{\boldsymbol{x}}_{\boldsymbol{b}}) \qquad \text{(Eq. 3-62)}$$

and the *continuity of the current*, including the effect of different top and bottom gap:

$$\frac{1}{a_t(\vec{\boldsymbol{x}}_{\boldsymbol{b}})}\frac{\partial}{\partial\vec{\boldsymbol{n}}}V_t(\overrightarrow{\boldsymbol{x}_{\boldsymbol{b}}}) = -\frac{1}{a_b(\vec{\boldsymbol{x}}_{\boldsymbol{b}})}\frac{\partial}{\partial\vec{\boldsymbol{n}}}V_b(\overrightarrow{\boldsymbol{x}_{\boldsymbol{b}}}) \qquad \text{(Eq. 3-63)}$$

The equations Eq. 3-61 are solved with the boundary conditions Eq. 3-62 and Eq. 3-63 by using a partial differential solver software package (FLEXPDE™). In order to find the right electrode shape, which corrects the standing wave effect, it is necessary to vary $a_b(\vec{x})$ and keep $V_b(\vec{x})$ constant.

Lens parameters

For the lens used in Chapter 7, the inter-electrode gap was fixed at $d_{gap} = 28[\text{mm}]$, i.e. $a_b(\vec{x}) \geq 28[\text{mm}]$. The vacuum design frequency was defined as $f_0 = 67.8[\text{MHz}]$. The size of the electrode is $1000[\text{mm}] \times 1168[\text{mm}]$. The resulting lens profile is shown in Fig. 7-1 in section 7.2.1.

3.4 Modelling for Comparison with Measurements

3.4.1 Modelled Electric Field Profiles for Vacuum Measurements

Cylindrical reactor

The theoretical cylindrical vacuum electric field profiles for the flat electrode in the experimental Chapter 6 were obtained by evaluating the Bessel function of Eq. 3-12. For the shaped Gaussian electrode designed for $69[\mathrm{MHz}]$ and for a RF excitation frequency of $13.56[\mathrm{MHz}]$ the electric field profile for the vacuum case was calculated approximately by a capacitive voltage division as indicated by Fig. 3-8 because there is no analytical solution for the electric field profile away from the design frequency. Under the assumption that $13.56[\mathrm{MHz}]$ generates approximately an *equipotential* voltage V_{RF} over the whole area of both electrodes, the vertical electrical field amplitude is

$$E_{z,\,13.56[\mathrm{MHz}]} = V_{RF}/z(r) \tag{Eq. 3-64}$$

where $z(r)$ is the total gap distance given by Eq. 3-29 for the vacuum design frequency of the lens. For higher frequencies where the equipotential approximation is no longer valid, a similar numerical approach as for the rectangular reactor had to be employed (see below).

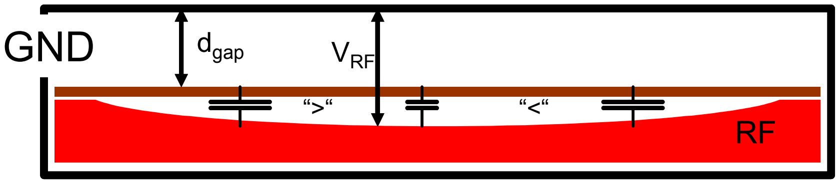

Fig. 3-8: Capacitive voltage division of Gaussian electrode as used for calculating the electric field profile at $13.56[\mathrm{MHz}]$. "GND" denotes the grounded housing of the reactor, and "RF" the driven shaped RF electrode.

Rectangular reactor

In the rectangular case, the E_z-profiles are obtained by solving numerically the two coupled partial differential equations Eq. 3-61 with the pertinent boundary conditions Eq. 3-62 and Eq. 3-63. One obtains the vacuum voltage distribution $V_t(x, y)$. This time it is the shape of the vacuum electrode $a_t(\vec{x}_b)$ which is given beforehand. For the flat electrode $a_t(\vec{x}_b)$ is simply the inter-electrode distance $d_{gap} = 28[\mathrm{mm}]$ and the vacuum electric field amplitude is again

$$E_z(x, y) = \frac{V_t(x, y)}{d_{gap}} \tag{Eq. 3-65}$$

For the shaped electrode $a_t(\vec{x}_b)$ is set to the vacuum lens computed in section 3.3.2. Then by voltage division we receive the electric field:

$$E_z(x, y) = \frac{V_t(x, y)}{a_t(\vec{x}_b)} \tag{Eq. 3-66}$$

3.4.2 Modelled Plasma Emission Profiles

Plasma uniformity

When calculating the plasma uniformity profile it is assumed that the local plasma density (optical emission intensity I_{oes} and/or ion flux I_{sat}) is approximately proportional to the local electrical power dissipation. The local electrical power dissipation in turn is in the first order approximation assuming a constant plasma impedance proportional to the squared vertical electrical field E_z. Thus all the plasma uniformity profiles are simply the normalized square of E_z at the corresponding frequency.

E_z with plasma

If the plasma is included, then for the voltage division $a_t(\vec{x}_b)$ must be reduced by the thickness of the plasma bulk to correct for the real impedance of the plasma.

3.5 Telegraph Effect

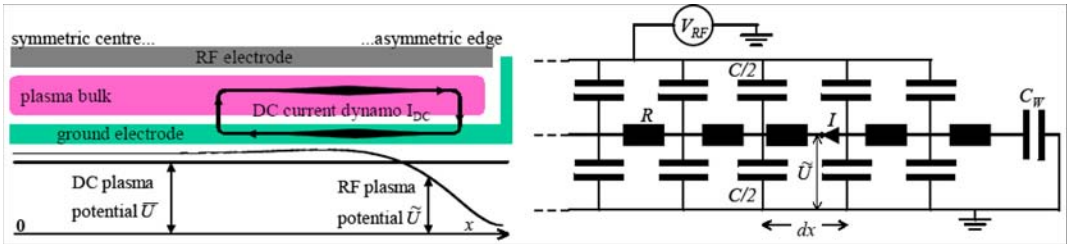

Fig. 3-9: Left: schematic cross-section of an asymmetric reactor, from the centre to the right hand sidewall, showing profiles of the RF and DC components of the plasma potential, and the circulating DC current between the ground electrode and the plasma. Right: the equivalent circuit used for the telegraph description. The sidewall sheath capacitance is represented by C_W.

The non-uniformity considered in this section is due to the redistribution of RF current in the vicinity of reactor sidewalls to maintain RF current continuity between asymmetric electrodes. Since the lateral impedance of the plasma cannot be neglected over the long dimensions of large-area plasmas, this current redistribution results in a RF plasma potential perturbation which propagates inwards from the sidewalls along the plasma between the capacitive sheaths.[6][64] This is analogous to signal propagation along the lossy conductor of a transmission line, hence we call this the "telegraph effect" following SCHMITT et al.[1] The damping length of the potential perturbation can be determined with the telegraph equation.

3.5.1 The Telegraph Equation applied to Large-Area Reactors

In order to preserve RF current continuity, the RF sheath voltage at the larger area electrode will locally be less than the RF sheath voltage at the smaller electrode, the sum of the potentials being equal to the applied RF voltage. In the middle of the reactor, however, the electrode areas are symmetric and both RF sheath voltages would be expected to equal half of the RF voltage V_{RF}. The different sheath potentials in these two zones can be reconciled by allowing the RF plasma potential to vary across the reactor with a characteristic damping length Λ due to the non-zero plasma resistivity.[1] The redistribution of the sidewall RF current is represented by a lateral RF current in the simplified 1D equivalent circuit model in Fig. 3-9.

In the presence of a perturbation $\boldsymbol{V}(x,t)$ due to the sidewall, the ground sheath RF potential is

$$\tilde{\boldsymbol{U}}(x,t) = \frac{\boldsymbol{V}_{RF}}{2} \cdot e^{j\omega t} + \boldsymbol{V}(x,t) \qquad \text{(Eq. 3-67)}$$

A lateral current $\boldsymbol{I}(x,t)$ flows through R and L, the plasma resistance and inductance per unit length, where voltage and current are related by

$$\frac{\partial \boldsymbol{V}}{\partial x} = -R \cdot \boldsymbol{I} - L\frac{\partial \boldsymbol{I}}{\partial t} \qquad \text{(Eq. 3-68)}$$

$$\frac{\partial \boldsymbol{I}}{\partial x} = -C \cdot \frac{\partial \boldsymbol{V}}{\partial t} \qquad \text{(Eq. 3-69)}$$

Telegraph equation

where C is the combined sheath parallel capacitance per unit length. We therefore obtain the telegraph equation Eq. 3-70:

$$\frac{\partial^2 \boldsymbol{V}}{\partial x^2} = LC\frac{\partial^2 \boldsymbol{V}}{\partial t^2} + RC\frac{\partial \boldsymbol{V}}{\partial t} \qquad \text{(Eq. 3-70)}$$

The damping term dominates if $R/(\omega L) = \nu_m/\omega \gg 1$, i.e. high pressure, low excitation frequency. In 1D CARTESIAN coordinates, with $\boldsymbol{V}(x, t) = \boldsymbol{V}(x)e^{j\omega t}$ the particular solution is

$$V(x, t) = B \cdot e^{\left(\pm x/\underline{\Lambda}\right)} \cdot e^{j\omega t} = B \cdot e^{(\pm x/\Lambda)} \cdot e^{j(\omega t \pm x/\Lambda)} \tag{Eq. 3-71}$$

where $\underline{\Lambda}$ and Λ are given by:

$$\underline{\Lambda} = \frac{\Lambda}{(1+j)} \tag{Eq. 3-72}$$

$$\Lambda = \sqrt{\frac{2}{\omega RC}} = \omega_{pe}\sqrt{\frac{ag}{\omega\nu_m}} \tag{Eq. 3-73}$$

with a the sheath width, g the plasma bulk height, ν_m the electron-neutral collision frequency, and ω_{pe} the electron plasma frequency. The voltage perturbation is a strongly-damped wave; the value of Λ increases with electron density, sheath thickness and bulk plasma height, and decreases with higher excitation frequency and collision frequency (higher pressure). If the inductance is included, the damping length increases and the wavelength decreases. The boundary condition at the sidewall is

$$\left.\frac{\partial}{\partial x}\tilde{\boldsymbol{U}}\right|_{x=L} = -I_{\text{Sidewall}}R = -\tilde{\boldsymbol{U}}(L)j\omega C_W R \tag{Eq. 3-74}$$

where C_W is the sheath capacitance at the sidewall.

Note that this simple model assumes the plasma to be a uniform slab. The RF plasma potential is the same as the ground sheath RF voltage in this simple model where the impedance of the bulk plasma is neglected compared to the sheath impedance. The combination of a reduced and augmented sheath potential at the asymmetric edge results in a net increased power deposition at the edge. Comparison between this solution and solution of MAXWELL's equations for the voltage distribution in a lossy dielectric shows that the telegraph model is a good approximation.

Consequences of non-uniform RF plasma potential

Since the DC plasma potential is uniform across the plasma, and a conducting electrode is an equipotential surface (in absence of a dielectric substrate), a consequence of the non-uniform RF plasma potential is that local ambipolarity cannot be satisfied over all the electrode surface. This is because the RF and DC sheath voltages, $\tilde{\boldsymbol{U}}$ and $\bar{\boldsymbol{U}}$ respectively, cannot everywhere simultaneously satisfy the self-rectification condition for zero DC current flow, which is

$$\bar{\boldsymbol{U}} = \frac{T_e}{2}\ln\left(\frac{M_i}{2.3m_e}\right) + T_e\ln\left[I_0\left(\frac{\tilde{\boldsymbol{U}}}{T_e}\right)\right] \tag{Eq. 3-75}$$

(a sinusoidal plasma potential, and therefore sinusoidal sheath voltages, have been assumed for the sake of convenience in this simplified model). Any spatial variation in the plasma RF potential will necessarily lead to time-averaged current flow across the sheaths. However, the reactor is capacitively coupled which prevents any DC current in the external circuit. Therefore, any DC current which flows across the sheaths must circulate through the plasma and return via the conducting surface of the electrode, so that the integral of the DC current over the electrode area is zero. The DC plasma potential adjusts to satisfy this condition at the ground electrode, and the self-bias of the RF electrode adjusts to satisfy this condition at the RF electrode. Consequently, the reactor asymmetry drives a circulating DC current within the reactor as shown in Fig. 3-9.

3.5.2 Consequences of the non-uniform RF Plasma Potential

Some consequences of the telegraph model are summarized for an asymmetric reactor (with RF electrode smaller than ground electrode) for plasma conditions so that $\Lambda < L$, where L is the half-width of the reactor. The telegraph model predicts the following[6]:

(i) The RF plasma potential and sheath RF voltages vary across the reactor. The net RF power dissipation is therefore non-uniform, with the plasma becoming more intense near to the edges. In contrast, an intense edge plasma due to fringing fields[38] is confined to the immediate vicinity of the edge discontinuities. In the examples shown in [6], the variations in RF power due to the telegraph effect are only a few percent if summed for both sheaths, but they are much larger for each individual sheath.

(ii) For a sufficiently thin substrate, the substrate surface potential and charge are negative and non-uniform across the substrate, and not only positive and uniform. Negative substrate charging has been observed experimentally. For a sufficiently thick substrate, the surface potential can become positive or even bipolar. Non-uniform DC potential on the substrate surface in the presence of a uniform DC plasma potential results in non-uniform ion bombardment energy, which is detrimental for some plasma processes.

(iii) The self-bias is different from that estimated using the conventional “area law.” For example, it depends on the plasma parameters and the dimensions of the reactor. It becomes more negative for a thin dielectric substrate partially covering the ground electrode.

(iv) DC current circulates internally via the plasma across the sheath and returns along the electrode conducting surfaces. This distribution of DC current flow across the sheaths has been observed experimentally.[62] A localized peak of electron flux from the plasma can arise at the edge of a substrate and also at the edge of the excitation electrode.

The telegraph effect can be simply eliminated by using symmetric sidewalls. The telegraph effect and the standing wave effect are necessary and sufficient to describe all the electromagnetic non-uniformity in an axial symmetric reactor (except for the edge modes).[98][124]

3.6 Expected Uniformity Topology

Depending on the RF excitation frequency used, different plasma density profile topologies are expected. Table 3-1 breaks down the shapes anticipated and the terms used to denote them. *Over-, under- and perfect compensation* refer to the shaped electrode only. Vacuum electric field profiles would show the same trend, but much less pronounced, as they are not “worsened” by the effective dielectric constant ε_{eff} of the plasma. For simplicity’s sake only radial profiles across the cylindrical reactor are used to illustrate the shapes.

Table 3-1: Expected plasma profile shapes (disregarding edge effects) in a $1[\mathrm{m}]$ reactor and used terms to denote a profile shape.

f_{RF} **vs.** f_{Design}	**Actual RF Frequencies** [MHz]	**Expected Plasma Intensity Profile Shape**	
		With conventional flat electrode	With shaped electrode
below f_{Design}	13.56 **Reference Frequency**	“almost” flat, good uniformity 	strong overcompensation ⇒ deeply concave 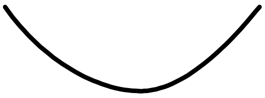
	27.12	non-uniform 	overcompensation ⇒ concave 
	40.68	very non-uniform 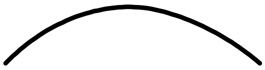	slight overcompensation ⇒ slightly concave 
at f_{Design}	67.8 **Work Frequency**	highly non-uniform 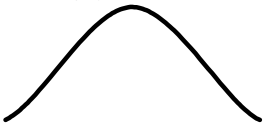	perfect compensation ⇒ good uniformity 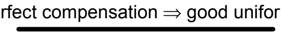
above f_{Design}	100 **Control Frequency**	extremely non-uniform 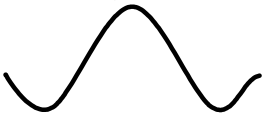	undercompensation ⇒ convex 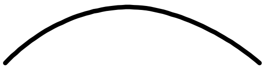

Flat electrode

Predominantly convex, arched or dome-like profiles are to be expected at all frequencies for the flat electrode. At low frequencies and special process conditions other profiles may appear because of possible interplay with edge and telegraph effects. At very high frequency (VHF) the visibility of the 1st Bessel minimum is expected within the reactor confines.

Shaped electrode

Three different topologies are expected. Concave, flat and convex shapes depending if the excitation frequency is below, around or above the design frequency.

3.7 Conclusion

It was the objective of this chapter to show theoretically, that voltage non-uniformities due to the standing wave between two metallic plates can be successfully removed i.e. it is possible to compensate under certain conditions (cf. 3.2.3) the standing wave effect. A uniform voltage field is necessary to ignite and sustain a uniform plasma discharge.

Cylindrical

For a cylindrical geometry it is possible to find a solution of the reduced MAXWELL's equations which allows to create a uniform vertical electrical field and thereby to suppress the radial electromagnetic standing wave non-uniformity in vacuum. One of the electrodes must be shaped according to the GAUSSIAN approximation (Eq. 3-29) of the exact lens solution. Its shape is a function of four parameters: the RF excitation frequency, the electric permittivity of a dielectric in the concavity, the gap distance between the two electrode plates and the radius of the reactor. The symmetry of the cylindrical configuration guarantees a uniform boundary condition.

Rectangular

The rectangular geometry requires the solution of two coupled equations (Eq. 3-45 and Eq. 3-46) in a complex 3D geometry. In addition the excitation at the border is no longer intrinsically uniform. The voltage non-uniformity in a rectangular parallel-plate vacuum capacitor and an optimized shape electrode to suppress this standing wave non-uniformity in vacuum were calculated numerically.

Possible limitations

A limitation for a shaped electrode can come from the power dissipation caused by the radial electric field E_r. Its effect is negligible as long as the electrode gap remains small compared to the vacuum wavelength of the excitation frequency. Also plasma perturbation effects, especially in rectangular geometry, can impair the lens correction if the effective dielectric constant of the plasma differs widely from the one for which the lens is designed.

Shape calculation

Section 3.3 gives the parameters for which the electrodes installed in the reactors described in Chapter 4 and used in Chapter 6 and Chapter 7 were calculated.

Part III: Materials and Methods

Chapter 4: Setup & Diagnostics

This chapter describes the experimental tools and setups used for this work, except RF equipment such as RF power generation, matching networks and transmission lines, which are discussed in Chapter 5.

The basic hardware comprises the reactor and the vacuum system for the cylindrical (See 4.1) and rectangular reactor (See 4.2). The diagnostics used to characterize the non-uniformity either in vacuum or air are detailed in 4.3, those used with a plasma are described in section 4.4. The RF probes in section 4.5 are used to determine the electrical characteristics of a plasma and are used to assure stable discharge conditions during non-uniformity measurements.

4.1 Cylindrical Reactor Setup

4.1.1 Vacuum Scheme and Pumping System

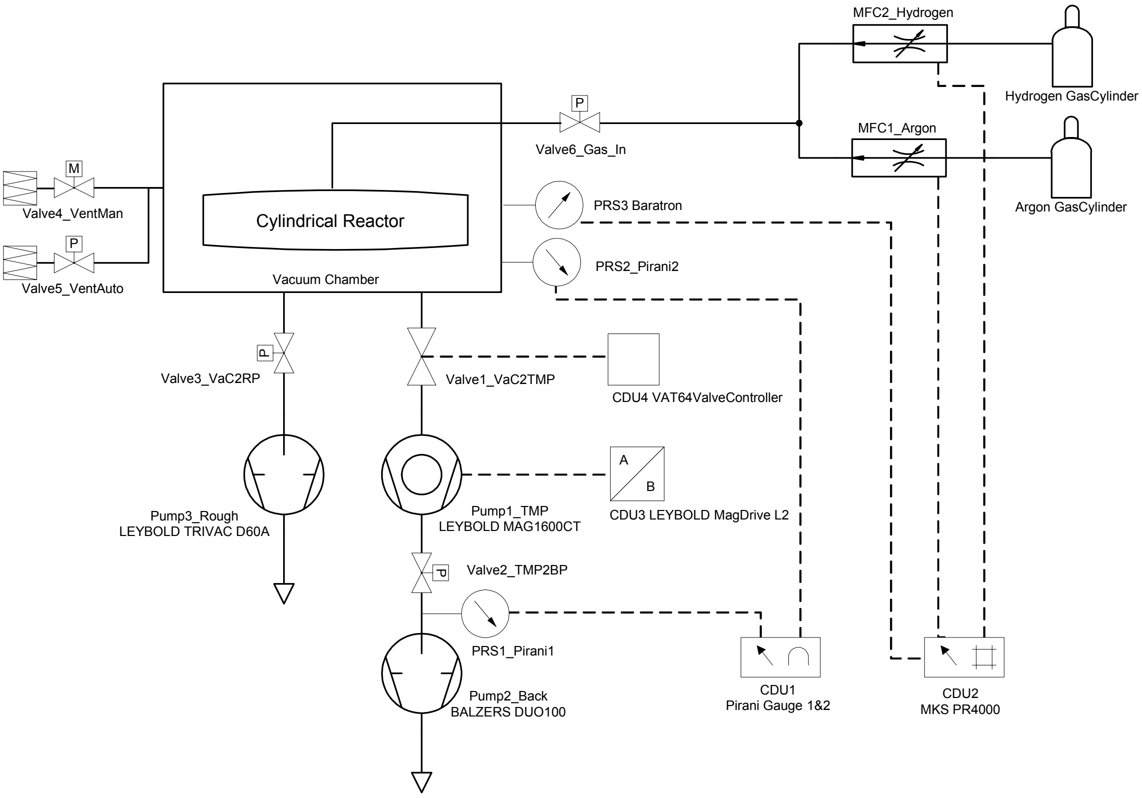

Fig. 4-1: Pumping system, gas inlet and exhaust of the cylindrical reactor.

Single Pressure Chamber

Figure Fig. 4-1 shows the vacuum system used for the cylindrical test reactor. The vacuum chamber is a single pressure chamber, that is, there is no differential pumping of the chamber with respect to the reactor. The process gases enter the reactor via a four-point gas inlet through the top plate of the reactor. The gas-inlets consist of perforated discs with tiny holes in order to prevent any hollow cathodes striking in the gas lines. The gases escape the reactor through its windows (cf. Fig. 4-2). At the pump side, a roughing pump (Pump 3) lowers the chamber pressure from atmospheric pressure to a level before the turbo-pump (Pump 1) can be used with its backing pump (Pump 2). Effluent gases leave the system by a gate valve (Valve 1) needed for coarse control of the pumping speed of the turbo-pump. The pressure is finely regulated by upstream mass flow controllers (MFC 1 and MFC 2) linked to a Baratron pressure gauge (PRS 3) via a PID pressure controller (CDU 2). Two Pirani pressure gauges are available to check the fore vacuum pressure (PRS 1) and the chamber pressure during roughing (PRS 2). As no toxic or corrosive gases are to be used in this reactor, no exhaust gas treatment is employed.

4.1.2 Reactor Cross Section

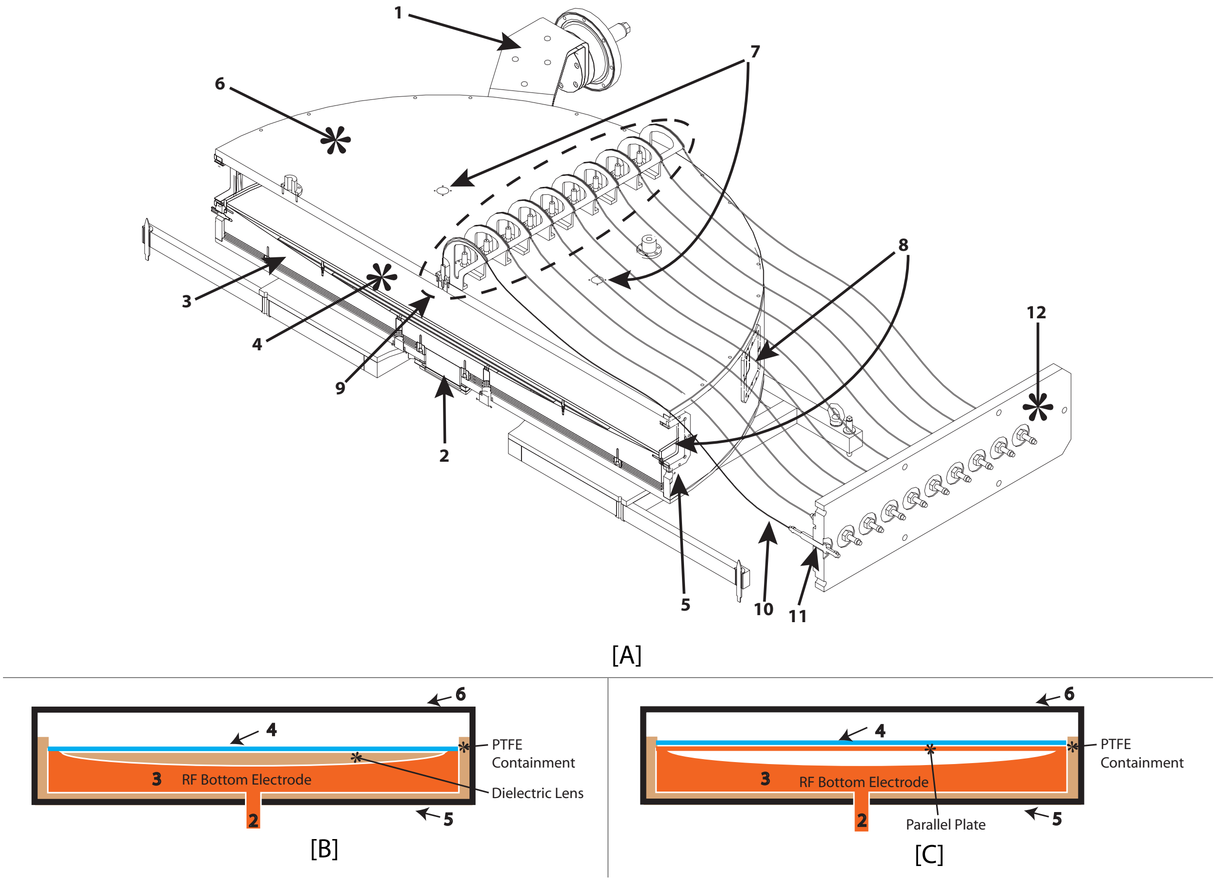

[A]

[B]

[C]

Fig. 4-2: Cross-section of the cylindrical reactor:
[A] True-to-scale representation where half of the reactor is removed to allow a view into the interior of the reactor: 1) RF ribbon with vacuum feedthrough, 2) central RF feeding point, 3) bottom RF electrode with 4) dark glass plate on top, 5) grounded housing of reactor, 6) top plate and top electrode, 7) two of four gas inlets, 8) viewing windows with fine-meshed wire netting, 9) half of the optical fibres with anti-bend fibre support and vertical straight angle collimators and electrostatic surface probes (not visible) (See Fig. 4-7 in section 4.4.1), 10) optical fibre in metal ferrule protection. 11) vacuum feedthroughs for optical fibres, 12) flange of vacuum chamber.
[B] Simplified front view not to scale of lens configuration and [C] parallel plate configuration.

The cylindrical reactor is a large, asymmetric RF plasma capacitor. It is designed in order to test the principle of the cylindrical lens concept and at the same time to stay as close as possible to the KAI architecture, which is the final application platform for the shaped electrode. It is kept as simple as possible and is deliberately stripped of any complex fittings needed for deposition (e.g. heating, gas shower-head, substrate loading mechanism, resilience to process gases, etc.) but superfluous for the proof of principle with non-reactive gas in contrast to the rectangular reactor described in section 4.2.2.

The cylindrical reactor consists primarily of two large mechanical parts: a large $1.02[\mathrm{m}]$ inner diameter cylindrical grounded housing (5 in Fig. 4-2) which contains a $1.0[\mathrm{m}]$ diameter round, circular RF electrode (3). The RF electrode can be either the shaped lens (Fig. 4-2-[B]) or if necessary it can be covered with a tightly screwed flat metal plate in order to convert it to the conventional parallel plate, flat electrode configuration (Fig. 4-2-[C]). The RF electrode is fitted into a mantle of PTFE underneath and laterally in order to prevent parasitic discharges in the gaps. In the case of the flat electrode configuration, only the top facing the plasma volume is kept empty of PTFE. In the case of the shaped electrode, the concavity is filled with a dielectric lens made of PTFE as well. A dark glass plate is put on top of the RF electrode to minimize stray light reflections. A metal ribbon is inserted laterally between the RF electrode and the PTFE skirt in order to change the two electrodes' surface ratio. The RF supply (1) passes through a hole (2) in the centre of the bottom plate of the housing. The grounded housing contains fine-meshed wire netting windows (8) which serve for visual inspection of the interior of the reactor and as an outlet for the process gases. The wire netting ensures the ground continuity across the window areas and is necessary for the confinement of the plasma. The upper plate (6) of the housing includes the uniformity measurement system as depicted in Fig. 4-7. Nineteen optical fibre telescopes and the surface mounted electrostatic probes (9) are distributed across one diameter (cf. 4.4.1).

Screening Effect of Conductive Substrate

Note that either the RF electrode or the ground electrode can be chosen to have the GAUSSIAN-lens shape. Also, if a conducting substrate is to be used, it should be placed on the plane electrode, and not above the GAUSSIAN-lens electrode, to avoid screening the electric field in the vicinity of the lens.

4.2 Rectangular Reactor Setup

4.2.1 Vacuum Scheme and Pumping System

For industrial use

The KAI 1000 reactor is a full-scale industrial type reactor designed for mass production of thin films. Its use within a production line imposes stringent conditions for industrial manufacturing, i.e. uniformity of the gas composition and low residual gas impurities. Therefore its vacuum scheme conforms to the so-called plasma-box design after SCHMITT.[115][105][104] The system is equipped with differential pumping, one for the reactor (Pump 4) and one for the vacuum chamber (Pump 1, Pump 2, Pump 3). The gas feed is arranged in such a way that each part of the substrate area is supplied with fresh process gas by means of a perforated top showerhead electrode. The pressure is controlled by a downstream butterfly valve (Valve 11) linked to a BARATRON pressure gauge (PRS 3) in the gas exhaust manifold of the reactor. The vacuum chamber is evacuated by a completely separate pumping system (Pump 1, 2, 3). Pump 3 is only used for roughing the chamber.

Plasma box principle

The main purpose of the vacuum chamber is to maintain a differential pressure between the plasma box and the enclosing vessel. By mechanical construction, the leak gas conductance between the inner and outer volumes of the reactor can be kept small enough to achieve this. Two cases are possible:

1. In order to achieve high gas purity in the reactor, the plasma box is pressurized with respect to the enclosing vessel. During PECVD operation mode, the outer pressure remains about one hundred times smaller than the inner process pressure, so that impurities outgassing from the cold wall chamber and mechanical parts or heating

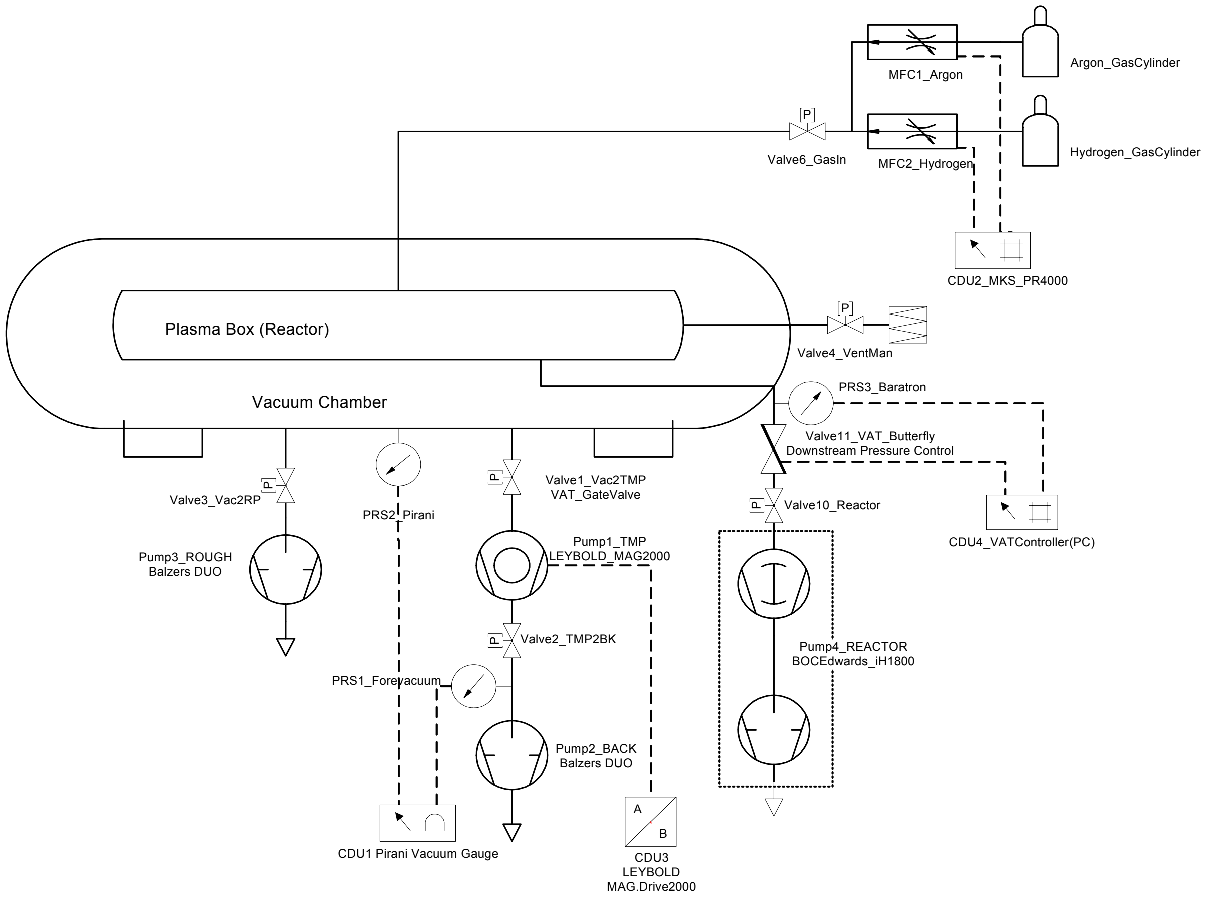

Fig. 4-3: Vacuum scheme of KAI 1000. The system disposes of a differential pressure system.

elements are prevented from diffusing inside the plasma box, which guarantees the excellent purity of the deposited film.

2. Conversely to prevent the escape of gases the pressure gradient is reversed during the etching mode to clean the reactor between successive PECVD runs. One establishes an overpressure of N_2 outside the plasma box in order to prevent leakage of corrosive fluorinated species, as well as sulphur by-products (when using SF_6) condensable on the cold-wall chamber. Since the inner walls of the plasma box are made of Al which is resistant to fluorine at high temperature (this is not the case for stainless-steel), the etch-cleaning cycle does not leave any residue except for a thin layer of AlF_3, and PECVD can be immediately performed after etching without requiring a pre-coat of the reactor walls.[61]

4.2.2 Reactor Cross Section

The principal architecture of the rectangular reactor is that of a large $1[\mathrm{m}^2]$ rectangular capacitively-coupled RF plasma reactor, equipped to make it suitable for industrial deposition processes. The RF power is supplied via a long RF stripline (1 in Fig. 4-4) which makes contact to the reactor via four feeding points (2). The RF electrode (3) is suspended from the top plate in contrast to the cylindrical reactor where it is sitting on the bottom. The top electrode has a special design to allow a uniform working gas injection across the electrode. This so-called "showerhead" is essential for a uniform gas flow and a homogeneous gas distribution during deposition processes.[104] The effluent gases are drawn off by two lateral pumping outlets (5). The bottom plate (6) of the reactor serves as the grounded electrode. Due to the complexity of showerhead RF electrode it was chosen to replace the bottom electrode with a shaped one (cf. Fig. 4-4-[B] and cf. Fig. 4-4-[C]) and not the RF electrode (in contrast to the cylindrical reactor). The optical diagnostics (cf. 4.4.2) are set into the bottom electrode. They are arranged as four columns,

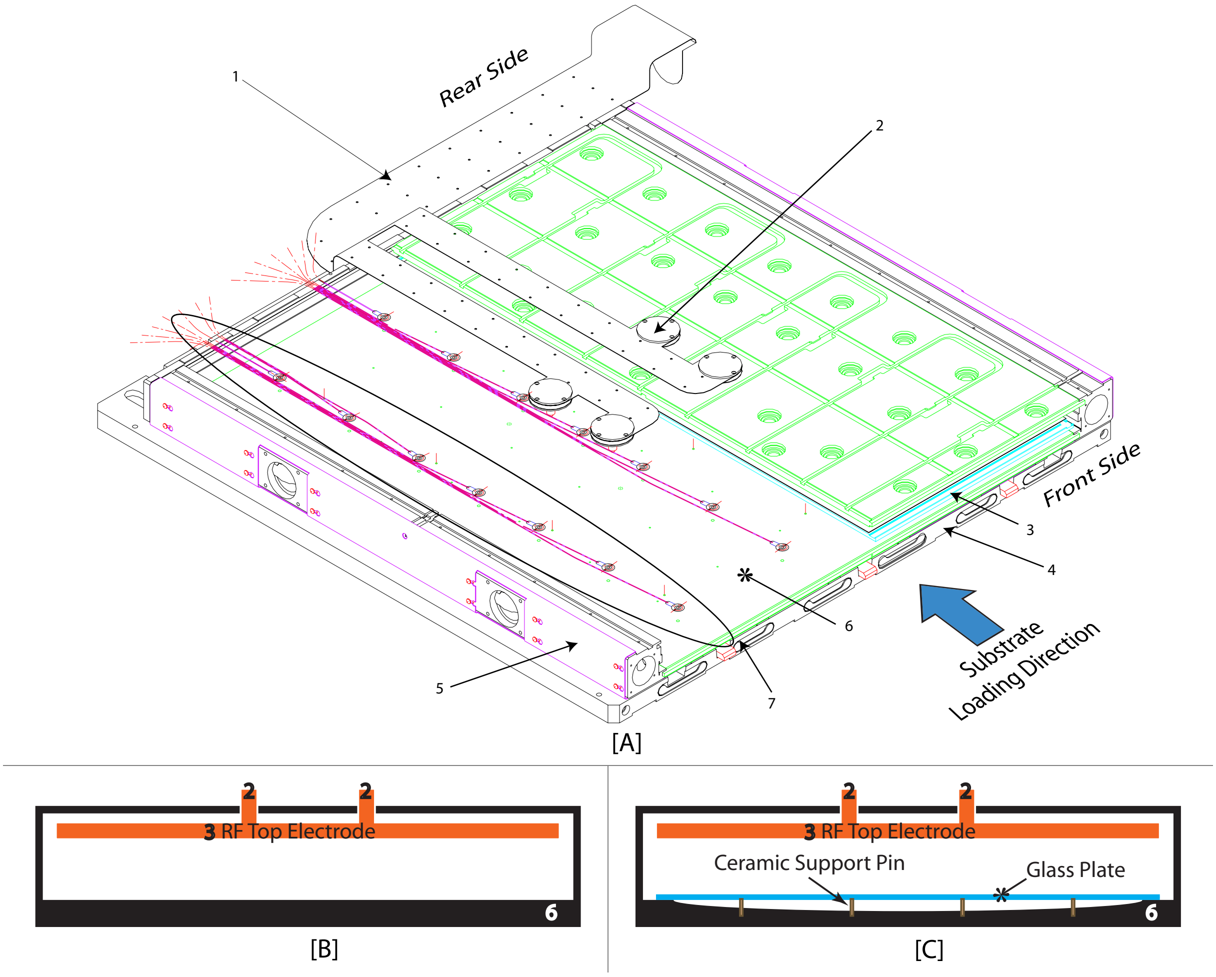

[A]

[B]

[C]

Fig. 4-4: Schematic drawing of KAI 1000 plasma box.
[A] True-to-scale representation where half of the top plate and top electrode are removed to allow a view into the interior of the reactor: 1) RF ribbon, 2) one out of four RF feeding points, 3) suspended top RF electrode with showerhead, 4) chassis of plasma box, 5) lateral pumping outlet, 6) bottom plate and bottom electrode, 7) one of four columns of seven optical fibres with collimators (cf. 4.4.2.2). The optical fibres pass below the bottom electrode and are shown to illustrate better the diagnostics. Substrates are loaded and unloaded from the front.
[B] Simplified cross section not to scale of parallel plate configuration and [C] lens configuration with ceramic support pins for glass substrate.

each has seven points of observation. Two out of four columns are depicted in Fig. 4-4 (7), the other two strands of optical fibres are distributed similarly across the covered half of the reactor. The optical fibres run outside the reactor between the bottom plate and the chassis (4) towards the fibre vacuum feedthroughs in the rear wall of the vacuum chamber. The whole plasma box is sitting on a chassis (4) which serves also as a temperature stabilizer during deposition processes.

Differentially pumped lens

The bottom electrode exists in two variants: flat electrode (Fig. 4-4-[B]) and shaped electrode (Fig. 4-4-[C]). The flat electrode is the standard configuration and does not need any additional arrangements. If the shaped electrode is used, then a transparent glass substrate has to be placed on the electrode which serves as the dielectric plate needed to separate the plasma volume from the lens concavity as shown in Fig. 3-4. As the optical diagnostics observe the plasma from the bottom plate, it is not possible to fill the lens concavity with a dielectric, because it would block the view of the plasma. This means that the lens concavity must be kept clear of any dielectric and becomes a vacuum lens. The only solution to avoid the same breakdown conditions as in the plasma volume is to have a differential pressure. This is obtained by evacuating the lens concavity via the vacuum chamber, which is pumped out by an independent pumping system. Therefore we have a differentially pumped vacuum lens.

Pin support for glass substrate

As described earlier in the theoretical section, the depth of the concavity behind the dielectric plate (Fig. 3-1(b)) must be preserved during operation to guarantee the correct compensation by the shaped electrode. The weight of the glass substrate and/or a differential pressure, where the pressure in the vacuum lens is lower than in the plasma, volume would exert a net force downwards on the glass substrate and would cause a sagging of the substrate; which in turn would reduce the geometrical thickness of the lens unless the dielectric plate were properly supported.

Glass flexion negligible

It was chosen to install 6×6 ceramic pins distributed evenly across the lens area of $1000[\mathrm{mm}] \times 1168[\mathrm{mm}]$. The maximum pin-to-pin distance is ca. $190[\mathrm{mm}]$ or ca. $160[\mathrm{mm}]$ respectively depending on the direction. Assuming a maximum pressure of $2000[\mathrm{mTorr}]$ in the plasma volume and perfect vacuum in the lens would exert a force similar to the one caused by a mass of $\approx 30[\mathrm{kg}]$. Distributed across roughly 7×7 grid squares this load yields a load of $\approx 0.6[\mathrm{kg}]$ per square. A small test glass substrate of $3[\mathrm{mm}]$ thickness was underpinned at four points of a rectangle $(180[\mathrm{mm}] \times 220[\mathrm{mm}])$, and its flexion was measured with a mechanical comparator. Putting a mass of $0.6[\mathrm{kg}]$ in the centre of the support rectangle made the glass bend $0.065[\mathrm{mm}]$, one of $1.5[\mathrm{kg}]$ caused a sagging of $0.14[\mathrm{mm}]$. The flexion of the glass due to its own weight was not measurable with this setup. Taking into account the factors of the applied lens aberration (7.2.2), it was concluded that the flexion of the glass can be successfully prevented by the use of support pins and the residual flexion remains subcritical.

4.3 E-Field Probe

Prior art voltage probe

An in situ voltage probe was already used by Sansonnens[15][4] to measure the voltage distribution in a large-area reactor due to the standing wave effect. This method requires that the probe can make a direct contact between the top and the bottom electrode. Is is not possible to use the same technique if there is a dielectric on one of the electrodes (either by putting deliberately a substrate, a PTFE sheet or unintentionally by a thin insulating oxide layer on the Al electrode) and/or the inter-electrode gap is variable.

E-field probe

The in situ electric field probe used in this thesis is a further development of the aforementioned diagnostic. It avoids its main shortcoming, the necessity to make electrical contact. Basically, the probe measures the voltage between the two probe antennae as shown in Fig. 4-5. The practicality of a similar design to be used in a $2.45[\mathrm{GHz}]$ microwave plasma reactor was successfully demonstrated by Pleuler et al.[44]

The E-field in $[\mathrm{V/m}]$ is simply the measured voltage divided by the antennae distance. The induced voltage between the two antennae is rectified by a Schottky diode. The high resistances along the line have the purpose of minimizing perturbation caused by the E-field. The $1[\mathrm{k\Omega}]$ resistors are carefully chosen among 50 pieces in order to have the smallest resistance deviation. A low dielectric stiff fibreglass tube is used as a support because the reactor is very long. Before measuring the resulting DC voltage, a $50[\mathrm{Hz}]$ low-pass filter is inserted in order to suppress any signal originating from the mains power frequency passing the RF generator. The advantage of this probe is that it measures a DC voltage which is proportional to the RF voltage amplitude.

Resolution, reactor gap and directionality

The two probes of the antenna are at a distance of ca. $10[\mathrm{mm}]$. A bigger antenna distance would yield a higher voltage and a better resolution, but the distance is restricted by the reactor gap (in this case by the reactor height of the KAI 1000 which is $28[\mathrm{mm}]$). The measurement is directional; it has to be kept in a perpendicular position with respect to the parallel plate flat electrode or at right angles to a substrate on a lens to measure the vertical electrical field E_z. This is achieved by a PTFE sledge at the head of the probe as shown in Fig. 4-5-[B], which fixes the probe vertically.

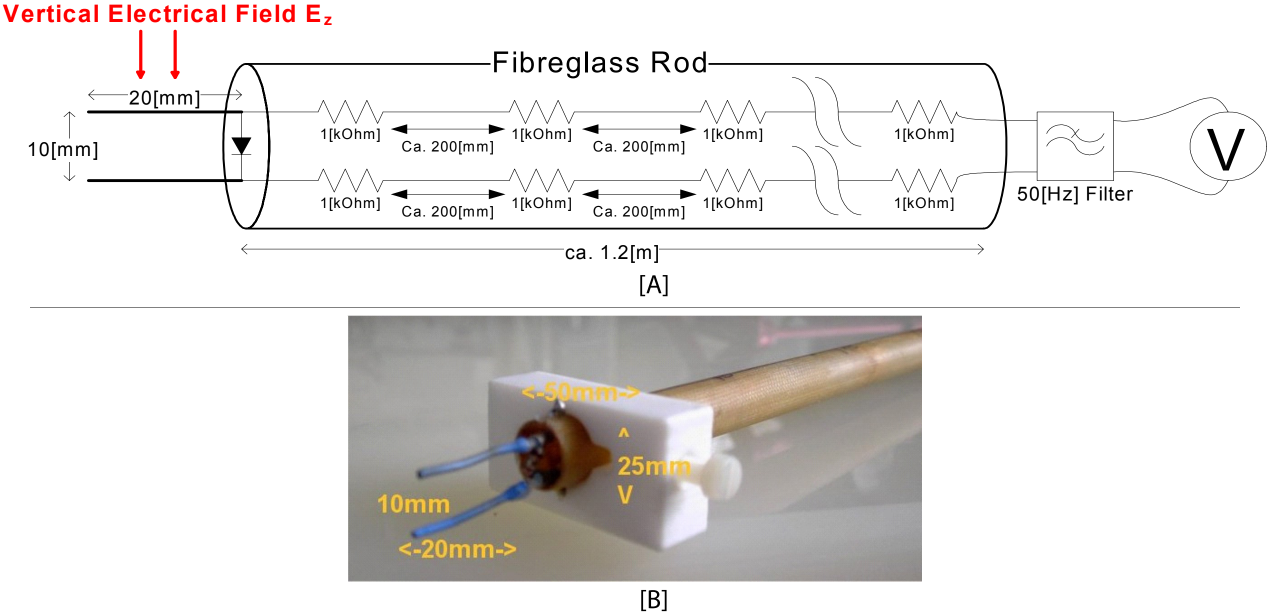

[A]

[B]

Fig. 4-5: Electric field probe: [A] Circuit diagram and [B] snapshot of the probe head antennae.

Boundary condition

The probe was inserted into the reactor via small windows (cylindrical reactor) or orifices in a metal plate fixed on the reactor mouth (rectangular reactor in Fig. 4-6). If no metal plate is used, then the boundary condition for the standing wave is disturbed and causes a distorted electric field profile which has its maximum at the door side of the rectangular reactor (cf. 7.4.3).

Fig. 4-6: Orifices in a metal plate contacting top and bottom plate of the KAI 1000 reactor. The shaft on the right side is the inserted E-field probe.

Data normalization

A xy-scan of the rectangular reactor consists of 24 x 9 points and takes about $30[\mathrm{min}]$. All the measurements have to be done at very low RF power (ca. $\leq 50[\mathrm{W}]$), firstly to avoid saturation of the E-field probe signal and secondly, because without plasma load, virtually all the delivered RF power is reflected and has to be absorbed either by resistive effects in the matchbox or stripline or by the generator itself. Exceeding the maximum threshold of reflected power can cause the RF source to behave unpredictably or to shut off automatically. On the other hand, operating in the minimum output region of a RF generator can bring about stability problems at the lower end of its regulation scale and the delivered RF power does not remain sufficiently constant during the time span of a whole scan. Therefore the voltage readings from the E-field probe are normalized to the peak-to-peak voltage measured by a commercial HF oscilloscope probe (PMK PHV-641, bandwidth $400[\mathrm{MHz}]$) on the stripline. The purpose is to correct for slow RF power oscillations and drifts.

4.4 Probes for Plasma Uniformity Measurements

Possible methods

The most crucial point in the development of large area plasma systems is to achieve a high uniformity of the plasma and of the related etch and deposition rates. Thus we need to dispose of a diagnostic for both the cylindrical and rectangular reactors, to characterize the uniformity of the plasma experimentally. There are several possibilities to measure this:

(i) *in situ* e.g. by measuring the spatially-resolved local optical emission intensity by a photometer, by measuring the local electrical properties such as ion fluxes and local electron temperature by the well established Langmuir probe method or by measuring the ground state radical densities by laser induced fluorescence (LIF); or

(ii) *ex situ* by measuring the thin film deposition rate or etch rate on a substrate.

In situ advantageous

In situ measurements offer advantages over *ex situ* methods in terms of speed of measurements and the possibility to use simple gases instead of reactive ones. However it means that the experimental setup of the reactor becomes more intricate. For this thesis the potentialities of *in situ* measurements outweigh by far its main drawbacks.

Optical spatially-resolved measurements

Measurement of the local optical emission by fibre optics as a means to determine the uniformity in a transverse RF excited discharge of slab-type CO_2 laser has been described by Colley et al.[34] and Lapucci et al.[23] A fibre-optic system combined with optical emission spectroscopy (OES) for in-situ monitoring of the spatial distribution of plasma during the fabrication of large-area amorphous silicon photovoltaic modules in DC PECVD has been reported by Carlson et al.[100] They installed a system of nine probes distributed over an area of $60[\mathrm{cm}] \times 115[\mathrm{cm}]$ in a reactor used for coating $0.8[\mathrm{m}^2]$ substrates. The fibres are oriented perpendicular to the substrate so that they measure the plasma emission only in a localized region. Heinrich et al.[116] reports a 16 channel optical process monitor for the locally resolved in situ process control of a $69[\mathrm{cm}] \times 47[\mathrm{cm}]$ distributed quadruple ICP source. Buie et al. [45][46] and Pender et al.[47] use transverse spatially resolved optical imaging for in situ etch uniformity measurements of the GEC reference cell. Böhm and Perrin[114] use an optical multi-channel with a lens and an interference filter for vertically resolved optical emission spectroscopy.

Electrical spatially-resolved measurements

Many authors report on spatially-resolved probe measurements in large-area CCP or ICP reactors with a *movable* Langmuir probe (e.g. Mashima[9], Kawai[20], Wickramanayaka[33] and Heinrich[116]). Langmuir probes' characteristics are very difficult to measure in RF because of the RF pick-up, although ion flux measurements are much simpler. This technique requires a very stable discharge and RF supply during the whole scan, which was not the case for all configurations and frequencies used in the cylindrical reactor. Baker et al.[112] reports a different approach for spatially-resolved probe measurements of the electrical properties of a RF laser by means of four *surface probes* set into one of the electrodes. His method allows in principle a straightforward parallel read-out of the four probe heads with e.g. a four channel oscilloscope. The technique can be extended to multiple probes with the use of a suitable data acquisition system (DAQ).

Two independent diagnostics

Considering the above experience and the requirements for the cylindrical reactor, a combined electro-optical plasma uniformity measurement system was developed. The combination of both, electrostatic probes and optical observation enables to instantaneously cross-check the measurement results at an early stage by two independent methods.

4.4.1 Combined Optical and Electrostatic Probes for the Cylindrical Reactor

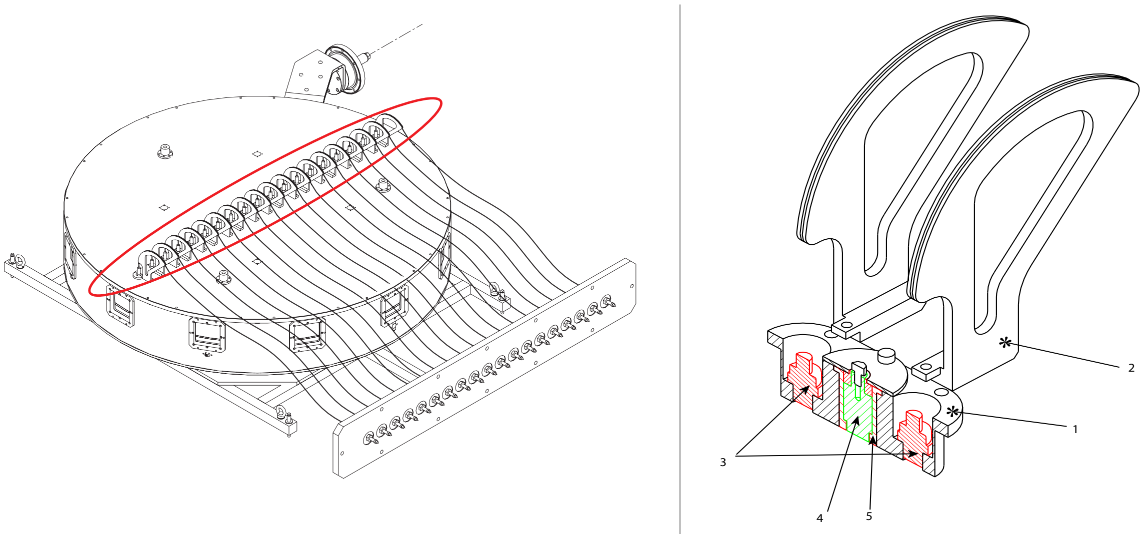

[A]

[B]

Fig. 4-7: Plasma non-uniformity diagnostic system for the cylindrical reactor: [A] Arrangement of the 19 optical and 10 electrostatic probes along a diameter in the surface of the grounded top electrode. [B] Diagnostics front end module consisting of 1) body to be fixed in the top electrode, 2) “anti-bend” support for optical fibres, 3) two straight angle collimators for fibres (cf. 4.4.1.2) and 4) one surface electrostatic surface probe of diameter $10[\mathrm{mm}]$ (4.4.1.1) embedded in 5) an electrically insulating MACOR casing.

The cylindrical reactor is equipped with 19 fibre optical telescopes distributed across the diameter as shown in Fig. 4-7-[A]. In addition 10 surface mounted electrostatic probes are installed, one between each second pair of telescopes as shown in Fig. 4-7-[B]. Each electrical probe measures the local ion saturation current $I_{sat}(r)$ as outlined in section 4.4.1.1. Each fibre optic probe measures the local optical emission intensity $I_{oes}(r)$ as described in section 4.4.1.2. The conditioning of both signals for the analog-digital converter (ADC) is explained in section 4.4.1.3, followed by a short description of the calibration procedure and computer aided DAQ in 4.4.1.4.

4.4.1.1 Electrostatic Surface Probe

The surface mounted electrostatic probe is technically a planar LANGMUIR probe.[40] The front head of the probe as shown in Fig. 4-7-[B] is flush with the electrode surface and faces the plasma, a potential is applied and the current drawn by the probe is recorded. A DC voltage sweep produces a characteristic current-voltage (I - V) curve shown schematically in Fig. 4-8.[58] Let the plasma potential (space potential) be V_s, and the potential applied to the probe be V_p. When $V_p \gg V_s$, an electron current I_e is collected. When $V_p \ll V_s$, an ion current I_i is collected. It is customary to plot I - V curves with I_e positive and I_i negative. The floating potential V_f is defined by the probe potential at which the net current to the probe becomes zero, i.e. where the ion and electron currents are equal.

For the plasma uniformity across the diameter of a large-area reactor we are interested in three quantities:

1. In order to measure the ion saturation current I_{sat} it is necessary to bias the probe sufficiently negative to achieve $V_p \ll V_s$, e.g. at $-50[\mathrm{V}]$, and measure the current through the probe.
2. To measure the DC current I_{DC} with $V_p = 0[\mathrm{V}]$ it is necessary ground the probe and measure the current.
3. An unbiased probe and measuring the voltage yields the DC floating potential V_f where $I_i = I_e$.

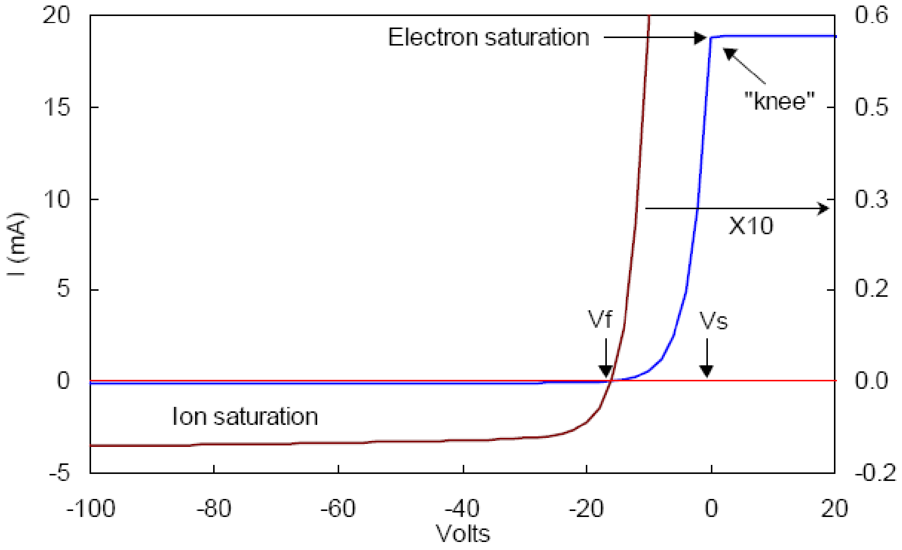

Fig. 4-8: An idealized I-V curve. The left curve is vertically expanded 10 times to show the ion current. Reproduced from [58]. V_s denotes the plasma potential (space potential), V_f the floating potential.

(1.) is used for plasma uniformity analysis related to the standing wave effect, (2.) and (3.) for the telegraph analysis given elsewhere.[62][64] The signal conditioning circuit (cf. Fig. 4-11) provides three measurement modes for each quantity. The I_{sat} to the electrostatic probe can be estimated as follows: The BOHM velocity to the sheath edge is given by Eq. 4-1with T_e in [eV]:

$$v_{Bohm} = \sqrt{\frac{e \cdot T_e}{m_i}} \tag{Eq. 4-1}$$

For the ion flux to the sheath edge it follows that

$$\Gamma_i = n_i \cdot v_{Bohm} = n_i \cdot \sqrt{\frac{e \cdot T_e}{m_i}} \tag{Eq. 4-2}$$

where n_i is the ion density at the sheath edge. For the ion current impinging on the surface of the probe, where A is its surface:

$$I \sim n_i \cdot e \cdot \sqrt{\frac{e \cdot T_e}{m_i}} \cdot A \tag{Eq. 4-3}$$

Assuming standard values for an Ar$^+$ plasma with $n_i \sim 10^{16}[\mathrm{m}^{-3}]$, $m_i \sim 40 \times 10^{-27}[\mathrm{kg}]$, $T_e = 3[\mathrm{eV}]$ and $e = 1.603 \times 10^{-19}[\mathrm{C}]$, we obtain for a surface $A = \pi \cdot (d / 2)^2$ with $d = 10[\mathrm{mm}]$ a current of the order of $I \sim 0.5[\mathrm{mA}]$.[117]

4.4.1.2 Optical Probes

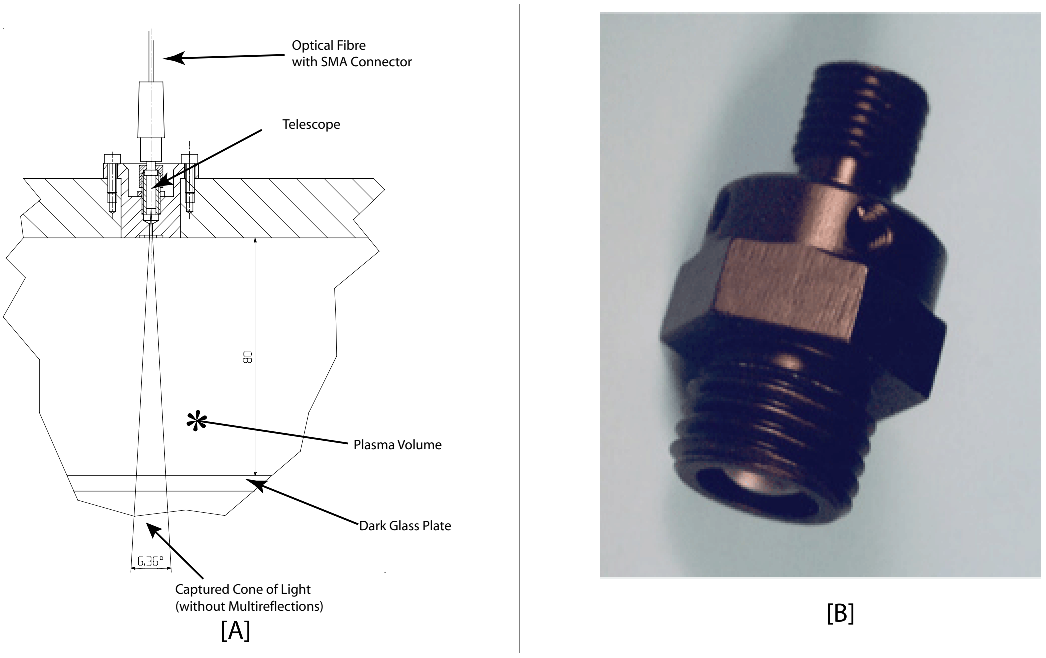

[A]

[B]

Fig. 4-9: Cross section of the head of the optical probe: [A] shows the optical fibre connected to the telescope. [B] depicts a commercial SMA straight angle telescope.

List of components

The in situ sensor of the optical system consists of five components:

1. The light is captured by a straight angle telescope (model AVANTES COL-UV) as shown in Fig. 4-9-[B]. It is made up of a lens of fused silica ($Ø = 6[\mathrm{mm}], f = 8.7[\mathrm{mm}]$) optimized for the UV/VIS/NIR range (wavelength 200 - $2000[\mathrm{nm}]$) and it is built into a black anodized aluminium housing. Its lens collimates the divergent cone of light as shown in Fig. 4-9-[A] into a conical beam, which is directed onto the front port of the first optical fibre. The position of the fibre can be adjusted in axis direction of the telescope to allow for a minimal insertion loss.
2. The first optical fibre (length $1[\mathrm{m}]$, see the 19 strings in Fig. 4-7-[A]) guides the light to the vacuum feedthrough. Its operating wavelength is 180 - $1100[\mathrm{nm}]$ with a $200[\mu\mathrm{m}]$ fibre core and it is encased by a flexible metal tube (CERAMOPTEC UV 200/220P).
3. The vacuum feedthrough is mounted on the diagnostic flange. It contains a short length of a $200[\mu\mathrm{m}]$ optical fibre with a wavelength range of 200 - $800[\mathrm{nm}]$ (AVANTES UV/VIS). Connected to it is
4. the second optical fibre (same type as in 2.), which guides the light to
5. a SMA silicon planar PIN photodiode with a small $1[\mathrm{mm}^2]$ active surface area (model OMC H3R880IR fibre optic receiver) permitting the collection of light with high efficiency for all fibres up to $1000[\mu\mathrm{m}]$ core size. Its photosensitivity spectral range is 400 - $1100[\mathrm{nm}]$ with its peak response wavelength at $850[\mathrm{nm}]$. The typical photocurrent rise time is $5[\mathrm{ns}]$. A photodiode with a small active area offers a low-noise signal detection and a low-cost solution compared to expensive CCD or photomultiplier equipment.

Calibration

The light throughput from channel to channel can differ strongly. The difference is above all due to insertion losses[96] and connector misalignments[95] of the SMA type connector. In order to account for the different optical losses, the optical probes are calibrated with a $1[\mathrm{m}]$ fluorescent tube and a PTFE sheet as a diffuser.

4.4.1.3 Signal Conditioning

Mapping of “raw” values

The signal conditioning takes the low-level signal from the sensor and maps it to the input range and polarity of the DAQ equipment next in line. In our case the analog-to-digital converter (ADC, See 4.4.1.4) expects a voltage signal in the range of $-10[\mathrm{V}]$ to $+10[\mathrm{V}]$ for all channels, optical and electrostatic probes alike.

Photodiode

The photodiodes deliver a photocurrent which is proportional to the light intensity hitting the active surface of the PIN-diode. To convert this current into a proportional voltage, a transimpedance amplifier (Fig. 4-10-[A]) is used. This first stage is in close proximity to the photodiode. Then as a second stage a voltage amplifier (Fig. 4-10-[B]) adapts the converted photocurrent to the input range of the ADC. The total gain achieved by this double-stage approach is 271×10^6[V/A].

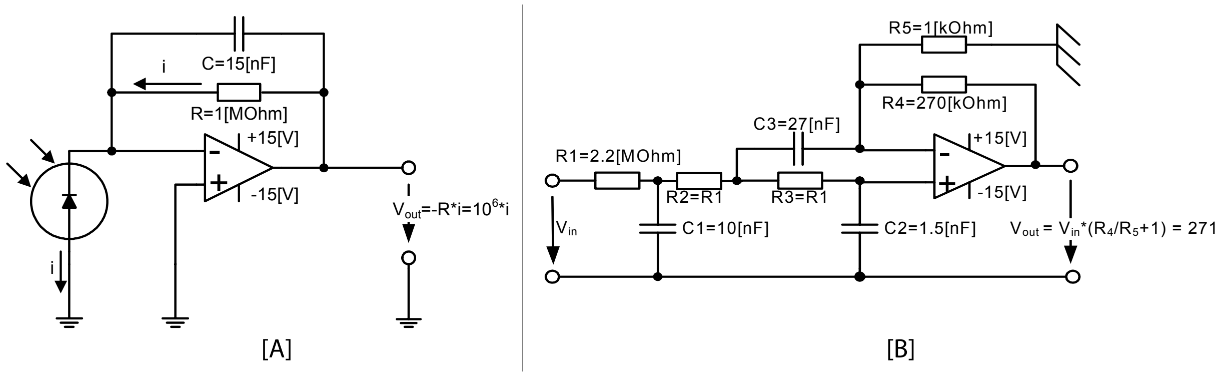

Fig. 4-10: Circuit used to condition and amplify the photocurrent: [A] Transimpedance amplifier with photodiode and [B] associated voltage amplifier.

Surface probes

For the electrostatic probe, we need to measure the currents I_{sat} and I_{DC} and the voltage V_f. The first two require a current-voltage conversion as above which is done by the circuit grouped around the operational amplifier sketched in Fig. 4-11. The bias state -50[V] or 0[V] (GND) is controlled by the 'Bias Selector' relay. This relay is common to all 10 channels. A series of ten double relays is used to bypass the current measurement circuit and to short circuit the output of each electrostatic surface probe to the input of the ADC via a voltage limiter. As we want to measure only DC signals a HF filter at the input of each electrostatic probe blocks any HF signal. In addition at the front end module the probe head and the ground (item (4) and (1) in Fig. 4-7-[B]) can be connected by an RF grounding capacitor of 22[nF].

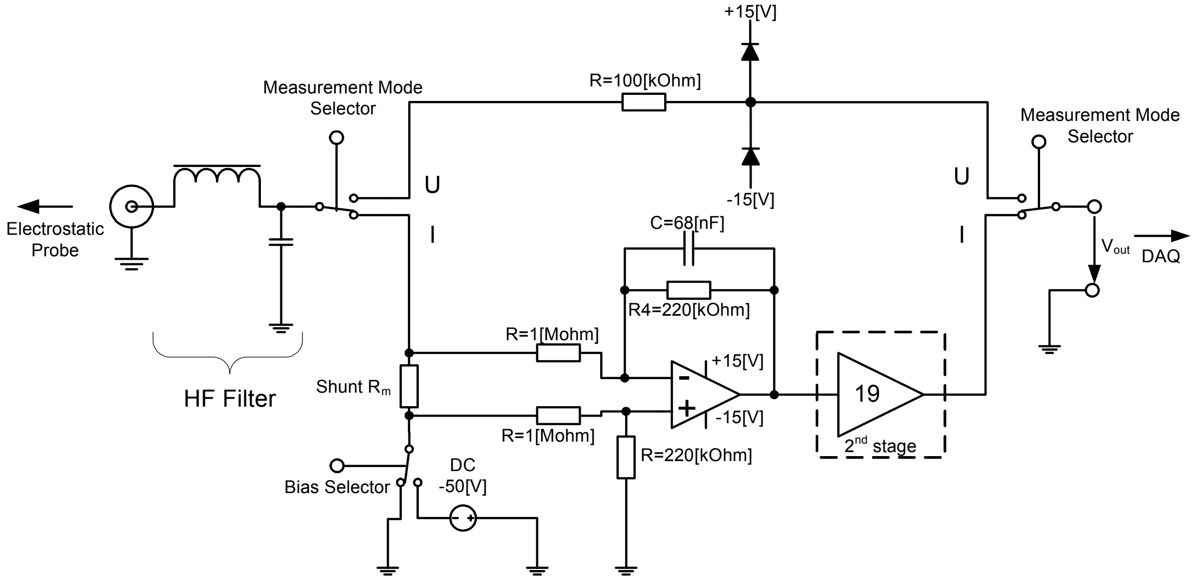

Fig. 4-11: Circuit used to condition and amplify the electrostatic surface probe signals I_{sat}, I_{DC} and V_f. R_m is a variable shunt element, resistors of 10[kΩ] were used. The total gain of both amplification stages for the current is 4.18.

4.4.1.4 Data Acquisition (DAQ) and Calibration

Hardware & Calibration

The conditioned data is acquired by a PC-based analog-to-digital converter (ADC) from NATIONAL INSTRUMENTS (NI PCI-6031E). Its resolution is 16 bit and the 64 channel single-ended ADC is operated in a 32 channel differential input mode to minimize noise effects. The actual input range used is from $-10[\mathrm{V}]$ to $+10[\mathrm{V}]$ with a measurement precision of ca. $300[\mu\mathrm{V}]$. Two analog outputs are use to control the relays for the bias state of the LANGMUIR probes and the measurement mode current or voltage. During a measurement run, the actual readings are corrected for the background readings and the calibration factor (cf. 4.4.3).

Software

A small LABVIEW® programme reads the data from the ADC board and controls, via the analog output, the biasing and the measurement mode for the surface LANGMUIR probes. Settling times of ca. $500[\mathrm{ms}]$ are respected when changing the bias states of the electrostatic probes. A read-out of a block of channels is done quasi parallel and one complete datataking for all photodiodes and electrostatic probes for all biasing states including settling times takes about $5[\mathrm{s}]$, where the time to acquire the non-uniformity dataset I_{sat} and I_{OES} amounts to ca. $1[\mathrm{s}]$. Measurements are plotted instantaneously and archived to permanent storage.

4.4.2 Matrix Optical System for the Rectangular Reactor

The rectangular reactor requires a 2D array of optical probes, as opposed to the cylindrical reactor. Ion flux probes cannot be used in the rectangular reactor because access is possible only through the lens electrode. Because of the large number of optical probes, a commercial multiplexer system was used for data acquisition.

4.4.2.1 Scheme

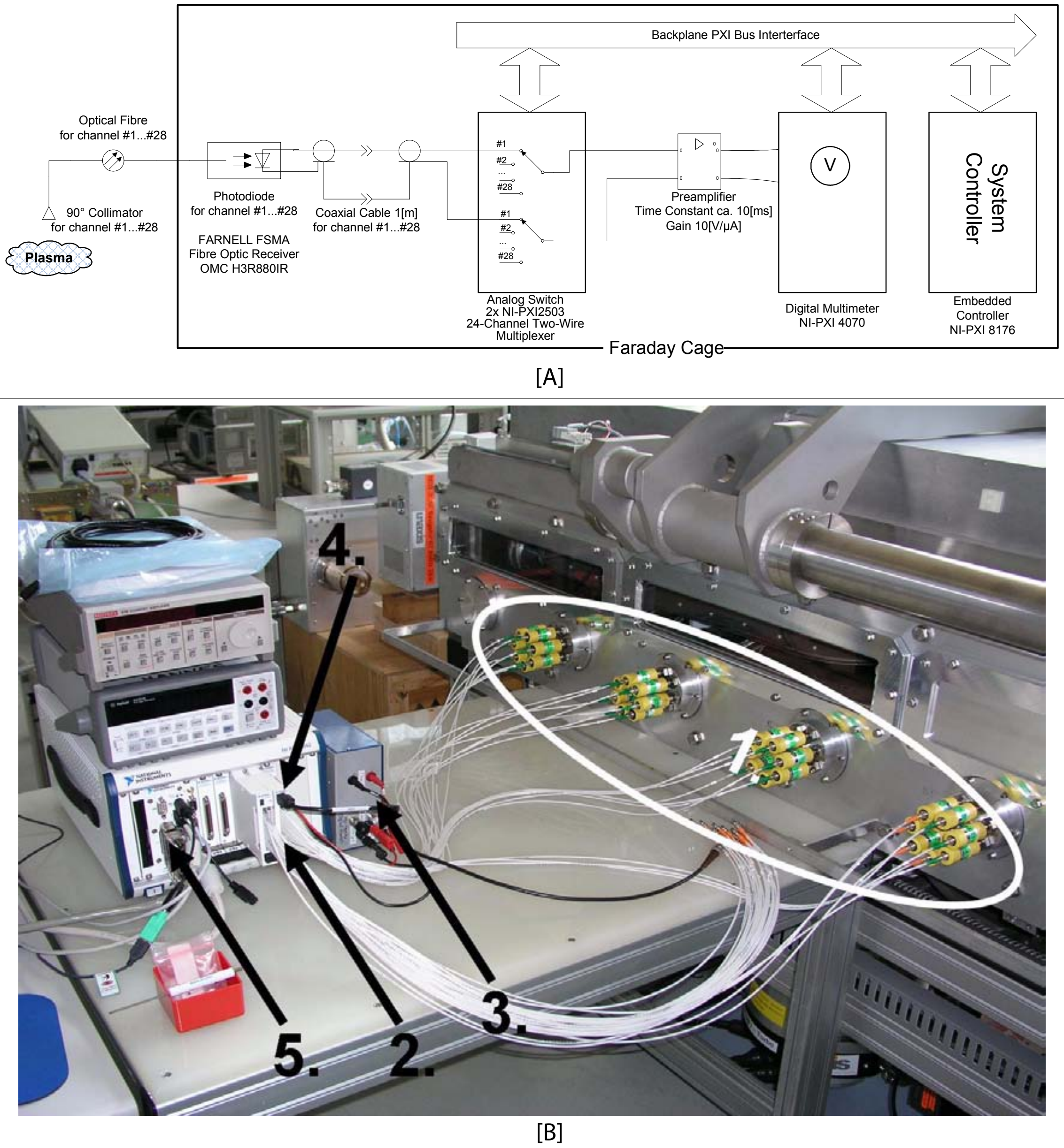

Fig. 4-12: Scheme of the optical plasma intensity measurement system [A] and snapshot of the DAQ system [B] outside the reactor without Faraday cage consisting of: (1) 28 Photodiodes attached to the fibre-optic vacuum feedthroughs, (2) PXI Multiplexer, (3) Preamplifier, (4) PXI DMM, (5) Embedded PXI controller.

A complete 28 channel (7 × 4 matrix) optical uniformity detection system (Fig. 4-12) was developed including the design of a special miniaturized, vacuum and process compatible 90° angle light collimator (4.4.2.2). This probe head is inserted into the rectangular electrode (cf. Fig. 4-4) as the front end of an array of multiplexed photodiodes. The captured light is inserted into an optical fibre which connects to the optical fibre vacuum feedthrough. At the back end for the intensity detection there is a series of photodiodes. Their photocurrent is routed by two analog switches (NI-PXI 2503) to a preamplifier (4.4.2.3), followed by a digital multimeter (DMM, NI-PXI 8176) whose datataking is synchronized with the analog switches. The whole DAQ system was enclosed in a Faraday cage (not shown Fig. 4-12) in order to avoid spurious pick-up from the RF sources and it was separated electrically with an isolation transformer to any avoid ground loops.

4.4.2.2 Right-Angle Collimator

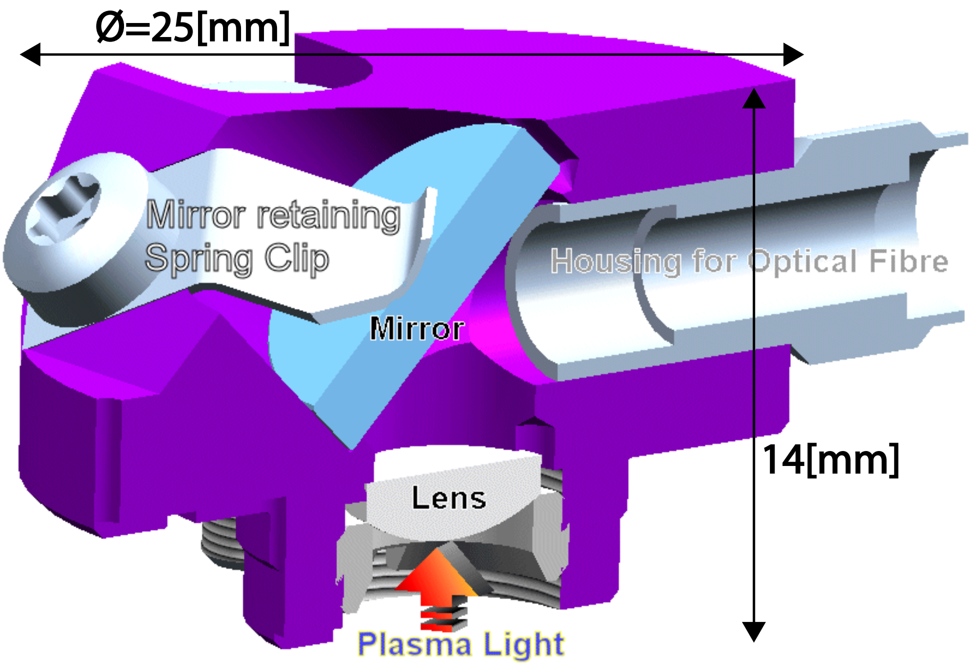

Fig. 4-13: Schematic drawing of the special miniaturized 90° angle light collimator for in situ plasma observation.The maximum height is 14[mm] and the housing has a maximum diameter of 25[mm].

For the KAI 1000 system, a special process-compatible optical collimator was developed as depicted in Fig. 4-13. Its housing is made of Al, lens and mirror material are sapphire (Al_2O_3), the reflecting layer on the mirror is vapour-deposited Al. The spring clip for the mirror is made of Nimonic 90 to maintain its spring force even at high deposition temperatures (ca. 300[°C]). In front of the lens, there is a sapphire protection window set in a PEEK ring (not shown). The housing of the optical fibre can be shifted forth and back in the direction of the fibre for optimum light insertion for a fibre with a given aperture.

4.4.2.3 Signal Conditioning

Fig. 4-14 shows the scheme for the two-stage preamplifier used to condition the analog photocurrent from each photodiode into a voltage, which can be measured by the digital multimeter (DMM) next in line. The first stage consists of a transimpedance converter of gain 1[V/µA] similar to the one in section 4.4.1.3. The second stage is an optional voltage amplifier of gain 10. The total gains used are either 1[V/µA] or 10[V/µA] depending on the luminosity detected by the photodiodes. The unit has a time constant of ca. 10[ms].

4.4.2.4 Data Acquisition (DAQ)

The DAQ system consists of a commercial PXI system from National Instruments except for the preamplifier 4.4.2.3. PXI is a modular system for measurement and control based on the standard PCI-architecture which provides an integrated trigger bus and a reference clock for accurate synchronization. PXI-system

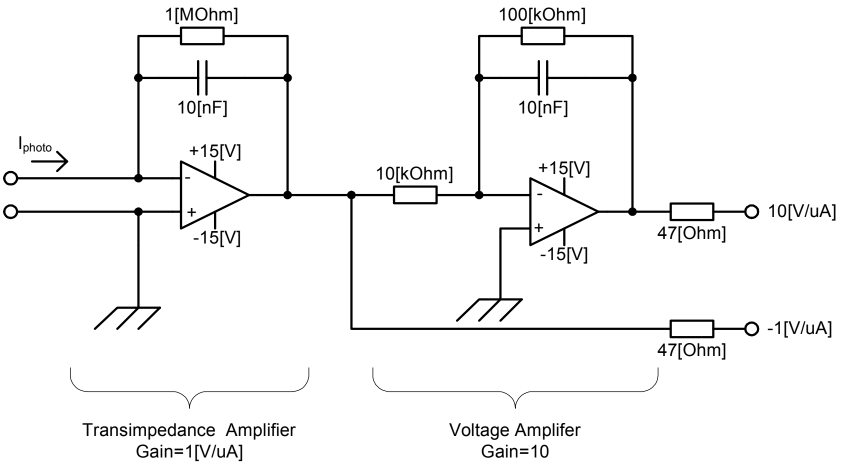

Fig. 4-14: Transimpedance amplifier inserted between analog switch and DMM (cf. Fig. 4-12)

DAQ work cycle

In our case the analog switches NI-PXI 2503 are configured to route the photocurrent output of each photodiode one by one to the preamplifier which converts it to a voltage and passes the analog signal to the input of the digital multimeter (DMM) NI-PXI 8176 (See Fig. 4-12-[A]). The switch module uses a built-in "scanner advance" trigger line as an event to indicate to the DMM that its relays have closed and settled. On completion of its measurement the DMM sends a "voltmeter complete" signal across the backplane trigger bus to the switch to make it advance in its scan list and connect the next path. The handshaking is continued until all channels are scanned and their values acquired. All the readings are transferred from the DMM to the system controller in one single block operation.[118] The acquisition of a whole dataset respecting settling times of the electromechanical relays, integration time of the preamplifier and measurement time of the DMM takes less then $10[\mathrm{s}]$.

4.4.2.5 Calibration

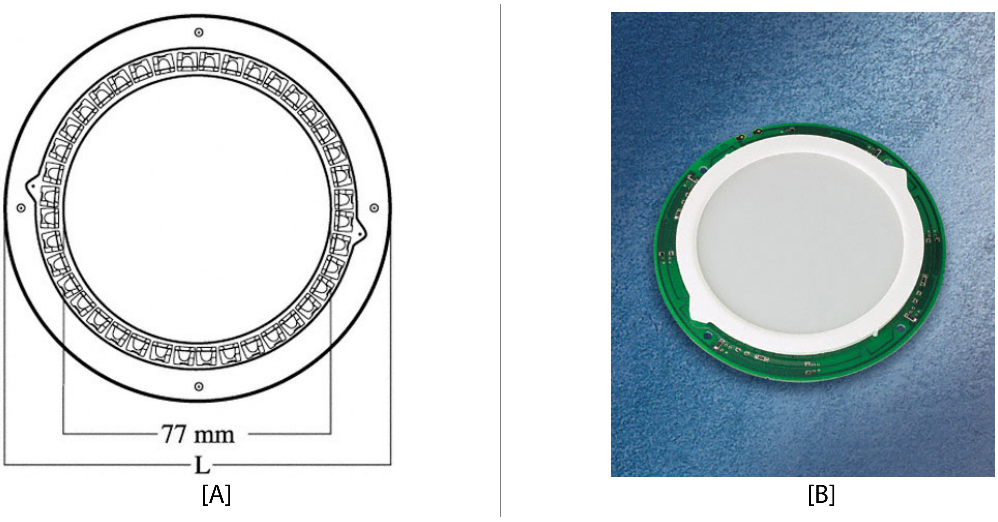

[A] [B]

Fig. 4-15: OSRAM MARKERLIGHT OS-ML03A-W1 used for calibration of the optical system (Drawings and Pictures OSRAM). [A] 40 LEDs arranged in a circle ensure high luminance. [B] Diffuser plate makes light more homogeneous.

Flat light source

For the in-situ calibration of the whole optical system, a flat homogeneously-illuminated surface is needed. To guarantee a constant brightness during a calibration scan, a semiconductor LED based light source was selected (OSRAM MARKERLIGHT OS-ML03A-W1). The model has 40 white LEDs arranged in a circle (Fig. 4-15-[A]). The light is homogenized by a diffuser plate (Fig. 4-15-[B]).

The light source was put in front of the optical collimator mounted in the reactor. During the calibration procedure, the light source is driven at constant voltage (@ 20[V]) and the DC current is monitored to assure constant light intensity. The result of the final calibration procedure is shown in Fig. 4-16. By careful selection of the optical components, flawless optical interconnects and a good shielding for the whole DAQ system, the maximum channel-to-channel difference in the measured voltage for constant light input does not exceed 30%, normalized with respect to channel 6, which has the maximum light throughput.

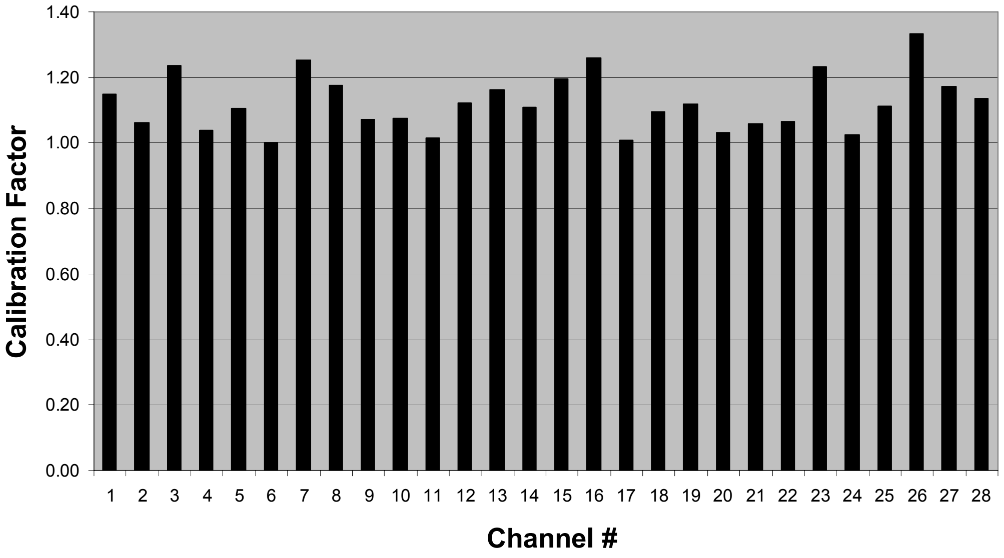

Fig. 4-16: Calibration factor for each channel

4.4.3 Correction Techniques for uniformity probes

Optical probes

All readings from the optical probes of both systems are submitted to a numerical correction to account for the dark currents and the different light throughputs of each channel. First, in absolute darkness, a reading for the background current (I_{dark}) is acquired for each channel. I_{dark} is always subtracted from any raw reading I_{raw}. The difference is then multiplied by the calibration factor CF for each channel. The product yields the unnormalized luminosity ($L_{unnormalized}$) for each channel in arbitrary units (Eq. 4-4).

$$L_{unnormalized} = (I_{raw} - I_{Background}) \cdot CF \tag{Eq. 4-4}$$

The whole set of corrected channels is then normalized to its maximum or minimum value.

Electrical probes

The current signals (I_{raw}) retrieved from the electrical probes via the circuit depicted in Fig. 4-11 are submitted to a numerical offset correction, but no individual gain correction is necessary. The offset (I_{offset}) is measured with the signal conditioning unit switched on and the plasma off.

$$I_{unnormalized} = I_{raw} - I_{Offset} \tag{Eq. 4-5}$$

Voltage readings do not need correction for an offset. The whole set of channels is then normalized to the maximum or minimum value for the respective measurement mode I_{sat}, I_{DC} or V_f.

4.5 RF Probes

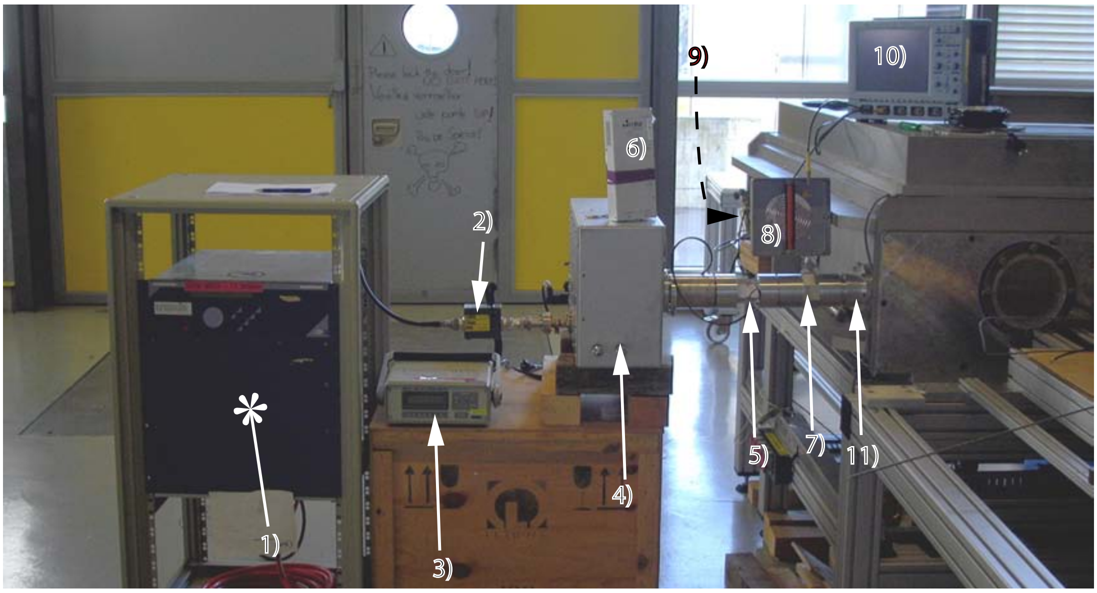

Fig. 4-17: Typical setup of the RF equipment during operation on the KAI 1000 plasma reactor: (1) RF Generator, (2) BIRD THRULINE® directional power sensor (different model depending on frequency and maximum power), (3) BIRD Model 4421 digital RF power meter, (4) Lumped matching network, (5) MKS-ENI VIP probe (cf. 4.5.1) with (6) its analysis board, (7) coaxial T-piece for (8) $U_{self\text{-}bias}$ plasma DC self-bias voltage filter (cf. 4.5.2), (9) capacitive electrode voltage probe (cf. 4.5.3.2) attached to electrode (not visible), (10) digital oscilloscope for synchronized measurement of (8) and (9), (11) RF vacuum feedthrough.

RF monitoring

RF probes were extensively used on both reactors to monitor the RF conditions and the electrical properties of the reactor during a plasma process and to assure stable discharge conditions during the datataking of non-uniformity measurements. It was observed that experimental shortcomings such as poor matching quality, non-sinusoidal RF voltage signals or other RF malfunctions can completely invalidate the measurements. In the same way, detrimental plasma instabilities and parasitic discharges can be detected before taking any non-uniformity measurements.

Setup

Fig. 4-17 shows the typical setup for the rectangular reactor KAI 1000. The setup for the cylindrical reactor differs only in the type of electrode voltage probe (9) (See 4.5.3). The directional power sensor (2) and its read-out unit (3) are mainly used to independently verify the forward and reflected power as indicated by the generator (1). The directional power sensor (2) is designed for a nominal impedance of $50[\Omega]$ with a VSWR range of 1.0 to 2.0. The voltage-current-phase probe ((5) and (6)) is a frequency-selective diagnostic and is used to check how much RF power is passing the matching network at a specific frequency. With the filter (8) it is possible to measure a DC component from the voltage signal on the transmission line. The probe head of (9) is in close proximity to the RF electrode and measures the peak-to-peak voltage and, depending on its design, also the DC signal on the electrode. It is the only RF probe within the vacuum chamber. In the following sections the voltage-current-phase probe (5) & (6), the DC voltage probe (8) and the electrode voltage probe (9) are described in more detail.

4.5.1 Voltage-Current-Phase Probe (VIP)

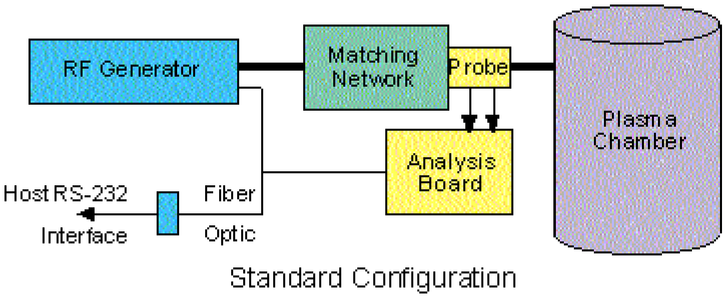

Fig. 4-18: Configuration of MKS-VIP Probe: The probe is inserted after the matching network. Its raw values are treated by the analysis board nearby which communicates digital data to a host, typically a standard PC.

Non-intrusive probe

The frequency scanning VIP from MKS-ENI is a non-intrusive RF impedance analyser tool designed to accurately measure basic parameters associated with RF power and to provide real-time analysis for process control, monitoring, frequency stability and optimization. The VIP can be inserted anywhere on a RF line.

Probe head and Analysis board

The VIP consists of two main assemblies (cf. Fig. 4-18): The analysis board assembly and the probe head assembly. The analysis board receives analog low-level RF signals from the VIP probe head and utilizes a digital signal processor (DSP) to provide three basic RF parameters (see below). Its DSP is linked to a local oscillator circuit. On request, the analysis board transmits the measured parameters by either fibre optic or serial protocol to a host PC. The probe head assembly is designed as coaxial line segment to be inserted into the RF line section with minimal insertion loss and to provide two voltage outputs:

1. Voltage representation of the time varying electric field present in the probe head assembly and
2. Voltage representation of the time varying magnetic field present in the probe head assembly.

Basic RF parameters

The primary function of the VIP probe is to accurately measure the three basic quantities of RMS voltage V_{RMS} (Eq. 4-6), RMS current I_{RMS} (Eq. 4-7) and the phase angle ϕ (Eq. 4-8) between the voltage and current wave of the load. The frequency range covered is 0.6 to $100[\mathrm{MHz}]$ and the measurement frequency is user selectable. The measurements are made within $50[\mathrm{ppm}]$ of the frequency at which it is programmed to operate. The secondary function of the VIP is to calculate other RF parameters as described below. An illustration of how the measured parameters are used to derive the delivered power is depicted in Fig. 4-19.

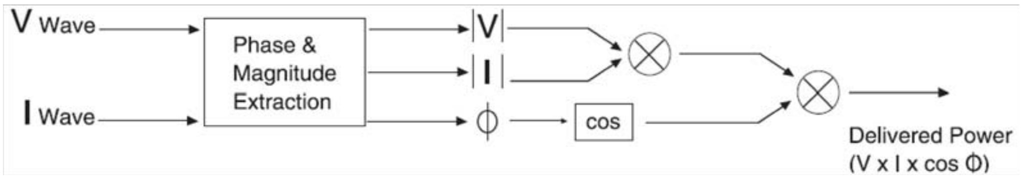

Fig. 4-19: Measurement of V_{RMS}, I_{RMS} and ϕ.

$$|V| = \sqrt{\langle V^2 \rangle} = V_{RMS} \tag{Eq. 4-6}$$

$$|I| = \sqrt{\langle I^2 \rangle} = I_{RMS} \tag{Eq. 4-7}$$

$$\phi = \angle(V) - \angle(I) \tag{Eq. 4-8}$$

Derived RF parameters

In addition, the VIP probe calculates and displays the derived RF parameters of the impedance Z (Eq. 4-9), the real R (Eq. 4-10) and imaginary part X (Eq. 4-11) of the load impedance, delivered power P_{real} (Eq. 4-12) and reactive power P_{VAR} (Eq. 4-13). Other quantities such as reflection coefficient Γ, forward P_f and reverse power P_r can be derived, if the probe is operated on a nominal $50[\Omega]$ line.

$$|Z| = |V|/|I| \tag{Eq. 4-9}$$

$$R = |Z| \cdot \cos(\phi) \tag{Eq. 4-10}$$

$$X = |Z| \cdot \sin(\phi) \tag{Eq. 4-11}$$

$$P_{real} = |V| \cdot |I| \cdot \cos(\phi) \tag{Eq. 4-12}$$

$$P_{VAR} = |V| \cdot |I| \cdot \sin(\phi) \tag{Eq. 4-13}$$

Power loss in matching unit

The main advantage of the VIP is that it can be used to estimate the RF power after the matchbox and, in conjunction with the BIRD power meter before the matching unit, it allows to assess what fraction of power is lost in the matching unit.

Note: The reader is reminded that all the quantities delivered by the VIP probe, and in particular the impedance Z (Eq. 4-9), reflect the values of the load at the insertion point of the probe. This load is subject to the transmission line characteristics, reactor capacitance and the impedance of any ignited plasma. Without a proper transformation of the measured values it is not possible to make detailed statements on the electrical properties of the plasma itself. However general assessments of the process stability and the upper limit for the dissipated power can be made.

4.5.2 DC Voltage Probe

This is a passive probe used to measure the DC component in the voltage signal on the transmission line which is due to the plasma DC self bias of the glow discharge in the reactor. As the DC signal is location independent, there is no need for it to be placed inside the vacuum chamber. It can be conveniently inserted outside the vacuum chamber after any DC blocking capacitor, typically between the matching network and the vacuum feedthrough. By a coaxial T the voltage on the internal conductor is guided to a box (item (8) in Fig. 4-17) containing the low pass filter as sketched in Fig. 4-20. The coaxial T piece is constructed in such a way that the characteristic impedance of the short transmission line between matchbox and vacuum feedthrough is preserved and partial reflections at the mechanical connectors are minimized.

Single-pole low-pass filter

The filter is a single-pole filter and consists of a massive coil designed for high currents in series with a high-value capacitor. The inductance has a double layer of windings (ca. $10[\mathrm{turns/cm}]$) on a epoxy core, $15[\mathrm{cm}]$ long and $2[\mathrm{cm}]$ diameter. The coil is air cooled from two sides by fans shielded with a fine-meshed wire netting.

For the DC component U_{DC} of the input voltage $U_{in} = U_{RF} + U_{DC}$ the output value is given by

$$U_{out}(U_{DC}) = \left[\frac{Z_{C,DC}}{R_{L,DC} + Z_{C,DC}}\right] \cdot U_{DC} \approx U_{DC} \tag{Eq. 4-14}$$

which is the DC component itself for negligible resistance of the coil. However the output voltage for the high frequency RF component U_{RF} of the voltage is blocked by the coil's inductance and the output voltage is given by

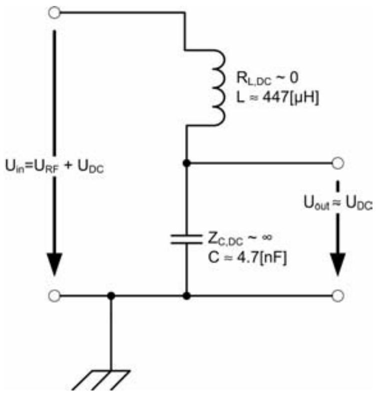

Fig. 4-20: Circuit scheme of DC voltage probe.

$$U_{out}(U_{RF}) = \left[\frac{1/j\omega C}{1/j\omega C + j\omega L}\right] \cdot U_{RF} = \left[\frac{1}{1-\omega^2 LC}\right] \cdot U_{RF} \approx 0 \qquad \text{(Eq. 4-15)}$$

which is practically zero provided $\omega^2 LC$ takes a very high value. The $3[\mathrm{dB}]$ attenuation frequency is

$$f_{-3\mathrm{dB}} = \frac{1}{2\pi} \cdot \sqrt{1+\sqrt{2}} \cdot \frac{1}{\sqrt{L \cdot C}} = 171[\mathrm{kHz}] \qquad \text{(Eq. 4-16)}$$

far below the lowest RF excitation frequencies as shown in Fig. 4-21. The attenuation of the high-frequency component for all the RF frequencies used is marked in the same figure.

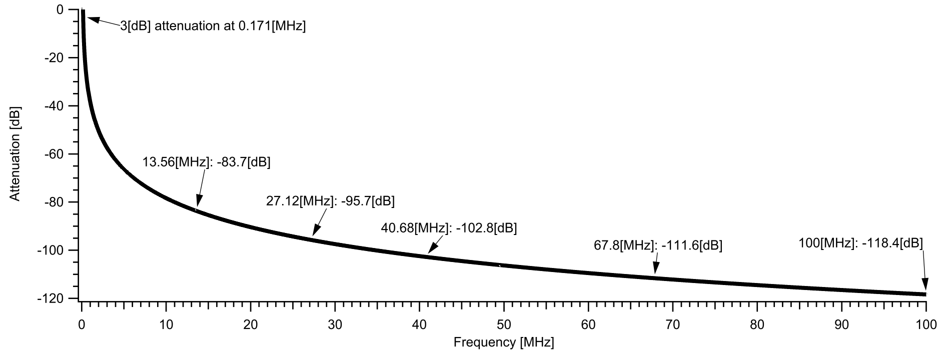

Fig. 4-21: Attenuation curve of the single-pole filter shown in Fig. 4-20.

4.5.3 Electrode Voltage Probe (EVP)

The voltage on the electrode of a CCP plasma consists of a oscillating, time varying component V_{pp} (peak-to-peak voltage) at the excitation frequency and a DC component V_{DC} due to the asymmetric surface ratio of the electrodes. Commercial, wide-band passive voltage probes are not suited to the plasma environment with vacuum and eventually reactive gases and high temperatures. Therefore, for measuring the voltage on the electrode, a special active electrode voltage probe (EVP) was developed. Two versions were used, one which directly contacts the RF electrode was installed on the cylindrical reactor (Fig. 4-22-[A]), another one which is capacitively coupled to the RF electrode was mounted on the rectangular reactor (Fig. 4-22-[B]).

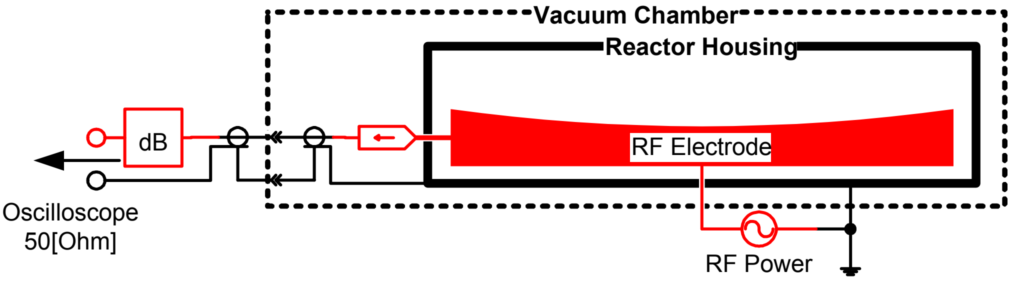

[A] Direct-contact voltage probe in cylindrical reactor

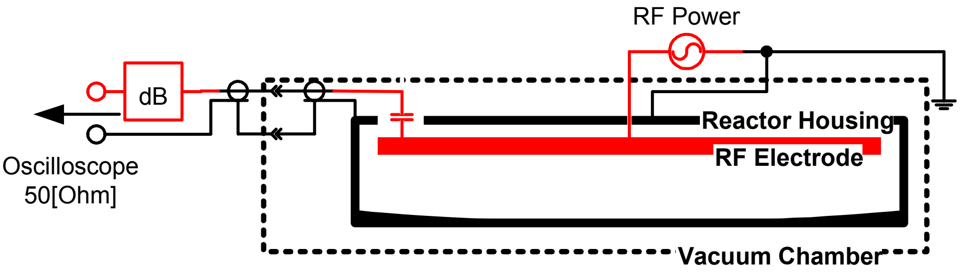

[B] Capacitive voltage probe in rectangular reactor

Fig. 4-22: Working principle of the two versions of voltage probes: [A] EVP whose probe head is directly contacting the electrode and [B] which is capacitively coupled to the top of the RF electrode. “dB” is the active buffer and attenuator

4.5.3.1 Direct Contact EVP

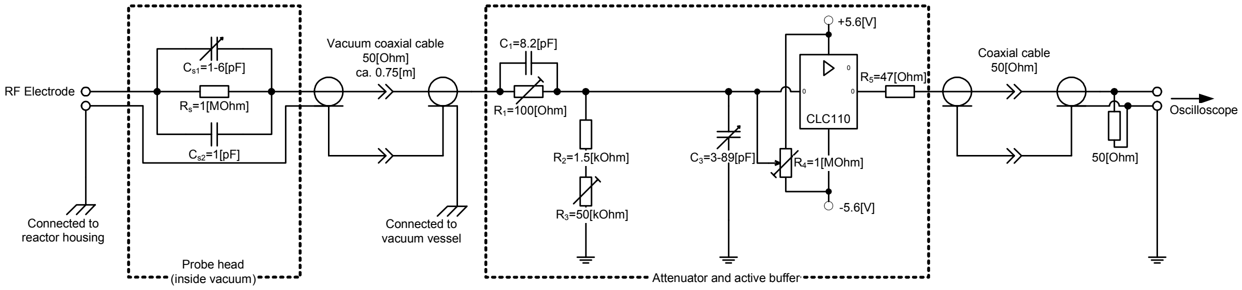

Fig. 4-23: Circuit of the active EVP with direct contact to the electrode. Attenuation factor: $1/100$. Bandwidth: $\mathrm{DC} - 150[\mathrm{MHz}]$. The end of the $50[\Omega]$ coaxial cable must be terminated with $50[\Omega]$. Component labelling is consistent with respect to Fig. 4-24.

The direct contact EVP is a slight modification of the version already used by SANSONNENS[15]. Fig. 4-23 depicts its circuit. It is a high impedance probe with a voltage divider ($1/100$). The probe head is vacuum sealed and connected to the lateral side of the RF electrode as indicated in Fig. 4-22-[A]. Its chassis is linked to the reactor housing. A vacuum compatible coaxial cable links it via a vacuum passage to the actual probe circuit outside the vacuum chamber. The components $R_1 - R_3$ and C_1, C_3 are chosen so as to achieve the voltage division of roughly $1/100$ from DC to $150[\mathrm{MHz}]$. The signal is fed into an operational amplifier used as a voltage follower. R_4 serves to correct the offset of the operational amplifier. Its output is connected to a floating oscilloscope via a $50[\Omega]$ coaxial cable terminated by $50[\Omega]$.

4.5.3.2 Capacitive EVP

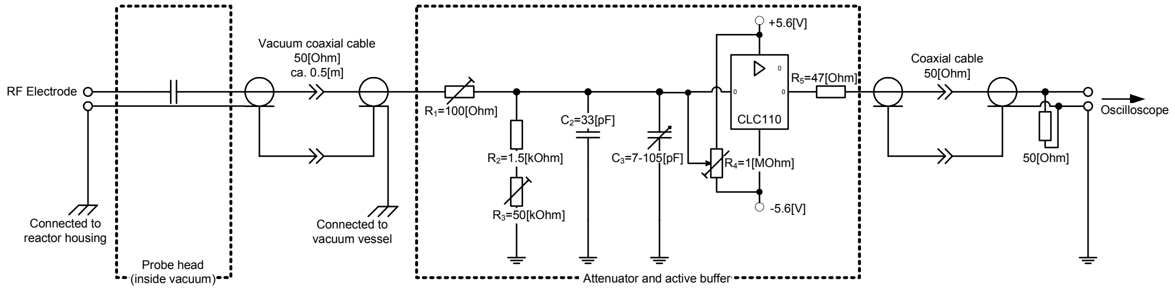

Fig. 4-24: Circuit of the active EVP with capacitive contact to the electrode. Attenuation factor: $1/250$. Bandwidth: $25[\mathrm{kHz}] - 100[\mathrm{MHz}]$. The end of the $50[\Omega]$ coaxial cable must be terminated with $50[\Omega]$. Component labelling is consistent with respect to Fig. 4-23.

The electronics in the probe head of Fig. 4-23 are not very plasma resistant and it is difficult to make it fail-safe for a harsh reactive plasma environment. Therefore for the industrial rectangular reactor a capacitive design was chosen which is easier to implement in existing production lines. Fig. 4-24 shows the associated circuit diagram. As sketched in Fig. 4-22-[B], it is connected to the upper side of the suspended RF electrode. The probe head's circuit was essentially reduced to two large metallic surfaces facing each other. The circuit of the attenuator and the active buffer are the same apart from the numerical values of some components.

By virtue of its capacitive connection, the DC signal information on the electrode is lost and the probe can measure only the peak-to-peak voltage. As the DC signal is location independent, we can measure it anywhere on the transmission line, e.g. outside the reactor by the diagnostic described in 4.5.2.

Chapter 5: RF at VHF - Impedance Analysis and Matching

5.1 Introduction

Multi-frequency operation

The KAI 1000 system was initially designed for operation at $13.56[\mathrm{MHz}]$. At $13.56[\mathrm{MHz}]$ (HF band) the total electrical path length (RF input to plasma gap) is only a fraction of the vacuum wavelength λ, but at the highest RF excitation frequency used to ignite plasma at $100[\mathrm{MHz}]$ (VHF band), the wavelength is already less than the total electrical path length (ca. 1.5 - 2 times). For multi-frequency operation over nearly an order of magnitude requires a thorough analysis and understanding of the system's impedance properties at each frequency. In addition, the modelling at HF can be done straightforwardly by a relatively simple lumped circuit whilst for VHF a distributed transmission line model approach is more appropriate.

Motivation for this chapter

To excite the plasma, the RF power is transferred after the matching network along a transmission line, which consists of a coaxial vacuum feedthrough, a long stripline and the reactor itself before the energy is coupled into the glow discharge. In fact the whole system, consisting of the matching unit, transmission line, and plasma, can be fairly described by the equivalent circuit shown in Fig. 5-1.

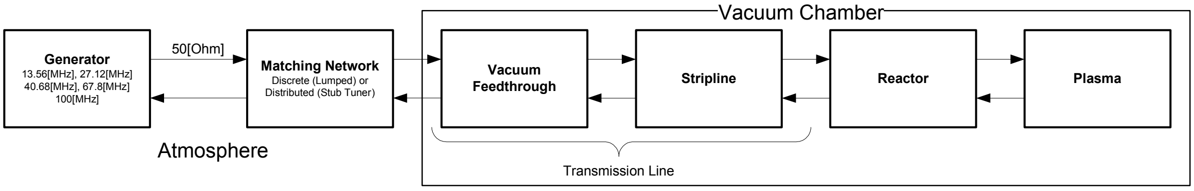

Fig. 5-1: Simplified RF equivalent circuit for a large-area reactor supplied by a long transmission line. Modified after[61].

The requirements for the transmission line are stability, reproducibility, high efficiency (power limitation of RF generators), no overheating and inhibition of parasitic plasma. The efficiency of the transmission line depends on the mechanical design and the presence of a plasma, which changes the terminating impedance. The vacuum feedthrough has a coaxial architecture. The stripline is a relatively long flat, shielded construction which has a ribbon centre conductor that is enclosed by two outer ground conductors with a uniform dielectric material filling the space between the two. Both reactors have their RF connection points in the centre of the electrodes, therefore the length of the stripline is at least half the diameter or width of the reactor. The length of the stripline is not negligible compared to the RF wavelength and thus it should be regarded as a transmission line. It can possess resonances as the equivalent circuit will show. When operated at high RF powers, heating of the stripline caused by ohmic heating of the conductors and due to imperfect dielectric ("loss tangent") occurs commonly. Moreover this JOULE heating under vacuum cannot be easily reduced by cooling. Melt-down of the stripline has been observed in a commercial system. As the RF frequency increases ohmic losses increase due to the reduction of the skin depth in the metallic strips or plates.

Frequency bands and Z-matching

Since commercial RF power generators are usually designed to operate with a $50[\Omega]$ output impedance, an impedance matching unit has to be inserted between the generator and load to allow maximum power transfer. As we are working in different frequency bands, different impedance matching techniques are commonly applied depending on the frequency. The selection of the type of matching network needs to consider e.g. its simplicity, bandwidth, feasibility of manufacturing and ease of tunability. These experiments work in two RF subregions:

- High Frequency (HF): The frequency ranges from 3 - $30[\mathrm{MHz}]$ and the wavelength from 10 - $100[\mathrm{m}]$. Typical excitation frequencies used are the standard frequency 13.56 and its 2nd harmonic $27.12[\mathrm{MHz}]$. Matching techniques are exclusively discrete networks of lumped elements (cf. 5.4.1).
- Very High Frequency (VHF): The frequency ranges from 30 - $300[\mathrm{MHz}]$ and the wavelength from 1 - $10[\mathrm{m}]$. The typical excitation frequencies are the harmonics of the standard frequency 40.68, 67.8, 81.36 and $100[\mathrm{MHz}]$. Up to ca. $80[\mathrm{MHz}]$, the same matching techniques as for the HF region can be used. Starting with the FM broadcast region 90 - $110[\mathrm{MHz}]$ and using high power ($\geq 500[\mathrm{W}]$), the component size or circuit size becomes comparable with the wavelength, which suggests the use of distributed techniques (cf. 5.4.2). Also stray impedance is problematic at VHF, i.e. capacitors behave as inductances.

Distributed matching at VHF

Impedance matching at VHF (at ca. $100[\mathrm{MHz}]$) with nominal RF powers of several $100[\mathrm{W}]$ became only feasible with the installation of a *stub tuner*. Reasons for its construction were inadequate matching capabilities of existing lumped matching networks and persistent, recurring instabilities of the RF generator. A stub tuner is a distributed matching network and transforms the load to a characteristic input impedance (typically $50[\Omega]$) by virtue of several parallel, short-circuited transmission lines of variable length ("shunt stubs").

View of the RF engineer

This thesis is essentially motivated by the effect of a standing wave at VHF in a large area plasma reactor ("VHF" and "large" mean that $L/\lambda \geq 1/10$, where L = lateral dimension and λ = vacuum wavelength). But RF power has to be coupled in for generating and sustaining a plasma; and from the point of view of impedance matching it is important to see that the travelling wave encounters the end of an open transmission line in the reactor cavity which under discharge conditions becomes a variable, distributed, highly reactive and weakly dissipative medium. Through this medium, the travelling waves set up a standing wave.

The series inductance per square and associated parasitic resistance of the transmission line and of the reactor, as well as their respective capacitance to ground, scale directly with the reactor dimensions, whereas the plasma resistance decreases as the inverse power of the electrode area. This means that the problem of RF power matching and losses becomes more and more challenging as the reactor dimension increases, since the parallel capacitance to ground tend to draw a large RF current ($\sim 100[\mathrm{A}]$ for a $1[\mathrm{m}^2]$ reactor).[61]

Most of the impedance measurements on the cylindrical reactor used for modelling were carried out before any plasma experiments. Hence constructional measures to curb parasitic plasma discharges are primarily not considered in the components' analysis. In addition the reactor gap throughout the impedance analysis is $80[\mathrm{mm}]$. The rectangular reactor shows similar impedance characteristics and is not shown in detail.

5.2 Transmission Line

5.2.1 Standing Wave

Sinusoidal wave on transmission line

If a sinusoidal voltage is supplied to a transmission line, it can be represented in *phasor* notation as a wave travelling in the positive x-direction $V_+(x)$ and in the negative x-direction $V_-(x)$

$$V_+(x) = \boldsymbol{V}_+ \cdot e^{-j\beta x} \qquad V_-(x) = \boldsymbol{V}_- \cdot e^{+j\beta x} \tag{Eq. 5-1}$$

where $\boldsymbol{V}_+ = |V_+|e^{j\omega t}$ and $\boldsymbol{V}_- = |V_-|e^{j\theta_p}e^{j\omega t}$. $\boldsymbol{V}_-$ contains the phase angle between the reflected and incident wave at $x = 0$. The quantity β is called the *phase constant* of the line and is defined as $\beta = \omega\sqrt{L \cdot C}$, where L and C are the inductance and capacitance per unit length. For the current it follows with the characteristic impedance $Z_0 = \sqrt{L/C}$ of the line analogously:

$$I_+(x) = \frac{\boldsymbol{V}_+}{Z_0} \cdot e^{-j\beta x} \qquad I_-(x) = \frac{\boldsymbol{V}_-}{Z_0} \cdot e^{+j\beta x} \tag{Eq. 5-2}$$

TL theory[1] tells us that for the total voltage on the line, the two travelling waves add according to Eq. 5-3

$$V(x) = V_+(x) + V_-(x) \tag{Eq. 5-3}$$

however the total current is the difference of both waves:

$$I(x) = I_+(x) - I_-(x) \tag{Eq. 5-4}$$

Open transmission line

If we have a forward travelling voltage wave on a transmission line, which is either open, closed or purely reactive terminated, then all the wave's energy is reflected at the end. For the moment we will only consider the open transmission line. The open circuit imposes the boundary condition that, at $x = 0$ (See Fig. 5-2), the current must be always zero,

$$I(0) = I_+(0) - I(0) = 0 \Rightarrow \boldsymbol{V}_+ = \boldsymbol{V}_- \tag{Eq. 5-5}$$

i.e. the phasors $\boldsymbol{V}_+$ and $\boldsymbol{V}_-$ are equal and there is no phase angle $\theta_p = 0$ between them. Substituted in equations Eq. 5-3 and Eq. 5-4 it follows immediately for the total voltage and current on the line[2]:

$$\begin{aligned} V(x) &= \boldsymbol{V}_+ \cdot \left[e^{-j\beta x} + e^{+j\beta x}\right] = \boldsymbol{V}_+ \cdot 2\cos(\beta x) \\ I(x) &= \frac{\boldsymbol{V}_+}{Z_0} \cdot \left[e^{-j\beta x} - e^{+j\beta x}\right] = \frac{\boldsymbol{V}_+}{Z_0} \cdot (-2j)\sin(\beta x) \end{aligned} \tag{Eq. 5-6}$$

As already shown above by Eq. 3-3, Eq. 5-6 creates a stationary pattern of voltage and/or current nodes and antinodes on the line. As the current is always zero at $x = 0$, the voltage has its maximum at the end of the transmission line. This stationary voltage pattern on the line is called the *standing wave effect* (SWE). Fig. 5-2 illustrates the values of $V(x)$ and $I(x)$ along the line for different temporal values of $\omega \cdot t$. As we have a voltage antinode at the end, moving backwards on the TL makes the voltage decrease as we approach the first voltage node, i.e. a voltage minimum. Then the voltage rises again and we reach the next crest. Adjacent nodes and antinodes are always λ/4 apart, where λ is the wavelength of the travelling wave.

---

[1] *[106]*, p. 216f

[2] *[106]*, p. 254f

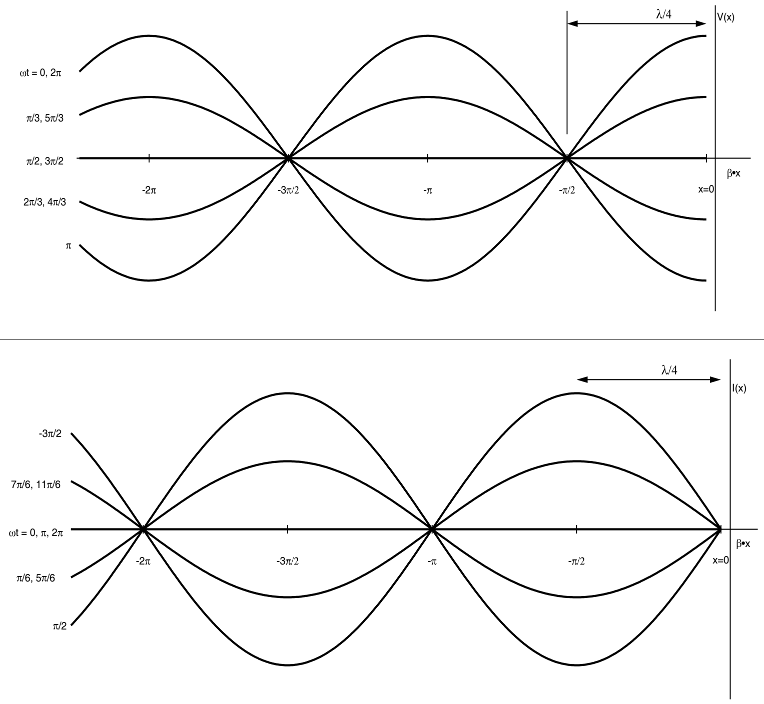

Fig. 5-2: Time evolution of voltage and current on an open transmission line. The nodes (“zeros”) and antinodes (“crests”) remain at the same locations.

Capacitively coupled

Capacitively coupled systems are from the electrical point of view nothing other than open transmission lines. This is to say we have always a voltage maximum at the end, which decreases when moving away from the “geometrical” centre of the end of transmission line. However as shown in 3.2.1 and 3.2.2 the shape of the voltage distribution is not necessarily $\cos(\cdot)$ like as we change to 2D geometries.

Closed transmission line

If the transmission line is closed at its end, then the boundary conditions are reversed and the closed circuit imposes that, at $x = 0$ the voltage must be always zero, Eq. 5-5 becomes now Eq. 5-7

$$V(0) = V_+(0) + V_-(0) = 0 \Rightarrow \boldsymbol{V}_+ = -\boldsymbol{V}_- \qquad \text{(Eq. 5-7)}$$

and Eq. 5-6 becomes now Eq. 5-8 where $\cos(\cdot)$ and $\sin(\cdot)$ change their roles:

$$\begin{aligned} V(x) &= \boldsymbol{V}_+ \cdot \left[e^{-j\beta x} - e^{+j\beta x}\right] = \boldsymbol{V}_+ \cdot (-2j)\sin(\beta x) \\ I(x) &= \frac{\boldsymbol{V}_+}{Z_0} \cdot \left[e^{-j\beta x} + e^{+j\beta x}\right] = \frac{\boldsymbol{V}_+}{Z_0} \cdot 2\cos(\beta x) \end{aligned} \qquad \text{(Eq. 5-8)}$$

This has important mechanical implications for the construction of the shunted short stub in section 5.4.2.4, as we see that at the moving end of a closed transmission line there is always at maximum current. Moving contacts under a maximum current load are difficult to realize.

5.2.2 Impedance Transformation

Impedance Transformation by Transmission Line

A wave travelling on a transmission line with characteristic impedance Z_0 (or characteristic admittance Y_0) produces a well known input impedance as a function of the load impedance Z_{load}, distance from the load l and wave number $\beta = 2\pi\nu/c$, where ν is the frequency of the RF source in [Hz]:

$$Z_{in}(l) = Z_0 \cdot \frac{Z_{load} + j \cdot Z_0 \tan(\beta \cdot l)}{Z_0 + j \cdot Z_{load} \tan(\beta \cdot l)} \qquad \text{(Eq. 5-9)}$$

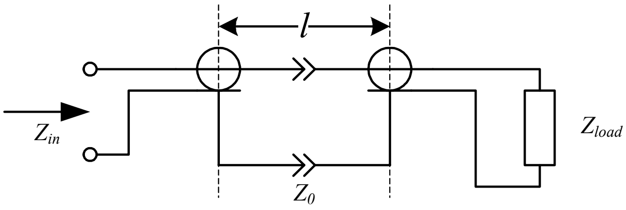

Fig. 5-3: Impedance mapping of a load Z_{load} by a transmission line of length l and characteristic impedance Z_0.

Standing Wave

If the transmission line is terminated with $Z_{load} = Z_0$, we have a pure travelling wave vanishing in the load. In all other cases partial or full reflections occur at the impedance discontinuity at the end. Forward and reflected travelling waves superpose and create a *standing wave* as already shown above (cf. Fig. 5-2). For the two extreme cases where the transmission line is either open-circuited ($Z_{load} = \infty$) or short-circuited ($Z_{load} = 0$), the impedance at distance l from the end (Z_{OC} for the open transmission line and Z_{SC} for the short-circuited variant) is purely reactive:

$$\begin{aligned} Z_{OC} &= -j \cdot Z_0 \cdot \cot(\beta \cdot l) \\ Z_{SC} &= j \cdot Z_0 \cdot \tan(\beta \cdot l) \end{aligned} \qquad \text{(Eq. 5-10)}$$

5.3 Impedance Measurements and Modelling

5.3.1 Impedance Meter and Probe Self-Impedance

Frequency Sweeps

Impedance measurements were acquired with a HP4193 VECTOR IMPEDANCE METER, doing full-range frequency sweeps from $0.4[\mathrm{MHz}]$ to $110.0[\mathrm{MHz}]$ at a step width of $0.01[\mathrm{MHz}]$.

Probe inductance L_{Probe} and contact resistance $R_{contact}$

The contribution of the active probe head of the utilized *HP4193 Vector Impedance Meter* was estimated using a copper plate in short-circuit mode. Depending on the frequency, its parasitic self-impedance L_{Probe} varied between $8[\mathrm{nH}]$ at low and $10[\mathrm{nH}]$ at very high frequency. To facilitate the fitting procedure, the value was arbitrarily set to $9[\mathrm{nH}]$ throughout the whole analysis, where the exact value could not be established by the nature of the fitting procedure. A value for the contact resistance was only derived when the equivalent circuit scheme required the insertion of a additional resistor at the input of the circuit diagram in order to satisfy the fitting constraints otherwise it was set to the total resistance needed for fitting the measurement.

Corrected measurements

In generally and for completeness, measurements are always shown including the effect of the serial probe impedance. On the other hand, some data analysis (e.g. calculation of characteristic impedances of transmission lines) is useful only if the dataset was corrected by the effect of the measurement probe.

Skin effect

Modelling was always done with frequency independent loss resistances. A more accurate modelling would include an inverse square root frequency effect dependence due to the skin effect, since the RF current is restricted to a smaller cross sectional area beneath the surface as the frequency is increased. The skin effect effectively increases the resistance.

In the following, measurements and equivalent circuits (Fig. 5-4 trough Fig. 5-12) are shown for the cylindrical reactor: The impedance of the reactor is treated first, then the RF feedings systems and the whole system as seen by matching network at the vacuum feedthrough. The impedance for the rectangular setup is similar.

5.3.2 Parallel Plate Reactor

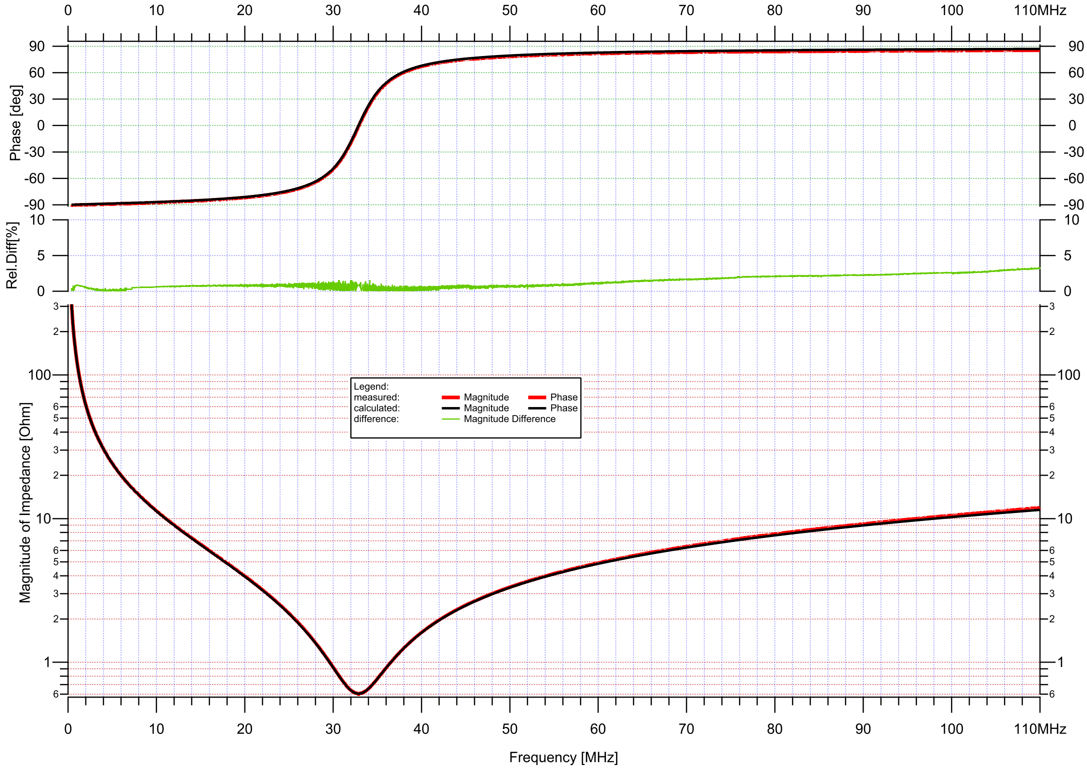

Fig. 5-4: Impedance measurement and modelling of the cylindrical reactor. The top graph depicts the phase of the impedance and the bottom graph its magnitude for the measurement (red line) and the modelling (black line). The green line in the middle represents the difference of the measured and modelled magnitude in %. The measurement shows a series resonance at about 33[MHz].

The impedance of the reactor was measured as is shown in Fig. 5-5 without stripline and any PTFE fillings.

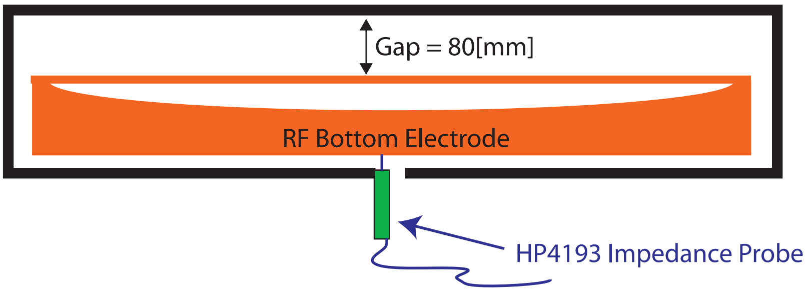

Fig. 5-5: Setup for the impedance measurement of the cylindrical reactor. Probe of HP4193 is making a direct contact to the RF bottom electrode through the RF feeding opening. The holder of the probe is in good contact with reactor housing. The gap between the electrode and the top plate was 80[mm].

The reactor is highly capacitive in the HF-RF region, but tends to become inductive in the VHF-RF region due to its size compared to $\lambda/4$ or due to capacitive impedance diminishing ($\propto 1/\omega C$) and the inductance increasing ($\propto \omega L$). The measurement in Fig. 5-4 shows a series resonance at about 33[MHz]. The reactor was modelled with a simple equivalent circuit (Fig. 5-6) consisting of a series resistance $R_{s,R}$, a series inductance $L_{s,R}$ and a series capacitance $C_{s,R}$ as shown in Fig. 5-6 and given in Eq. 5-11:

$$Z_R(\omega) = j\omega L_{Probe} + R_{contact} + R_{s,R} + j\omega L_{s,R} + \frac{1}{j\omega C_{s,R}} \qquad \text{(Eq. 5-11)}$$

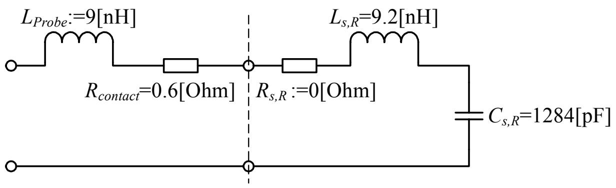

Fig. 5-6: Equivalent circuit for reactor modelling. L_{Probe} denotes the parasitic inductance of the measurement probe and $R_{contact}$ its contact resistance.

The series resistance $R_{s,R}$ was arbitrarily set to $0[\Omega]$ as its true value could not be distinguished from the contact resistance by the simple fitting procedure. Modelling and experimental data show a fairly good agreement. The difference in the impedance magnitude across the whole frequency sweep is less than 5%. If the impedance Z is corrected by the presumed effect of the probe, i.e. by dropping the term containing L_{Probe} and by considering its uncertainty, then the series resonance frequency is moves up to the frequency interval 44 - $50[\mathrm{MHz}]$.

5.3.3 Ancillary System Components

5.3.3.1 Stripline

Stripline Geometry

Fig. 5-7-[A] shows the construction of the stripline sandwich structure. It consists of two outer grounded conductors which enclose the RF ribbon. Distance holders made of ceramic are used keep a constant gap of $3[\mathrm{mm}]$. Later these ceramic parts were replaced by large flat teflon (PTFE) sheets as shown in Fig. 5-7-[B] in order to prevent parasitic discharges. Measurements and modelling below apply to the original configuration Fig. 5-7-[A] only.

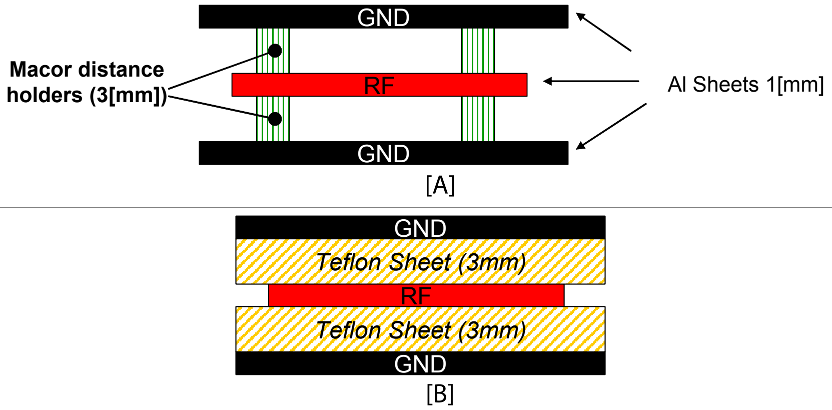

Fig. 5-7: Construction of the stripline in its original state [A] and after the teflon modification [B].

Modelling

The stripline was measured and modelled for an open and closed configuration. Two approaches exist to model it: It can be modelled with a discrete (lumped) model using one or several T-Sections (depending on the length of the stripline and the maximum frequency) or it can be modelled as a transmission line with a characteristic impedance Z_0 (Eq. 5-9 and Eq. 5-10). The imperfections[74] of the measurements require that the open measurement is modelled with a terminating stray capacitance[126] $C_{stray,OC}$ and analogously the closed measurement with a stray inductance $L_{stray,SC}$ as shown in Fig. 5-8:

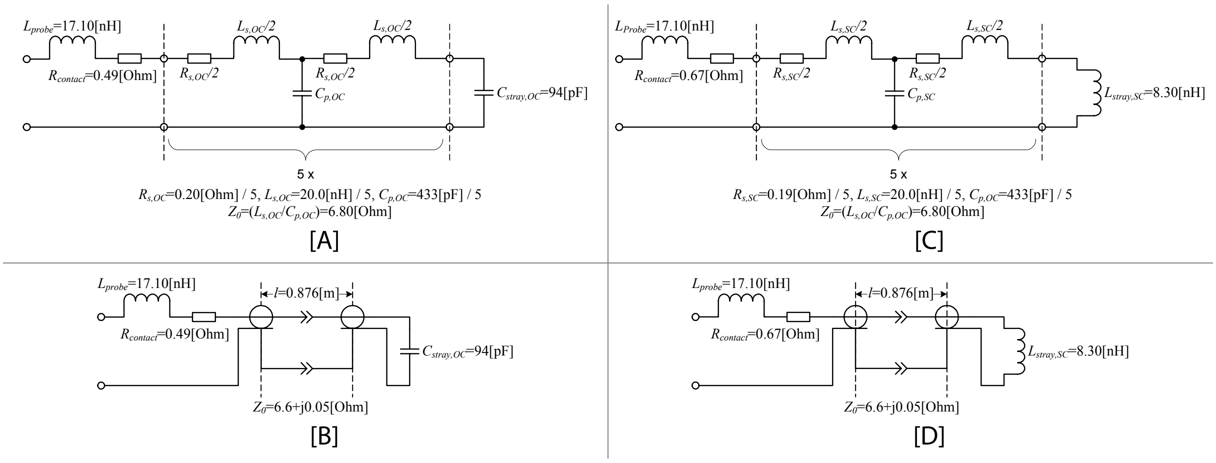

Fig. 5-8: Equivalent circuit for stripline modelling: [A] and [B] show the open, [C] and [D] the closed configuration with their respective stray components $C_{stray,OC}$ and $L_{stray,SC}$. L_{Probe} denotes the parasitic inductance of the measurement probe and $R_{contact}$ its contact resistance.

When using an equivalent circuit consisting purely of lumped components (Fig. 5-8-[A] and [C]), it was necessary to use at least 5 repetitive T-sections to obtain a sufficiently good modelling. For the transmission line modelling as shown in Fig. 5-8-[B] and [D]) the used formulae are:

$$\begin{aligned} Z_{SL,\,OC} &= j\omega L_{probe} + R_{contact} + Z_{in}(l,\, Z_0,\, 1/j\omega C_{stray,\,OC}) \\ Z_{SL,\,SC} &= j\omega L_{probe} + R_{contact} + Z_{in}(l,\, Z_0, j\omega L_{stray,\,SC}) \end{aligned} \qquad \text{(Eq. 5-12)}$$

Both models yield a fairly good fit, the deviation is generally less than $\leq 5\%$. The transmission line approach also delivers the theoretical length, which is about $0.876[\mathrm{m}]$ and is close to the measured length of $0.9[\mathrm{m}]$.

Characteristic Impedance Z_0

The characteristic impedance for the stripline can be obtained by several ways. It can be extracted from the T-section analysis assuming that L and C values are per unit length. Then by applying Eq. 5-13 we get a characteristic impedance of about $6.80[\Omega]$.

$$Z_0 = \sqrt{L/C} \qquad \text{(Eq. 5-13)}$$

Fitting with the transmission line model, Eq. 5-12 give a characteristic impedance of about $6.60[\Omega]$. Theoretically the combination of the open and closed measurement according to Eq. 5-14 should yield the constant, characteristic impedance of the stripline, using

$$Z_0 = \sqrt{Z_{OC} \times Z_{SC}} \qquad \text{(Eq. 5-14)}$$

The phases should cancel and the magnitude should be constant. The measurements have to be corrected by the effect of the probe and the parasitic stray elements before the formula can be applied. This approach yields a value close to the methods above, as shown in Fig. 5-9, between 6 and $7[\Omega]$.

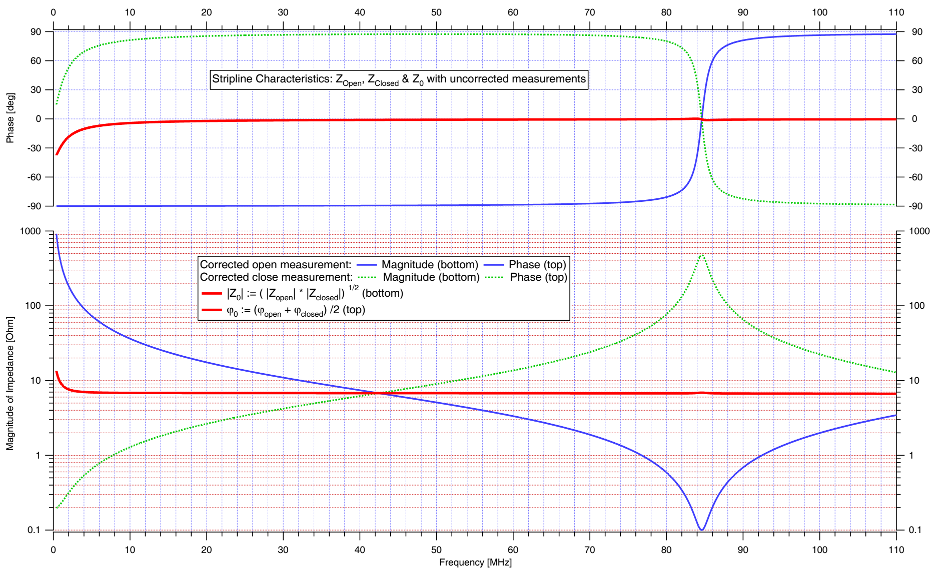

Fig. 5-9: Corrected open and close measurements and the characteristic impedance.

Calculated Z_0

The characteristic impedance for a ribbon geometry as depicted Fig. 5-7 with two outer grounded strip conductors enclosing an inner equidistant RF conductor can be estimated[1] by starting from Eq. 5-13

$$Z_0 = \sqrt{\frac{L}{C}} = \frac{\sqrt{L \cdot C}}{C} = \frac{1}{v_p \cdot C} \qquad \text{(Eq. 5-15)}$$

The capacitance per unit length of a stripline is approximately

$$C \approx 4 \cdot \varepsilon_0 \cdot \varepsilon_r \cdot \frac{w}{b-t} \qquad \text{(Eq. 5-16)}$$

where w denotes the width of the inner conductor, t is the thickness of the RF ribbon and b the distance to the two outer ground conductors. This formula disregards fringe effects and other contributions.[63] With the phase velocity

$$v_p = \sqrt{L \cdot C} = c / \sqrt{\varepsilon_r} \qquad \text{(Eq. 5-17)}$$

we obtain an estimation for Z_0:

$$Z_0 \approx \frac{1}{4 \cdot c \cdot \varepsilon_0 \cdot \sqrt{\varepsilon_r}} \times \frac{b-t}{w} = \frac{\mu_0 \cdot c}{4} \times \frac{1}{\sqrt{\varepsilon_r}} \times \frac{b-t}{w} = 94.2[\Omega] \times \frac{1}{\sqrt{\varepsilon_r}} \times \frac{b-t}{w} \qquad \text{(Eq. 5-18)}$$

In our case, we obtain for $w = 78[\mathrm{mm}]$, $t = 1[\mathrm{mm}]$ and $b = 7[\mathrm{mm}]$ and characteristic impedance of $7.2[\Omega]$, which is close to the empirical values.

5.3.3.2 Feedthrough

Impedance characterization of the feedthrough was done with the stripline disconnected and in open mode. The phase of the measurement across the whole frequency range is nearly always -90[°], i.e. the circuit is highly capacitive and modelling can be done with a simple series model consisting of a resistive, inductive and capacitive element as shown in Fig. 5-10 and Eq. 5-19. The initial guess for $C_{p,F}$ is extracted from the impedance at the lowest measurable frequency at $0.4[\mathrm{MHz}]$ and yields $34.2[\mathrm{pF}]$. The lumped circuit model conforms well to the measurement data with less than $\leq 2\%$ deviation.

---

[1] [43], p.153ff

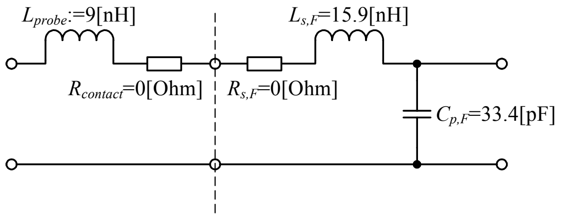

Fig. 5-10: Equivalent circuit for feedthrough modelling. L_{Probe} denotes the parasitic inductance of the measurement probe.

$$Z_F(\omega) = j\omega L_{Probe} + R_{contact} + R_{s,F} + j\omega L_{s,F} + \frac{1}{j\omega C_{p,F}} \qquad \text{(Eq. 5-19)}$$

5.3.4 Complete System

Modelling

Fig. 5-11 shows the detailed impedance characteristic for the full cylindrical system and its corresponding equivalent circuit fitting parameters. The complete system was modelled by adding consecutively all RF components (reactor, stripline, feedthrough). The final equivalent circuit used to model the entire system is depicted in Fig. 5-12.

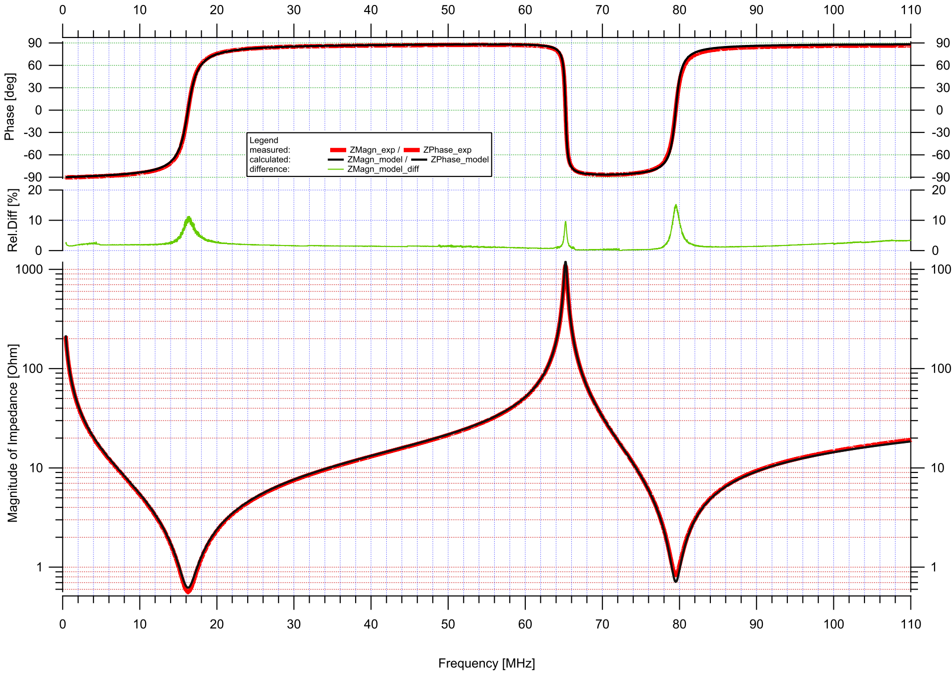

Fig. 5-11: The final Z characteristic of the complete cylindrical system (reactor with an inter-electrode gap of $80[\text{mm}]$, stripline and vacuum feedthrough) shows 3 resonances: 2 serial, 1 parallel. The 1st at about $16[\text{MHz}]$ is mainly caused by the dominant capacitance of the reactor in conjunction with the inductance of the stripline. The higher resonances are transformation effects of the stripline.

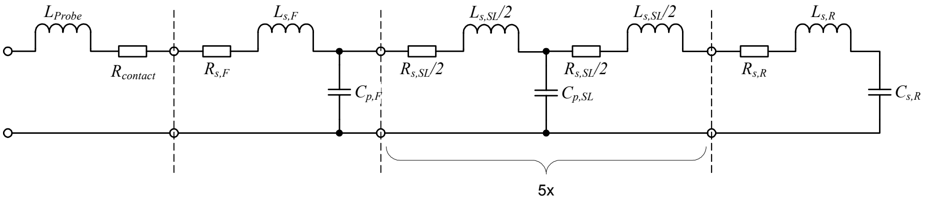

Fig. 5-12: Equivalent modelling for the entire system.

5.4 Matching Networks

Significance of matching

As already mentioned in Chapter 2, matching networks are needed for optimum power transfer from the RF source to the plasma load. The impedance seen by the generator determines its ability to inject power depending on its load tolerance.[87][88][57] Changes in the external power circuit may influence strongly and unexpectedly the discharge.[29]

5.4.1 Discrete Matching Networks

For impedance matching at HF and low VHF frequencies it is customary to use lumped matching networks built from discrete elements like coils and vacuum capacitors. Compared to the wavelength, their geometric dimensions are negligible and can thus be modelled as a lumped network. The classical networks are the T, Π, L and the N-type architecture.[56][86] They have been exhaustively considered in the literature and their properties analysed in terms of RF plasma application. [31][57][30]

For this work commercial impedance matching systems were available. At $13.56[\mathrm{MHz}]$ an Aurion PRODIK-T 160 system with autotuning controller and $10[\mathrm{kW}]$ maximum RF input power was used. For the frequencies 27.12, 40.68 and $67.8[\mathrm{MHz}]$, different Advanced Energy Navigator networks were installed with a maximum RF input power of $2[\mathrm{kW}]$. These system were also capable of automatching. As this is standard industry equipment, no further details are given.

5.4.2 Distributed Matching Networks

The available discrete matching units failed to work at $100[\mathrm{MHz}]$ under all process conditions. To provide a versatile impedance matching at the highest frequency, the construction of a so called stub tuner was carried out. A stub tuner adjusts impedances by inserting, along a backbone transmission line, shunted “sub” transmission lines without a load and which are either short or open-circuited (cf. Fig. 5-13). An adjustable stub-line tuner is able to match highly reactive parts of the load impedance to a generator under all process conditions ensuring optimum power transfer.

5.4.2.1 Triple Stub Tuner

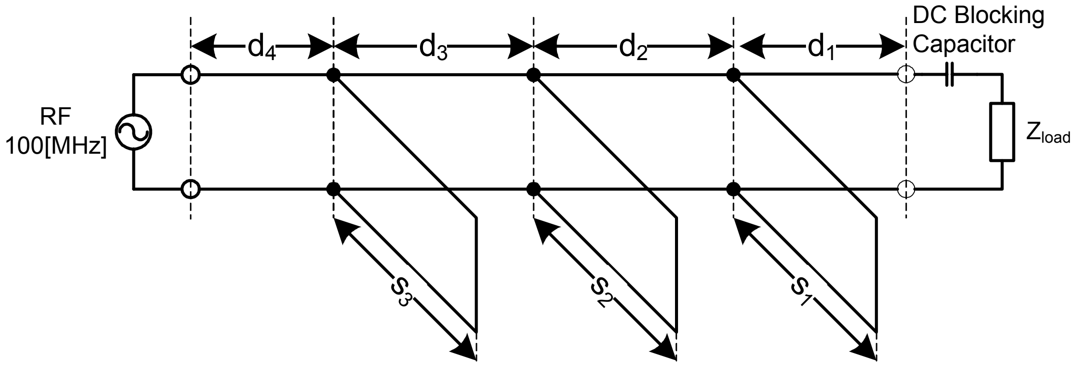

Fig. 5-13: Scheme of a triple stub tuner: d_i denotes the fixed length of the intermediate transmission lines. s_i is the variable length of the respective shorted shunt stub. d_1 through d_4 form the backbone of the stub tuner. A DC blocking capacitor is inserted before the first intermediate transmission line in order to preserve the plasma DC self bias and prevent circulating DC current in the RF systems.

A stub tuner can be implemented with one or several shunted stubs. The most important difference is that single and double-stub tuners do not permit to map all possible loads to the nominal input impedance, i.e. they are able to cover only partially the area of the SMITH chart. However with a triple stub tuner it is possible to reach any point on the SMITH chart without having to adjust the intermediate transmission lines d_1, d_2, d_3 or d_4 (cf. Fig. 5-13), i.e. a triple stub tuner covers fully the SMITH chart.[79] d_i is an arbitrarily fixed length except for $\lambda/2$ and it multiples. The practical significance is that a triple stub as shown in Fig. 5-14 allows to map any Z_{load} to the nominal $50[\Omega]$ of the RF power source, irrespective of whether the load is highly reactive and shows minute resistivity. The impedance at the load side and the generator's view of the transformed load can be calculated according to KIRCHOFF's law using admittances, which is explained in the next section.

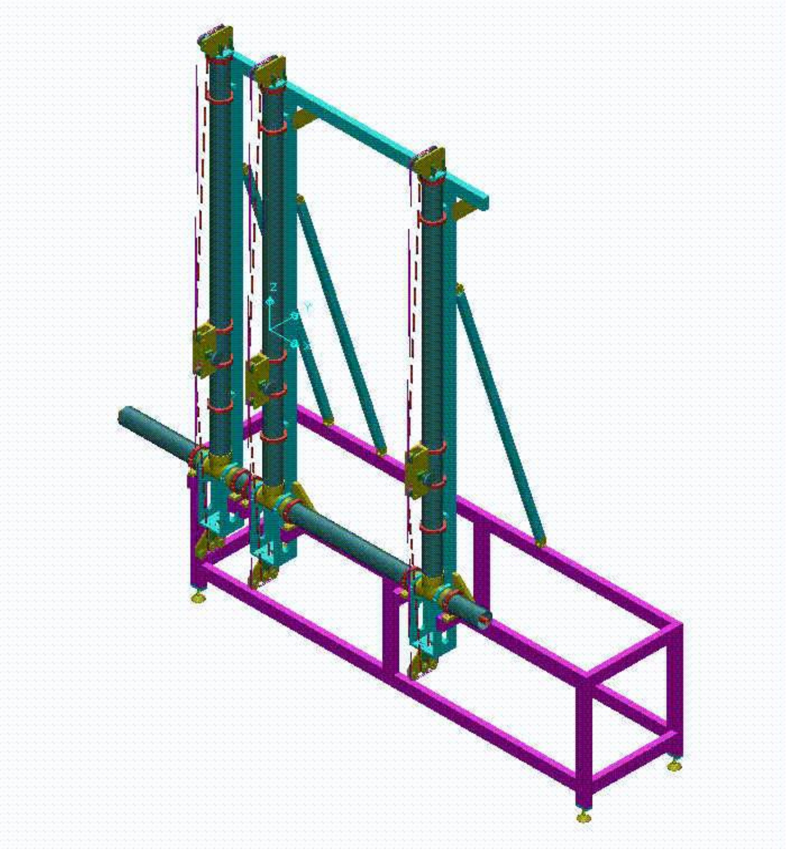

Fig. 5-14: Schematic design of the constructed triple stub tuner. Dimensions ca. $3[\mathrm{m}] \times 3[\mathrm{m}]$.

5.4.2.2 Calculation of Stub Positions

A small LABVIEW™ program was used to simulate single, double and triple stub tuner based on lossless transmission lines (Fig. 5-15). The calculations explained hereafter refer to this software.

The cutoff frequency for a hollow waveguide of diameter $\varnothing = 100[\mathrm{mm}]$ is about $1.5[\mathrm{GHz}]$[1], therefore it is impossible to transmit $100[\mathrm{MHz}]$ in such a hollow conducting tube and we must have a coaxial waveguide. The large diameter copper tubes ($\varnothing = 105[\mathrm{mm}]$) were chosen for the ground shielding and $\varnothing = 35[\mathrm{mm}]$ for the RF conductor. A coaxial line with inner diameter a and outer diameter b and a dielectric ε_r between has a characteristic impedance of:

$$Z_0(a, b) = \sqrt{\frac{\mu_0 \cdot \mu_r}{\varepsilon_0 \cdot \varepsilon_r}} \cdot \ln\left(\frac{b}{a}\right) \qquad \text{(Eq. 5-20)}$$

Z_0 amounts to $66[\Omega]$ for the copper tube used, which is near the nominal $50[\Omega]$ of the RF source. The impedance seen at the RF input is then calculated consecutive-

---

[1] [14], p. K21

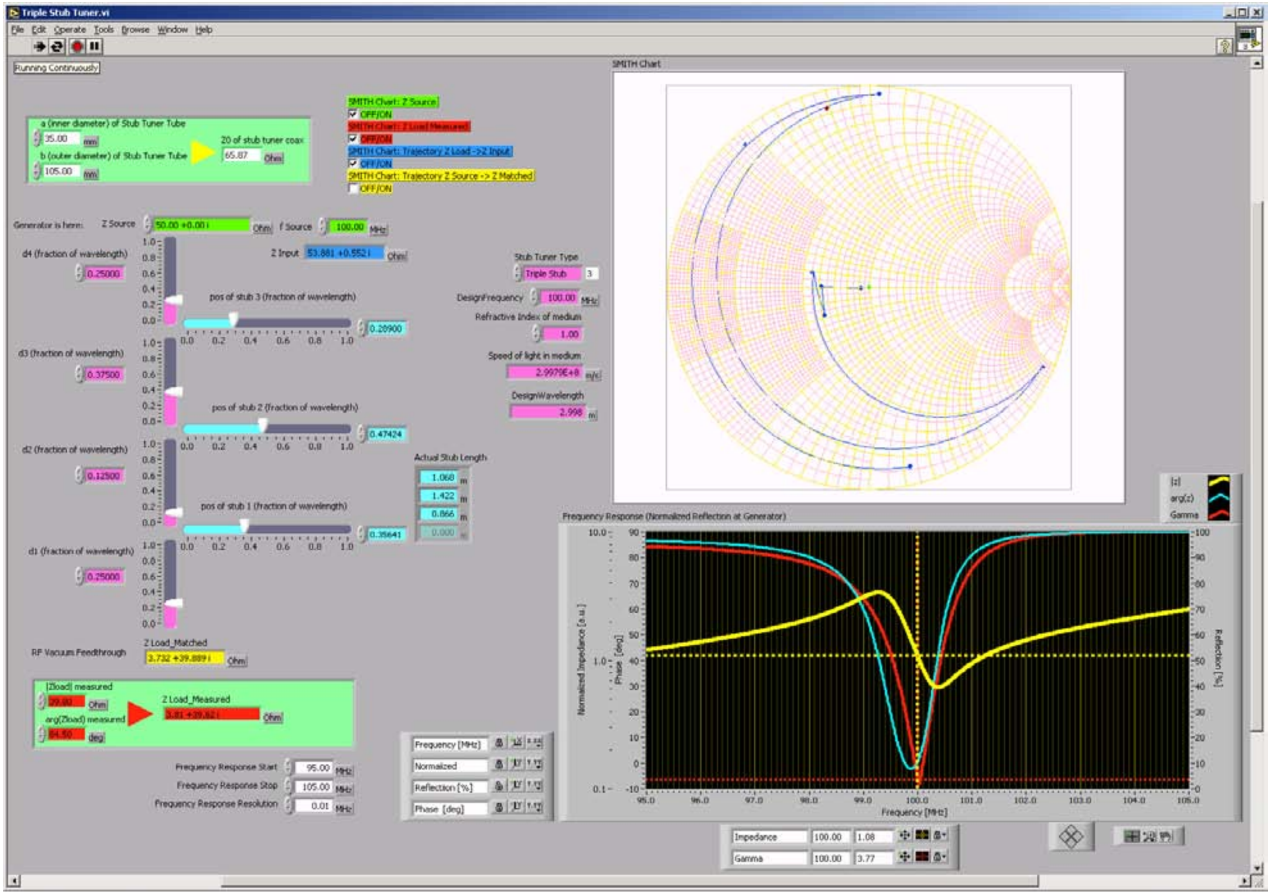
Triple Stub Tuner.vi

Running Continuously

a (inner diameter) of Stub Tuner Tube: 35.00 mm
b (outer diameter) of Stub Tuner Tube: 105.00 mm
Z0 of stub tuner coax: 65.87 Ohm

SMITH Chart: Z Source ☑ OFF/ON
SMITH Chart: Z Load Measured ☑ OFF/ON
SMITH Chart: Trajectory Z Load ->Z Input ☑ OFF/ON
SMITH Chart: Trajectory Z Source -> Z Matched ☐ OFF/ON

Generator is here: Z Source 50.00 +0.00 i Ohm
f Source 100.00 MHz
Z Input 53.881 +0.552 i Ohm

d4 (fraction of wavelength) 0.25000
pos of stub 3 (fraction of wavelength) 0.20900
d3 (fraction of wavelength) 0.37500
pos of stub 2 (fraction of wavelength) 0.47424
d2 (fraction of wavelength) 0.12500
pos of stub 1 (fraction of wavelength) 0.35641
d1 (fraction of wavelength) 0.25000

Stub Tuner Type: Triple Stub 3
DesignFrequency 100.00 MHz
Refractive Index of medium 1.00
Speed of light in medium 2.9979E+8 m/s
DesignWavelength 2.998 m

Actual Stub Length: 1.068 m, 1.422 m, 0.866 m, 0.000

RF Vacuum Feedthrough
Z Load_Matched 3.732 +39.889 i Ohm

|Zload| measured 39.80 Ohm
arg(Zload) measured 84.50 deg
Z Load_Measured 3.81 +39.62 i Ohm

Frequency Response Start 95.00 MHz
Frequency Response Stop 105.00 MHz
Frequency Response Resolution 0.01 MHz

Impedance 100.00 1.08
Gamma 100.00 3.77

Fig. 5-15: Snapshot of the LABVIEW™ programme used to simulate single, double and triple stub tuners and their ability to match the measured load without plasma of the KAI 1000 reactor at $100[\mathrm{MHz}]$.
On the left side are the input controls for the length of the intermediate pieces and the stub positions (labels are consistent with Fig. 5-13). Two calculation modes are possible: Calculate the matched load starting from the RF source or vice versa use the measured load impedance and calculate the view of the generator.
On the right hand is a SMITH chart depicting here the admittance trajectory of the intermediate steps multiplied with the characteristic impedance. The graph below shows the frequency response of the impedance and the normalized reflection $|\Gamma|(f_{RF})$ viewed from the RF generator.

ly from the load towards the RF generator by applying KIRCHHOFF's law. First the load impedance is converted to a normalized load admittance value y_{load}. Then the first part of the intermediate transmission line d_1 is added according to Eq. 5-9, it transfers the y_{load} by an angle $2\beta d_1$ on a constant $|\Gamma|$ circle counter clockwise in the admittance chart, where β is the wavenumber. The stub line s_1 adds a susceptance according to Eq. 5-10 and moves the locus in the SMITH chart clockwise on a constant susceptance circle. We continue with the second transition piece d_2 and the corresponding stub s_2 etc. until we reach d_4. Then final admittance value is converted to an impedance value. This is the impedance value z_{input} seen by the generator.

The frequency response is obtained by calculating the z_{input} similarly for some interpolation frequencies in the vicinity of the design frequency. The magnitude of the reflection coefficient is $|\Gamma|$ is calculated from the complex value Γ computed for each frequency point:

$$\Gamma = \frac{z_{input} - 1}{z_{input} + 1} \le 1 \qquad \text{(Eq. 5-21)}$$

A rough matching point is found by adjusting manually the length of the stub positions. In the following, construction issues for a stub tuner are addressed.

5.4.2.3 Movable Contact

Short or open stub

For the shunted stubs we need a transmission line of variable length. For a coaxial line or a waveguide as a transmission line media, use of shorted stubs is preferred because the open stubs may radiate, causing power losses and thus making the stub no longer a purely reactive element.[1] A shorted stub translates technically into a movable contact, customarily called a piston. This piston has to move inside a coaxial line and make a good galvanic contact between the inner RF conductor and the outside grounded shielding. For construction, two issues have to be addressed, the type of movable contact and how to reciprocate the piston inside the coaxial line. Both are examined below.

Movable contacts

For a good RF contact, we need a material of high surface conductivity. Unfortunately the best materials like silver and copper are very soft and likely to show abrasion when constantly moved under mechanical pressure. Different techniques were examined like BAL SEAL™ coil springs made from copper and aluminium or carbon brushes. The final laboratory prototype uses flexible multicontact shielding gaskets made of copper. It was observed that such contacts can be susceptible to verdigris.

Reciprocation of the piston

The second most important constructional issue is the displacement of the piston. It is necessary that the technique first and foremost complies with RF shielding requirements and that the piston can accurately be positioned. In order to achieve a good matching along a stub of about $2.5[\mathrm{m}]$ a position accuracy in the range of $\pm\, 0.5[\mathrm{mm}]$ is necessary. The required positioning precision depends on the mismatched power output capability of the RF generator too. Then there is still the question of available footprint in the laboratory.

The simplest method is to use a long hollow handle as illustrated in Fig. 5-16-[A] to reciprocate the piston. Its main drawback is that when the piston is at is maximum outermost position, i.e. the handle is completely pulled out, we need the double length of the shunt to operate. If the piston is moved horizontally, a very large clearance is necessary, which can reach in total easily 4 - $5[\mathrm{m}]$, a footprint not always available in a laboratory. An alternative shown in Fig. 5-16-[B] is to use cord traction with a cable winch. This technique was put into practice for the second prototype shown in Fig. 5-14. In this version the piston reciprocates vertically and much less clearance is need. However orifices have to be made in the ground shielding for the cord to pass, which are not good for electromagnetic interference (EMI) compliance. Fig. 5-16-[C] proposes a hydraulically actuated piston which would permit a better EMI compliance, offered a length reduction and arc protection at high powers if an appropriate hydraulic oil is used (e.g. transformer oil has a dielectric constant of $\varepsilon_r = 2.2$. and thus a wavelength reduction of $n = \sqrt{\varepsilon_r} \approx 1.5$). But such a solution would entail a much more complicated engineering.

5.4.2.4 Lambda/4 Piston

λ/4 piston

We have seen in section 5.2, that the end of a closed transmission line always exhibits a current maximum. High currents can be very harmful to delicate moving contacts which form the end of the transmission line. In order to avoid this handicap, a so-called λ/4 piston can be used. As shown in Fig. 5-17, this particular design has exactly the length of λ/4 of the RF excitation frequency at $100[\mathrm{MHz}]$. The effective end of the transmission line coincides with the end of the piston, which is simply a massive piece of metal. There we now have the current maximum and

---

[1] [13], p. 404

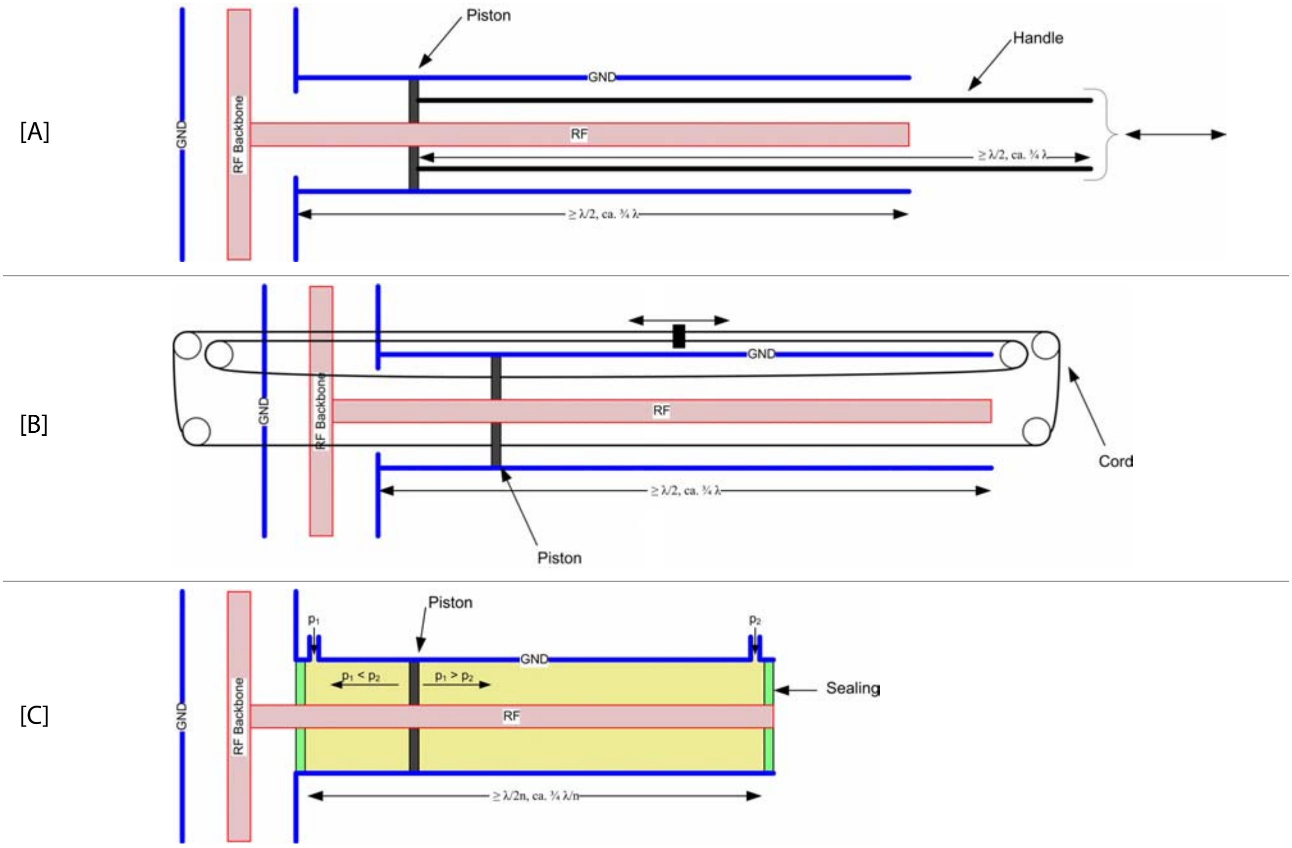

Fig. 5-16: Techniques to reciprocate a contact piston for a short shunt stub mechanically connected to the RF backbone of the stub tuner: [A] by a long hollow handle, [B] by cable traction and [C] hydraulically.

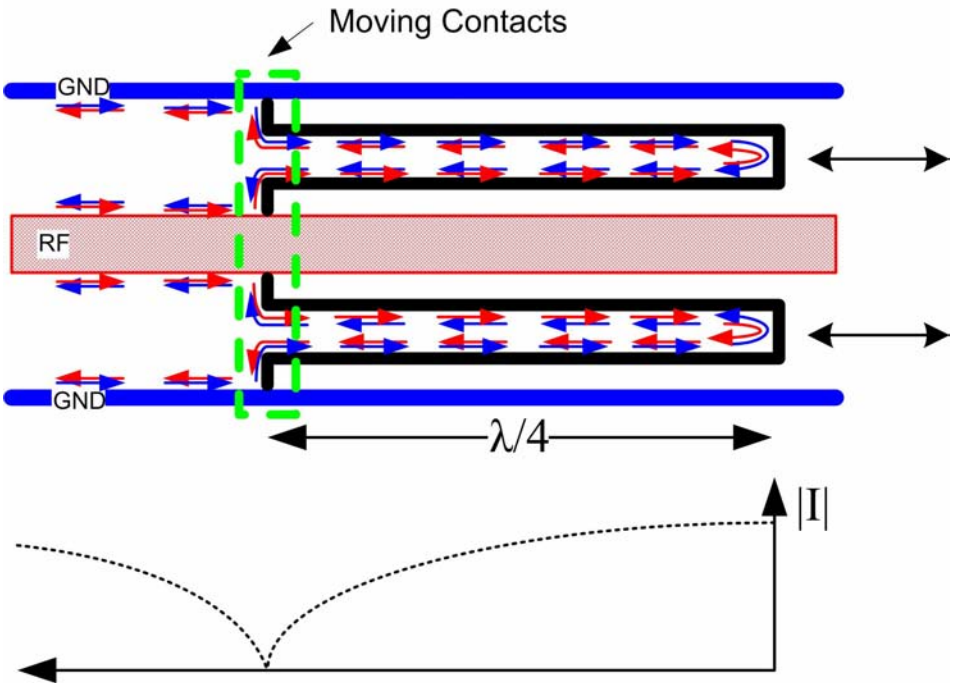

Fig. 5-17: Lambda / 4 piston, after [14], p. L56.

probably most of the JOULE heating. At the contacts (a distance of λ/4 to the left in Fig. 5-17) we now have a current minimum and voltage maximum. The moving contacts are thus protected from high currents. The main shortcoming of the λ/4 piston stems from the fact that its special design works best at the design frequency (or its odd harmonics), otherwise we forfeit its advantage.

5.4.2.5 Stub Tuner Summary

Advantages

The stub tuner makes impedance adjustment at VHF more predictable and calculable than with lumped matching networks which become dominated by parasitic stray impedance elements at about $80[\mathrm{MHz}]$. By a triple stub construction and by adding an extra length to the shunted stubs to facilitate matching (accounting for losses and mechanical imperfections), a full coverage of the SMITH Chart is guaranteed, i.e. all possible load impedances can be mapped to a nominal impedance (in our case $50[\Omega]$). In addition, by the position of the stubs it is theoretically possible to derive the exact load impedance. As the skin effect gets worse at VHF, the large surface of the copper tubes offer potentially much less loss than a conventional lumped matching network.

Disadvantages

On the debit side it is the sheer size of the stub tuner which makes it impractical. Nevertheless the footprint would shrink if the excitation frequency were increased or if dielectric media could be inserted into the transmission lines. Moving, durable RF contacts cannot easily be realized and for the moment no automatching procedure is available.

Part IV: Results and Discussion

Chapter 6: Cylindrical Reactor

6.1 Introduction

Experiments in a reactor using a lens-shaped *circular* electrode to measure the correction of plasma non-uniformity due to the standing wave effect in a large area very high frequency plasma reactor are described here. This work is the experimental verification of the theoretical reactor design in cylindrical geometry described[8] in Chapter 3.

Advantages of cylindrical geometry

The cylindrical geometry was chosen in order to have a axially symmetric setup. The theory as presented in Chapter 3 is easier than in the rectangular case and it is possible to give an analytical solution. In addition as the reactor is axially symmetric, all the profile measurements can be carried out across a single radius. Measurements were done across a diameter to have an immediate check for the validity.

6.2 Cylindrical Lens

6.2.1 Theoretical Shape

A special RF electrode was designed whose surface was machined according to a GAUSSIAN profile specified in Eq. 6-1 (cf. Eq. 3-29 in section 3.2.1.5 and cf. Eq. 3-51 in section 3.3.1),

$$z = a_0 \exp\left(-\frac{k_0^2 r^2}{4}\right) \qquad \text{(Eq. 6-1)}$$

where k_0 is the vacuum wave number for the chosen excitation frequency and a_0 corresponds to the total electrode gap on axis. The plasma gap height is therefore given by Eq. 6-2.

$$d_{gap} = a_0 \exp\left(-\frac{k_0^2 R^2}{4}\right) \qquad \text{(Eq. 6-2)}$$

where R is the reactor radius. In this work, $R = 50[\mathrm{cm}]$, $d_{gap} = 3[\mathrm{cm}]$, $a_0 = 3.9[\mathrm{cm}]$, and the lens thickness on axis, a_0 - $d_{gap} = 0.9[\mathrm{cm}]$. The GAUSSIAN profile is a good approximation to the exact profile given in 3.2.1.5[8] provided $k_0 \cdot a_0 = 0.082 \ll 1$, which is satisfied here. The electrode was constructed for uniform electric field at a design frequency of $100[\mathrm{MHz}]$. Conventional parallel-plate electrodes were also used for comparison.

6.2.2 Dielectric Lens

A dielectric convex "lens" can be used to fill the gap below the dielectric plate to prevent any possible ignition of a parasitic plasma there, in which case the wave number becomes $k_0 \cdot \sqrt{\varepsilon_r}$ and the design frequency is reduced by a factor $\sqrt{\varepsilon_r}$ (see also Eq. 3-52). The dielectric used in this work was polytetrafluoroethylene (PTFE, relative dielectric constant $\varepsilon_r = 2.1$) and so the modified design frequency of the lens filled with PTFE was $100[\mathrm{MHz}] / \sqrt{2.1} = 69.0[\mathrm{MHz}]$.

6.2.3 Applied Lens Aberration

Concept from optics

The term "lens" for a shaped electrode is already borrowed from optics. In its proper sense, lens refers to its function as an optical element for either converging or diverging light or other types of electromagnetic radiation. In this respect a shaped electrode does not have anything in common with the optical lens. But looking at the cross-sectional shape of a plano-concave lens, we notice the striking similarity of the shaped electrode and such an optical element. Another concept from optics can be transferred: *aberration*. Aberration in an optical system designates all possible factors which cause the non-convergence of rays of light, reflected or refracted, to one focus and which produce a blurred image. Aberrations fall into three classes: chromatic, monochromatic and spherical aberrations. A "lens"-shaped electrode also suffers from factors which impair a perfect correction of the electrical field. Chromatic aberrations could be related by analogy to the difference between design frequency of the shaped electrode and RF operation frequency. Monochromatic aberrations could be linked to the mechanical deviation of the shaped electrode from its ideal curvature and a non-vanishing radial electric field E_r (cf. 3.2.1.5 and Eq. 3-23) could be related to spherical aberration. Henceforth aberration is used to encompass all possible errors causing a deviation from a perfect correction of the electric field.

Permissible deviation from ideal shape

Industrial applications typically require a uniformity in film thickness to better than $\pm 10\%$. Supposing that the deposition rate is approximately proportional to the plasma intensity, and under the assumption that the plasma intensity is roughly proportional to the dissipated RF power, which is in turn proportional to the square of the electric field strength, we conclude that in plasma an E-field uniformity of about $\pm 5\%$ is necessary. The uniformity for the E-field will depend on the wavelength reduction factor, thus for a $\sqrt{\varepsilon_{eff}} = 3$ we obtain finally a required non-uniformity of $\pm 5/3\%$ for the E-field in vacuum. Numerical simulation of a stepped lens curvature (10 vertical levels, maximum step height $5[\mathrm{mm}]$, step width $50[\mathrm{mm}]$ across $R = 500[\mathrm{mm}]$, designed for $f_0 = 100[\mathrm{MHz}]$, electrode gap $d_{gap} = 8[\mathrm{cm}]$) predicted a uniformity of the vertical electrical field better than $\pm 2\%$. Thus for the fabrication of a continuous lens curvature a vertical mechanical tolerance of $\pm 0.1[\mathrm{mm}]$ per $[\mathrm{mm}]$ radius was specified. For cost reasons the final mechanical tolerance was relaxed to $\pm 1[\mathrm{mm}]$.

Sources of aberration

From the mechanical point of view three main contributions to the lens aberration can be identified:

a) Fabrication accuracy of the lens curvature.

b) Torsion of shaped metal plate due to internal mechanical stress:
The lens curvature was submitted to a quality check after fabrication in *unclamped state* (i.e. after removing the workpiece from the milling machine). It revealed a maximum deviation from the specified lens depth of $0.9[\mathrm{mm}]$. This difference is mainly attributed to the distortion of the metal plate on the account of internal mechanical stress and less to fabrication inaccuracy. The stress deformation can be reduced by either a deliberate choice of low-stress material and/or the use of mechanical stiffeners on the back.

c) Dielectric homogeneity and precision of dielectric "lens" (cf. 6.2.2):
The dielectric antilens was manufactured with an accuracy of $\pm 0.2[\mathrm{mm}]$ from a single block. PTFE is a relatively soft material and under mechanical stress it will fill in even better the mould of the shaped electrode.

The corresponding section for the rectangular shaped electrode (cf. 7.2.2) discusses more experimental evidence on the lens aberration and tries to quantify further the influence of the lens error on the precision of the electric field correction.

6.3 Non-Uniformity and Extended Definition

Thin film non-uniformity

As mentioned in the introduction of this thesis, deposited or etched thin films must comply with certain large-area "flatness" in order to be useful for technological applications. Various hardware and process-related parameters influence the shape of such profiles. Their overall evenness is often quantified by a figure called *(non-)uniformity* or *(non-)homogeneity,* U, of the process. This quantity is usually defined as the percentage of the ratio of the difference of the maximum and minimum thicknesses over the sum of both across a well-defined substrate area (See Eq. 6-3). Max and Min denote the maximum and minimum of the measured physical quantity.

$$U = \frac{|Max - Min|}{|Max + Min|} \times 100\% \qquad \text{(Eq. 6-3)}$$

Plasma non-uniformity

An analogous consideration can be applied to a plasma being used to deposit or etch a thin film. Physical properties of the plasma such as electron temperature T_e, electron density n_e, ion density n_i, $EEDF$, IED, IAD etc. and combinations of them play a important role to obtain uniform film treatment. Spatial variations of these plasma parameters across the plasma will cause a change of the thin film properties and a local change of the in situ deposition or etching rate. Thus it is reasonable to adapt the notion of *(non-)uniformity* as well for a large slab of plasma.

E-field non-uniformity

The same holds for the spatial variation of the magnitude of an RF electric field, which excites and sustains a capacitively coupled plasma.

Two types of symmetrical spatial plasma or E-field profiles types recur: (i) convex or dome-like profiles and (ii) concave or basin-like profiles (See Fig. 6-2 for examples of both). To facilitate the mathematical treatment, the definition of U is extended by a sign to indicate the shape of profile:

(i) Convex or dome-like profile: If the maximum of the measured profile is in the centre region surrounded by a ring-like valley then U is defined as a positive uniformity $\Rightarrow + U > 0\%$.

(ii) Concave or basin-like profile: If the minimum of the measured profile is in the centre region surrounded by a higher ridge, then the uniformity as calculated by Eq. 6-3 is negated $\Rightarrow$ - $U < 0\%$.

(iii) If the profile cannot be unequivocally related to one of these shapes above, e.g. a saddle-like profile, then the non-uniformity is explicitly marked as $\Rightarrow \pm U$.

From the experiments, some general rules could be derived. In case of flat electrodes, standing wave effect dominated profiles tend to show a positive non-uniformity $U > 0\%$, whereas telegraph or edge effect dominated profiles display rather a negative non-uniformity $U < 0\%$ and process conditions in which both effects counterbalance each other or both effects vanish at the same time exhibit a non-uniformity nearly equal to zero $U \approx 0\%$. With a lens shaped electrode the non-uniformity is positive $U > 0\%$ for an excitation frequency f_{RF} above the design frequency f_0 of the lens, nearly zero $U \approx 0\%$ for f_{RF} in the vicinity of the design frequency and negative $U < 0\%$ for f_{RF} below the design frequency of the lens (cf. 3.6).

6.4 Calculated E-Field Non-Uniformity

Two configurations

Here the calculated E-field non-uniformity for two hardware configurations is shown: one for the conventional parallel plate *flat* electrode configuration and one for the proposed *lens* shaped electrode, which compensates the standing wave at the *design frequency* f_0 in vacuum. Because the plasma experiments with shaped electrode are done with a lens of effective design frequency $69.0[\mathrm{MHz}]$ (See 6.2.2), for the calculations in this section, the design frequency f_0 is arbitrarily set to $f_0 = 67.8[\mathrm{MHz}]$, which is a convenient harmonic of $13.56[\mathrm{MHz}]$.

Vacuum and plasma

Fig. 6-1 depicts five curves for each hardware configuration: one curve plots the simple vacuum case ($\varepsilon_{eff} = 1$), four curves ($\varepsilon_{eff} = 3, 5, 6.25$ and 12.25) show the effect of the presence of dielectric in the plasma volume on the spatial electric field non-uniformity. The left-hand graph for the flat electrode case shows clearly that:

(i) The non-uniformity goes up with increasing RF frequency for any relative dielectric constant and it rises stronger than linear ("supralinear") with the frequency.

(ii) The non-uniformity is "worsened" due to the wavelength reduction caused by the dielectric property of a plasma, expressed by an increase of the parameter ε_{eff}. The empirical "worsening factor" is process dependent (See 6.6.4).

Over- and under-compensation

The right-hand graph shows the evolution of the electric field non-uniformity under the same conditions and reactor dimensions, but with a lens electrode for the design frequency $f_0 = 67.8[\mathrm{MHz}]$. All the curves have their zero-crossings, i.e. perfect compensation and disappearing non-uniformity, at *exactly* the design frequency f_0. A negative value means that the lens is *overcompensating* the standing wave effect and we shall see later that we obtain indeed a depressed, a *concave* electric field or plasma intensity profile. Conversely, a positive sign of the non-uniformity is synonymous with an *undercompensated* correction and we shall have a dome-like or *convex* profile. Furthermore, the plot shows that the effective action of the lens shaped electrode when going from Fig. 6-1-[A] to Fig. 6-1-[B] is to shift downwards each curve until it intersects the abscissa at the design frequency. This shift corresponds in terms of the non-uniformity to a subtraction by an approximate value of $U_{Flat}(f_0)$ as defined by the rule of thumb Eq. 6-5.

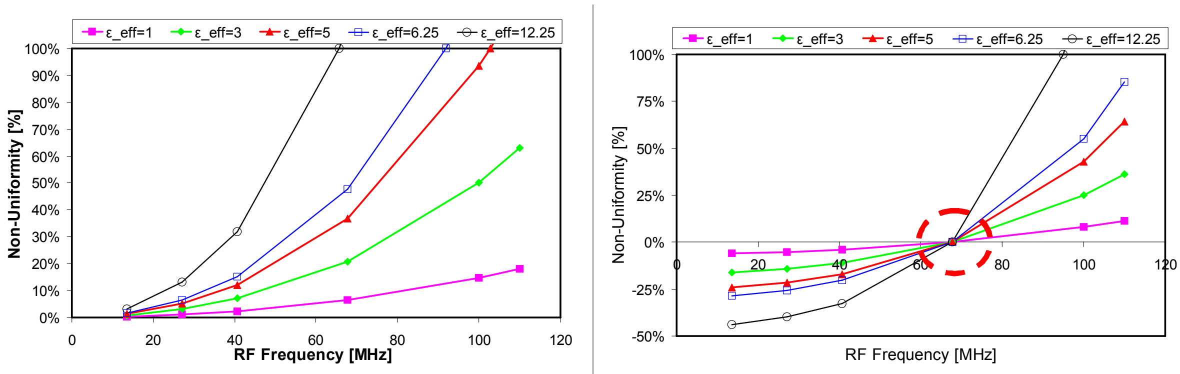

[A] Flat Electrode [B] Lens Shaped Electrode for $67.8[\mathrm{MHz}]$.

Fig. 6-1: Calculated E-field non-uniformities for the cylindrical test reactor in vacuum and with assumed plasma for both hardware configurations. All calculations were done assuming $R_{max} = 0.5[\mathrm{m}]$. Numerical figures are worked out for the frequencies 13.56, 27.12, 40.68, 67.8, 100.0 and $110.0[\mathrm{MHz}]$ respectively. For [A] calculations were done according to Eq. 6-4, for [B] according to section 3.2.1.5. All curves in [B] cross the abscissa exactly at $67.8[\mathrm{MHz}]$.

Calculation of non-uniformity

Formula Eq. 6-4 gives the theoretical electric field non-uniformity for an axial-symmetric cylindrical reactor with conventional parallel plate flat electrode and a central RF power feeding. The formula disregards any edge effects. It is only valid as long as the first node of the BESSEL function lies outside the reactor wall, i.e. $k_0 \cdot \sqrt{\varepsilon_{eff}} \cdot R_{max} \leq 2.405$. J_0 denotes the 0-th order BESSEL function, k_0 the vacuum wave number $k_0 = 2\pi \cdot f / c$, ε_{eff} the effective electric permittivity of the plasma medium and R_{max} the maximum distance considered from the central axis (see also Eq. 3-12 in section 3.2.1.2 for the vacuum case and Eq. 3-19 in section 3.2.1.4 in combination with a dielectric). If the first node lies within the boundaries of the reactor, it follows that U_{Flat} takes its maximum value 100%.

$$U_{Flat}(f) = \frac{1 - J_0(k_0 \cdot \sqrt{\varepsilon_{eff}} \cdot R_{max})}{1 + J_0(k_0 \cdot \sqrt{\varepsilon_{eff}} \cdot R_{max})} \times 100\% \qquad \text{(Eq. 6-4)}$$

Non-uniformity for shaped electrodes

The exact non-uniformity for the shaped electrode configuration can be retrieved only by numerical methods. An estimation can be inferred from the graphs above when considering as aforementioned, that when going from the left-hand graph [A] to the right-hand graph [B], the application of the lens shifts downwards the non-uniformity characteristics. In the frequency range considered and for the used cylindrical geometry formula Eq. 6-5 is a good approximation for the vacuum case, where the absolute error is less than $\pm\, 0.3\%$ and weak plasma conditions (less than $\pm\, 10\%$ for $\varepsilon_{eff} \leq 3$).

$$U_{Lens}(f) \approx U_{Flat}(f) - U_{Flat}(f_0) \qquad \text{(Eq. 6-5)}$$

Eq. 6-5 is purely based on an empirical fit and does not have any analytical mathematical derivation.

6.5 E-Field Measurements

The radial profile of the RF vertical electric field strength in vacuum was measured by drawing a calibrated diode probe (See 4.3) across the reactor diameter at mid-gap height through a small window in the reactor sidewall.

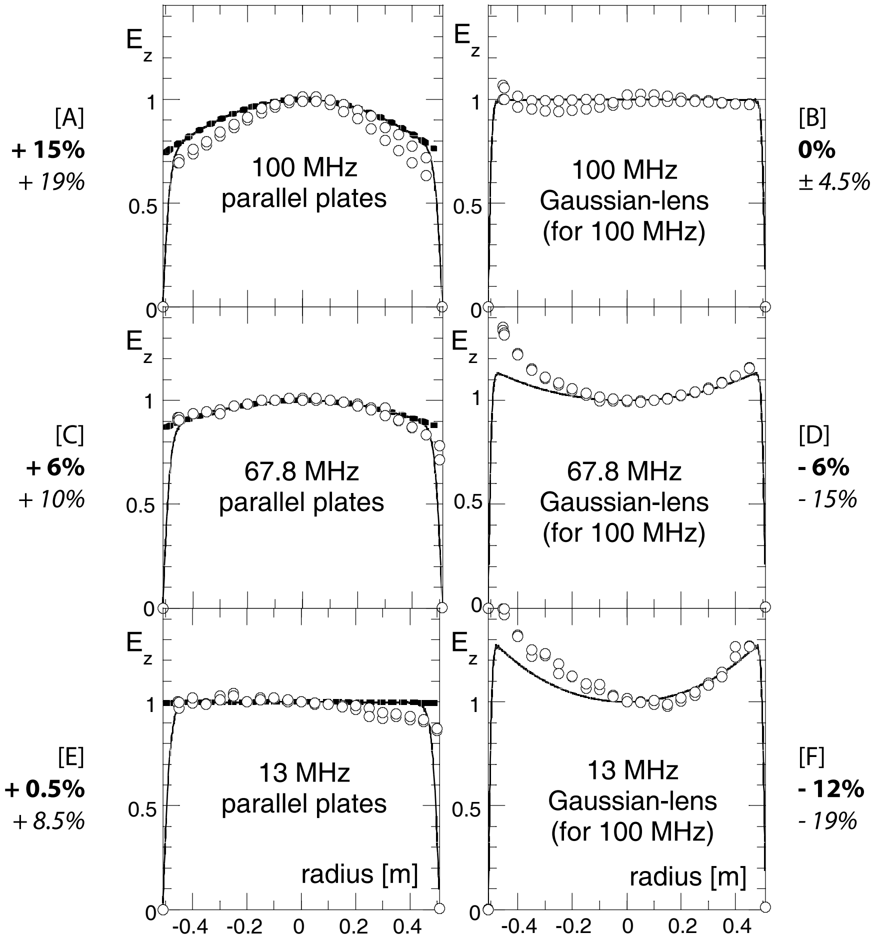

Fig. 6-2: Measured and modelled radial profiles of the vertical electric field in vacuum for frequencies 13.56, 67.8, and $100[\mathrm{MHz}]$. Left-hand column [A], [C] and [E]: with parallel plate electrodes. Right-hand column [B], [D] and [F]: using the GAUSSIAN vacuum lens electrode (design frequency $100[\mathrm{MHz}]$).
The data points are compared with numerical solutions of MAXWELL's equations (continuous line) for the corresponding electrode geometry, and also with the BESSEL functions (dotted line) for the parallel plate case. Error bars of $\pm 7\%$ are omitted for clarity. All data are normalized to the values on axis. Percentages in the margin denote the non-uniformity U for the theoretical profile (upper line in **bold**) and the measurement (lower line in *italic*) for the respective plot without considering the outermost point of zero E-field magnitude.

6.5.1 Results for the Flat Electrode

The radial profile of the vertical electric field strength $E_z(r)$ without plasma was measured for three frequencies as shown in Fig. 6-2 for parallel plates ([A], [C] and [E]) and for the GAUSSIAN-lens electrode designed for $100[\mathrm{MHz}]$ without the PTFE dielectric filling ([B], [D] and [F]). Solution of MAXWELL's equations with parallel electrodes gives a BESSEL function profile (Eq. 6-6). where k_0 is the vacuum wave number at the excitation frequency (cf. 3.2.1.2).

$$E_z(r) = E_0 \cdot J_0[k_0 \cdot r] \qquad \text{(Eq. 6-6)}$$

A first node would occur at radius r_1 for the first zero of the BESSEL function at $k_0 \cdot r_1 = 2.405$; at $100[\mathrm{MHz}]$ excitation frequency, $r_1 = 1.15[\mathrm{m}]$ or conversely for the radius of the actual reactor $r_1 = 0.5[\mathrm{m}]$ the first node would appear inside the reactor at about $230[\mathrm{MHz}]$. So there is no node for the vacuum electric field within the reactor for the range of frequencies investigated here. The data in the figure are also compared with a numerical solution of MAXWELL's equations which accounts for the boundary conditions imposed by the grounded sidewall. The deviation of the measurements from the theoretical curves is probably due to perturbations caused by the probe shaft and the window in the grounded sidewall.

At $13.56[\mathrm{MHz}]$ and with the flat electrode, the standing wave is negligible, therefore the profile is flat. For $100[\mathrm{MHz}]$ and the GAUSSIAN lens, the standing wave is compensated, therefore the measurement is flat too.

6.5.2 Results with the Lens Electrode

The solution for the GAUSSIAN-lens electrode predicts a uniform radial profile for the vertical electric field at the design frequency of the lens. Convex (undercompensated) or concave (overcompensated) curves would be observed for frequencies above or below the design frequency, respectively. The measured profiles correspond well with the theoretical curves, as expected for the vacuum case. The theory and the design and construction of the reactor with a GAUSSIAN-lens electrode are therefore validated for the case of vacuum (no plasma). The next section investigates whether the uniform condition is maintained or perturbed by the presence of plasma in the parallel-sided gap between the plane electrode and the plane glass surface.

6.6 Plasma Uniformity Measurements

All experiments were performed using argon gas. The pressure range was 5 - 750[mTorr] with RF power from 50 to 300[W]. Three different RF generators with frequencies 13.56, 67.8, and 100[MHz] were used. The RF generators were capacitively coupled to the reactor axis via an impedance matching network and stripline. The RF power was measured with a voltage, current, and phase wideband RF probe (cf. 4.5.1) placed after the impedance matching network.

The plasma uniformity was monitored by means of two probe arrays positioned along the same diameter. Nineteen fibre optic telescope probes with photodiode sensors, calibrated *in situ*, measured the optical emission intensity averaged over the vertical profile to give a rough indication of the plasma power radial profile (cf. 4.4.1.2).[34] Data acquisition was carried out with a multichannel analog/digital PC plug-in card, which allows to measure all nineteen optical emission intensity signals and ten ion flux signals in differential mode simultaneously (cf. 4.4.1.4). All signals were acquired in less than 1[s]. The upper surface of the glass covering the lens had a matt black coating to minimize stray reflections into the fibre optic telescope probes. Ten surface mounted biased (- 50[V]) electrostatic probes measured the ion Bohm current through the sheath to give an estimation of the ion flux onto the plane ground electrode (cf. 4.4.1.1).

6.6.1 Flat Electrodes

Using parallel plate electrodes, radial profiles of the plasma optical emission intensity $I_{oes}(r)$ and ion saturated current $I_{sat}(r)$ were measured for the three frequencies as shown in the left- and right-hand columns, respectively, of Fig. 6-3. Since the dependence of the non-uniformity on pressure was generally stronger than for the power, only the pressure range is shown with the RF power fixed at 200[W]. All profiles are normalized to on-axis values. A general agreement between the $I_{oes}(r)$ and $I_{sat}(r)$ profiles is found. In presence of plasma in the parallel plates case, the vertical electric field Bessel function profile is modified to

$$E_z(r) = E_0 \cdot J_0(k_{eff} \cdot r) = E_0 \cdot J_0\left[k_0 \cdot r \cdot \Re(\sqrt{\varepsilon_{eff}})\right] \qquad \text{(Eq. 6-7)}$$

where $k_{eff} = k_0 \cdot \Re(\sqrt{\varepsilon_{eff}})$ is the increased wavenumber of the wave propagating in the dielectric (with complex relative permittivity ε_{eff}) formed by the plasma-sheath combination (cf. 3.2.1.4). $\Re(\sqrt{\varepsilon_{eff}})$ is called the "wavelength reduction factor" and applies to the electric field ($electric\ field \propto 1 / \Re(\sqrt{\varepsilon_{eff}})$). It is related to the "worsening factor" $\Re(\varepsilon_{eff})$ as introduced by Schmitt et al.[1] which makes the uniformity of the squared electric field (and plasma) worse than for the vacuum case; the worsening factor applies to power quantities only ($power \propto 1 / \Re(\varepsilon_{eff})$).

In order to compare the measured intensity profiles with theory for the case of parallel plates, we make an assumption that the optical emission intensity and ion flux are proportional to the square of the electric field which is approximately proportional to the local electrical power dissipation. The optical emission profiles $I_{oes}(r)$ in Fig. 6-3 are therefore compared with Eq. 6-8 and similarly for $I_{sat}(r)$.

$$I_{oes}(r) = I_0\left\{J_0\left[k_0 \cdot r \cdot \Re(\sqrt{\varepsilon_{eff}})\right]\right\}^2 \qquad \text{(Eq. 6-8)}$$

Because the plasma permittivity shortens the vacuum wavelength, the first node at 100[MHz] now occurs within the reactor radius at $r_1 \approx 0.325$[m], where the plasma optical emission intensity and ion flux fall close to zero. This clearly demonstrates the strong non-uniformity when using VHF in large, parallel plate reactors. Since $k_0 \cdot r_1 \cdot \Re(\sqrt{\varepsilon_{eff}}) \approx 2.405$, we deduce a wavelength reduction factor of $\Re(\sqrt{\varepsilon_{eff}}) \approx 3.5$ for the plasma at 100[MHz]. Using the approximation

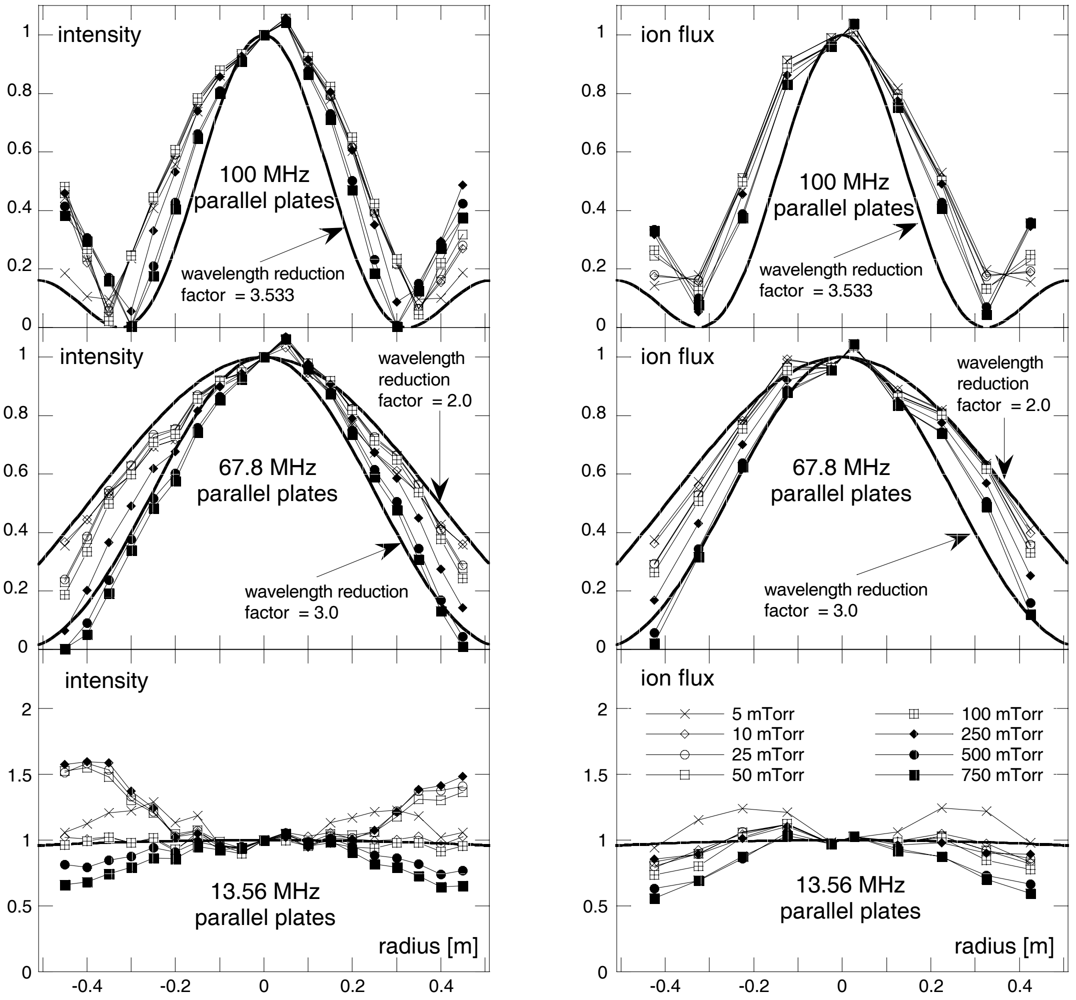

Fig. 6-3: Measured radial profiles of the plasma optical emission intensity $I_{oes}(r)$ (left-hand column) and ion flux $I_{sat}(r)$ (right-hand column) for three frequencies with parallel plate electrodes. The curves represent the square of the electric field described by a BESSEL function and the corresponding wavelength reduction factor. All values are normalized to the values on axis. Error bars of ± 10% are omitted for clarity. Argon pressure $0-750[\mathrm{mTorr}]$ and $200[\mathrm{W}]$ RF power.

$\Re(\sqrt{\varepsilon_{eff}}) \approx \sqrt{d_{gap}/2d_{sh}}$ in 3.2.1.4, this corresponds to a sheath width of about $1.2[\mathrm{mm}]$ which is reasonable for this VHF plasma.[81]

6.6.2 GAUSSIAN Lens Electrode

6.6.2.1 With Dielectric “Lens”

The profiles in Fig. 6-4 were obtained using the GAUSSIAN-profile electrode filled with PTFE dielectric, designed for uniform vertical electric field at 69.0[MHz] excitation frequency.

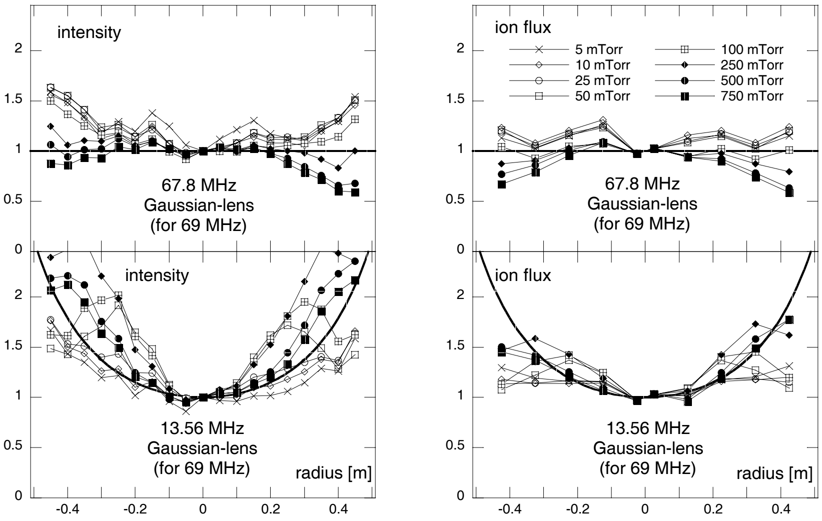

Fig. 6-4: Measured radial profiles of the plasma optical emission intensity $I_{oes}(r)$ (left-hand column) and ion flux $I_{sat}(r)$ (right-hand column) for the GAUSSIAN-lens electrode filled with PTFE dielectric (design frequency 69.0[MHz]). For the data at 13.56[MHz], the data are compared with the square of the electric field assuming capacitive division between the plasma sheath (assumed width 3.75[mm]) and the electrode lens. All values are normalized to the values on axis. Error bars of ± 10% are omitted for clarity. Argon pressure 5 – 750[mTorr] and 200[W] RF power.

Flat at 67.8[MHz]

The measured profiles using this GAUSSIAN-lens electrode at 67.8[MHz] are more uniform than the corresponding profiles at 67.8[MHz] with parallel plates in Fig. 6-3. Only edge effects remain to perturb the flat profile, which is similar to the situation for 13.56[MHz] with parallel plates.

Concave at 13.56[MHz]

Fig. 6-4 also shows the measured profiles when using 13.56[MHz]. Using this frequency, which is below the lens design frequency, gives overcompensated, concave profiles.

Convex at 100[MHz]

Conversely, excitation frequencies above the design frequency gives undercompensated, convex profiles. Fig. 6-5 depicts measured profiles using 100[MHz] with the same hardware configuration. The used RF frequency lies about 30[MHz] above the design frequency and thus standing wave is only partially compensat-

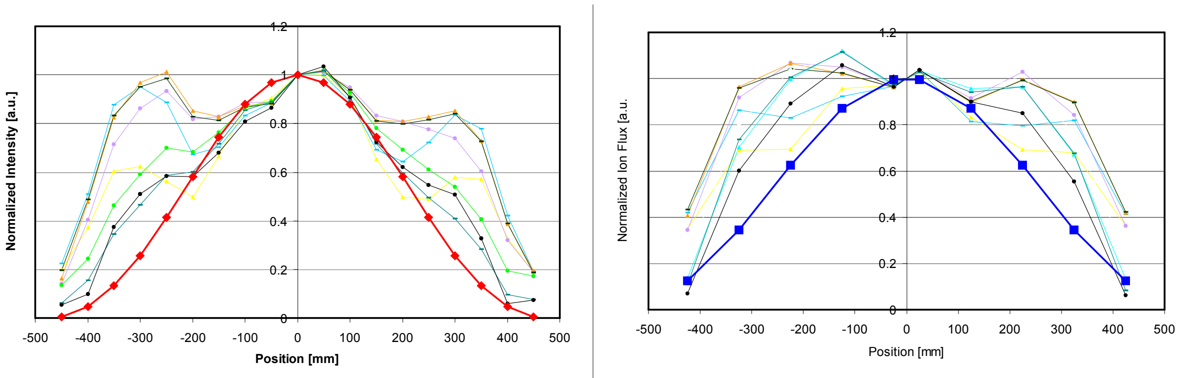

[A] intensity

[B] ion flux

Fig. 6-5: Same as Fig. 6-4 but $f_{RF} = 100$[MHz]. Process pressure 5 - 1000[mTorr] at 200[W]. BESSEL curves for comparison are shown in [A] as red diamonds for $\Re(\sqrt{\varepsilon_{eff}}) = 2.4$ and in [B] as blue squares for $\Re(\sqrt{\varepsilon_{eff}}) = 2.0$.

ed. At low pressures (5 - 100[mTorr]) the profiles shows an additional hump at about 300[mm] off the reactor centre. At higher pressures ($\geq$ 250[mTorr]) the measured profiles become Bessel-like. The origin of this phenomenon is not clear, it may be a periodic variation in plasma intensity due to rotating border plasmoids.

6.6.2.2 Plasma in Lens Concavity

Plasma corrupts lens

Without the glass disk to confine the plasma between parallel planes, the observed plasma profiles (Fig. 6-6) are similar to the parallel-plate measurements, because the plasma “short circuits” the electric field within the lens volume. The same is true if a plasma ignites underneath the glass when the power is too high and the volume is not evacuated—this was the case when using the lens at 100[MHz] with no dielectric filling. Due to this parasitic plasma and the availability of RF power at 67.8[MHz], PTFE was used to fill the concavity and the design frequency was therefore lowered to 69.0[MHz] (cf. Eq. 3-52). This is why all the measurements in this work were made at 67.8[MHz], close to the design frequency.

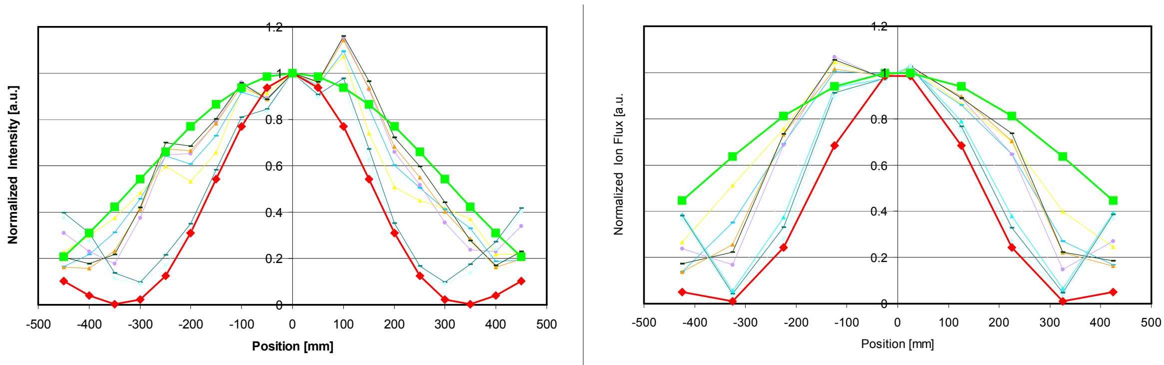

[A] intensity

[B] ion flux

Fig. 6-6: 67.8[MHz] plasma in lens concavity. Used configuration: 67.8[MHz] vacuum lens, no PTFE antilens, no dark glass plate. The shiny metal surface may have caused optical multi-reflections, the signal of the optical plasma emission intensity may be overrated. Process conditions: 100% argon, 5 - 1000[mTorr] at 200[W].Bessel curves for comparison are shown in [A] as red diamonds for $\Re(\sqrt{\varepsilon_{eff}}) = 5.0$ and green squares for $\Re(\sqrt{\varepsilon_{eff}}) = 2.5$ and in [B] as red diamonds for $\Re(\sqrt{\varepsilon_{eff}}) = 4.8$ and as green squares for $\Re(\sqrt{\varepsilon_{eff}}) = 2.0$.

The current definition of $\Re(\sqrt{\varepsilon_{eff}})$ in 3.2.1.4 covers only the parallel plate case. Notwithstanding here a wavelength reduction factor is extracted under the assumption that the plasma is “quasi standing wave like”. It turns out that $\Re(\sqrt{\varepsilon_{eff}})$ can assume values between 2.5 and 5.0, which is even “worse” than in the parallel plate case (last row of Table 6-1). The fact is particular important e.g. for a cleaning processes which are run after each deposition. If the lens action is not guaranteed, then a thorough and exhaustive reactor cleaning at VHF frequency will likely not be possible in due time.

6.6.3 Symmetrization of the Electrodes

Skirt Height and Edge Plasma

The effect of changing the area ratios of the RF electrode to the grounded electrode was investigated. The area of the RF electrode was increased with a flexible metal ribbon, whose height above the lens face could be continuously varied between 0[mm] and 20[mm]. The additional area influences the edge voltage uniformity and thus the incidence of edge plasma. It was observed that the medium height is best to avoid instable plasma conditions. All the measurements in the preceding sections were done with medium skirt height as shown in Fig. 6-7-[B]. In the following the two extreme cases [A] and [C] are compared for the configurations where the standing wave is least noticeable, i.e. parallel plate at 13.56[MHz] and lens configuration at 67.8[MHz].

[A] Without skirt

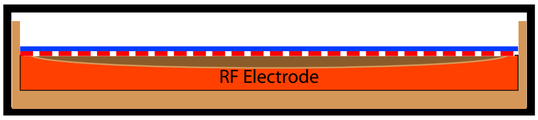

[B] Medium skirt height 12[mm], best symmetrization.

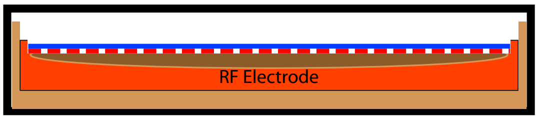

[C] Maximum skirt height 20[mm]

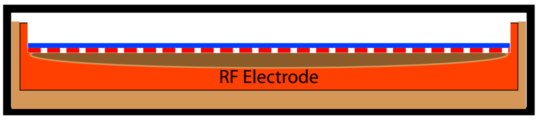

Fig. 6-7: Cross-section of the cylindrical reactor without the skirt [A], medium skirt height [B] and maximum skirt height [C]. Different skirt heights were used with lens and/or with flat electrode. The dashed line indicates the parallel plate.

Parallel Plate

In case of the parallel plate a change in the area asymmetry is best demonstrated by looking at the edge plasma at 13.56[MHz] as depicted in Fig. 6-8. As at this frequency the SWE is negligible, effects at the border emerge more clearly. The relative edge intensity of the profiles in [A] and [B] vary much stronger with the maximum skirt height than without and the maximum intensity in [B] is $\approx 2.5\times$ the normalization value vs. $\approx 1.8\times$ in [A].

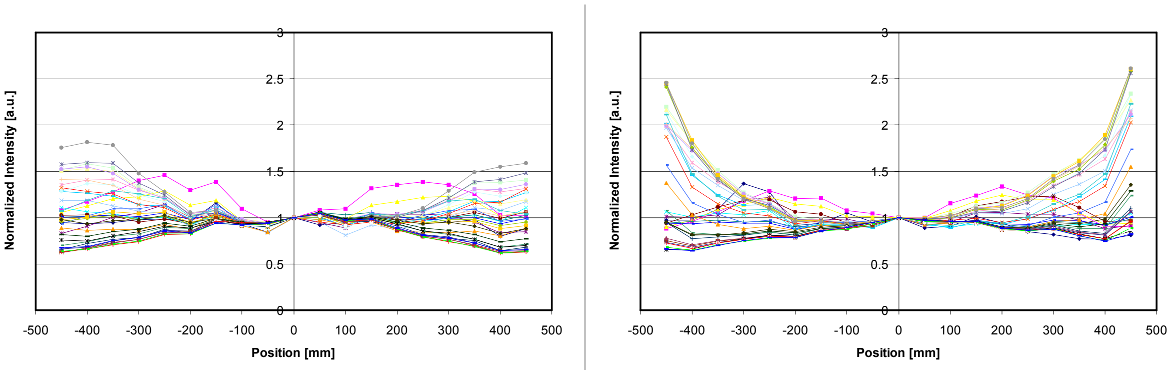

[A] Without skirt

[B] Maximum skirt height 20[mm]

Fig. 6-8: Effect of different skirt height on plasma intensity at 13.56[MHz] and 100% argon. All available process conditions from 5[mTorr] to 1000[mTorr] are plotted and normalized to 1.0 at the reactor centre.

Lens

Analogous with the lens configuration, the skirt height has more relative influence on the intensity profiles at RF frequencies near the design frequency than in strong under- or overcompensated regimes. In Fig. 6-9 at $67.8[\mathrm{MHz}]$ the right hand graph [B] with maximum skirt height shows again a much stronger border effect than without the skirt in [A].

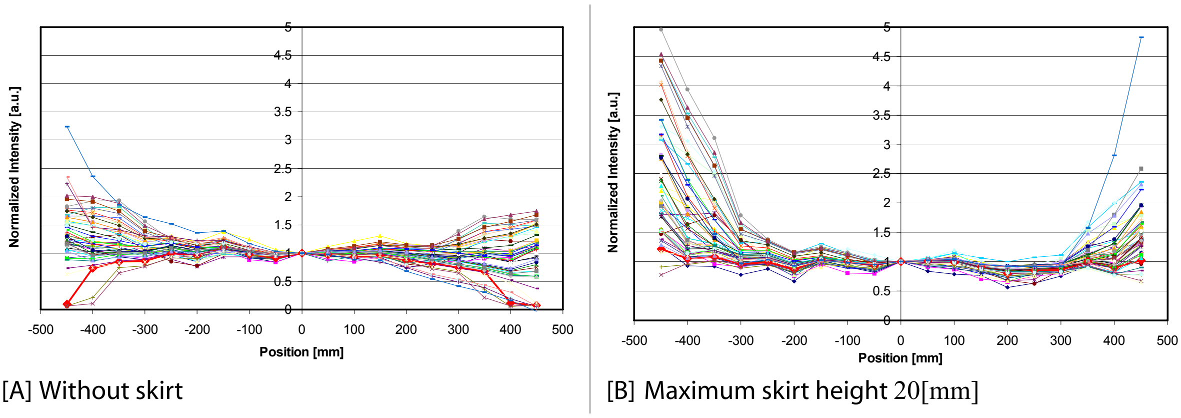

[A] Without skirt

[B] Maximum skirt height $20[\mathrm{mm}]$

Fig. 6-9: Effect of different skirt height on plasma intensity at $67.8[\mathrm{MHz}]$ with lens and 100% argon. All available process conditions from $5[\mathrm{mTorr}]$ to $1000[\mathrm{mTorr}]$ are plotted and normalized to 1.0 at the reactor centre.

6.6.4 Wavelength Reduction Factor and Non-Uniformity

The wavelength reduction factors for the profiles at $67.8[\mathrm{MHz}]$ in Fig. 6-3 were in the range $2 < \Re(\sqrt{\varepsilon_{eff}}) < 3$, which corresponds to sheath widths from 3.75 to $1.66[\mathrm{mm}]$ using the model in 3.2.1.4, as the pressure increased from 5 to $750[\mathrm{mTorr}]$. The deduced sheath width is therefore observed to decrease with increasing pressure[28][83] and frequency[81][84] in general agreement with the literature. Note that the profiles at 67.8 and $100[\mathrm{MHz}]$ are very non-uniform, and dominated by the standing wave effect for the whole parameter range investigated. The profiles at $13.56[\mathrm{MHz}]$, where standing wave effects are expected to be negligible for this reactor size, are approximately uniform except for edge effects, seen on many of the measured profiles, caused by fringing fields ("focusing" of the electric field at the corners), hollow cathode and electrode area asymmetry.[62]

For all the plasma parameters (pressure, power) in the parallel plates case at the VHF frequencies 67.8 and $100[\mathrm{MHz}]$, the principal non-uniformity in Fig. 6-3 is frequency dependent and can be explained by the standing wave effect. PERRET et al.[17] found that edge or inductive effects[38] can strongly modify the standing wave power deposition profile at RF power densities higher than used in this work.

The strong non-uniformity due to the standing wave effect would normally prohibit the use of very high frequency for applications in large area reactors[85][104][4][38][8], thereby renouncing the advantages of VHF operation such as high deposition rate, and reduced sheath voltage and ion bombardment energy[5][12][1][11]. The improved uniformity using VHF in a small highly asymmetric reactor[12] was most likely due to an interplay with the dominant edge effects which coincidentally resulted in a better uniformity at $70[\mathrm{MHz}]$ than at $13.56[\mathrm{MHz}]$.

Fitting Procedure

Table 6-1 gives the extracted wavelength reduction factors for all the frequencies in the parallel plate configuration. The range of $\Re(\sqrt{\varepsilon_{eff}})$ was determined graphically by plotting a lower (i.e. high $\Re(\sqrt{\varepsilon_{eff}})$) and upper envelope (i.e. low $\Re(\sqrt{\varepsilon_{eff}})$) for the family of curves of the entire power vs. pressure scan as sketched in the middle row of Fig. 6-3. The last row with the data for a lens with a plasma in the concavity is given here for completeness (See 6.6.2.2).

13.56[MHz]

At 13.56[MHz], we expect the standing wave to be the smallest effect or even negligible. Therefore interpreting the non-edge non-uniformity in terms of the standing wave gives no realistic value of $\Re(\sqrt{\varepsilon_{eff}})$. Nevertheless the values for 13.56[MHz] are given for completeness in Table 6-1.

Table 6-1: Overview of the wavelength reduction factor $\Re(\sqrt{\varepsilon_{eff}})$ in plasma as function of RF excitation frequency, skirt height and gas composition for a pressure range of 5 to 1000[mTorr] and power range of 50 to 300[W]. The skirt height is dealt with in section 6.6.3.

Configuration f_{RF}	**Skirt Height**	**100% Ar**		**Ar : H_2 = 2 : 1**	
		Optical (I_{oes})	Electrical (I_{sat})	Optical (I_{oes})	Electrical (I_{sat})
Parallel Plate 13.56[MHz][a]	0[mm]	≤ 9	≤ 9	≤ 10.0	≤ 4.0
	12[mm]	5 – 15	≤ 10	5 – 10	≤ 4.0
	20[mm]	≤ 7	≤ 6.0	n.a.	≤ 3.5
Parallel Plate 67.8[MHz]	0[mm]	2.0 – 3.4	1.8 – 3.2	1.9 – 5.8	1.6 – 8.0
	12[mm]	2.0 – 3.5	1.7 – 3.1	2.0 – 4.5	1.5 – 4.0
	20[mm]	2.0 – 3.5	1.7 – 3.5	1.5 – 4.5	1.5 – 4.5
Parallel Plate 100[MHz]	0[mm]	2.2 – 3.4	2.0 – 3.0	n.a.	n.a.
	12[mm]	2.5 – 3.8	2.2 – 3.0	1.5 – 2.9	1.8 – 3.0
	20[mm]	2.3 – 3.5	2.0 – 3.0	1.5 – 2.5	1.5 – 2.5
Lens with Plasma in Concavity 67.8[MHz] (cf. 6.6.2.2)	12[mm]	2.5 – 5.0	2.0 – 4.8	2.0 – 4.0	2.0 – 4.3

a. data not interpretable in terms of standing wave effect.

From the values at VHF in Table 6-1, we deduce that $\Re(\sqrt{\varepsilon_{eff}})$ is essentially independent of the degree of symmetrization as expected and after checking against Fig. 6-3 we see that $\Re(\sqrt{\varepsilon_{eff}})$ increases with the pressure.

6.7 Conclusion

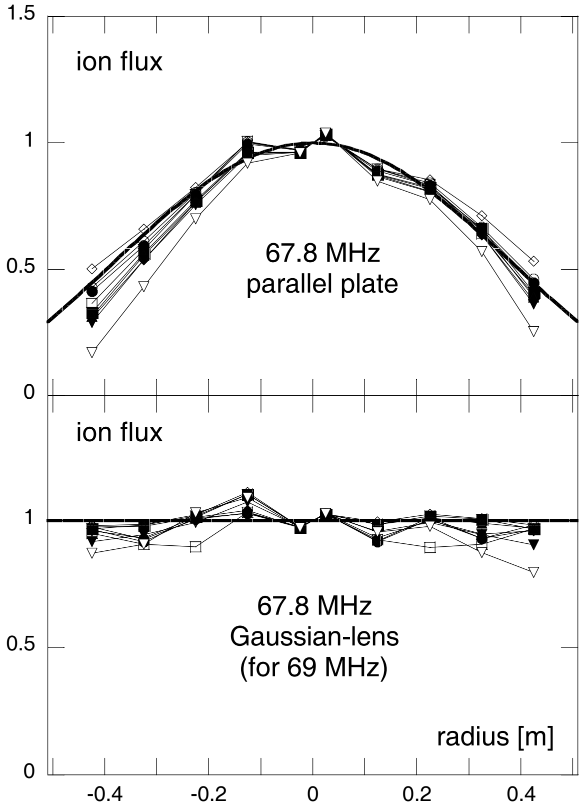

[A] Range of non-uniformity:
+ 35% – + 74%

[B] Range of non-uniformity:
± 7% – ± 19%

Fig. 6-10: Bottom: Measured radial profiles of the ion flux $I_{sat}(r)$ at 67.8[MHz] for the GAUSSIAN-lens electrode filled with PTFE dielectric (design frequency 69.0[MHz]). Top: the same measurements but with parallel plate electrodes. Uniform profiles can be obtained using the lens electrode by suitable choice of pressure and RF power, whereas the profiles for parallel plate electrodes are strongly non-uniform and dominated by the standing-wave effect for all plasma parameters indicated. Plasma parameters: 5[mTorr] (100 and 300[W]), 10[mTorr] (50 and 100[W]), 25[mTorr] (50 and 100[W]), 50[mTorr] 50[W], 100[mTorr] 50[W], and 250[mTorr] 200[W]. All values are normalized to the values on axis. Error bars of ± 10% are omitted for clarity.

Standing Wave and Edge Effect

To resolve the problem of non-uniformity when high frequency is combined with large area reactors, it is clear that two distinct issues must be addressed: the standing wave effect and the edge effects. The *standing wave* effect is compensated by the GAUSSIAN-lens electrode, whereas *edge effects* always exist even at low frequency in parallel plate reactors. In practice, edge effects are reduced by reactor design and process optimization—a process window of plasma parameters is empirically determined where the necessary plasma properties are sufficiently uniform for the required application. In Fig. 6-10, for example, it is possible to select pressures and RF powers for good overall uniformity of the ion flux at 67.8[MHz] using the GAUSSIAN-lens electrode, whereas the profiles obtained with the parallel plate electrodes at this frequency remain dominated by the standing wave effect for all plasma parameters. This demonstrates the effectiveness of the GAUSSIAN-lens electrode for compensating the standing wave effects for VHF plasmas in large area reactors.

Plasma perturbation

All the results shown in this chapter were obtained using plasmas in argon. Experiments using argon/hydrogen mixtures gave similar results. Since the GAUSSIAN-lens electrodes were designed for a vacuum solution of MAXWELL's equations[8], the perturbation due to the plasma increases as the plasma permittivity (Eq. 3-13) deviates from that of vacuum, as demonstrated by numerical simulations.[70][71][72] Plasmas in *electropositive gases*, such as argon, with high electron density (high electron plasma frequency, ω_{pe}) and low pressure (low electron-neutral collision frequency, ν_m) present the *worst case* for uniformity as they are the experimental case farthest from the vacuum solution. On the other hand, plasmas in *electronegative gas* mixtures (such as Ar/SF_6) typically have lower electron density and are therefore expected to present even less perturbation and better uniformity than the argon experiments described here.

Chapter 7: Rectangular Reactor

7.1 Introduction

Rectangular geometry and implication

This section extends the “proof of principle” of the preceding chapter to a rectangular lens geometry used in the context of an *industrial-type* reactor setup. It begins with the theoretical lens shape and some mechanical aspects of the shaped electrode. The expected calculated non-uniformity points out an important difference between cylindrical and rectangular shape: The boundary condition on the electrode edge. The section details the uniformity measurements performed. Similar to the previous chapter, uniformity measurements are done in air and with plasma using non-reactive gases only.

Experience from cylindrical reactor

Constructional restrictions due to the vacuum lens allowed only the use of optical diagnostics to characterize the spatial variation of the plasma intensity. From the experience with the cylindrical reactor’s results, fibre-optic based diagnostics are a validated technique of measuring the homogeneity of a large plasma slab. Two additional frequencies (27.12 and 40.68[MHz]) were available, thus allowing a better documentation of the frequency effect in the high HF and low VHF band. The main findings are directly compared to the associated sections in Chapter 6 “Cylindrical Reactor”.

VHF operation in industrial 13.56[MHz] system

Working within the scope of an industrial reactor imposed constructional restrictions. No reactor modifications were made for specific VHF operation. It is known that due to reduced sheath thickness at VHF[78][80], plasma can ignite in smaller gaps than at 13.56[MHz]. Therefore it is more likely to have unwanted (parasitic) plasma in the border regions and we shall see that in many cases optical emission intensity profiles of VHF plasmas are influenced by non-standing wave effects or problems not due to the lens operation.

7.2 Rectangular Lens

7.2.1 Theoretical Shape

Numerical solution

In contrast to the cylindrical reactor, there is no analytical solution for the rectangular case, as already outlined in section 3.2.2. The numerical solution[10] as depicted in Fig. 7-1 is optimized for a RF operation frequency of 67.8[MHz], *vacuum case* $\varepsilon_{eff} = 1$ and an inter-electrode gap of 28[mm]. The solution allows for four RF power feedings, which are distributed on the back of the driven electrode.

Along the longer edges (left and right) the lens has two shoulders which guide the lens surface from the level of the margin smoothly down to the area of maximum depression (7[mm] below the border height). The shoulders are easily recognizable by the dense contour lines (every 0.2[mm]). The higher density indicates the

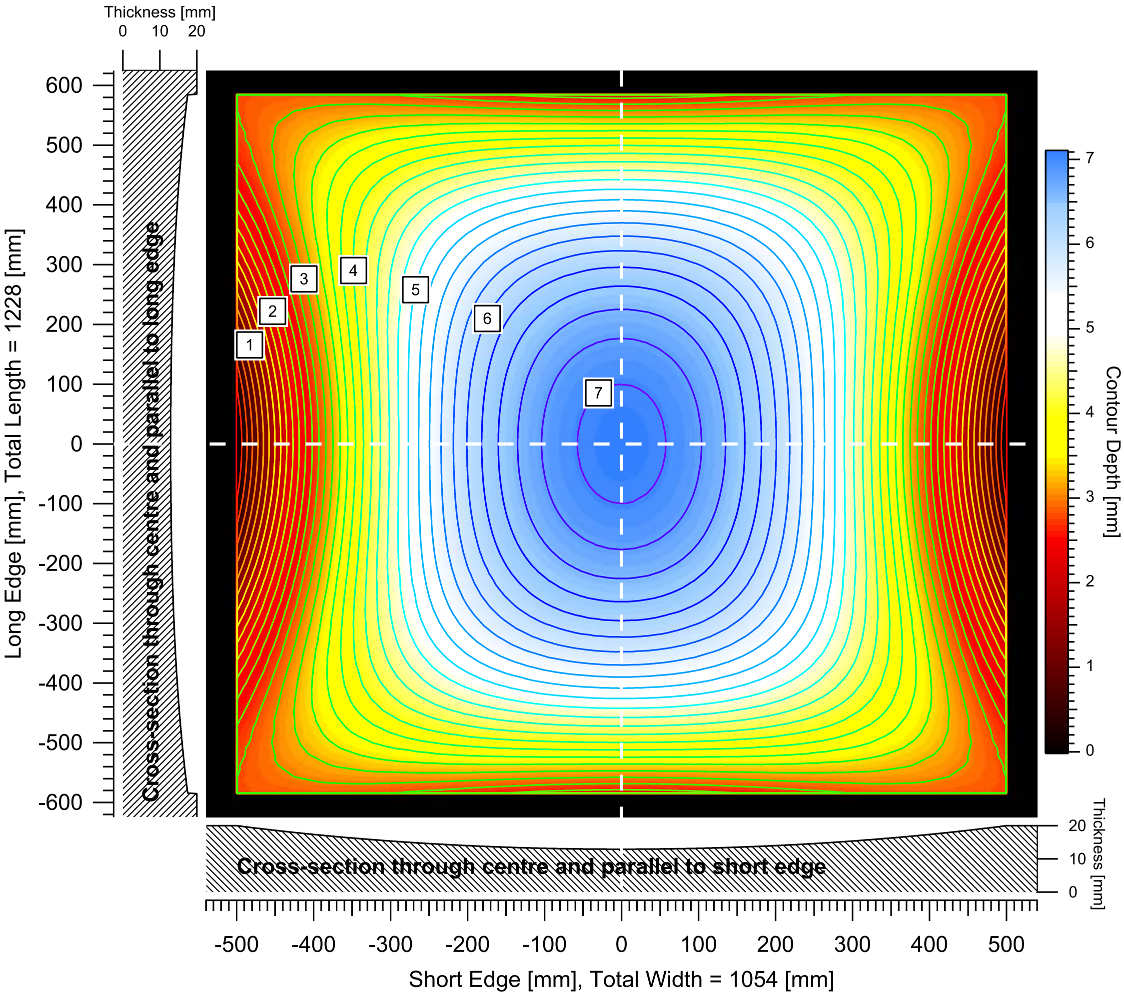

Fig. 7-1: Combined contour-image plot and cross-sections of the shape of the rectangular electrode. Numerical figures in the image denote the depth of the milled profile in [mm]. Contour lines are drawn for every 0.2[mm]. The black strip around the lens indicates a flat border surface, which serves as the seating for the glass substrate.
Total area of electrode visible to plasma: 1054[mm] × 1228[mm]; Total lens area: 1000[mm] × 1168[mm].
The two hatched areas represent cross-sections of the electrode plate (thickness 20[mm]) through the centre of the lens as indicated by the white dashed lines: Once parallel to the long edge (left) and once parallel to the short edge (bottom).

area of strongest vertical gradient. Along the shorter edges (top and bottom) and in the four corner we have an abrupt height discontinuity up to 3[mm]. This discontinuity between the lens surface and the flat border will give rise to a sharp change in the vertical electric field magnitude. The flat border surface supports the glass substrate and is thought to provide a "sealing" to allow a differential pressure between the plasma volume and the lens concavity to suppress plasma below the glass (cf. 4.2.2 and cf. 7.5.3.1).

7.2.2 Applied Lens Aberration

Specified accuracy

The objective of correcting the standing wave for deposition to less than 10% non-uniformity allows some tolerance in the electric field correction in terms of exact shape and machining precision of the lens. A practical estimation is given elsewhere (cf. 6.2.3), which shows that a stepped lens can be sufficient to attain the overall process goal of low non-uniformity for deposition at VHF. For the rectangular lens, a machining precision of ± 0.1[mm] in clamped state (i.e. on the machining fixture) and a residual vertical waviness of ± 25[µm] was specified. On the other hand, it is clear that unwanted influences like mechanical distortion of the support plate and correct positioning of the dielectric plate have to be considered as well.

Sources of aberration

For practical use of the rectangular lens, four principal impairments of the electric field correction can be identified:

a) The fabrication inaccuracy of the lens curvature: This is the same as for the cylindrical case (cf. p.84).
b) A torsion of the shaped metal plate due to internal mechanical stress can occur. This is again the same as for the cylindrical case (cf. p.84).
c) Imperfect contact of the substrate with the electrode can cause an undesired voltage division. In addition a glass substrate sagging under its own weight or under differential pressure can cause a reduction in the effective lens depth. This effect can be minimized by spacer supports (cf. 4.2.2).
d) Thermal expansion during heated operation occurs generally only during deposition processes. The effect can be reduced by appropriate stiffeners' design.

Ideal vs. real shape of lens

The first two cases a) and b) were checked after fabrication of the prototype lens and the results are shown in Fig. 7-2; the last two cases c) and d) were not dealt with in detail. Graph Fig. 7-2-[A] depicts the manufacturing imprecision with the workpiece still clamped on its fixture. We see that the shape is largely close to its ideal form and complies with the specifications, except in the four corner regions where variations are ascertained of up to ca. $0.4[\mathrm{mm}]$. There, slightly too little material was removed because the size of the cutter head does not permit to mill sharp-edged corners. Generally the most probable sources of machining error were determined as: multiple data conversion and the rounding errors involved, or limited memory capacity of CNC machines, programming errors and tool wear.

Graph Fig. 7-2-[B] shows the same workpiece in identical orientation, but with fixing screws released. The right rear and left front corner bend upwards. It is a sign, that internal mechanical stress considerably twists the metal plate of $20[\mathrm{mm}]$ thickness, whose one-sided face is shaped and the other is planar. It is thought that the lens distortion is partly eliminated when the lens is housed by the reactor chassis and braced by the stiffeners.

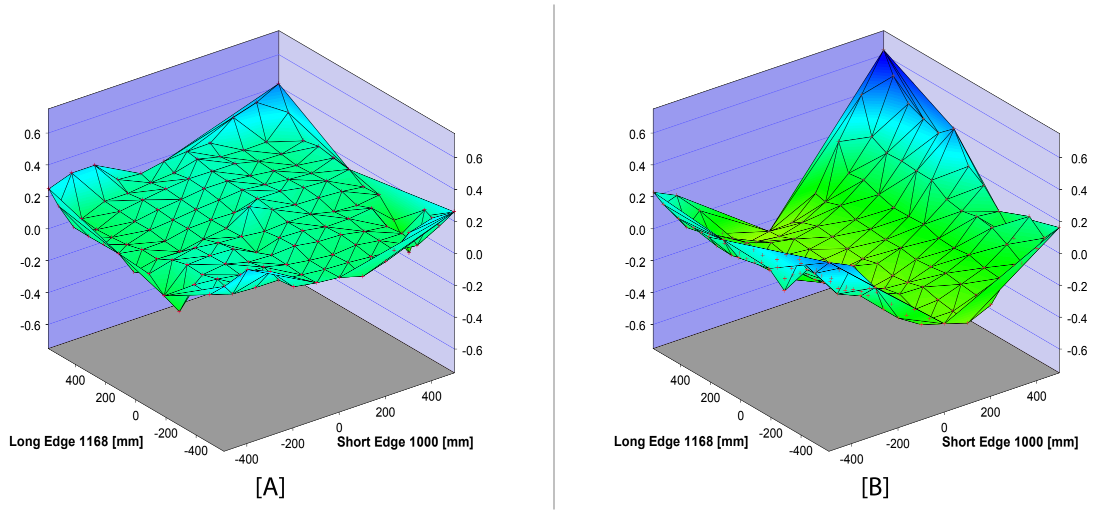

Fig. 7-2: Mechanical lens deviation: [A] Lens in clamped state on machining fixture. [B] Lens in unclamped state. Vertical scale gives the deviation in $[\mathrm{mm}]$ of measured lens depth from specified depth (See Fig. 7-1). Positive values mean that the real shape is too shallow, conversely a negative value indicates a too deep shape. The reference point for calibration for both measurements is the border in the right front corner.

Error assessment

All the above mentioned mechanical flaws were summarily assessed by a simulation. A hypothetical systematic lens error was added to the ideal shape and the non-uniformity of the electric field at the design frequency calculated. The lens error was assumed to grow from left to right from $0[\mathrm{mm}]$ to $+0.5[\mathrm{mm}]$. The calculation revealed that the "corrected" vertical electric field in vacuum would suffer from an absolute non-uniformity error of 1%, which in turn might give rise to 3% - 4% absolute error for deposition processes. It shows that the effect of mechanical shortcomings is rather small and can be neglected for practical purposes.

7.3 Calculated E-Field Non-Uniformity

Numerical modelling only

The theoretical parallel-plate flat-electrode standing-wave non-uniformity figures for the cylindrical reactor (cf. 6.4) are determined by the value of the BESSEL function at the reactor edge, whereas the non-uniformity numbers for the rectangular parallel-plate configuration are obtained by numerical electric field modelling (cf. 3.2.2). For the shaped electrode, the 3-D cylindrical case can be treated analytically, whereas the 3-D rectangular case necessitates numerical calculations. The model for the rectangular reactor takes into account two additional geometrical factors:

(i) a two-dimensional cartesian system with non-constant boundary conditions and
(ii) multiple RF power feedings and their distributed positions on the backside of the suspended top RF electrode.

The above two points are the main distinctions between the cylindrical and rectangular geometries, which account for the calculation of the electric field variation and its correction at VHF due to the standing wave effect.

KAI 1000 architecture

Computed non-uniformity figures for a rectangular parallel-plate reactor of type KAI 1000 are shown in Fig. 7-3. The non-uniformity is calculated by using the lowest/highest value of the electric field up to a distance of 3.8[cm] from the reactor wall. The considered surface covers an area of 1054[mm] by 1228[mm] (cf. Fig. 7-1). The sign of the uniformity is determined as described in section 6.3. Frequencies used are 13.56[MHz], 27.12[MHz], 40.68[MHz], 67.8[MHz], 100[MHz] and 110[MHz].

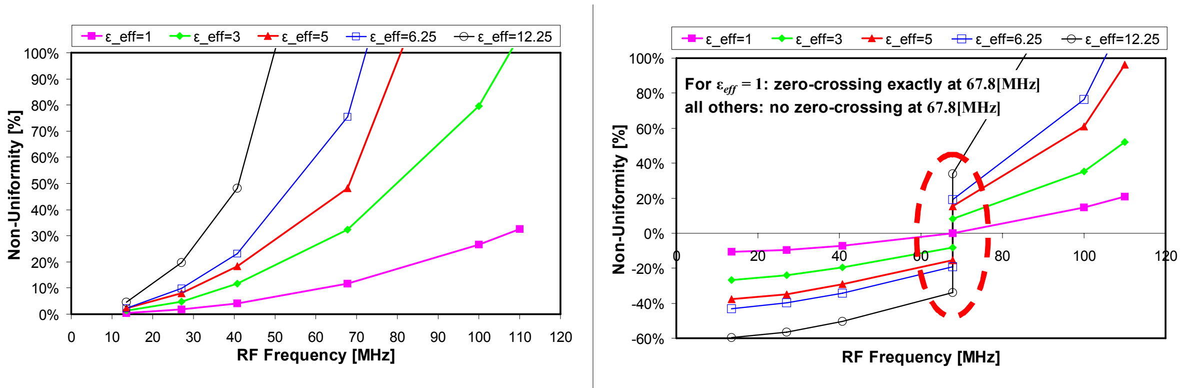

[A] Flat Electrode [B] Lens Shaped Electrode for 67.8[MHz]

Fig. 7-3: Calculated E-field non-uniformity figures for a rectangular reactor of type KAI 1000. RF and grounded electrodes are the same size. [A] plots the case for the standard parallel-plate electrodes. [B] shows the case for a vacuum lens designed for $f_0 = 67.8$[MHz]. Dimensions of the plasma area are given in Fig. 7-1. Numerical figures are given for the frequencies 13.56, 27.12, 40.68, 67.8, 100.0 and 110.0[MHz] respectively and for five different values (1.0, 3.0, 5.0, 6.25, 12.25) of the effective dielectric constant ε_{eff}.

Vacuum and plasma

As for the cylindrical reactor, different cases are considered for each electrode configuration: the vacuum case ($\varepsilon_{eff} = 1$) and in presence of plasma ($\varepsilon_{eff} = 3, 5, 6.25$ and 12.25). The former is to illustrate the behaviour of the electric field under varying frequency and its precise correction by the lens, the latter four cases are to emphasize how the overall uniformity evolves under plasma conditions and its perturbation on the correction mechanism. The values of the last two cases ($\varepsilon_{eff} = 6.25$ and 12.25) correspond to a "wavelength reduction factor" of $\sqrt{\varepsilon_{eff}} = 2.5$

and 3.5 respectively and are chosen for consistency with the modelled power dissipation profiles in section 7.5.

Flat electrode: Similar to cylindrical case

The main findings for the flat electrode (Fig. 7-3-[A]) are the same as for the cylindrical reactor: The non-uniformity rises with the frequency. Likewise the modelling predicts that the presence of plasma makes the standing wave effect even more pronounced. The transition of the effective dielectric constant from $\varepsilon_{eff} = 1$ to $\varepsilon_{eff} = 12.25$ shows clearly that the presence of a dielectric medium in the plasma volume can cause the electric field non-uniformity to exceed the threshold of 10% at 27[MHz] for the size of a KAI 1000 and can become already 50% at 40[MHz]. Thus increasing the RF frequency to the triple harmonic of 13.56[MHz] already requires some sort of correction mechanism in order to keep the non-uniformity for plasma processes reasonably low. The empirical findings corroborate that the overall electric field non-uniformity increases with the frequency (Fig. 7-5) and likewise that plasma non-homogeneity (Fig. 7-18) in the same reactor vessel can produce much stronger values.

Lens: Different boundary conditions

For the lens calculations (Fig. 7-3-[B]), the same electrode size and dielectric conditions are assumed as for the flat case. However calculations are for a vacuum lens for design-frequency $f_0 = 67.8$[MHz] with a 3.8[cm] flat strip at the border of the lens. The graph shows that for the vacuum case ($\varepsilon_{eff} = 1$), the non-uniformity is zero *by design of the vacuum lens* at exactly the design frequency f_0. But this is no longer true for the four conditions at $\varepsilon_{eff} > 1$. Their non-uniformity figures at the design frequency come to ± 8%, ± 15%, ± 19%, ± 33% with increasing ε_{eff} respectively. Their curves have no zero-crossing at the design-frequency as it is indicated by their discontinuity in Fig. 7-3-[B]. This discontinuity is because the profiles can neither be defined as concave nor as convex, in fact they are saddle-like. As Fig. 7-4 below demonstrates, the absolute non-uniformity can only slightly be reduced by varying the frequency in the vicinity of the design frequency. It was found e.g. for $\varepsilon_{eff} = 2.5^2 = 6.25$ that the minimum non-uniformity is at 75.3[MHz] with about 0.5% less non-uniformity than at the vacuum design frequency 67.8[MHz].

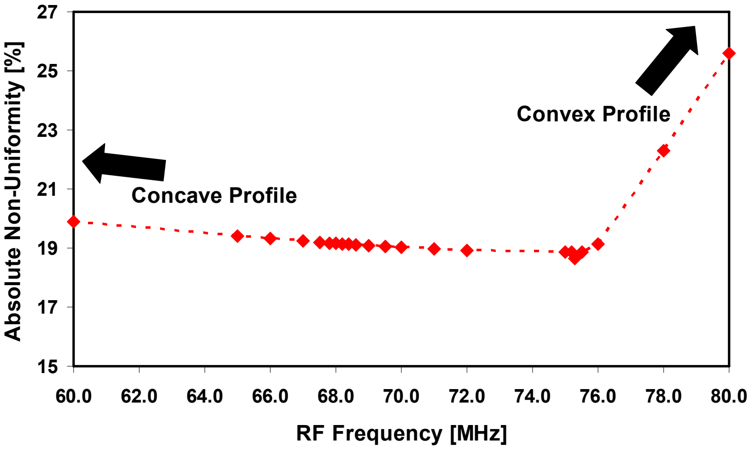

Fig. 7-4: Calculated absolute E-field non-uniformity for a KAI 1000 reactor equipped with a vacuum lens and effective dielectric constant $\varepsilon_{eff} = 2.5^2 = 6.25$ in the frequency range from 60[MHz] to 80[MHz]. Same conditions apply as for Fig. 7-3-[B]

The reason for this behaviour is found in the boundary condition: The RF voltage at the boundary is no longer constant along the edge of the model electrode under variation of the effective dielectric constant ε_{eff} as opposed to the cylindrical case. Because the distance of the circumference of the RF electrode from the RF feeding points is no longer equidistant or symmetric, the plasma effect turns out to be perturbative.

7.4 E-Field Measurements

Matrix scan

This section describes the electric field measurements in a rectangular, parallel-plate reactor of type KAI 1000 with a flat electrode and with a shaped electrode. The same probe as for measurements in the cylindrical reactor was used (See 4.3 and cf. 6.5). In the cylindrical reactor we looked for the vertical component $E_z(r)$ across the diameter, whereas in the rectangular reactor we study the vertical component $E_z(x, y)$ in cartesian space. Measurements were done scanning a matrix of 24×9 points distributed across the electrode. The columns are parallel to the long side and the rows parallel to the short side. Four out of the nine columns are aligned with the columns of the optical plasma intensity detection system (132, 402, 672 and $942[\mathrm{mm}]$). The alignment allows an easier comparison of the electric field measurements with the optical plasma intensity profiles.

Impaired measurement quality

One manual scan of the electric field takes about $30[\mathrm{min}]$ compared to $10[\mathrm{s}]$ for the automated scan of the optical plasma intensity. It is obvious that slow temporal changes in the system like heating, drifting matching conditions and RF source instabilities are more likely to affect the outcome of the electric field measurements than the "snapshot" like characterization of the optical intensity. Typical indications of drifts are tilted or distorted profiles (cf. 7.4.3). In order to minimize such interfering phenomena, the measurement data were re-normalized to a RF voltage measured at a point on the stripline.

The definition and calculation of the non-uniformity number used below is in accordance with section 6.3.

7.4.1 Results for the Flat Electrode

A series of measurements with the flat electrode at different excitation frequencies up to $110[\mathrm{MHz}]$ was conducted. The purpose was to demonstrate the necessity to correct the standing wave at VHF in the rectangular geometry.

Shape of profile

Fig. 7-5 depicts the measured and the modelled electric field profile for the flat electrode. The probe was directly put on the bottom electrode. Only VHF measurements are shown ($70.0[\mathrm{MHz}]$ and $110[\mathrm{MHz}]$); for comparison, the modelled electric field distribution at the standard frequency $13.56[\mathrm{MHz}]$ is given as well. Both measured shapes have in the centre an elevated back from front to back. The flanks of the longer edge descend steeply between the two corners. It is always one of the midpoints of the aforesaid flanks where we discover the minimum of the vertical electrical field. The midpoints of the shorter side behave similarly, but much less strongly. Towards the four corners, the profiles level out. Altogether the electric field distribution forms a "tortoise shell"-like structure.

Frequency effect

Increasing the frequency from $70.0[\mathrm{MHz}]$ to $110[\mathrm{MHz}]$ makes the contour more pronounced. The non-uniformity doubles from 30% to 70% for the experimental profile and triples from 12% to 33% in case of the numerical solutions.

Experimental vs. Modelled

In shape and form, modelling and experiment correspond well. But there is an gross discrepancy of non-uniformity numbers. Primarily it is the tilt of the shape that exaggerates the experimentally obtained non-uniformity numbers as can easily be seen by comparing the percentages per row. The reason for the slant could not be established, the issue is addressed in 7.4.3. Except for their tilted position, the experimental profiles show a fairly good symmetry in column and row direction.

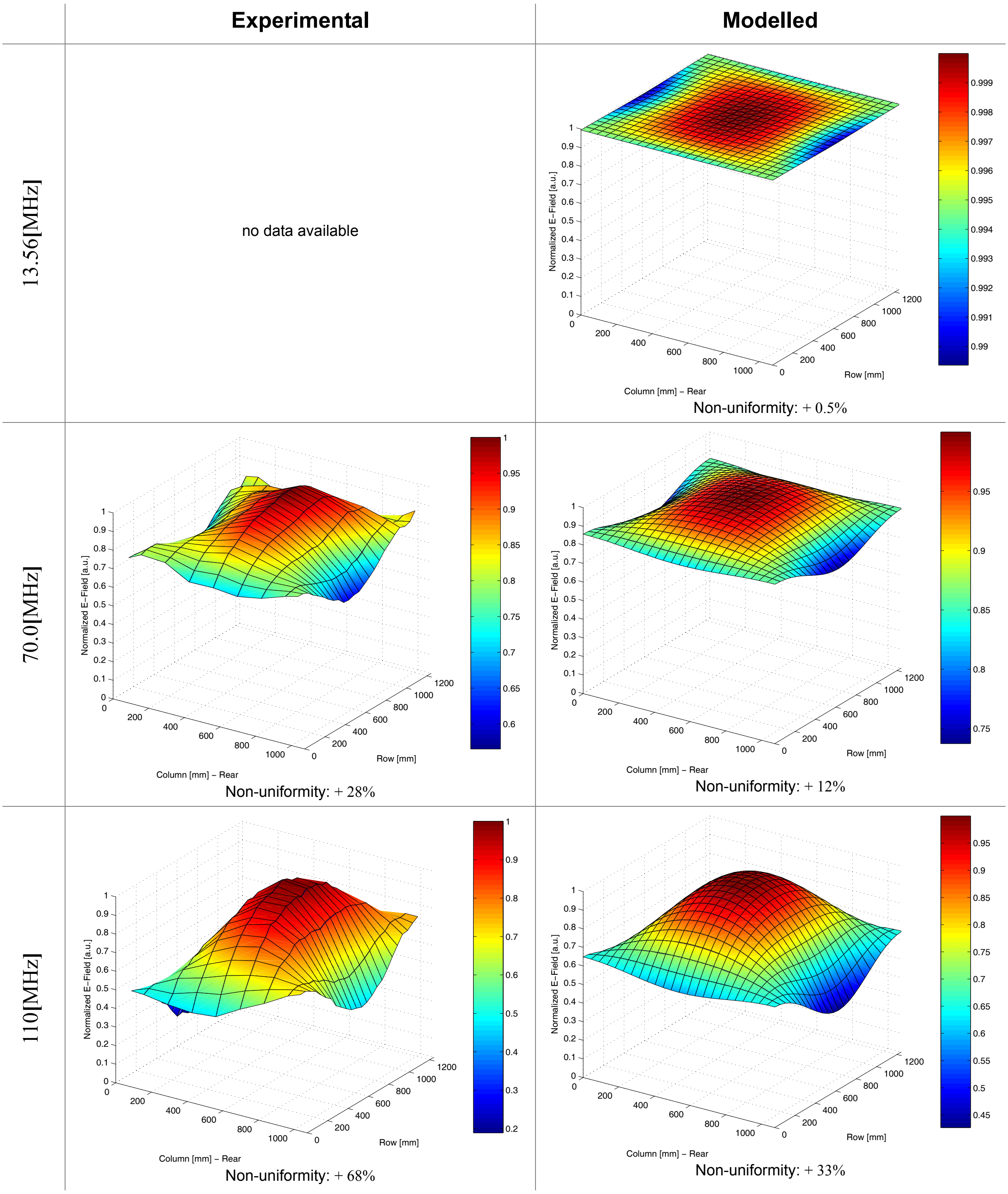

Fig. 7-5: Measured and calculated electric field profiles for a rectangular flat electrode at two VHF RF frequencies as specified in the row heading for 70.0[MHz] and 110[MHz]. For comparison, the modelled electric field profile for the reference frequency 13.56[MHz] is shown as well.
The left column shows the measurements, in the right column are the calculated profiles for comparison. The Z axis denotes the normalized electrical field in arbitrary units with respect to the maximum of the centre region of interest. The mesh points mark the (x, y) position of the measurement and calculation respectively.

7.4.2 Results for the Lens Electrode

Glass substrate

For the measurements, a 3[mm] glass plate was put on the shaped electrode as a gliding support for the probe. In principle the dielectric property of the glass plate has to be considered in the modelling, but its effect cannot be easily integrated into the present model. But as the glass covers almost the entire electrode area, it should not affect too strongly the non-uniformity of the measurement area. In addition we are not interested in absolute values of the electric field, only in the nor-

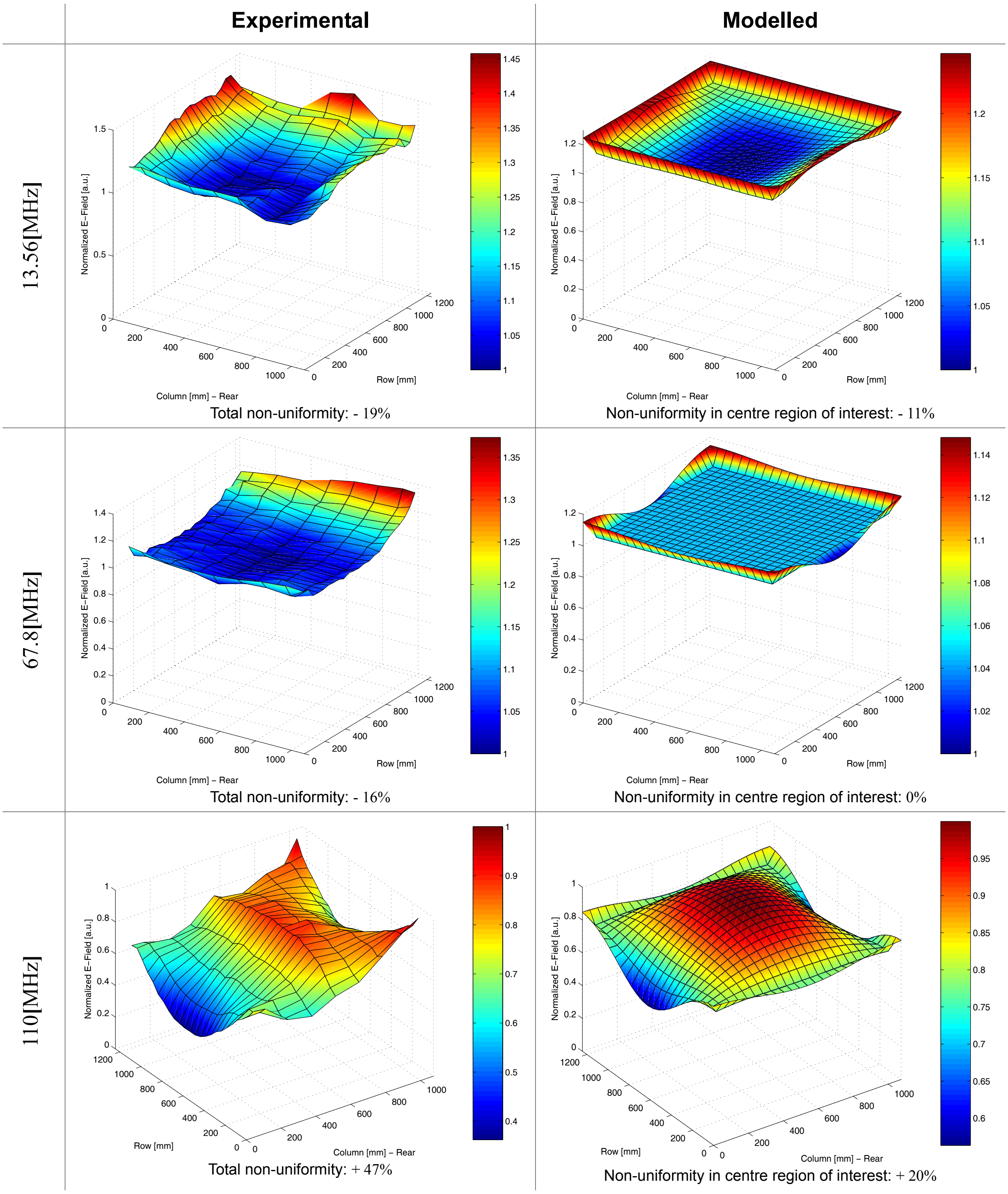

Total non-uniformity: - 19%

Non-uniformity in centre region of interest: - 11%

Total non-uniformity: - 16%

Non-uniformity in centre region of interest: 0%

Total non-uniformity: + 47%

Non-uniformity in centre region of interest: + 20%

Fig. 7-6: Measured and calculated electric field profiles for the rectangular lens electrode shown in Fig. 7-1 with a 3[mm] glass substrate on top. Measurements for three RF frequencies (left column) are compared to their respective modelling (right column). The Z axis denotes the normalized electrical field in arbitrary units with respect to the minimum value (13.56[MHz] and 67.8[MHz]) or the maximum value (110[MHz]) of the centre region of interest. The mesh points mark the (x, y) position of the measurement and calculation respectively. The plots for 110[MHz] are rotated azimuthally 90° in counter-clockwise direction for better view of the shape.

malized profile. Thus the effect of the substrate was regarded as of minor importance.

Measurements and modelling of electric field measurements with the rectangular shaped electrode are compared in Fig. 7-6. The proof of the vacuum lens is established as outlined in Table 3-1 by investigating the electric field variation at different excitation frequencies: At 13.56[MHz] (reference frequency below the design frequency f_0), at 67.8[MHz] (the design frequency f_0) and at 110[MHz] (control frequency above the design frequency f_0).

Below the design frequency f_0

At any RF frequency much less than f_0, the lens acts too strongly, i.e. it overcompensates the electric field. The result should be a depressed, concave shape of the profile over the lens area. Above the electrode's planar border, we expect the electric field to behave differently due to the reduced inter-electrode distance. Where the lens surface touches the margin, we have a smooth transition. There where we have a discontinuity, the electric field is bound to rise sharply by the reduced gap. The experimental result at 13.56[MHz] in Fig. 7-6 confirms the prediction. The overcompensation leads to a concave profile of the vertical electric field $E_z(x, y)$. Perturbing influences near the flat edge contribute to the overall non-uniformity of - 19%.

At the design frequency f_0

When using an excitation frequency in the proximity of the design frequency f_0, the lens ought to compensate almost perfectly for the standing wave RF excess voltage in the centre region. Its effect can best be seen by comparing the middle row of Fig. 7-5 to the middle row of Fig. 7-6. The former bump is suppressed by the application of the shaped electrode. Over the edge strip of the electrode, no correction takes place. Hence we expect a sharp local rise or a gentle transition in $E_z(x, y)$ depending if at the lens circumference we encounter a discontinuity or the lens surface touches the border. The measurements at the design frequency $f_0 = 67.8$[MHz] prove that the absolute non-uniformity number of the electric field profile is distinctly lower with the lens (16%) than without it (ca. 30%). Furthermore, the experimental finding shows that at f_0 the shape is less depressed than at the standard frequency 13.56[MHz] (- 16% vs. - 19%).

Above the design frequency f_0

Above the design frequency, we expect an undercompensation, i.e. the standing wave effect is only partially corrected and a "quasi" standing-wave-like effect should re-emerge. Towards the perimeter of the lens the electric field will rise or fall depending on the lens border transition. Measurements were done approximately 40[MHz] above the design frequency of the lens, which is sufficient for the electrode area of the KAI 1000 to see a standing wave effect to re-appear. Except for the superposed slope of the surface, the measurements reveal the undercompensation of the lens. The shape is similar to a flat electrode case: convex and arched, but less explicit as for 110[MHz] (47% vs. 68%).

7.4.3 Sensitivity of the E-Field Measurements

Some of the electric field measurements presented above show slopes or tilts, e.g. from front to back or left to right, or even a shift in the maximum ("open-door" effect). Some perturbing influences could be identified and removed, others remain not fully explained. Various reasons can be put forward for the these effects:

(i) Unbalanced power feeding by the distributed RF feeding points on the top of the electrode,
(ii) displacement and misalignment of the suspended top electrode,
(iii) drifting matching conditions and non linear voltage probe,
(iv) pick-up of the probe during measurements,
(v) open reactor door and disrupted front shielding.

Open door and countermeasure

The most influential effect has been identified due to an open reactor door. An open door disrupts electrically the grounded housing at the front. It changes the boundary condition at the front side, which is immediately reflected in the electric field profile having its maximum at the door side. The effect is shown in Fig. 7-7. The open door changes the system to an open cavity similar to the one of a RF excited laser slab with unterminated electrodes.[21] The front-back shape becomes cosine-like. The "open-door" effect can be successfully eliminated by using a metal screening sheet with passages for the electric field probe (See Fig. 4-6).

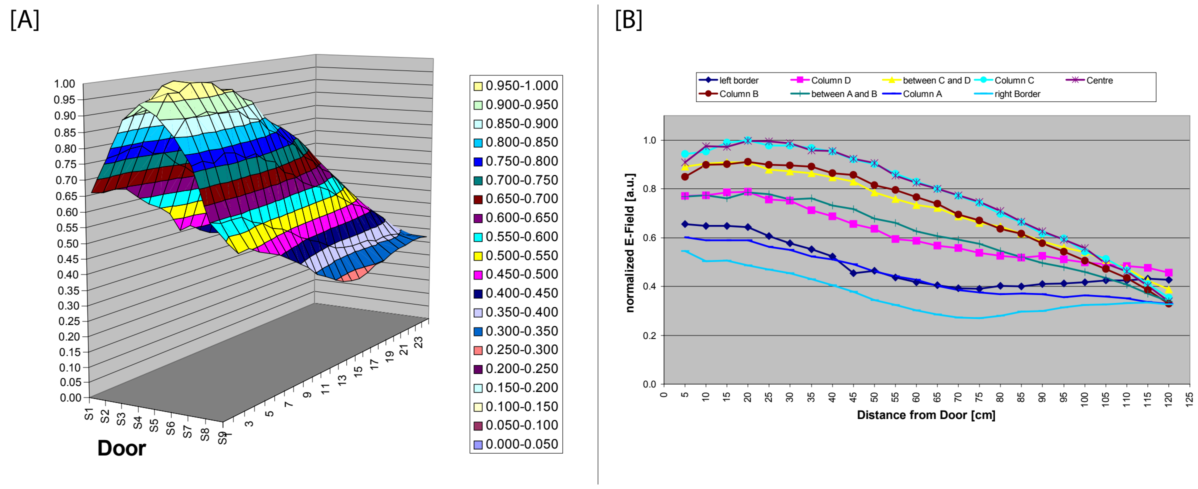

Fig. 7-7: Electric field measurement with open reactor door at $100[\mathrm{MHz}]$. [A] 3D view and [B] Front-back cross section.

Open door and lens

Technically it is important to be aware of it, because a not properly closed door or in general a disrupted grounded housing (e.g. caused by a large viewing port) risks perturbing the boundary condition of the reactor by displacing the maximum of the electric field. A lens as designed herein for a closed door condition expects the maximum in the centre, therefore an “open-door” effect would incapacitate the lens.

7.5 Optical Plasma Intensity Profile Measurements

Line of reasoning

As in the preceding Chapter 6 “Cylindrical Reactor”, the proof of principle for the rectangular lens is split into two parts:

First an extensive investigation of the optical plasma intensity profiles with the standard flat electrode in parallel plate configuration is made (See 7.5.2). The aim is to establish where and when the standing wave effect becomes dominant and to try to quantify the non-uniformity for different types of gases, pressures and RF powers and RF frequencies.

Secondly the same series of measurements are done with the rectangular vacuum lens as used for the electric field measurements (cf. 7.4.2). In this section we shall turn our attention to the change of a initially strongly concave profile at the reference frequency $13.56[\mathrm{MHz}]$ into a more uniform profile at the design frequency $67.8[\mathrm{MHz}]$ (See 7.5.3).

Experimental annotation

The optical plasma intensity profiles are measured by an array of 7×4 optical probes in the bottom electrode (cf. 4.4.2). The corresponding photo current is acquired in a serial scan lasting $\leq 10[\mathrm{s}]$. Compared with this, the electric field profiles were acquired with a much better spatial resolution in a 24×9 matrix, but the scan was done on a much longer time scale (ca. $30[\mathrm{min}]$). On the other hand in the cylindrical reactor we looked at the variation of the optical intensity and the ion saturation current across *one single diameter only* because of the intrinsic symmetry of the cylindrical reactor.

7.5.1 Conventions for Optical Plasma Intensity Profiles

For consistency, all optical measurement plots for all process conditions and hardware configurations are given the same graphical layout. This facilitates the direct comparison of different plasma conditions. Their graphic properties are defined as below:

1. The X- and Y-axis denote the column and row coordinate in $[\mathrm{mm}]$ of the reactor. They are scaled to the area exposed to the plasma ($1054[\mathrm{mm}] \times 1228[\mathrm{mm}]$, cf. Fig. 7-1). Their definition is consistent with the electric field profiles.
2. The Z-axis gives the normalized optical emission intensity with respect to the maximum data point in the 7×4 matrix. It is scaled from 0% to 120% for better view.
3. Mesh points of the black grid of the 3D-shape indicate the positions of the optical detectors in the bottom electrode plate. The total area visible to the optical system is $810[\mathrm{mm}] \times 1030[\mathrm{mm}]$. Column coordinates are $132, 402, 672$ and $942[\mathrm{mm}]$. Row coordinates are $115, 295, 475, 630, 785, 965$ and $1145[\mathrm{mm}]$.

The surface colour of the 3D-shape is always autoscaled to the range of the data points and its value interpolated from the colour map. The colour map extends from white (=maximum) over red, yellow, green, cyan, blue, pink to black (=minimum). The X-Y, X-Z and Y-Z planes contain projections of the 3D-shape in the Z-, Y- and X-direction respectively. Their colour coding is identical to the one for the 3D-shape.

7.5.2 Flat Electrode and Standing Wave Regimes

Motivation

The rectangular plasma is more complicated than the one in the cylindrical reactor, and other phenomena appear. This is why the plasma parameters of the flat configuration are explored more exhaustively here. This detailed investigation is necessary in order to clarify two points: How does the plasma non-uniformity behave under an increase of the RF excitation frequency and where are the SWE and non-SWE dominated regimes. It is decisive to know for the second stage of the proof, in which regime the standing wave effect becomes the most important one among all others. We must be able to delimit the valid process windows for the application of the rectangular case since the lens can work properly and show its effectiveness only with respect to the SWE.

Reference measurements

Reference measurements on the industrial reactor from the HF- to the VHF-region were done using the standard parallel plate setup. Available frequencies were 13.56[MHz], 27.12[MHz], 40.68[MHz], 67.8[MHz] and 100[MHz]. Their profiles were acquired and analysed for the visibility of the standing wave effect. The theoretical modelled power dissipation profiles for two worsening factors $\Re(\sqrt{\varepsilon_{eff}}) = 2.5$ and 3.5 (Fig. 7-8, Fig. 7-10, Fig. 7-12, Fig. 7-14) are shown before some detailed intensity profile measurements for selected process conditions at each frequency are given (Fig. 7-9, Fig. 7-11, Fig. 7-13, Fig. 7-15, Fig. 7-16). The profiles shown cover wherever possible two orders of magnitude of process pressure (25[mTorr] to 2000[mTorr]). Two gas compositions are used: one atomic gas (100% Ar) and one molecular gas diluted with argon (Ar : H_2 = 2 : 1). The profiles were selected to illustrate best when the standing wave effect becomes visible and dominant. Each of the four important frequencies (13.56[MHz] to 67.8[MHz]) are consecutively presented in the following four subsections. Each is introduced with the expected modelled SWE subject to two wavelength reduction factors. In advance it can be stated that the measurements prove, as predicted, that non-uniformity increases from less than 10% at 13.56[MHz] to 100% at 67.8[MHz] (in the pressure range of 500[mTorr] to 2000[mTorr]) due to the standing wave effect and the contraction of the wavelength in a effective plasma dielectric.

100[MHz] plasma

The 100[MHz] profiles in Fig. 7-16 had to be singled out from the standing wave analysis because the standing wave could not be shown, in contradiction to the theory. They are treated in a special section (7.5.2.5).

7.5.2.1 13.56[MHz]

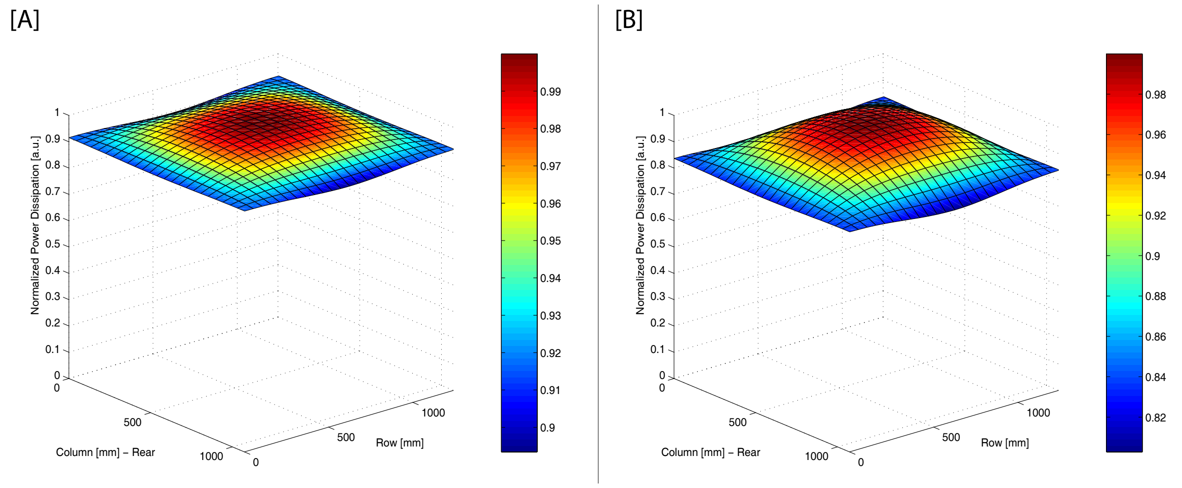

Fig. 7-8: Modelled power dissipation at 13.56[MHz] for two different wavelength reduction factors $\Re(\sqrt{\varepsilon_{eff}})$:
[A] $\Re(\sqrt{\varepsilon_{eff}}) = 2.5 \quad \Rightarrow \quad \lambda' / 4L \approx 1.4$, Non-uniformity + 6%,
[B] $\Re(\sqrt{\varepsilon_{eff}}) = 3.5 \quad \Rightarrow \quad \lambda' / 4L \approx 0.99$, Non-uniformity + 11%.
The Z axis denotes the normalized dissipated power with respect to the centre value.

Expected SWE in vacuum

A noticeable voltage non-uniformity due to the SWE and point like electrical connections appears when the electrode dimensions are comparable to $\lambda_0 / 4$, where λ_0 denotes the vacuum wavelength.[4] In our case at 13.56[MHz], the wavelength in vacuum is $\lambda_{13.56[\mathrm{MHz}]} = 22.1[\mathrm{m}]$ and comparing the quarter wavelength to the reactor diagonal of $L = 1.6[\mathrm{m}]$ gives a large ratio of ≈ 3.5. This is why in vacuum at this frequency the SWE hardly matters and only by colour coding in Fig. 7-5 (top row) we are able to make out the SWE-caused curvature in the calculated electric field profile.

Expected SWE with plasma

In a dielectric medium however the wavelength is contracted according to $\lambda' = \lambda_0 / \sqrt{\varepsilon_{eff}}$ and $\lambda' / 4$ becomes comparable to the reactor dimensions. Assuming a plasma with a wavelength reduction factor $\Re(\sqrt{\varepsilon_{eff}}) = 2.5$, it is convenient to compare $\lambda_0 / 10$ with the typical reactor dimension L, for $\Re(\sqrt{\varepsilon_{eff}}) = 3.5$ we set $\lambda_0 / 14$ against L. $\lambda_{13.56[\mathrm{MHz}]} / 10$ is 1.4 times the reactor diagonal. That is to say we are about to see the SWE in the electric field non-uniformity, but as $\lambda' > L$ it is not critical yet. At $\Re(\sqrt{\varepsilon_{eff}}) = 3.5$, $\lambda_{13.56[\mathrm{MHz}]} / 14$ amounts already to 0.99 of L and the SWE should becomes more visible in the electric field distribution.

SWE and power dissipation

For plasma uniformity considerations we have to take into account that the optical plasma intensity is roughly proportional to the power dissipation which is in turn proportional to the square of the voltage amplitude seen by the plasma. Fig. 7-8 shows two cases of calculated power dissipation for the discussed values of the wavelength reduction factor $\Re(\sqrt{\varepsilon_{eff}}) = 2.5$ ([A]) and $\Re(\sqrt{\varepsilon_{eff}}) = 3.5$ ([B]). The modelling shows that an increase in $\Re(\sqrt{\varepsilon_{eff}})$ results in an increase, also called a "worsening" of the non-uniformity. These two models compare well with the argon measurements at 500[mTorr] and 2000[mTorr] in Fig. 7-9.

Process conditions

Fig. 7-9 presents a selection of measured profiles at 13.56[MHz]. The process pressure extends over two orders of magnitude from 25[mTorr] to 2000[mTorr]. The profiles were acquired at a RF power of 400[W] measured after the matching unit. Two gas compositions ares used: Purely atomic (100% Ar) and a molecular gas (H_2) diluted with argon (gas flow ratio Ar : H_2 = 2 : 1).

Profile regimes

In contrast to the purely electromagnetic SWE, which stipulates only a single convex profile type, the measurements reveal more than one shape type. The acquired profiles at 13.56[MHz] fall into three categories:

(i) Edge dominated regimes up to 250[mTorr] with a negative non-uniformity,
(ii) centre-area dominated profiles starting from 500[mTorr] with a positive non-uniformity and
(iii) well-balanced profiles in the transition zone.

Below 250[mTorr] the strongest plasma intensity is always seen by the outermost optical detectors. Above 500[mTorr] the maximum moves to the centre region which is a sign of the SWE becoming prevalent. Compared to higher RF frequencies later, at 13.56[MHz] the SWE is not very pronounced yet. In the transition zone of both regimes at intermediate pressures, well-balanced uniformities without a clear tendency to either direction are possible. (e.g. Ar : H_2 = 2 : 1 at 500[mTorr] and 400[W] in Fig. 7-9).

Atomic vs. molecular gas

From the right column of Fig. 7-9 we learn that the most evident effect of H_2 addition is to reduce the overall non-uniformity. Argon tends to show more edge-effects in the lower pressure regime and stresses the standing wave at higher pressure, whereas hydrogen shows less edge effect at low pressure and at high pressure a rather well-balanced non-uniformity. This may be related to different cross-sections of atomic and molecular gases, different electron densities and different mean free paths for ionization, electronic excitation and molecular ro-vibrational excitation processes. In pure argon, low energy electrons will drift further; while with a molecular gas, more losses due to inelastic collision cross-sections at low electron energy can occur.

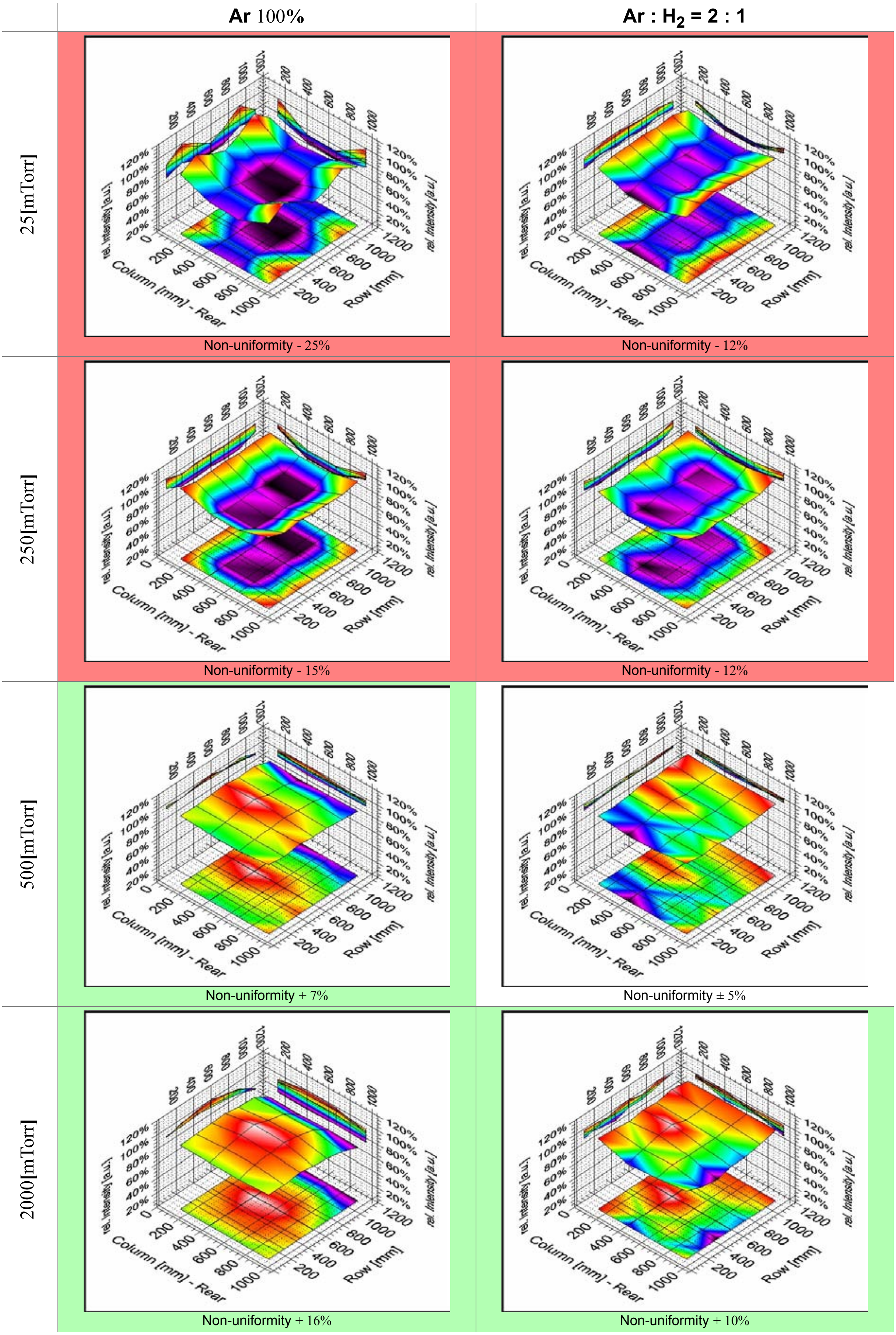

Non-uniformity - 25%

Non-uniformity - 12%

Non-uniformity - 15%

Non-uniformity - 12%

Non-uniformity + 7%

Non-uniformity ± 5%

Non-uniformity + 16%

Non-uniformity + 10%

Fig. 7-9: Selected intensity profiles in parallel plate, flat electrode configuration at 13.56[MHz]. Two gases are used: Ar 100% (left column) and Ar : H2 = 2 : 1 (right column). Pressure scan for constant RF power measured after the impedance matching network. ($P_{delivered}$ = 400[W]). Red underlaid profiles are edge dominated and not suitable for correction by the lens, green underlaid profiles are predominantly standing wave dominated.

7.5.2.2 27.12[MHz]

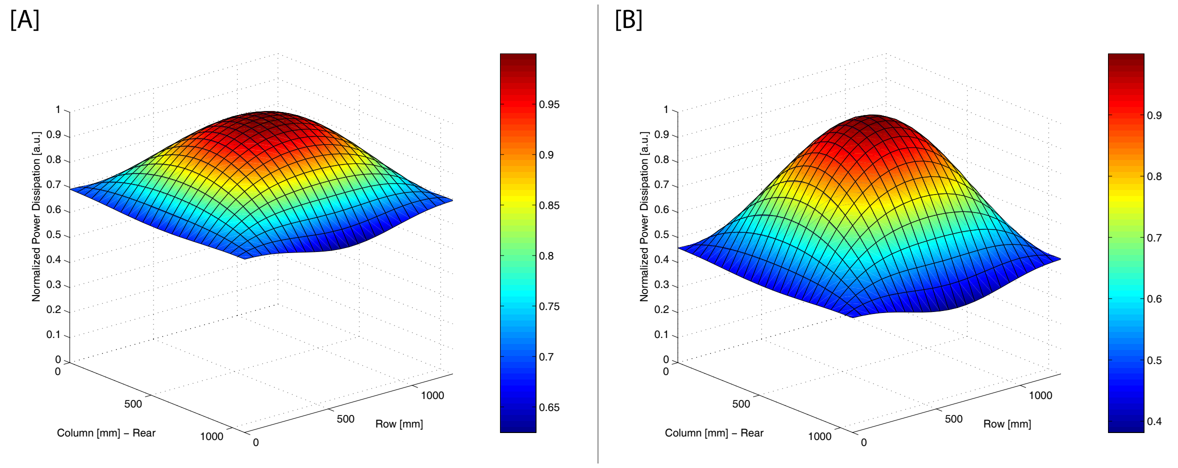

Fig. 7-10: Modelled power dissipation at 27.12[MHz] for two different wavelength reduction factors $\Re(\sqrt{\varepsilon_{eff}})$:
[A] $\Re(\sqrt{\varepsilon_{eff}}) = 2.5 \quad \Rightarrow \quad \lambda' / 4L \approx 0.7$, Non-uniformity + 23%,
[B] $\Re(\sqrt{\varepsilon_{eff}}) = 3.5 \quad \Rightarrow \quad \lambda' / 4L \approx 0.5$, Non-uniformity + 45%.
Notation and conventions same as in section 7.5.2.1 and Fig. 7-8.

Expected SWE

In vacuum $\lambda_{27.12[\mathrm{MHz}]} = 11.05[\mathrm{m}]$, and its quarter wavelength is ≈ 1.7 times the reactor diagonal $L = 1.6[\mathrm{m}]$. With plasma however, $\lambda' / 4L$ is already noticeably below 1.0 (see Fig. 7-10, [A] and [B]) and as we expect, the SWE becomes clearly visible in these measurements.

Process conditions

The 27.12[MHz] profiles in Fig. 7-11 cover the same process conditions as the 13.56[MHz] profiles: two orders of magnitude of process pressure from 25[mTorr] to 2000[mTorr] for constant RF power of 400[W] measured after the matching unit. Two gas compositions ares used: Purely atomic (100% Ar) and a molecular gas (H_2) diluted with argon (gas flow ratio Ar : H_2 = 2 : 1).

Profile regimes

The measurements fall again into three categories:

(i) Edge dominated regimes up to 100[mTorr] with a negative non-uniformity,
(ii) centre-area dominated profiles starting to appear from 250[mTorr] with a positive non-uniformity and
(iii) well-balanced profiles in a transitional zone where the non-uniformity may be better than ± 10%.

Below 250[mTorr] the strongest plasma intensity is always seen by the outermost optical detectors. Such non-uniformities cannot be corrected by the lens electrode. In argon at 25[mTorr] the edge effect is concentrated on the two border midpoints of the long edge. Above 250[mTorr] the maximum moves to the centre region which is a clear sign of the SWE becoming prevalent. Compared to 13.56[MHz], the SWE has become better recognizable. The non-uniformity worsens for constant power with increased pressure. At high pressure, much more RF power is needed to sustain a regular discharge over the whole area. In the transition zone of both regimes, well-balanced uniformities without a clear tendency to either direction are again detected (e.g. Ar : H_2 = 2 : 1 at 250[mTorr] and 400[W] in Fig. 7-11).

Atomic vs. molecular gas

At pressures up to 500[mTorr], H_2 addition tends to blur non-uniformities, in consistency with the observation at 13.56[MHz]. But at 1000[mTorr] and higher, the opposite effect is observed. It can be best seen in the corresponding graph of Fig. 7-18. This is attributed to higher wavelength reduction factors $\Re(\sqrt{\varepsilon_{eff}})$ in presence of hydrogen (See Table 6-1 in section 6.6.4) and a better dissipation of RF power.

Ar 100% | **Ar : H_2 = 2 : 1**

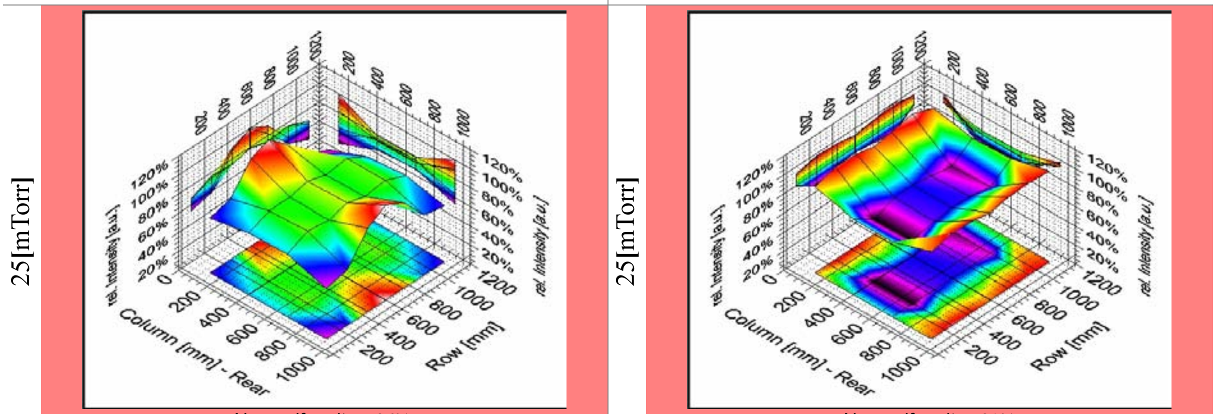

Non-uniformity ± 36%,
other effects superimpose the standing wave

Non-uniformity - 21%

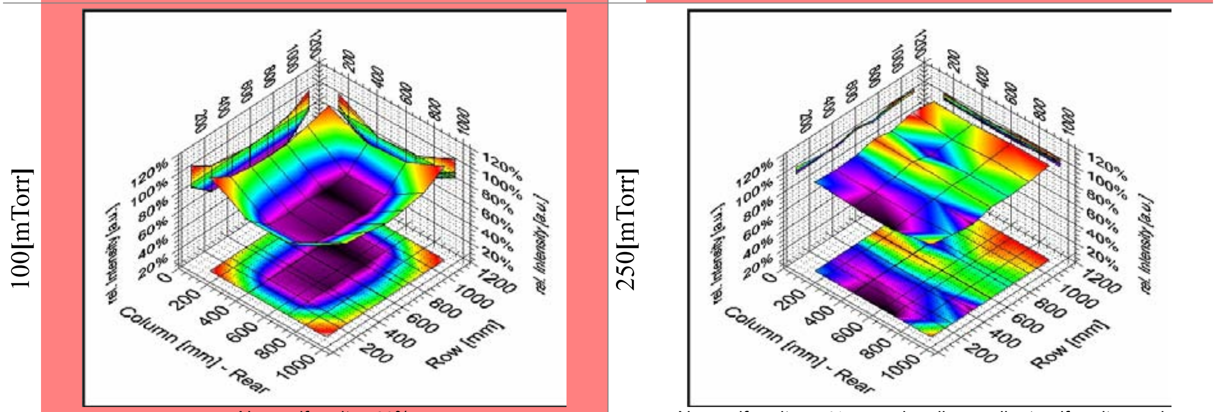

Non-uniformity - 30%

Non-uniformity ± 5%, occasionally excellent uniformity can be reached by process tuning.

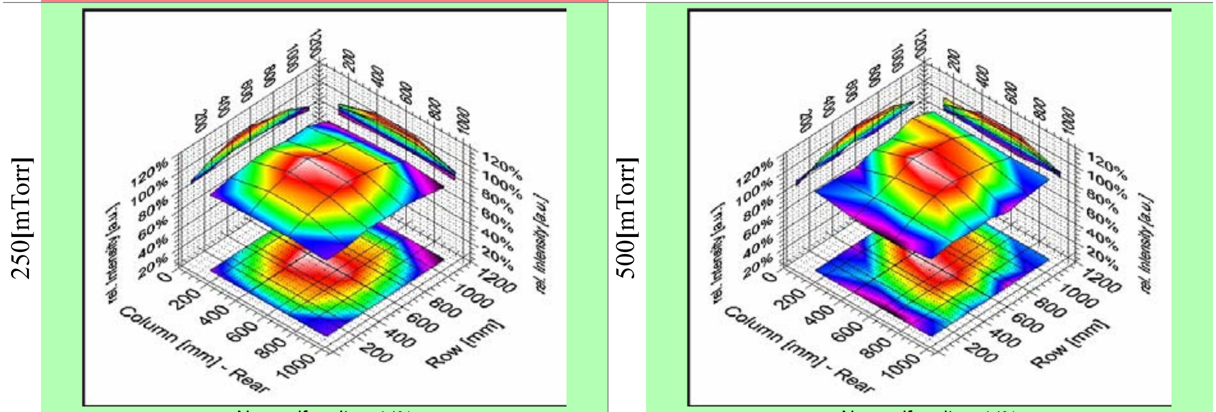

Non-uniformity + 14%

Non-uniformity + 14%

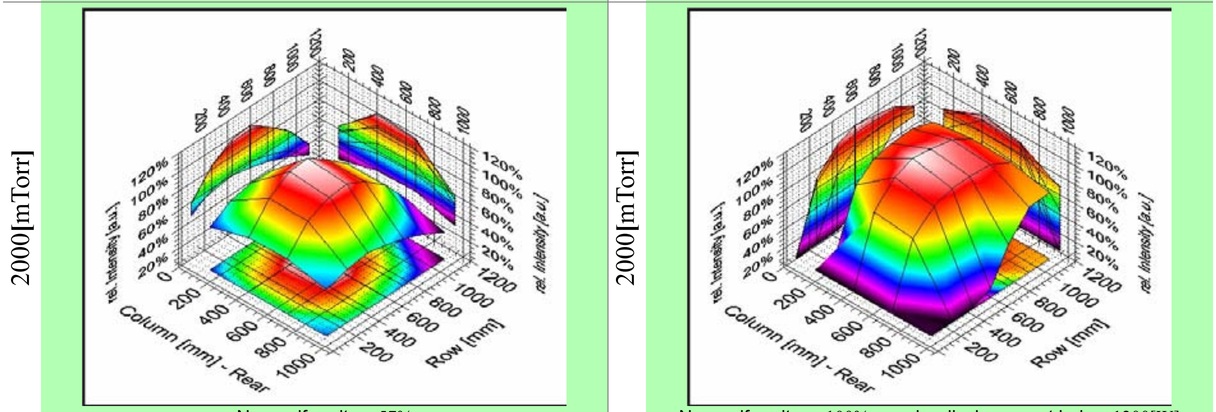

Non-uniformity + 57%

Non-uniformity: + 100%, regular discharge not below 1200[W]

Fig. 7-11: Selected profiles in parallel plate, flat electrode configuration at 27.12[MHz]. Two gases are used: Ar 100% (left column) and Ar : H2 = 2 : 1 (right column), Pressure scan for constant RF power measured after the impedance matching network. ($P_{delivered}$ = 400[W]) unless otherwise specified. Red underlaid profiles are edge dominated and not suitable for correction by the lens, green underlaid profiles are predominantly standing wave dominated.

7.5.2.3 40.68[MHz]

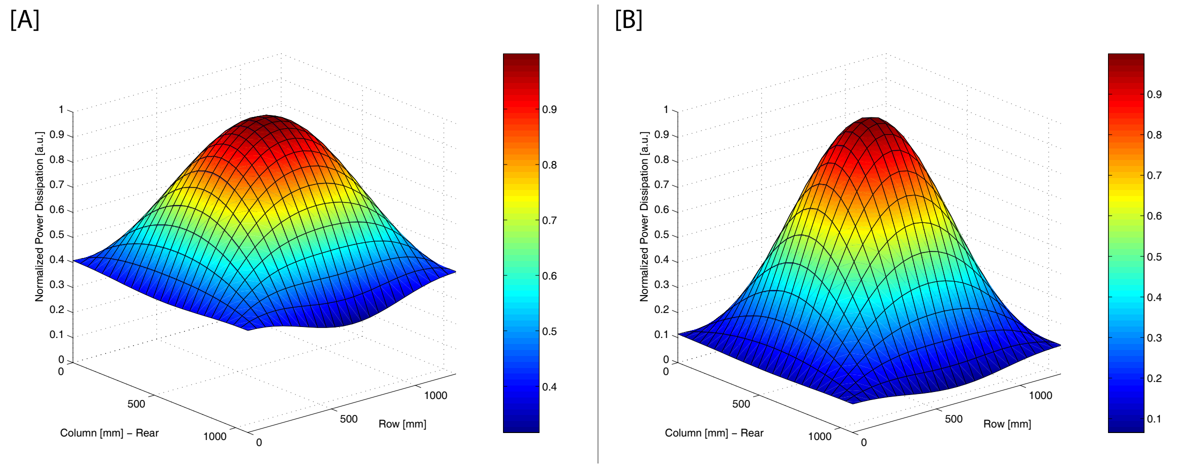

Fig. 7-12: Modelled power dissipation at 40.68[MHz] for two different wavelength reduction factors $\Re(\sqrt{\varepsilon_{eff}})$:
[A] $\Re(\sqrt{\varepsilon_{eff}}) = 2.5 \Rightarrow \lambda' / 4L \approx 0.46$, Non-uniformity + 52%,
[B] $\Re(\sqrt{\varepsilon_{eff}}) = 3.5 \Rightarrow \lambda' / 4L \approx 0.33$, Non-uniformity + 88%.
Notation and conventions same as in section 7.5.2.1 and Fig. 7-8.

Expected SWE

In vacuum $\lambda_{40.68[MHz]} = 7.4[m]$, and $\lambda_{40.68[MHz]} / 4$ is already close (≈ 1.15) to the reactor diagonal $L = 1.6[m]$. The reduced quarter wavelength drops in the modelling to 0.46 and 0.33 of the reactor diagonal. These values suggest that the profiles at higher pressure will indicate sharp falling light intensity gradients going from the centre to the periphery.

Process conditions

The 40.68[MHz] profiles in Fig. 7-13 cover two orders of magnitude of process pressure from 25[mTorr] to 2000[mTorr]. Two gas compositions ares used as before.

Profile regimes: predominantly SWE

The empirical findings in Fig. 7-13 largely corroborate the modelling. The acquired profiles are predominantly SWE formed. With pure argon, at low power (200[W]) SWE-only profiles were measured across the whole pressure range (cf. Fig. 7-18). But an increase of the delivered RF power at low pressure can ignite corner and edge plasma, e. g. at 50[mTorr], 600[W] lateral humps reappeared as in 27.12[MHz]. Process conditions with added H_2 showed only SWE dominated profiles.

Atomic vs. molecular gas

As seen from the right column of the table of profiles in Fig. 7-13, the most evident effect of H_2 addition is to render the surface shapes smoother and rounder.

Ar 100%

25[mTorr]

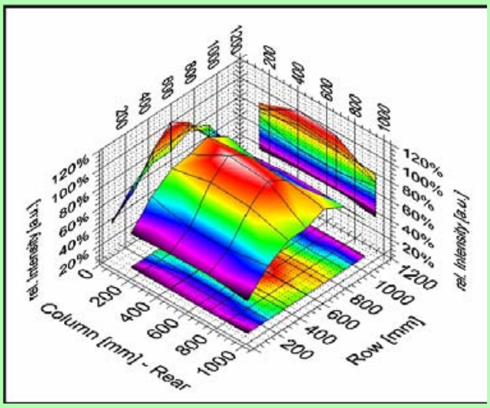

Non-uniformity + 50%

50[mTorr]

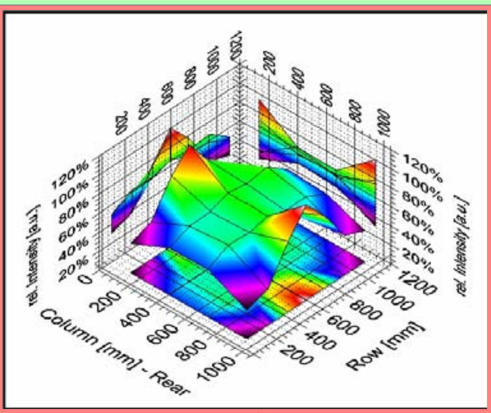

600[W], Non-uniformity ± 53%,
other effects superimpose the standing wave

100[mTorr]

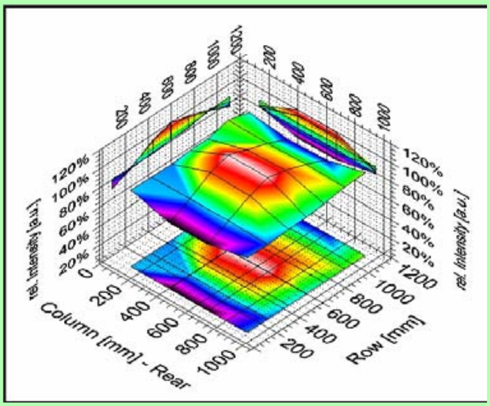

Non-uniformity + 18%

2000[mTorr]

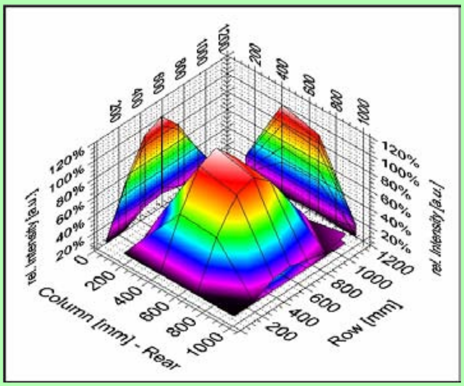

1000[W], Non-uniformity + 100%
much more power is needed to improve regularity and make the plasma touch the walls

Ar : H_2 = 2 : 1

25[mTorr]

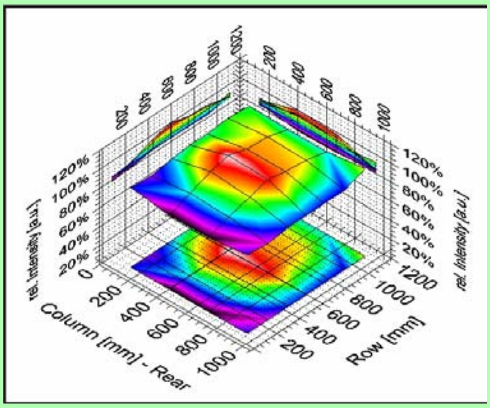

Non-uniformity + 12%

100[mTorr]

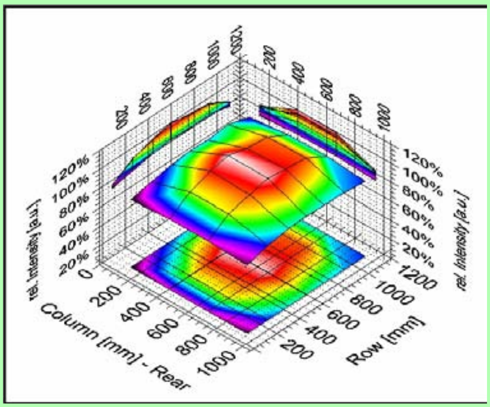

Non-uniformity + 17%

500[mTorr]

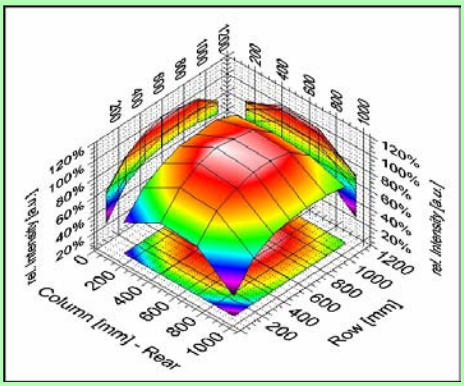

Non-uniformity + 64%, at least 600[W] are necessary to maintain an extensive, stable discharge

1000[mTorr]

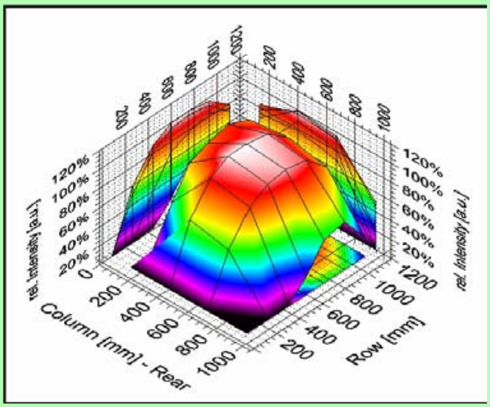

1000[mTorr], 1000[W], Non-uniformity + 100%

Fig. 7-13: Selected profiles in parallel plate, flat electrode configuration at 40.68[MHz]. Two gases are used: Ar 100% (left column) and Ar : H2 = 2 : 1 (right column), Pressure scan for constant RF power measured after the impedance matching network. ($P_{delivered}$ = 200[W]) unless otherwise specified.Red underlaid profiles are edge dominated and not suitable for correction by the lens, green underlaid profiles are predominantly standing wave dominated.

7.5.2.4 67.8[MHz]

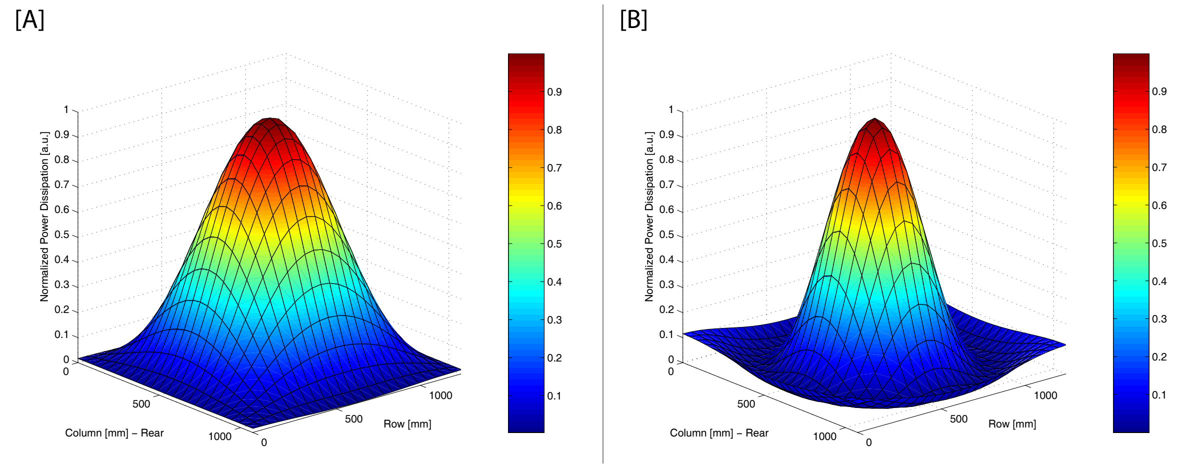

Fig. 7-14: Modelled power dissipation at 67.8[MHz] for two different wavelength reduction factors $\Re(\sqrt{\varepsilon_{eff}})$:
[A] $\Re(\sqrt{\varepsilon_{eff}}) = 2.5 \quad \Rightarrow \quad \lambda' / 4L \approx 0.3$, Non-uniformity $+ 100\%$,
[B] $\Re(\sqrt{\varepsilon_{eff}}) = 3.5 \quad \Rightarrow \quad \lambda' / 4L \approx 0.2$, Non-uniformity $+ 100\%$.
Notation and conventions same as in section 7.5.2.1 and Fig. 7-8.

Expected SWE

At 67.8[MHz], the quarter vacuum wavelength is only ≈ 0.7 of the reactor diagonal $L = 1.6$[m] (vacuum wavelength $\lambda_{67.8[\mathrm{MHz}]} = 4.4$[m]). In presence of plasma, assuming $\Re(\sqrt{\varepsilon_{eff}}) = 2.5$ and 3.5, the reduced quarter wavelength shrinks to 0.3 and 0.2. As a result the first node ($E = 0$) exists inside the reactor. For the bigger wavelength reduction factor this means even, that the modelling predicts a re-increase of the local dissipated power after traversing the first minimum.

Process conditions

The 67.8[MHz] profiles in Fig. 7-15 cover two orders of magnitude of process pressure from 25[mTorr] to 2000[mTorr]. Two gas compositions ares used as before.

Only SWE profiles for all gases

At 67.8[MHz], only SWE-like profile types were observed for purely atomic and molecular gases alike. As seen from the right column of the table of profiles in Fig. 7-15, the most evident effect of H_2 addition is to remove the corner plasmas. Argon tends to show more edge-effects in the whole pressure range. The strong corner plasma for conditions where the first minimum is visible is probably some combined effect of the telegraph effect, fringing fields and the nonlinear plasma reaction and parasitic discharges igniting above the electrode between the capacitive voltage dividers which propagate into the active plasma volume. These parasitic plasmas above the electrode have been observed frequently at this frequency.

	Ar 100%	**Ar : H_2 = 2 : 1**
25[mTorr]	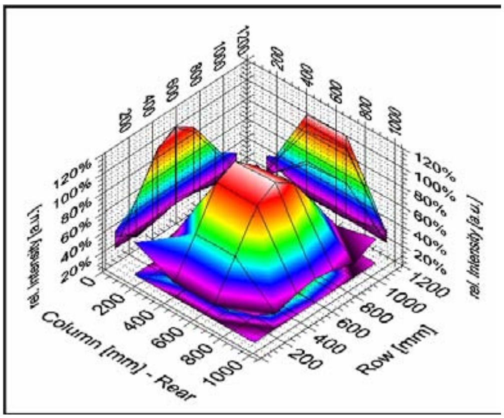 Non-uniformity + 80%	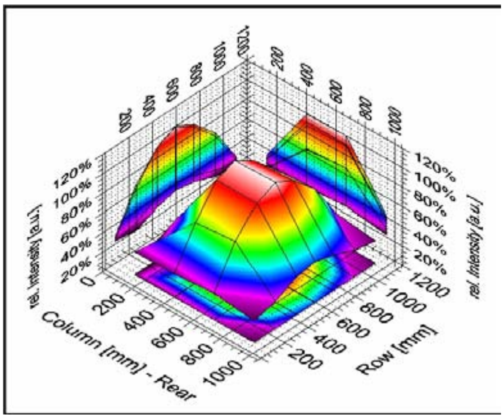 Non-uniformity + 70%
250[mTorr]	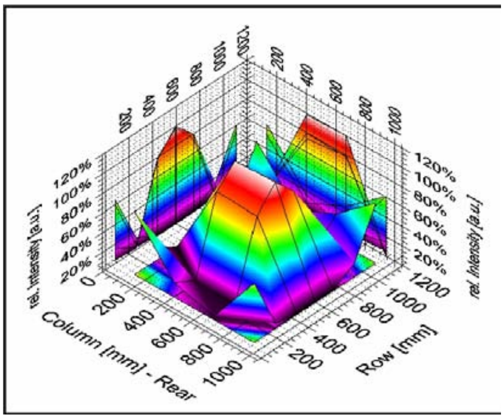 Non-uniformity + 100%	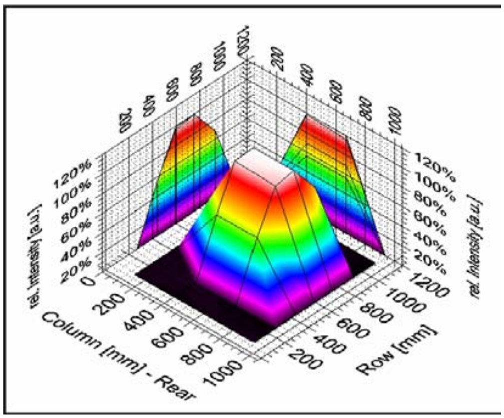 Non-uniformity: + 100%
500[mTorr]	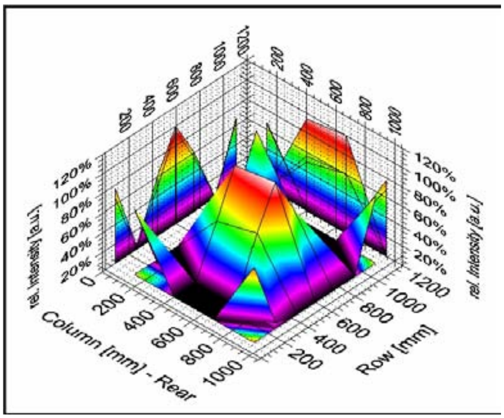 Non-uniformity + 100%	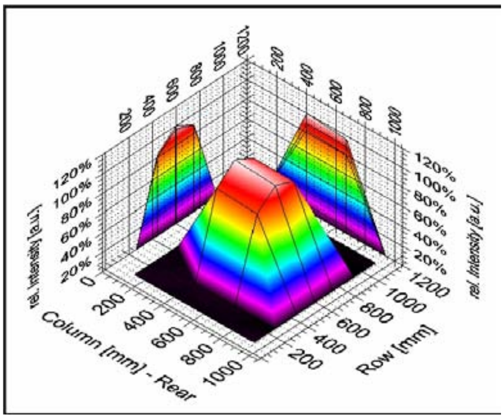 400[W], Non-uniformity + 100%
2000[mTorr]	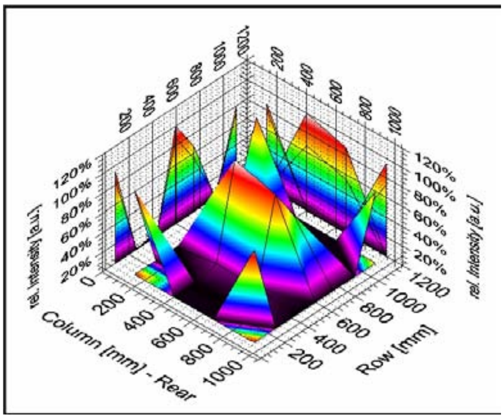 300[W], Non-uniformity + 100%	No data available.

Fig. 7-15: Selected profiles in parallel plate, flat electrode configuration at 67.8[MHz]. Two gases are used: Ar 100% (left column) and Ar : H2 = 2 : 1 (right column), Pressure scan for constant RF power measured after the impedance matching network. ($P_{delivered}$ = 200[W]) unless otherwise specified.

7.5.2.5 100[MHz]

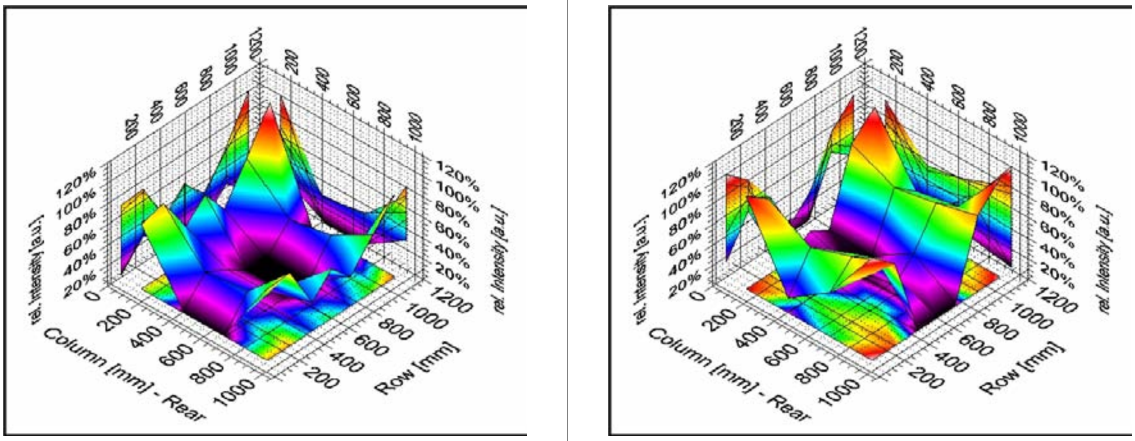
100% **Argon** | **Ar : H_2 = 2 : 1**

250[mTorr], 500[W], intensity “hole” in the centre region

100[mTorr], 400[W], intensity “hole” in the centre region

Fig. 7-16: Selected measured optical plasma intensity profiles at 100[MHz].

Expected SWE

At 100[MHz], the quarter vacuum wavelength is already half the reactor diagonal (vacuum wavelength $\lambda_{100.0[\mathrm{MHz}]} = 3.0[\mathrm{m}]$). We should see an even stronger SWE.

Experiment

However the experiments show no visible peak in the centre. On the contrary a “black hole” opens up in the middle where the standing wave effect would predict a higher voltage and thus a maximum of the optical light intensity. We have clearly seen the expected electric field SWE profiles at 110[MHz] (7.4.1), but why not with plasma? At first sight, the plasma seems to be dominated by parasitic discharges in the small gaps at the edges of the top electrode, which do not penetrate into the centre region. We make an attempt to explain this phenomenon based on PASCHEN breakdown and sustaining voltages (Fig. 7-17): The RF voltage is higher at the centre gap (due to standing wave), but this voltage is still too low to sustain a plasma for this gap length. Breakdown can occur in a small edge gap even if the voltage is smaller.

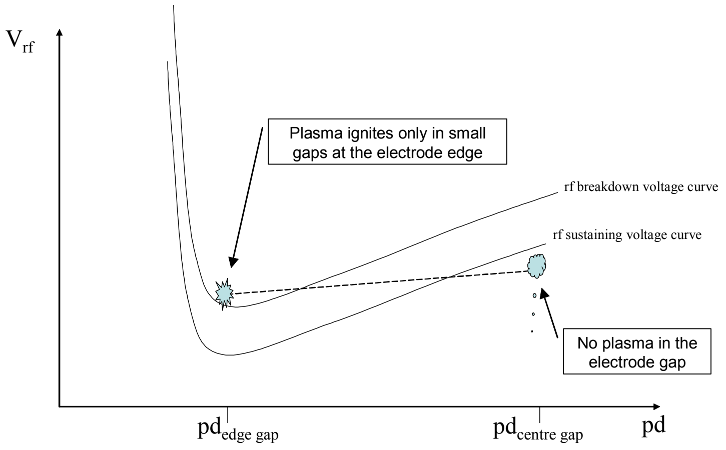

Fig. 7-17: RF sustaining voltage vs. RF breakdown voltage for the case when the RF voltage is sufficient to ignite a plasma at the edge but not enough to sustain a plasma in the centre region.

7.5.2.6 Summary of the Uniformity Measurements with Parallel Plate

13.56[MHz]

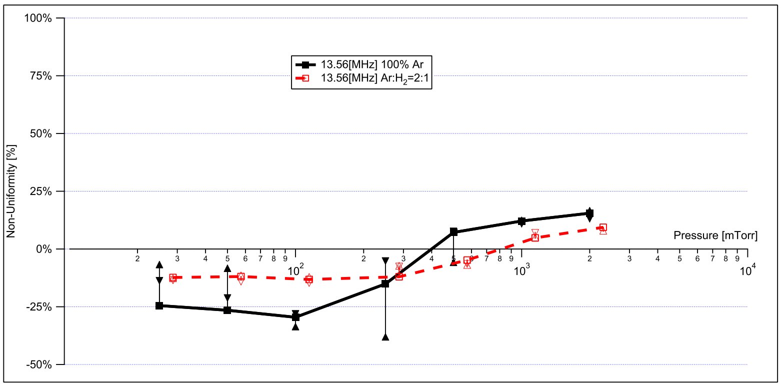

Model:
$+6\%$ (for $\Re(\sqrt{\varepsilon_{eff}}) = 2.5$)
$+11\%$ (for $\Re(\sqrt{\varepsilon_{eff}}) = 3.5$)

27.12[MHz]

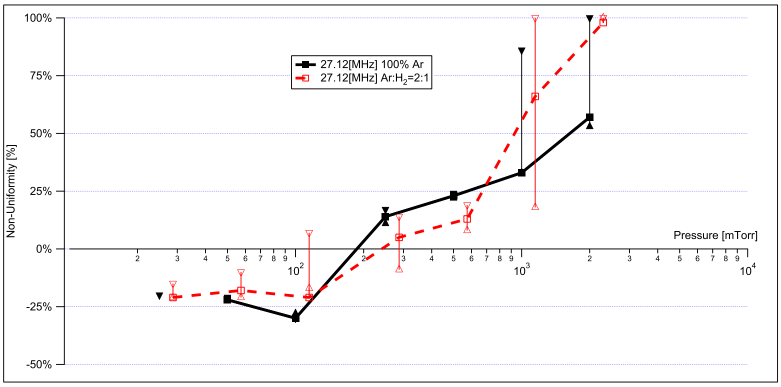

Model:
$+23\%$ (for $\Re(\sqrt{\varepsilon_{eff}}) = 2.5$)
$+45\%$ (for $\Re(\sqrt{\varepsilon_{eff}}) = 3.5$)

40.68[MHz]

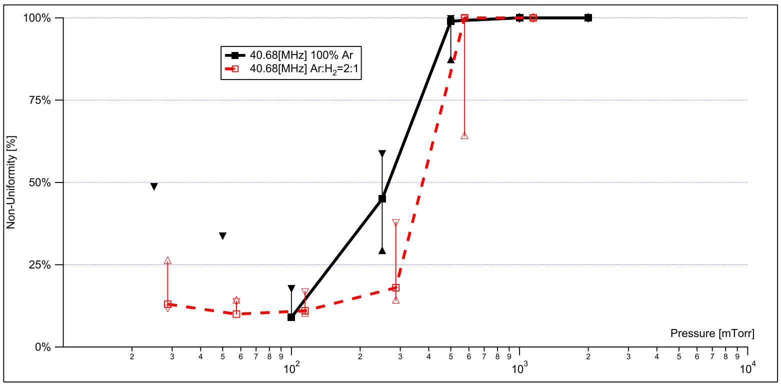

Model:
$+52\%$ (for $\Re(\sqrt{\varepsilon_{eff}}) = 2.5$)
$+88\%$ (for $\Re(\sqrt{\varepsilon_{eff}}) = 3.5$)

67.8[MHz]

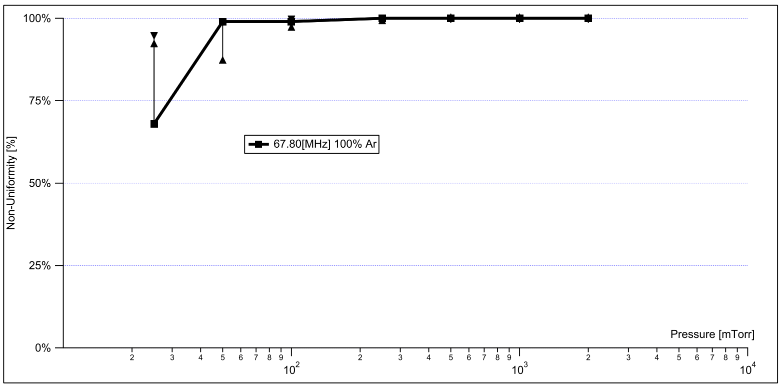

Model:
$+100\%$ (for $\Re(\sqrt{\varepsilon_{eff}}) = 2.5$)
$+100\%$ (for $\Re(\sqrt{\varepsilon_{eff}}) = 3.5$)

Fig. 7-18: Uniformity analysis for a flat electrode, parallel plate configuration. Each graph gives the measured uniformities for the RF excitation frequency specified in the row heading. Black solid lines denote pure Ar plasma. Red dashed lines are shifted slightly to the right for better view and indicate an Ar : H_2 = 2 : 1 gas mixture at the same pressure setpoints. Data points and corresponding vertical error bars indicate the measured non-uniformity for 400 ± 200[W] at 13.56[MHz], 27.12[MHz], 40.68[MHz] and 200 ± 100[W] at 67.8[MHz] respectively. The up-triangles (▲ and △) denote always the values for the higher power level and the down-triangles (▼ and ▽) for the lower power level respectively. Profiles which cannot be unambiguously classified as concave or convex are disregarded

The huge amount of experimental data calls for a condensed form of analysis. Here the attempt is made to use the uniformity as the tool for it.

General trend: Increase in non-uniformity

Fig. 7-18 shows how the non-uniformity number on the ordinate axis evolves by varying the pressure on the abscissa and power (vertical error bars) for the different frequencies (top down). Each graph shows (where available) two plots: one for pure argon and one for hydrogen diluted with argon. In conformity with earlier sections, positive non-uniformity values denote a dominant centre-plasma, negative values signify prevailing edge-discharges. Profiles which cannot be unambiguously classified as concave or convex are disregarded (cf. 6.3 “Non-Uniformity and Extended Definition”). Generally, all diagrams indicate an increase in non-uniformity with the pressure, except for $13.56[\mathrm{MHz}]$ where a slight increase in non-uniformity manifests itself only at high pressure. This rise can be amplified or attenuated by altering the delivered RF power and/or the gas composition.

Masking of SWE

We have already seen in the preceding sections that the measured plasma shapes can be *contradictory* to the expected shapes derived from the electromagnetic field distribution based on the standing wave effect. This observation is surprising in so far as it is commonly assumed that the standing wave effect “should” be the most important contribution to non-uniformity in large-area reactors. At high pressure it is nearly always clearly recognizable, but it can be more or less pronounced depending on the plasma conditions. However, at low pressure the standing wave can be completely masked by other effects, as confirmed up by the measurements at $13.56[\mathrm{MHz}]$ and $27.12[\mathrm{MHz}]$. This observation is reflected in the corresponding graphs of Fig. 7-18, where the non-uniformity curve changes its sign.

Worsening factor

The important point for the standing wave is the wavelength reduction factor (see also sections 3.2.1.4 and 6.6.4). At $40.68[\mathrm{MHz}]$, the vacuum standing wave is expected to cause about $\pm\ 10\%$ plasma non-uniformity for the whole electrode area (cf. Fig. 7-3). Therefore if we have a weak plasma (i.e. low electron density and high sheath thickness with $\varepsilon_{eff} \approx 1$) we should find less than $\pm\ 10\%$ plasma non-uniformity due to standing wave which can be masked by other non-uniformity sources. On the other hand, for a stronger plasma (higher electron density and lower sheath thickness) the worsening factor can be about 4, and in that case we can easily find about $\pm\ 30\%$ power/plasma non-uniformity (cf. Table 6-1).

“Worsening factor” gets “worse” at high pressure

In the case of the experiments shown in section 7.5.2.1 through 7.5.2.4, it seems that the transition between a weakly ionized plasma (low ε_{eff}) and a strongly ionized plasma (high ε_{eff}) is triggered by the pressure. The sheath thickness is a function of pressure [39][76][80]. At low pressure, we probably obtain a higher sheath thickness which corresponds to a low wavelength reduction factor $\Re(\sqrt{\varepsilon_{eff}})$ (about 1), while at high pressure we obtain a lower sheath thickness which correspond to a bigger wavelength reduction factor $\Re(\sqrt{\varepsilon_{eff}})$ and therefore a stronger standing wave effect (cf. 3.2.1.4 and Eq. 3-17).

Plasma breakdown and chamber geometry

Variations in plasma uniformity as a function of pressure from convex at high pressure via well-balanced at intermediate and concave at low pressure have been also reported by Carlson et al.[100][101] He investigated the uniformity of plasma in the same pressure range but in a large-area *DC anodic PECVD* reactor with pure H_2 and with a gas mixture of SiH_4, Ge and H_2. This may indicate that another effect plays a role which seems to be universal to glow discharges and cannot be tied neither to the SWE nor RF plasmas in particular. It might be the influence of the discharge chamber geometry upon the initiating plasma breakdown mechanism along the lines of description in Fig. 7-17. It was first described by Githens[103] for DC and RF discharges. Recently it was supported by Lisovskiy et al.[102] for large-area parallel plate reactors at $13.56[\mathrm{MHz}]$ by calculating the spatial electron density distribution at the time of discharge. Both authors report that at high pressures, the discharge ignites and sustains at the centre of parallel plate electrodes, but with decreasing pressure the ignition zone and region of most intense plasma move to the periphery of the parallel plate electrode and even further out of inter electrode gap.

Telegraph effect

The consequences of the non-uniform RF plasma potential (cf. 3.5) have also to be considered. In particular, the strong corner plasmas shown by HOWLING et al.[64] may be attributed to the TELEGRAPH effect.

Reactor size

Until now we have implicitly assumed an invariable reactor size. If the size were to be enlarged, it is probable that the change from $U < 0\%$ to $U > 0\%$ takes place at a lower pressure. Conversely we conclude that for smaller reactor sizes and lower pressure, VHF operation may not necessitate the use of a SWE compensating lens.

7.5.3 Lens Electrode Configuration

SWE pressure regimes

Besides looking into the plasma non-uniformity and validating the optical measurement system, we also established in the preceding section cf. 7.5.2 "Flat Electrode and Standing Wave Regimes" the range of pressure per frequency and gas, where the standing wave effect becomes clearly discernible. Table 7-1 gives an overview of the approximate minimum pressures for the RF powers used:

Table 7-1: Lower pressure limit for a dominant SWE in a KAI 1000 reactor, for the specified frequency and gas composition in the RF power range used.

	Ar 100%	**Ar : H_2 = 2 : 1**
13.56[MHz]	500[mTorr]	1000[mTorr]
27.12[MHz]	250[mTorr]	500[mTorr]
40.68[MHz]	100[mTorr]	25[mTorr]
67.8[MHz]	25[mTorr] (full range)	25[mTorr] (full range)

Outside these ranges it is questionable if the lens for the respective RF frequency could achieve a substantial contribution to the reduction of the overall non-uniformity, because other effects prevail.

When using the lens, yet another parasitic discharge can also exist in the lens volume. In the following subsections we will first consider a lens with this parasitic discharge and how to suppress it. Then we look into the lens operation below and at the design frequency. No measurements were done above the lens design frequency at 100[MHz] to illustrate undercompensation, as the SWE does not become manifest in the flat configuration (cf. 7.5.2.5).

Instabilities

Experimentally it was more difficult to sustain stable plasma discharges with the lens configuration. Especially at VHF, RF sources were very unsteady. It was difficult to find good matching conditions, possibly related to ignition, extinction and re-ignition of parasitic discharges. Therefore only a reduced set of profiles was taken and no systematic uniformity analysis was done.

7.5.3.1 Parasitic Discharge in the Lens Volume under the Glass

Differential pressure regime

The reactor and the enclosing vacuum chamber are differentially pumped, with the latter pumped down as far as possible to avoid parasitic discharges outside the reactor in the RF feedings (cf. 4.2.1). The lens concavity is sealed off from the plasma volume in the reactor by the substrate resting on the lens' flat borders and is evacuated via the vacuum chamber through small pumping holes in the lens plate (cf. 4.2.2). As the reactor pressure is always above the chamber pressure and a glass substrate lying on the electrode border is never a perfect seal, gas leaks from the reactor under the supporting area into the lens concavity. Hence the pressure in the concavity will always be larger than the pressure in the chamber.

Avoiding parasitic plasma in lens

Any plasma in the lens concavity short-circuits the electric field in the plasma volume (cf. 3.2.3.2) and thus severely compromises its proper operation as already shown for the cylindrical case (cf. 6.6.2.2). Empirically, it was seen that any plasma can be easily ignited in the electrode gap starting at about 50[mTorr] reactor pressure with moderate RF power between 200[W] and 600[W]. Below this pressure, more RF power is necessary to ignite a plasma. Thus 50[mTorr] was fixed as the maximum permissible pressure in the lens concavity.

Enhanced tightness and plasma in concavity

Preparatory measurements of the process chamber pressure vs. reactor pressure (See Fig. 7-19) revealed the necessity to improve the differential pressure regime in order to avoid simultaneous plasma ignition above the substrate and below it in the lens concavity. To enhance the pressure difference, several additional seals

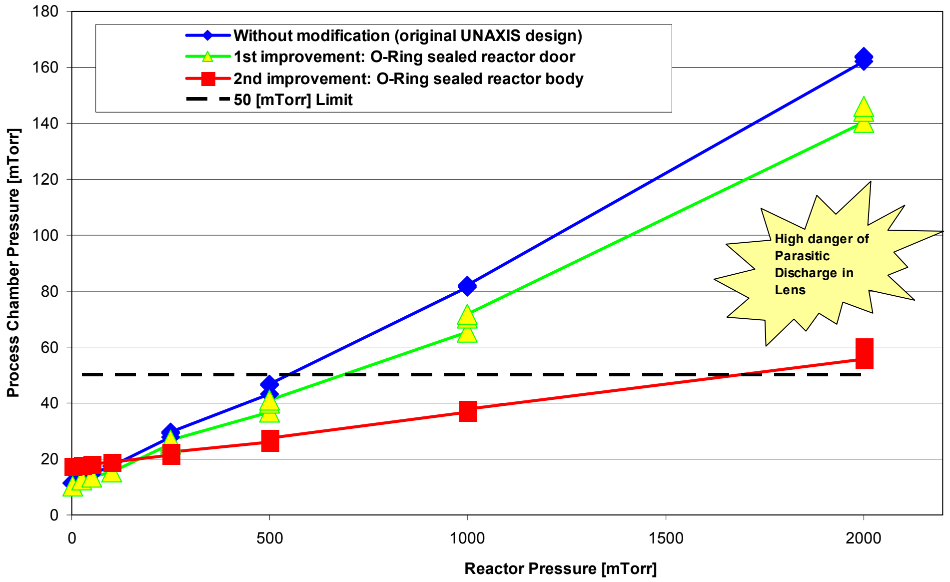

Fig. 7-19: Differential pressure regime before and after modification: Blue diamonds are for the original equipment, the red squares was the finally achieved. Target: In the vicinity or below 50[mTorr]

were introduced. First the border of the glass substrate was equipped with a self-adhesive 0.1[mm] thin TEFLON ribbon in order to improve the glass-aluminium leak tightness. The reactor door was replaced with an O-ring sealed, screwed flange. Bottom and top reactor plates and the pumping piping for the reactor were fitted with soft extra seals made of ELASTOMER. All these measures yielded a drastic gain in leakage reduction for medium and high reactor pressure as ascertained by the red line measurement in Fig. 7-19. Note that some of these modifications render the system incompatible with the requirements for heated operation and/or reactive gases.

A plasma was ignited at 2000[mTorr] process pressure in the reactor. The plasma

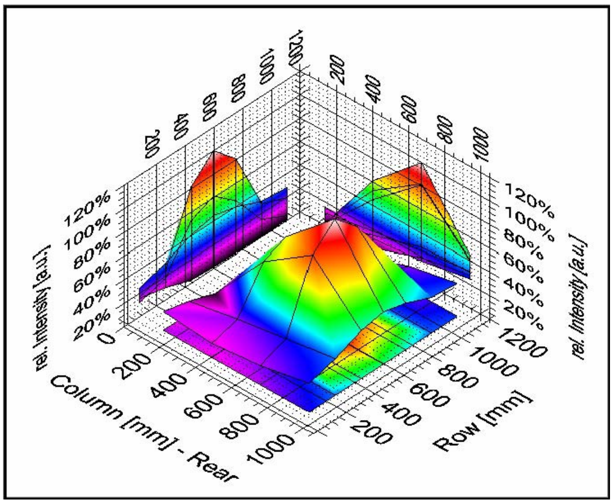

Fig. 7-20: Lens with parasitic plasma. Process Conditions: 67.8[MHz], 100% Ar, pressure in reactor 2000[mTorr], pressure in lens concavity not lower than 50[mTorr], delivered RF power ca. 500[W].

profile measurement in Fig. 7-20 shows a strong centre intensity. Except for the corners, it is striking similar to the intensity profiles shown in Fig. 7-15 at 25[mTorr]. As no reduction in the non-uniformity is observed, we conclude that no SWE correction takes places and the lens concavity must be filled by a parasitic discharge in this case.

Limited process ranges

This therefore limits the valid process range to less than 1500[mTorr] and low power. The pressure range for the lens investigation is therefore fixed by this upper limit (cf. Fig. 7-19) and the lower limit by Table 7-1. A possible solution for processing would be to insert a horizontal dielectric plate in the concavity in order to reduce the maximum depth if the vacuum lens concept is to be retained. Otherwise a dielectric lens can be applied as in the cylindrical case, as mentioned above.

7.5.3.2 Lens Operation below the Design Frequency

Undercompensation

We know from the introductory section 7.3 on non-uniformities and backed up by the electric field measurements with the lens in 7.4.2, that the rectangular lens should produce undercompensated, concave optical plasma intensity profiles at RF frequencies below the design frequency $f_0 = 67.8[\mathrm{MHz}]$ analogous to its cylindrical counterpart. It was not known beforehand how the plasma behaves at the mechanical discontinuity at the lens edge, which is needed to keep the glass substrate in place, and how strongly the plasma would perturb the vacuum solution.

Modelling

All the modelling in Fig. 7-21 was done with a wavelength reduction factor of $\Re(\sqrt{\varepsilon_{eff}}) = 2.5$. The modelling disregards the presence of a glass substrate and its dielectric property. The obtained normalized distribution of the voltage amplitude seen by the plasma was squared to get the theoretical power dissipation. The left column of Fig. 7-21 shows the normalized power dissipation for the whole electrode area including the discontinuity and the flat margin. At first sight the "over-dominant" border is striking, which can easily amount to $10 \times$ the minimum value in the centre of the electrode. The right column shows the same modellings but restricted and normalized to the area visible to the optical intensity system. Without the over-dominant border-effect and below the design frequency, all the calculated profiles are concave as expected and the absolute non-uniformity decreases from -45% to -34% by tripling the frequency from 13.56[MHz] to 40.68[MHz].

Argon measurements

The Ar measurements in the left column of Fig. 7-22 at 13.56[MHz], 27.12[MHz] and 40.68[MHz] all show a stronger plasma at the front side than at the rear. If we suppose an intense edge plasma as suggested by the modelling, then this can be partly explained by their relative position of the light collimators on the electrode with respect to the edge discontinuity of the lens. The front sensors have a shorter distance of 6.0[cm] to the discontinuity versus 8.0[cm] at the rear side of the lens. The lateral distance of the outermost optical sensors to the edge is 9.5[cm] each. An improvement of the non-uniformity by an increase of the frequency can be seen, but it turns out to be less strong than expected. It seems that a pure argon plasma is very susceptible to what happens 6 - 10[cm] beyond the observation point.

Argon - Hydrogen measurements

Compared with this, the argon-hydrogen plasma show less vulnerability to edge effects and thus leads to less non-uniform plasma.

It cannot be said with absolute certainty how much of the negative non-uniformity was brought about by the excessive edge effect and what is caused by the overcompensation of the lens. The author thinks that the hydrogen measurements are much more influenced by the overcompensation effect of the lens than are the pure argon measurements.

The measurements in Fig. 7-22 have been selected to best illustrate the frequency response of the shaped electrode. The pressure was chosen to ensure, that the SWE is dominant over the edge effect.

7.5.3.3 Lens Operation at the Design Frequency (67.8[MHz])

Modelling

The bottom row of Fig. 7-21 depicts the modelling and Fig. 7-22 the optical plasma intensity measurements at the design frequency. The modelling over the whole electrode area predicts again strong corner and edge plasmas. However, when the graph is restricted to the area visible to the optical system it is possible to see immediately that the concave profile disappeared and changed into a saddle-like structure with $\pm\ 21\%$ non-uniformity due to the increase in frequency and caused by the perturbations of a plasma with a wavelength reduction factor of $\Re(\sqrt{\varepsilon_{eff}}) = 2.5$.

Measurements

The measurement with Ar (last row of Fig. 7-22) show two strong corner plasma, H_2 addition does not show the edge effect. The strong centre-plasma as shown in Fig. 7-15 has disappeared for both cases, but there are secondary, subordinate effects, which now have to be taken into account. Argon seems to be easily influenced by the effects in the corner whereas hydrogen reveals nicely the perturbative plasma effect.

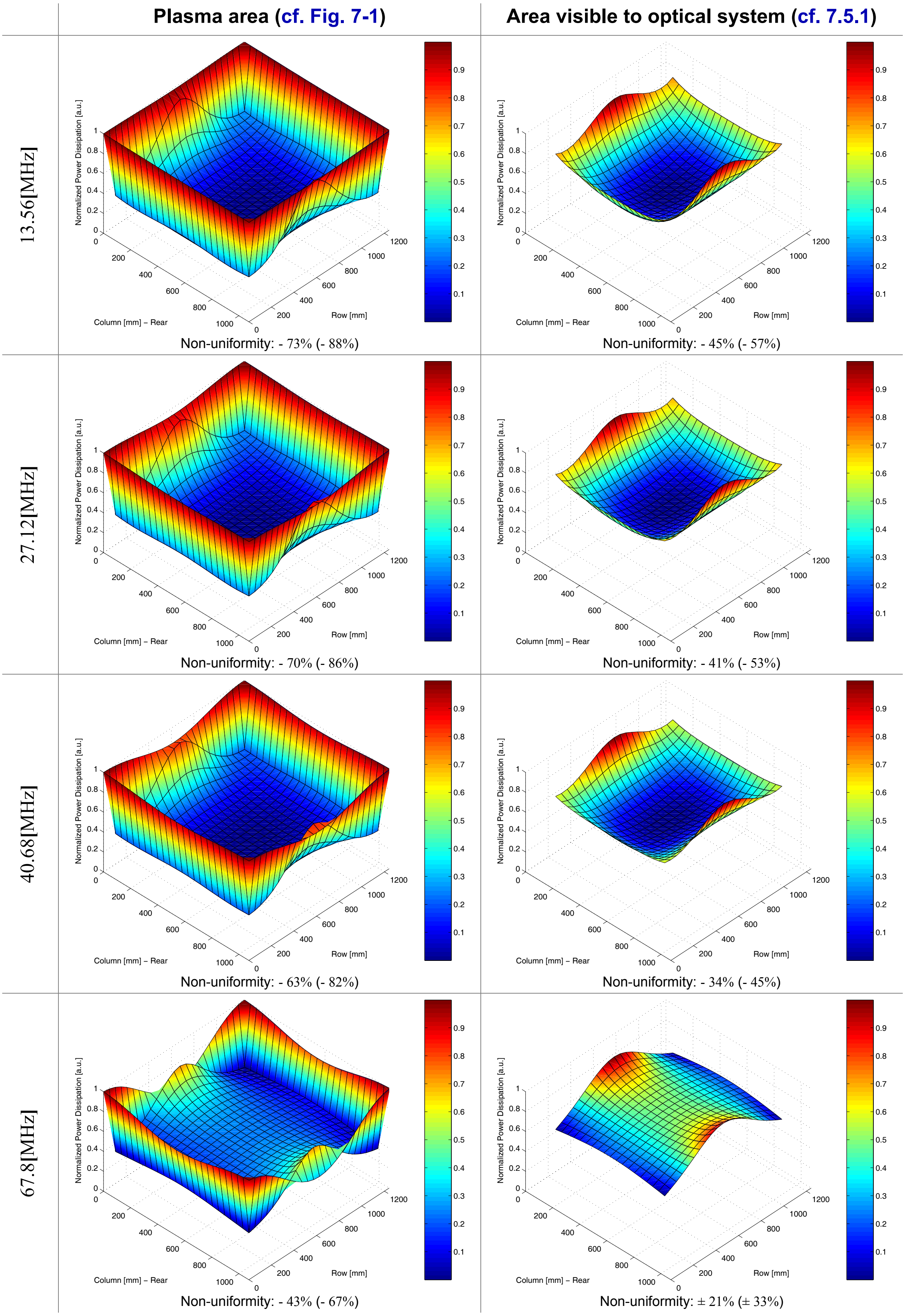

Fig. 7-21: Modelled plasma profiles for a parallel plate reactor configuration with the shaped electrode for four different RF excitation frequencies. The left column shows the calculation and the non-uniformity figures for the whole plasma area (cf. Fig. 7-1), the right column the same but restricted to the view of the optical system (cf. 7.5.1). The wavelength reduction factor for the depicted graphs and specified non-uniformity is $\Re(\sqrt{\varepsilon_{eff}}) = 2.5$; the percentages in parentheses give the respective non-uniformity for $\Re(\sqrt{\varepsilon_{eff}}) = 3.5$.

	Ar 100%	**Ar : H_2 = 2 : 1**
13.56[MHz]	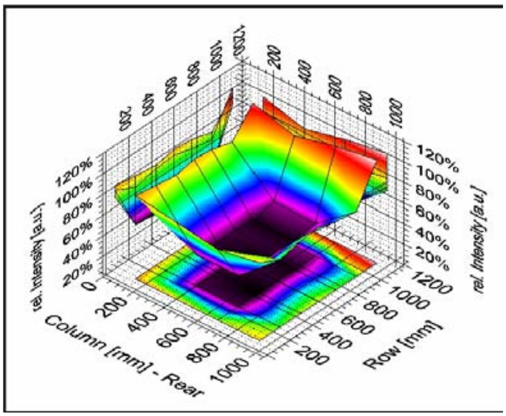 1000[mTorr], 300[W], Non-uniformity - 58%	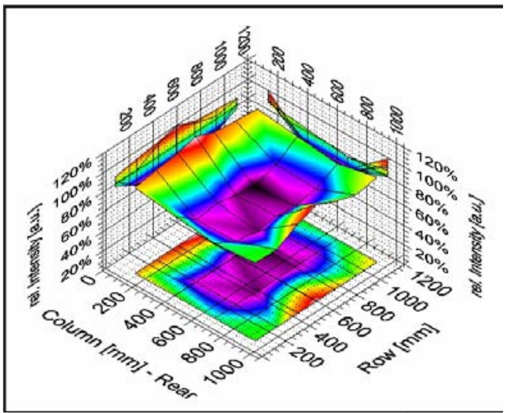 1000[mTorr], 300[W], Non-uniformity - 25% ($\Re(\sqrt{\varepsilon_{eff}}) \approx 1.5$)
27.12[MHz]	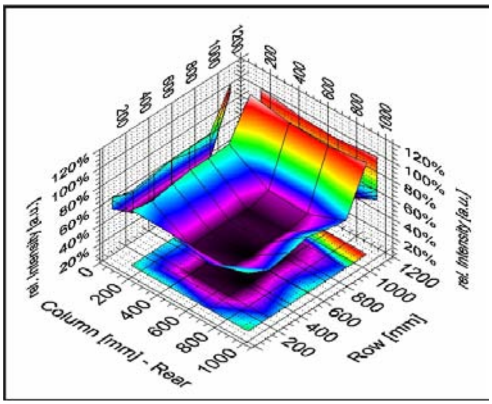 1000[mTorr], 300[W], Total non-uniformity ca. - 56%, without front edge effect ca. - 40%	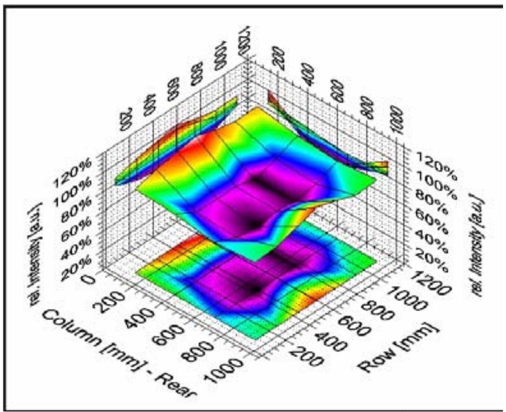 500[mTorr], 300[W], Non-uniformity - 20% ($\Re(\sqrt{\varepsilon_{eff}}) \approx 1.5$)
40.68[MHz]	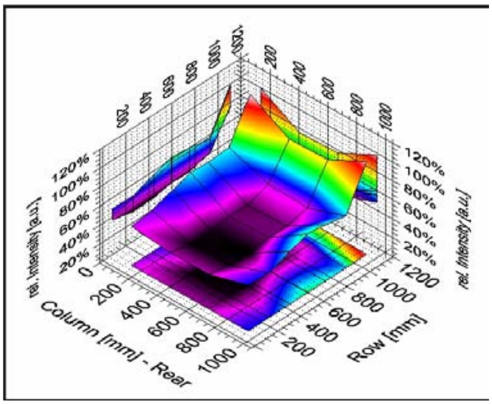 1000[mTorr], 300[W], Total non-uniformity ca. - 52%, without front edge effect ca - 35%	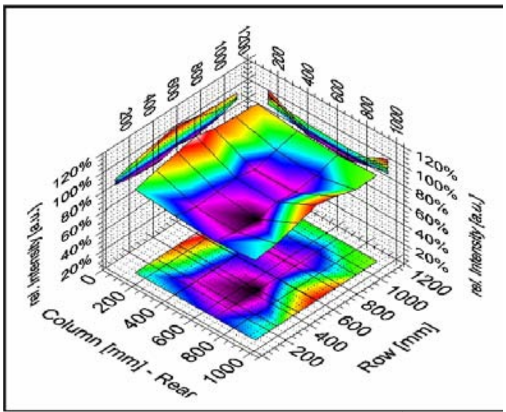 500[mTorr], 600[W], Non-uniformity - 15% ($\Re(\sqrt{\varepsilon_{eff}}) \approx 1.5$)
67.8[MHz]	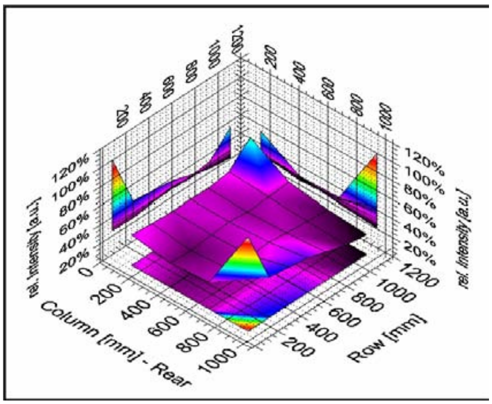 250[mTorr], ca. 400[W], Total non-uniformity ± 65%, centre region without corner plasma ca. ± 40%	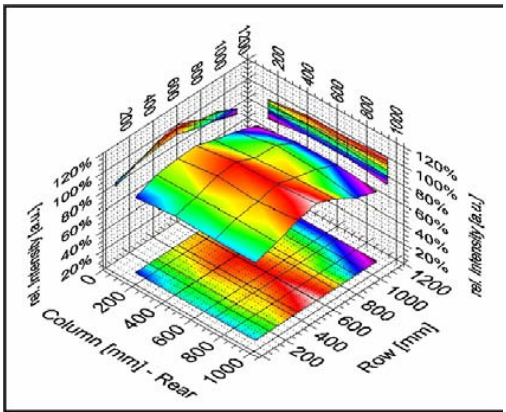 250[mTorr], ca. 600[W], Non-uniformity ± 18% ($\Re(\sqrt{\varepsilon_{eff}}) \approx 2.3$)

Fig. 7-22: Measured plasma profiles for a parallel plate reactor configuration with a shaped electrode for different RF excitation frequencies and two gases (Ar 100% and Ar : H2 = 2 : 1). The Ar:H_2 profiles give an estimated value of the wavelength reduction factor $\Re(\sqrt{\varepsilon_{eff}})$ for the respective non-uniformity.

7.6 Conclusion

	With standard flat electrode	**With shaped electrode designed for 67.8[MHz]**
Ar 100%	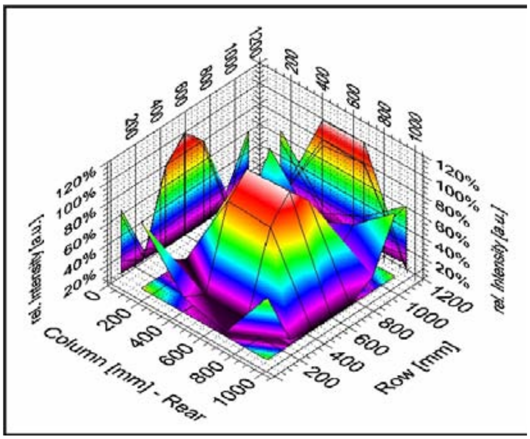 250[mTorr], 200[W], Non-uniformity + 100%	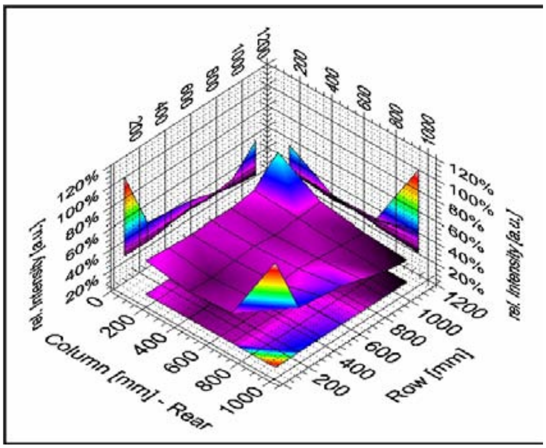 250[mTorr], ca. 400[W], Total non-uniformity ± 65%, **centre region without corner plasma ca.** ± 40%
Ar : H_2 = 2 : 1	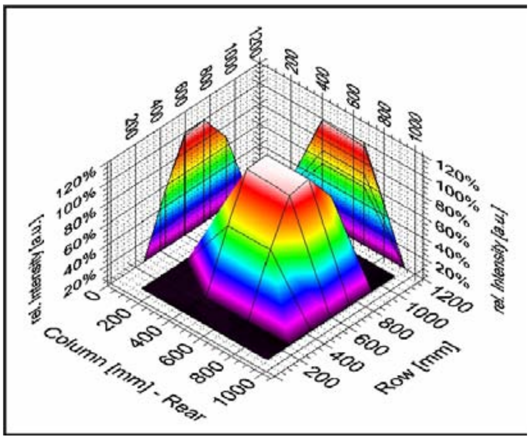 250[mTorr], 200[W], Non-uniformity: + 100%	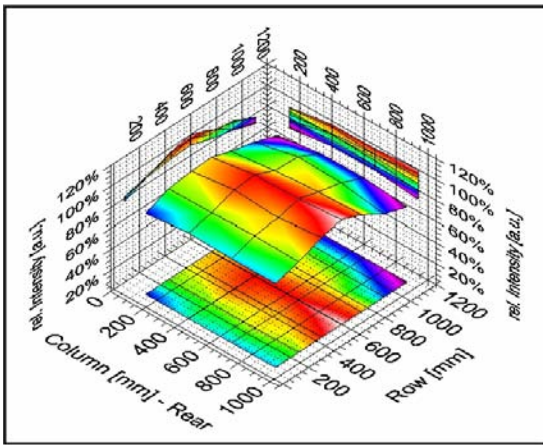 250[mTorr], ca. 600[W], Non-uniformity ± 18%

Fig. 7-23: Selected plasma profiles measured for the standard flat electrode vs. a shaped lens electrode. The excitation frequency used is equal to the design frequency f_0 = 67.8[MHz] of the lens. Two gases are used, purely atomic (Ar) in the top row and with molecular addition (Ar : H_2 = 2 : 1) in the bottom row. The delivered RF powers for the right hand column were chosen to ensure stable plasma conditions.

Proof of principle

Fig. 7-23 summarizes the main findings of this chapter by direct comparison of measured plasma profiles at an RF excitation frequency of 67.8[MHz] *with and without* a shaped electrode. The RF frequency is chosen to coincide with the design frequency of the lens electrode. The shape of the lens is described in detail in section 7.2.1. The left column shows the dominant centre plasma, attributed to the standing wave effect with parallel plate electrode. In the right column, the strong centre plasma is successfully levelled off and a much more uniform plasma fills the space with the lens electrode. The strong corner plasmas for Ar 100% are outside the active lens area but some stray light enters into the lens area. Regardless whether this is due to the second maximum of the standing wave effect and/or an edge effect, they cannot be removed by a lens; this can only be done by a careful design of the reactor corners.

Rectangular geometry more intricate than cylindrical

Generally the rectangular case is more difficult than the cylindrical configuration. First it is necessary to find a numerical solution for the lens shape rather than an analytical formula for the cylindrical lens. Secondly the likelihood of parasitic discharges striking in the lens concavity and in the RF stripline was minimized by a differential pumping system. No PTFE filling of the lens was possible in the configuration used, as this would have blocked the optical line-of-sight access for the uniformity diagnostics to the plasma volume. The differential pumping strategy works less well than the dielectric encapsulation used for the cylindrical reactor and it is difficult to apply it to areas inside the reactor. In particular, no precautions were possible to avoid parasitic discharges between the floating grids above the electrode at VHF without altering the experimental setup.

Once the standing wave effect has been corrected, other effects related to the geometry of the vessel emerged and proved to dominate depending on the process condition, including telegraph effect, plasma breakdown regimes and edge effects.

An extensive uniformity analysis for the lens electrode as outlined in 7.5.2.6 for the flat case, could not be repeated for the lens configuration because of limited plasma stability and the "over-dominant" effect of the flat border of the lens. Nevertheless, within the experimental constraints imposed by all these perturbations, the feasibility of a rectangular shaped electrode to compensate for the standing wave has been conclusively demonstrated, which was the primary motivation for the thesis work.

Part V: Conclusion

Chapter 8: Conclusion

Analysis of SWE in large-area reactor

The objective of this project was a feasibility study of a novel, large-area plasma-based thin film production technique. It is foremost an investigation into the standing wave effect (SWE) in a small gap, very large area capacitively coupled (CCP) radio-frequency (RF) plasma reactor. This study became necessary because in the current generation of industrial reactors the standing wave has become the main contributor to the electromagnetic non-uniformity. This is due to the fact that the ratio of the typical system length L to the wavelength λ of the RF excitation frequency exceeded the threshold of one tenth ($L/\lambda \geq 1/10$). If the aforementioned criterion is met, then the non-uniformity caused by the standing wave effect is so strong that it cannot be sufficiently reduced by conventional means such as, for example, process engineering, gas distribution and multiple RF feeding points. The reasons why this criterion is no longer met is either because the reactor size was enlarged to allow for larger substrates or because the RF excitation frequency was raised to the VHF region to achieve better film quality.

Feasibility study of a shaped electrode

It is generally acknowledged that for deposition and etching applications a compensation for the standing wave effect is indispensable if the above mentioned criterion is no longer satisfied. It was proposed by SANSONNENS and SCHMITT[8] to use a shaped electrode to correct the standing wave in vacuum. Their approach consists of shaping one of the parallel plate electrodes in order to correct the non-uniform voltage in the plasma gap by a capacitive voltage division. The aim of this thesis was to develop a twofold proof of principle for this shaped electrode: Firstly for a cylindrical reactor with central RF power feeding, taking advantage of the cylindrical symmetry, and secondly, for a rectangular reactor with distributed RF power feeding built on an industrial system.

Procedure

The two reactors had to be designed, set up and fitted with vacuum equipment, RF diagnostics, plasma diagnostics and data acquisition systems. A cylindrical test reactor with $1[\mathrm{m}]$ diameter was constructed and an industrial reactor with $1[\mathrm{m}^2]$ substrate size was adapted for this thesis. The standing wave effect in both reactors was characterized in vacuum and under a wide range of plasma process parameters for the parallel plate, flat electrode system. Then the fabricated shaped electrodes were installed after having their curvature meticulously verified. The same characterization procedure was executed for the shaped electrodes as for the flat ones. Measurements were compared to the theoretical predictions and modelling.

Dependencies of the SWE

With flat electrodes it was found for both reactors that the strength of the standing wave effect with and without plasma increases first and foremost with the applied RF frequency as expected. However, with plasma the RF wave propagation is affected by the dielectric property of the plasma and the excitation wavelength is reduced. As a result the standing wave effect is more pronounced than in vacuum, i.e. it is “worsened”. The worsening of the standing wave effect with plasma at a constant RF excitation frequency is influenced by the pressure which can be seen in the process-dependent worsening factors (cf. Table 6-1). The measurements in the cylindrical reactor with symmetric electrodes revealed an increase of the worsening factor with the pressure within the chosen process window (cf. Fig. 6-3). The applied RF power (or RF voltage) and the gas composition have a minor systematic effect on the worsening factor. Whereas in the asymmetric rectangular reactor it was found that at low pressure (i.e. long damping length), the telegraph effect can completely mask the standing wave effect and produce edge-accented concave plasma profiles. By contrast the standing wave effect manifests itself only at medium and high pressures when used at the frequencies 13.56, 27.12 and $40.68[\mathrm{MHz}]$. Going from medium to high pressure increases the worsening factor similar to the cylindrical case, which is reflected in a general increase of the non-uniformity (cf. Fig. 7-11). In the transition zone of both regimes, concave and convex shapes, it is possible to "tune" low uniformities. As the measurements were carried out with two gas types only (Ar, Ar:H_2), one which is electropositive and one slightly electronegative, it remains to be proven that strong electronegative plasmas (e.g. O_2) or typical deposition plasmas with silane (SiH_4) produce similar results when used for deposition. But a priori these process conditions are not guaranteed to produce the best film quality.

Gaussian lens

The shape of the electrode for the cylindrical electrode ("lens") can be derived analytically from Maxwell's equations and gives a solution for the compensation of the standing wave effect in vacuum (cf. Eq. 3-29) for a given design frequency. Electric field measurements without plasma in the $1[\mathrm{m}]$ diameter cylindrical reactor showed conclusively that such a lens built for $100[\mathrm{MHz}]$ can successfully eliminate the standing wave effect non-uniformity (cf. Fig. 6-2) by creating a uniform RF vertical electric field in the plasma volume. Plasma uniformity measurements of the optical emission intensity and the ion flux in the same setup but with a dielectric lens (reducing the effective design frequency to $69.0[\mathrm{MHz}]$) demonstrated the proof of principle for the Gaussian-lens electrode for removing the standing wave non-uniformity in large area reactors (cf. Fig. 6-10). The plasma is uniform, except for edge effects, for a wide range of parameters and consequently the design is suitable for plasma processing.

Rectangular lens

By contrast the shape for the rectangular electrode (cf. Fig. 7-1) was obtained by numerical methods. Electrical field measurements were repeated and gave evidence that the rectangular lens likewise corrects successfully the standing wave effect in vacuum (cf. Fig. 7-6). For plasma uniformity measurements, only localized optical emission intensity measurements were used. Evidence for the rectangular proof of principle could be given despite plasma perturbations and strong edge plasmas caused by the edge discontinuity of the lens curvature (See Fig. 7-23).

Plasma without SWE

For all the plasma parameters investigated using parallel plates at 27.12, 40.68, 67.8 and $100[\mathrm{MHz}]$ the principal non-uniformity can be explained by the standing wave effect. At VHF, when the standing wave effect has been corrected with a lens electrode then any remaining non-uniformity is primarily due to the process-dependent plasma perturbed lens correction, the telegraph effect, edge and parasitic effects.

Deposition and lens

The successful proof of concept for both reactors was given by E-field measurements and non-reactive plasmas (Ar and Ar:H_2) over a wide range of power and pressure process conditions, which cover typical deposition and etching regimes. It is necessary to emphasize that evidence was given without using reactive gases and without doing any deposition or etching. The ultimate proof that such a lens can effectively be used for deposition is demonstrated elsewhere.[97]

VHF operation and parasitic discharges

For the investigation of the standing wave effect at the various frequencies it is required to have stable plasma conditions. But a wide range of operating conditions at VHF exhibited strongly unstable discharges. Parasitic discharges in the cylindrical reactor were curbed by filling all possible ignition spaces by a low dielectric material (PTFE) and by confining the plasma to the space between the two electrodes. It was observed that by disallowing parasitic discharges, instable plasma conditions became less frequent but they did not disappear completely. By contrast, no special measures were taken in the rectangular reactor as to keep its set-up as close as possible to the original configuration. The stronger corner plasma at $67.8[\mathrm{MHz}]$ with argon (cf. Fig. 7-15) and the undetectable standing wave effect at $100[\mathrm{MHz}]$ (cf. Fig. 7-16) seem to be the direct consequence of discharges laterally and behind the RF electrode. As the sheath width becomes smaller with an increase of the frequency, plasma can ignite in smaller gaps. The only way to absolutely avoid it is to fill the spaces with dielectric material. An alternative would be to change the gap or change process conditions under observation of the typical sheath widths and the plasma extinction curves[125].

This experimental experience confirms that plasma operation at VHF is more delicate than at the standard frequency $13.56[\mathrm{MHz}]$, where such phenomena rarely occurred. On the one hand this has to be attributed to the lack of reliable, affordable RF power sources at VHF and inadequate, unstable impedance matching at the very beginning of this work, on the other hand experimental problems arose due to the fact that VHF plasma can ignite in smaller gaps as the sheath widths become smaller. When operated at VHF, standard industrial equipment designed for $13.56[\mathrm{MHz}]$ operation shows a strong tendency for various types of parasitic discharges. Initial plans to perform etching and/or deposition tests had to be dropped in the face of massive RF and parasitic problems. Hence the whole thesis covers only aspects achieved with non-reactive gases (Ar, H_2). It is thought that parasitic discharges can be controlled by pragmatic reactor design. One must be aware that parasitic effects can severely hamper the operation of a PECVD reactor unless they are properly dealt with.

By-products of this thesis

For the objectives of this thesis, the development of an in situ plasma uniformity measurement system and the successful adaptation of a distributed VHF matching technique (“stub tuner”) used in radio broadcasting and in microwave applications for PECVD reactors was necessary.

In-situ uniformity measurement

The developed plasma uniformity system relies on the local optical emission intensity and also on the local ion saturation current collected by surface electrostatic probes. Such an in-situ uniformity measurement systems enables not only the use of simple, non-toxic and non-reactive model gases, but also it allows a rapid scan of the entire process parameter space compared to costly deposition or etching processes which necessitate time-consuming ex-situ characterization.

Stub Tuner

The stub tuner makes impedance adjustment at VHF, in our case $100[\mathrm{MHz}]$, more calculable and predictable than with lumped matching networks. By using a triple stub construction and extending the variable length transmission line by a security margin (accounting for losses, end-effects and mechanical imperfections), a full coverage of the SMITH Chart is guaranteed, i.e. all possible load impedances can be mapped to a nominal impedance (in our case $50[\Omega]$). On the debit side it is the sheer size of the stub tuner (approximate area $\lambda \times \lambda$) which makes it impractical. But the footprint would shrink if the excitation frequency were further increased or if a dielectric media could be inserted into the coaxial transmission lines. Moving, durable RF contacts cannot easily be produced and for the moment no automatching procedure is available.

Net Result

Despite serious experimental shortcomings in terms of RF stability, matching and parasitic discharges, it was shown that shaped electrodes can be successfully used to reduce the non-uniformity of the standing wave effect in large area plasma reactors to a level which makes the technology usable for industrial manufacturing. Therefore the advantages of very high frequency excitation can be combined with large area reactors without having the non-uniformity problems of the standing wave effect.

References

[1] J. P. M. SCHMITT, M. ELYAAKOUBI, and L. SANSONNENS, "Glow discharge processing in the liquid crystal display industry," Plasma Sources Science and Technology, vol. 11(3A), pp. A206-A210, 2002.

[2] H. R. KOENIG and L. I. MAISSEL, "Application of RF Discharges to Sputtering," IBM Journal of Reasearch and Development, vol. 14(2), pp. 2345-2459, 1970.

[3] Y.-M. KIM, C. E. YOUN, J. W. RA, and Y. S. KIM, "Method for reducing the longitudinal voltage variation in transverse radio-frequency discharge waveguide lasers," Journal of Applied Physics, vol. 67(2), pp. 1127-1129, 1990.

[4] L. SANSONNENS, A. PLETZER, D. MAGNI, A. A. HOWLING, C. HOLLENSTEIN, and J. P. M. SCHMITT, "A voltage uniformity study in large-area reactors for RF plasma deposition," Plasma Sources Science and Technology, vol. 6(2), pp. 170-178, 1997.

[5] J. KUSKE, U. STEPHAN, O. STEINKE, and S. RÖHLECKE, "Power Feeding in Large Area PECVD of a amorphous silicon," presented at Materials Research Society Symposium Proceedings, San Francisco, California, U.S.A., 1995.

[6] A. A. HOWLING, L. SANSONNENS, J. BALLUTAUD, C. HOLLENSTEIN, and J. P. M. SCHMITT, "Non-uniform radio-frequency plasma potential due to edge asymmetry in large-area radio-frequency reactors," Journal of Applied Physics, vol. 96(10), pp. 5429-5440, 2004.

[7] A. BOGAERTS, E. NEYTS, R. GIJBELS, and J. VAN DER MULLEN, "Gas discharge plasmas and their application," Spectrochimica Acta Part B, vol. 57, pp. 609-658, 2002.

[8] L. SANSONNENS and J. P. M. SCHMITT, "Shaped Electrode and lens for a uniform radio-frequency capacitive plasma," Applied Physics Letters, vol. 82(2), pp. 182-184, 2003.

[9] H. MASHIMA, Y. TAKEUCHI, M. NODA, M. MURATA, H. NAITOU, I. KAWASAKI, and Y. KAWAI, "Uniformity of VHF plasma produced with ladder shaped electrode," Surface and Coantings Technology, vol. 171(1-3), pp. 167-172, 2003.

[10] L. SANSONNENS, "Calculation of the electrode shape for suppression of the standing wave effect in large area rectangular capacitively coupled reactors," Journal of Applied Physics, vol. 97(063304), pp. 1-6, 2005.

[11] W. SCHWARZENBACH, A. A. HOWLING, M. FIVAZ, S. BRUNNER, and C. HOLLENSTEIN, "Sheath impedance effects in very high frequency plasma experiments," Journal of Vacuum Science & Technology A, vol. 14(1), pp. 132-138, 1995.

[12] A. A. HOWLING, J.-L. DORIER, C. HOLLENSTEIN, U. KROLL, and F. FINGER, "Frequency Effects in silane plasmas for plasma enhanced chemical vapour deposition," Journal of Vacuum Science & Technology A, vol. 10(4), pp. 1080-1085, 1992.

[13] M. M. RADMANESH, *Radio Frequency and Microwave Electronics Illustrated*. Upper Saddle River, NJ 07458, USA: Prentice Hall PTR, 2001.

[14] H. H. MEINKE and F.-W. GUNDLACH, *Taschenbuch der Hochfrequenztechnik*, 5th ed. Berlin-Heidelberg: Springer-Verlag, 1992.

[15] L. SANSONNENS, "Déposition assistée par le plasma radiofréquence dans un réacteur de grande surface: Effets de la contamination particulaire et de la fréquence d'excitation," Ph.D. dissertation, Département de Physique, CRPP, École Polytechnique Fédérale de Lausanne, Lausanne, 1998.

[16] N. MATSUKI and Y. MORISADA, 2003, "Plasma CVD Film-Forming Device," United States, Patent Specification US 6,631,692 B1, US 10/328,331, ASM Japan K.K., 11 p.

[17] A. PERRET, P. CHABERT, J. JOLLY, and J.-P. BOOTH, "Ion energy uniformity in high-frequency capacitive discharges," Applied Physics Letters, vol. 86(021501), pp. 1-3, 2005.

[18] J.-L. DORIER, C. HOLLENSTEIN, A. A. HOWLING, and U. KROLL, "Powder dynamics in very high frequency silane plasmas," Journal of Vacuum Science & Technology A, vol. 10(4), pp. 1048-1052, 1992.

[19] W. T. BLONIGAN and C. A. SORENSEN, "RF Matching Network with Distributed Outputs," US Patent US6,552,297 B2, 10/003,129, 22.4.2003.

[20] Y. KAWAI, M. YOSHIOKA, T. YAMANE, Y. TAKEUCHI, and M. MURATA, "Radio-frequency plasma production using a ladder shaped antenna," Surface and Coantings Technology, vol. 116-119, pp. 662-665, 1999.

[21] A. LAPUCCI, F. ROSSETTI, M. CIOFINI, and G. ORLANDO, "On the Longitudinal Voltage Distribution in Radio-Frequency-Discharged CO2 Lasers with Large-Area Electrodes," IEEE Journal of Quantum Electronics, vol. 31(8), pp. 1537-1542, 1995.

[22] J. D. STROHSCHEIN, W. D. BILIDA, H. J. J. SEGUIN, and C. E. CAPJACK, "Computational Model of Longitudinal Discharge Uniformity in RF-Excited CO2 Slab Lasers," IEEE Journal of Quantum Electronics, vol. 32(8), pp. 1289-1297, 1996.

[23] A. LAPUCCI, S. MASCALCHI, and R. RINGRESSI, "Parameters Affecting the Power Distribution in the Radio Frequency Discharge of Large-Area Diffusion-Cooled CO2 Lasers," IEEE Journal of Quantum Electronics, vol. 34(4), pp. 616-621, 1998.

[24] W. J. GOEDHEER, "Lecture notes on radio-frequency discharges, dc potentials, ion and electron distributions," Plasma Sources Science and Technology, vol. 9(4), pp. 507-516, 2000.

[25] Y. P. RAIZER and M. N. SHNEIDER, "Localization of an rf capacitive discharge in a long strip line," Technical Physics Letters, vol. 23(1), pp. 75-77, 1997.

[26] Y. P. RAIZER, M. N. SHNEIDER, and N. A. YATSENKO, *Radio-frequency capacitive discharges*. Boca Raton: CRC Press 1995.

[27] T. KITAJIMA, Y. TAKEO, and T. MAKABE, "Two-dimensional CT images fo two-frequency capacitively coupled plasma," Journal of Vacuum Science & Technology A, vol. 17(5), pp. 2510-2516, 1999.

[28] V. A. GODYAK, R. B. PIEJAK, and B. M. ALEXANDROVICH, "Electrical Characteristics of Parallel-Plate RF Discharges in Argon," IEEE Transactions on Plasma Science, vol. 19(4), pp. 660-676, 1991.

[29] S. RAUF and M. J. KUSHNER, "The effect of radio frequency plasma processing reactor circuitry on plasma characteristics," Journal of Applied Physics, vol. 83(10), pp. 5087-5094, 1998.

[30] O. DEMOKAN, "Critical Analysis of Matching Schemes in Capacitively Coupled Discharges," IEEE Transactions on Plasma Science, vol. 31(5), pp. 1100-1102, 2003.

[31] M. M. SALEM, J.-F. LOISEAU, and B. HELD, "Impedance Matching for optimazation of power transfer in a capacititively excited RF plasma reactor," European Physical Journal: Applied Physics, vol. 3, pp. 91-95, 1998.

[32] U. STEPHAN, J. KUSKE, H. GRÜGER, and A. KOTTWITZ, "Problems of Power Feeding in Large Area PECVD of Amorphous Silicon," in Materials Research Society Symposium Proceedings, vol. 557. San Francisco, California, U.S.A., 1999.

[33] S. WICKRAMANAYAKA, Y. NAKAGAWA, Y. SAGO, and Y. NUMASAWA, "Optimization of plasma density and radial uniformity of a point-cusp magnetic field applied capacitive plasma," Journal of Vacuum Science & Technology A, vol. 18(3), pp. 823-829, 2000.

[34] A. D. COLLEY, H. J. BAKER, and D. R. HALL, "Planar waveguide, 1kW cw, carbon dioxide laser excited by a single transvere rf discharge," Applied Physics Letters, vol. 61(2), pp. 136-138, 1992.

[35] H. SCHMIDT, L. SANSONNENS, A. A. HOWLING, C. HOLLENSTEIN, M. ELYAAKOUBI, and J. P. M. SCHMITT, "Improving plasma uniformity using lens-shaped electrodes in a large area very high frequency reactor," Journal of Applied Physics, vol. 95(9), pp. 4559-4564, 2003.

[36] P. CHABERT, J.-L. RAIMBAULT, J.-M. RAX, and A. PERRET, "Suppression of the standing wave effect in high frequency capacitive discharges usng a shaped electrode and a dielectric lens: Self-consistent approach," Physics of Plasmas, vol. 11(8), pp. August 2004, 2004.

[37] P. CHABERT, J.-L. RAIMBAULT, J.-M. RAX, and M. A. LIEBERMAN, "Self-consistent nonlinear transmission line model of standing wave effects in a capacitive discharge," Physics of Plasmas, vol. 11(5), pp. 1775-1785, 2004.

[38] M. A. LIEBERMAN, J.-P. BOOTH, P. CHABERT, J.-M. RAX, and M. M. TURNER, "Standing Wave And Skin Effects in Large-Area, High-Frequency Capacitive Discharges," Plasma Sources Science and Technology, vol. 11, pp. 283-293, 2002.

[39] M. J. COLGAN and M. MEYYAPPAN, "Very High Frequency Capacitive Plasma Sources," in *High Density Plasma Sources: Design, Physics and Performance*, O. A. POPOV, Ed. Park Ridge, New Jersey, USA: Noyes Publications, 1995, pp. 149-190.

[40] M. KONUMA, *Film Deposition by Plasma Techniques*. Berlin: Springer-Verlag, 1992.

[41] Y. P. RAIZER and M. N. SHNEIDER, "Radio-Frequency Capacitive Discharge in a Long Strip Line," IEEE Transactions on Plasma Science, vol. 26(3), pp. 1017-1021, 1998.

[42] Y. OHTSU and H. FUJITA, "Production of high-density capacitively coupled radio-frequency discharge plasma by high-secondary-electron-emission oxide," Applied Physics Letters, vol. 85(21), pp. 4875-4877, 2004.

[43] D. M. POZAR, *Microwave Engineering*, 2nd edition ed. New York: John Wiley & Sons, Inc., 1998.

[44] E. PLEULER, C. WILD, M. FÜNER, and P. KOIDL, "The CAP-reactor, a novel microwave CVD system for diamond deposition," Diamond and Related Materials, vol. 11, pp. 467-471, 2002.

[45] M. J. BUIE, J. T. PENDER, J. SONIKER, M. L. BRAKE, and M. ELTA, "In situ diagnostic for etch uniformity," Journal of Vacuum Science & Technology A, vol. 13(4), pp. 1930-1934, 1995.

[46] M. J. BUIE, J. T. PENDER, J. P. HOLLOWAY, and M. L. BRAKE, "In Situ Sensor of Spatially Resolved Optical Emission," IEEE Transactions on Plasma Science, vol. 24(1), pp. 111-112, 1996.

[47] J. T. PENDER, M. J. BUIE, T. VINCENT, J. P. HOLLOWAY, M. ELTA, and M. L. BRAKE, "Radial optical emission profiles of radio frequency glow discharges," Journal of Applied Physics, vol. 74(5), pp. 3590-3592, 1993.

[48] M. A. LIEBERMAN and A. J. LICHTENBERG, *Principles of plasma discharges and materials processing*, 2nd Edition ed. New York etc.: John Wiley & Sons, 2005.

[49] J. P. M. SCHMITT, 2001, "Plasma Reactor for The Treatment of Large Size Substrates," US, Patent Specification US 6,228,438 B1, US 09/401,158, UNAXIS Balzers Aktiengesellschaft (LI), 11 p.

[50] U. STEPHAN, J. KUSKE, W. FRAMMELSBERGER, P. LECHNER, W. PSYK, and H. SCHADE, "Large Area Deposition Technique for PECVD of Amorphous Silicon," in 26th PVSC. Anaheim, CA, 1997.

[51] J. P. M. SCHMITT, "Course: Waves in Plasma Capacitor," unpublished.

[52] J. P. M. SCHMITT, "Recent devlopments in plasma processing of large area substrates," presented at ISPC XV, Orléans, 2001.

[53] J. P. M. SCHMITT, "Glow Discharge Processing in the Liquid Crystal Display Industry," presented at ICPIG, Nagoya, 2001.

[54] H. CURTINS, N. WYRSCH, M. FAVRE, and A. V. SHAH, "Influence of plasma excitation frequency fora-Si:H thin film deposition," Plasma Chemistry and Plasma Processing, vol. 7(3), pp. 267-273, 1987.

[55] M. HEINTZE, R. ZEDLITZ, and G. H. BAUER, "Analysis of high-rate a-Si:H deposition in a VHF plasma," Journal of Physics D: Applied Physics, vol. 26(10), pp. 1781-1786, 1993.

[56] ADVANCED-ENERGY, "Impedance Matching," Advanced Energy, Fort Hills, Colorado, USA, Whitepaper SL-WHITE18-270-01 1M 03/01, 03/2001 1992.

[57] V. BROUK and R. HECKMAN, "Stabilizing RF Generator and Plasma Interactions," in 47th Annual Technical Conference. Dallas, TX, USA: Society of Vacuum Coaters, 2004, pp. 49-54.

[58] F. F. CHEN, "Langmuir Probe Diagnostics," presented at IEEE-ICOPS Meeting, Jeju, Korea, 2003.

[59] L. SANSONNENS, A. A. HOWLING, and C. HOLLENSTEIN, "Degree of dissociation measured by FTIR absorption spectroscopy applied to VHF silane plasmas," Plasma Sources Science and Technology, vol. 7(2), pp. 114-118, 1998.

[60] L. SANSONNENS, A. A. HOWLING, and C. HOLLENSTEIN, "Large Area Depostion of Amorphous and Microcrystalline Silicon by Very High Frequency Plasma," presented at Materials Research Society Symposium Proceedings, 1998.

[61] J. PERRIN, J. P. M. SCHMITT, C. HOLLENSTEIN, A. A. HOWLING, and L. SANSONNENS, "The physics of plasma-enhanced chemical vapour deposition for large-area coating: industrial application to flat panel displays and solar cells," Plasma Physics and Controlled Fusion, vol. B42(Suppl. 12B), pp. B353-B363, 2000.

[62] J. BALLUTAUD, C. HOLLENSTEIN, A. A. HOWLING, L. SANSONNENS, H. SCHMIDT, and J. P. M. SCHMITT, "Consequences of non-uniform RF plasma potential in large-area capacitive reactors," presented at ISPC-023, Int. Symp. Plasma Chemistry ISPC16, Taormina, Italy, 2003.

[63] A. A. HOWLING, "Power Transfer Efficiency to a RF Plasma Reactor via a Transmission Line (Balanced, Shielded) of Length Comparable to the RF Wavelength," unpublished.

[64] A. A. HOWLING, L. DERENDINGER, L. SANSONNENS, H. SCHMIDT, C. HOLLENSTEIN, E. SAKANAKA, and J. P. M. SCHMITT, "Probe measurements of plasma potential nonuniformity due to edge asymmetry in large-area radio-frequency reactors: The telegraph effect," Journal of Applied Physics, vol. 97(143511-1), pp. 143511-143513, 2005.

[65] S. P. NIKULIN and S. V. KULESHOV, "Generation of Homogeneous Plasma in a Low-Pressure Glow Discharge," Technical Physics Letters, vol. 45(4), pp. 400-405, 2000.

[66] J. RÜDIGER, H. BRECHTEL, A. KOTTWITZ, J. KUSKE, and U. STEPHAN, "VHF Plasma processing for in-line deposition systems," Thin Solid Films, vol. 427(1-2), pp. 16-20, 2003.

[67] J. M. WHITE and K. S. LAW, 2003, "Method and Apparatus for Substrate Processing," US, Patent Specification US 10/066,131, Applied Materials, Inc., 1-33 p.

[68] L. SANSONNENS, private communication, 2002.

[69] L. SANSONNENS, private communication, 2002.

[70] L. SANSONNENS, "Gaussian Lens Part I, First Theoretical Presentation," unpublished.

[71] L. SANSONNENS, "Gaussian Lens, Part II, First Theoretical Presentation," unpublished.

[72] L. SANSONNENS, "Solution of electrode shape including the effect of plasma for uniform radio-frequency capacitively-coupled plasma excitation," unpublished.

[73] L. SANSONNENS, B. STRAHM, L. DERENDINGER, A. A. HOWLING, C. HOLLENSTEIN, C. ELLERT, and J. P. M. SCHMITT, "Measurements and Consequences of Non-Uniform RF plasma Potential due to Surface Asymmetry in Large Area RF Capactive Reactors," Journal of Vacuum Science & Technology A, vol. 23(4), pp. 922-926, 2005.

[74] M. HONDA, and H. HARUTA, *Impedance Measurement Handbook*, 2nd ed: AGILENT Technologies, 2000.

[75] Y. OHTSU, T. SHIMAZOE, T. MISAWA, and H. FUJITA, "High-density plasma production with capacitively coupled RF discharge using high Gamma coefficient material electrodes," in XXVI International Conference on Phenomena in Ionized Gases ICPIG. Greifswald, Germany, 2003.

[76] M. SURENDRA and D. B. GRAVES, "Capacitively coupled glow discharges at frequencies above 13.56 MHz," Applied Physics Letters, vol. 59(17), pp. 2091-2093, 1991.

[77] H. CURTINS, "Process for Depositing Amorphous Hydrogenated Silicon in a Plasma Chamber," US Patent US 4,933,203, 376,952, Jul. 7, 1989.

[78] W. G. J. H. M. VAN SARK, H. MEILING, E. A. G. HAMERS, J. BEZEMER, and W. F. VAN DER WEG, "Sheath thickness in very-high-frequency plasma chemical vapor deposition of hydrogenated amorphous silicon," Journal of Vacuum Science & Technology A, vol. 15(3), pp. 654-658, 1997.

[79] P. KREJCIK, "Waveguide Stub-Line Tuning of RF Cavities with Heavy Beam Loading," presented at Particle Accelerator Conference, Vancouver, BC, CND, 1997.

[80] M. MEYYAPPAN and M. J. COLGAN, "Very high frequency capacitively coupled discharges for large area processing," Journal of Vacuum Science & Technology A, vol. 14(5), pp. 2790-2794, 1996.

[81] M. FIVAZ, S. BRUNNER, W. SCHWARZENBACH, A. A. HOWLING, and C. HOLLENSTEIN, "Reconstruction of the time-averaged sheath potential profile in an argon radiofrequency plasma using the ion energy distribution," Plasma Sources Science and Technology, vol. 4(3), pp. 373-378, 1995.

[82] E. V. BARNAT and G. A. HEBNER, "Plasma nonuniformities induced by dissimilar electrode metals," Journal of Applied Physics, vol. 98(013305), pp. 1-7, 2005.

[83] N. MUTSUKURA, K. KOBAYASHI, and Y. MACHI, "Plasma sheath thickness in radio-frequency discharges," Journal of Applied Physics, vol. 68(6), pp. 2657-2660, 1990.

[84] C. BENEKING, "Power dissipation in capacitively coupled rf discharges," Journal of Applied Physics, vol. 68(9), pp. 4461-4473, 1990.

[85] J. P. M. SCHMITT, "Amorphous silicon deposition: Industrial and technical challenges," Thin Solid Films, vol. 174(Part 1), pp. 193-202, 1989.

[86] AURION, "Impedance Matching Networks," 2005, http://www.aurion.de/p_enpri.htm.

[87] MKS-ENI, "New Performance Standards For RF Power Generators In Plasma Applications," 2005, http://www.mksinst.com/eni-WATTS-TN.html.

[88] AMPLIFIER-RESEARCH, "Application Note 27: The Importance of Load Tolerance in Specifying RF Power Amplifiers For Immunity/Susceptibility Testing Applications," 2005, http://www.arww-rfmicro.com/pdfs/appNotes/AppNote27.pdf.

[89] D. HE and D. R. HALL, "Longitudinal voltage distribution in transverse rf discharge waveguide lasers," Journal of Applied Physics, vol. 54(8), pp. 4367-4373, 1983.

[90] R. L. SINCLAIR and J. TULIP, "Radio-Frequency Excited CO2 Waveguide Lasers," Review of Scientific Instruments, vol. 55(10), pp. 1539-1541, 1984.

[91] E. F. PLINSKI, J. S. WITKOWSKI, and K. M. ABRAMSKI, "Algorithm of RF-excited slab-waveguide laser design," Journal of Physics D: Applied Physics, vol. 33, pp. 1823-1826, 2000.

[92] G. A. GRIFFITH, "Improved discharge uniformity for transverse radio frequency waveguide CO2 lasers," presented at Advanced laser technology and applications, Arlington - Virginia, USA, 1982.

[93] G. A. GRIFFITH, 1982, "RF Pumped Waveguide Laser With Inductive Loading for Enhancing Discharge Uniformity," US, Patent Specification US4,352,188, Appl. No.: 165,524, Hughes Aircraft Company, 6 p.

[94] K. D. LAAKMANN, 1979, "Waveguide Gas Laser With High Frequency Transverse Discharge Excitation," US, Patent Specification US4,169,251, Appl. No.: 869,542, Hughes Aircraft Company, 6 p.

[95] Optics For Reasearch (OFR), "Fiber-Optic Formulas," 2002, http://www.ofr.com/tech_fiber_formula_1.htm, http://www.ofr.com/tech_fiber_formula_2.htm, http://www.ofr.com/tech_opticformula.htm, http://www.ofr.com/tech_opticformula1.htm.

[96] KINGFISHER, "Application Notes," 2005, http://www.kingfisher.com.au/ApplicationNotes.htm.

[97] L. SANSONNENS, H. SCHMIDT, A. A. HOWLING, C. HOLLENSTEIN, C. ELLERT, and A. BUECHEL, "Application of the shaped electrode technique to a large area rectangular capacitively-coupled plasma reactor to suppress standing wave nonuniformity," presented at AVS 2005, 2005.

[98] L. SANSONNENS, A. A. HOWLING, and C. HOLLENSTEIN, "Electromagnetic nonuniformities due to standing wave and electrode asymmetry (telegraph) effects in large area, high-frequency capacitive plasma reactors," Plasma Sources Science and Technology, submitted 2005.

[99] T. YAMAGISHI, H. ARAI, and K. SATOH, 2004, "Plasma Treatment Apparatus," US, Patent Specification US 2004/0194709 A1, ASM Japan, 1-17 p.

[100] D. E. CARLSON, M. DiCOLLI, F. JACKSON, G. GANGULY, and M. BENNETT, "The use of plasma emission diagnostics to improve the performance of large-area a-Si PV modules," presented at Twenty-Ninth IEEE Photovoltaic Specialists Conference, New Orleans, Louisiana, 2002.

[101] D. E. CARLSON, G. GANGULY, J. N. NEWTON, G. WOOD, M. BENNETT, F. WILLING, and R. R. ARYA, "Amorphous Silicon Solar Cell Research at BP Solar," presented at NCPV Program Review Meeting, 2001.

[102] V. A. LISOVSKIY, S. MARTINS, K. LANDRY, D. DOUAI, J.-P. BOOTH, V. CASSAGNE, and V. D. YEGORENKOV, "The effect of discharge chamber geometry on the ignition of low-pressure rf capacitive discharges," Physics of Plasmas, vol. 12(093505), pp. 1-8, 2005.

[103] S. J. GITHENS, "The Influence of Discharge Chamber Structure Upon the Initiating Mechanism the High Frequency Discharge," Physical Review, vol. 57(9), pp. 822-828, 1940.

[104] J. P. M. SCHMITT, "Problems in Large Size Amorphous Silicion Plate Manufacturing," presented at Materials Research Society Symposium Proceedings: Amorphous silicon technology - 1991, Anaheim, Californiy, 1991.

[105] A. BUBENZER and J. P. M. SCHMITT, "Plasma processes under vacuum conditions," Vacuum Surface Engineering, Surface Instrumentation & Vacuum Technology, vol. 41(7-9), pp. 1957-1961, 1990.

[106] S. RAMO, J. WHINNERY, and T. VAN DUZER, *Fields and Waves in Communication Electronics*, 3rd ed. New York: Wiley, 1994.

[107] J.-L. LACHAMBRE, J. MACFARLANE, G. OTIS, and P. LAVIGNE, "A transversely rf-excited CO2 waveguide laser," Applied Physics Letters, vol. 32(10), pp. 652-653, 1978.

[108] K. D. LAAKMANN, "Transverse RF Excitation for Waveguide Lasers," presented at International Conference on Lasers; organized by Society For Optical & Quantum Electronics, Orlando, Florida, USA, 1978.

[109] H. STÖCKER, *Taschenbuch der Physik*, 4. korrigierte Auflage Thun und Frankfurt am Main: Harri Deutsch, 2000.

[110] R. P. FEYNMAN, R. B. LEIGHTON, and M. SANDS, "The Feynman lectures on physics," vol. 2. Reading, MA, USA: Addison-Wesley, 1963-1965, pp. 23-21 through 23-26.

[111] H. J. PAIN, *The Physics of Vibration and Waves*, 4th ed. Baffins Lane, Chichester, England: WILEY, 1993.

[112] H. J. BAKER, G. A. J. MARKILLIE, J. G. BETTERTON, and D. R. HALL, "Spatially resolved measurement of the electrical properties of the rf discharge in a fast-axial-flow CO2 laser with a rectangular cross section," Measurement Science and Technology, vol. 9(9), pp. 1456-1461, 1998.

[113] R. SORRENTINO, "Planar Circuits, Waveguide Models, and Segmentation Method," IEEE Transactions on Microwave Theory and Techniques, vol. 33(10), pp. 1057-1066, 1985.

[114] C. BÖHM and J. PERRIN, "Spatially resolved optical emission and electrical properties of SiH4 RF discharges at 13.56 MHz in a symmetric parallel-plate configuration," Journal of Physics D: Applied Physics, vol. 24(6), pp. 865-881, 1991.

[115] J. P. M. SCHMITT, 1989, "Plasma-assisted method for thin film fabrication," US, Patent Specification US 4,798,739, 921072, Solems (Palaiseau, FR), January 17, 1989 p.

[116] F. HEINRICH, U. BÄNZIGER, A. JENTZSCH, G. NEUMANN, and C. HUTH, "Novel high-density plasma tool for large area flat panel display etching," Journal of Vacuum Science & Technology B, vol. 14(3), pp. 2000-2004, 1996.

[117] A. A. HOWLING, "Interpretation of Langmuir and Surface Probes in RF Capacitively-Coupled Reactors. - I/V characteristics for RF-driven sheaths, including the Telegraph effect.," unpublished.

[118] E. STARKLOFF, "Improve Your Systems with Timng and Synchronization," in NI Instrumentation Newsletter, The Worldwide Publication for Measurement and Automation, vol. First Quarter 2003, 2003, pp. 6-7.

[119] W. HAAG, UNAXIS-Balzers AG, Balzers, private communication, 24.11.2005.

[120] S. Y. CHOI, T. K. WON, and J. M. WHITE, "Method of controlling the uniformity of PECVD-deposited thin films: Increasing film deposition uniformity of deposited film over substrate surface for thin film transistor, by reducing electrode spacing between parallel plate electrodes, reducing electron density of plasma, and selecting plasma source gas," US Patent Appl. 962936, Publ. No. US 2005/0233092 A1, 2004.

[121] G. BRÄUER, H. KLOBERDANZ, H. G. LOTZ, J. M. SCHNEIDER, A. ZÖLLER, H. HAGEDORN, M. KÖNIG, J. MEINEL, and G. TESCHNER, 2000, "Vorrichtung zur Beschichtung von Substraten in einer Vakuumkammer," EU, Patent Specification EP 0 984 076 A1, 99110375.5, Leybold Systems GmbH, 11 p.

[122] E. TURLOT, T. EMERAUD, and J. P. M. SCHMITT, "Plasma treatment apparatus and method for operating same," US Patent US5515986, US 237575, 1996-05-14.

[123] H. CURTINS, N. WYRSCH, and A. V. SHAH, "High Rate Deposition of Amorphous Hydrogenated Silicon: Effect of Plasma Excitation Frequency," Electronics Letters, vol. 23(5), pp. 228-230, 1987.

[124] A. A. HOWLING, L. SANSONNENS, and C. HOLLENSTEIN, "Electromagnetic Sources of Non-uniformity in large-area capacitive reactors," Thin Solid Films, submitted 2005.

[125] V. A. LISOVSKIY, J.-P. BOOTH, S. MARTINS, K. LANDRY, D. DOUAI, and V. CASSAGNE, "Extinction of RF capacitive low-pressure discharges," Europhysics Letters, vol. 71(3), pp. 407-411, 2005.

[126] W. J. GETSINGER, "End-Effects in Quasi-TEM Transmission Lines," IEEE Transactions on Microwave Theory and Techniques, vol. 41(4), pp. 666-672, 1993.

Curriculum Vitae

Born in Bregenz/AT; August 17, 1971; Austrian.

Education

- Since 1.3.2001 Doctoral Candidate at CRPP/EPFL, Groupe Plasma Industriel with Dr. Ch. Hollenstein and Prof. M. Q. Tran.
- 1992-1999 Degree in Physics at Swiss Federal Instiute of Technology (ETHZ), Zurich and Diploma Thesis on Organic Light Emitting Diodes (IBM Zurich Research Lab).
- 1989-1992 Studies in Computer Science at ETHZ, with two terms of practical training, no graduation.
- 1981-1989 Grammar school Bundesgymnasium Feldkirch-Levis/AT with A-level and seminar paper in physics on the Fractal Geometry of Nature.

Work Experience and Practical Trainings

- 2001 UNAXIS Displays, Trübbach/CH, Basic Engineering.
- 2000-2001 Transfusion Centre of the Austrian Red Cross, Feldkirch/AT, Mandatory Community Service.
- 1999-2000 UNAXIS Displays, Palaiseau/Paris/FR, PECVD Process Engineering.
- 1999 HighQLaser/Hohenems/AT.
- 1996-1998 IBM Zurich Research Lab, Rüschlikon/CH, Display Group, Working Student.
- 1992-1999 Board member of the students' bookshop at ETHZ.
- 1991 HILTI AG, Schaan/FL, computer department (SAP R/2).
- 1990 BALZERS AG, Balzers/FL, software developement.
- 1990 HILTI AG, Thüringen/AT, computer department.
- 1988,89,90 IBM Austria, Bregenz/AT, Temporary worker at the technical service.

Publications

1. H. SCHMIDT, L. SANSONNENS, A. A. HOWLING, C. HOLLENSTEIN, M. ELYAAKOUBI, and J. P. M. SCHMITT, "Improving plasma uniformity using lens-shaped electrodes in a large area very high frequency reactor," Journal of Applied Physics, vol. 95(9), pp. 4559-4564, 2003.
2. L. SANSONNENS, J. P. M. SCHMITT, A. A. HOWLING, J. BALLUTAUD, H. SCHMIDT, and C. HOLLENSTEIN, "Challenges in RF plasma deposition on square-meter substrates," presented at 14th Int. Colloq. Pl. Processes, Antibes, France, 2003.
3. J. BALLUTAUD, C. HOLLENSTEIN, A. A. HOWLING, L. SANSONNENS, H. SCHMIDT, and J. P. M. SCHMITT, "Consequences of non-uniform RF plasma potential in large-area capacitive reactors," presented at ISPC-023, Int. Symp. Plasma Chemistry ISPC16, Taormina, Italy, 2003.
4. A. A. HOWLING, L. SANSONNENS, J. P. M. SCHMITT, J. BALLUTAUD, H. SCHMIDT, and C. HOLLENSTEIN, "Elimination of electromagnetic non-uniformities in large-area RF plasma reactors used for thin film deposition," in SSP, 2004.
5. A. A. HOWLING, L. DERENDINGER, L. SANSONNENS, H. SCHMIDT, C. HOLLENSTEIN, E. SAKANAKA, and J. P. M. SCHMITT, "Probe measurements of plasma potential nonuniformity due to edge asymmetry in large-area radio-frequency reactors: The telegraph effect," Journal of Applied Physics, vol. 97(123308), pp. 1-13, 2005.
6. L. SANSONNENS, H. SCHMIDT, A. A. HOWLING, C. HOLLENSTEIN, C. ELLERT, and A. BUECHEL, "Application of the shaped electrode technique to a large area rectangular

capacitively-coupled plasma reactor to suppress standing wave nonuniformity," presented at AVS 2005, submitted to JVSTA, 2005.